Biochemical Functions of Mitochondrial ADCK3 and Other Coenzyme Q Biosynthesis Proteins

By

Jonathan Allan Stefely

A dissertation submitted in partial fulfillment

of the requirements for the degree of

Doctor of Philosophy

(Biochemistry)

at the

UNIVERSITY OF WISCONSIN - MADISON

2015

Date of final oral examination: 7/30/2015

This dissertation is approved by the following members of the Final Oral Committee:
David J. Pagliarini, Associate Professor, Biochemistry
Joshua J. Coon, Professor, Chemistry and Biomolecular Chemistry
Elizabeth A. Craig, Professor, Biochemistry
Laura L. Kiessling, Professor, Chemistry and Biochemistry
Mark E. Burkard, Associate Professor, Medicine

Dedicated to Erin,

Mom, and Dad

Acknowledgments

My years in graduate school presented challenges and pressures, but my companions consistently brought excitement and joy to this journey. I am grateful for all of my supporters.

I thank Professor Dave Pagliarini, my advisor, for being an outstanding role model. I learned much by watching Dave build a research group, establish a scientific identity, collaborate with numerous scientists, and guide rigorous research. I thank Dave for giving me the opportunity to be a part of his group during this "start up" phase. Perhaps most importantly, Dave provided a model for how to interact with people. Some of my favorite moments at work were impromptu hallway conversations with Dave, which often led to breakthrough ideas. Outside of the lab, Dave's unwavering commitment to his family was always evident, and I thank him for going above and beyond to help me maintain my own family life.

I thank the members of my thesis committee for their support and stimulating questions. Professor Josh Coon enabled me to participate in cutting-edge, large-scale, collaborative science, and he showed me the value of leveraging new technologies. Professor Betty Craig graciously opened the doors of her lab, in which I first learned how to work with yeast. Professor Laura Kiessling kept me grounded to my organic chemistry training, always considering the basic chemical features of complex biological problems. Professor Mark Burkard provided valuable expertise on signaling and kinases and helped me to consider the medical implications of my basic science research. My committee members have also been outstanding role models, and I hope to follow their examples.

I thank all of my colleagues and collaborators, from whom I learn much and with whom I enjoy working. I especially thank 3 people with whom I have worked consistently over the past few years: Adam Jochem, Andrew Reidenbach, and Arne Ulbrich. Adam conducted numerous

cloning projects and joined the 18-hour shifts demanded by our Y3K project. Andrew Reidenbach and I worked together closely on ADCK3, over which we sweat, cried, and laughed. Arne Ulbrich expertly conducted ~2,000 LC-MS/MS runs for CoQ-related work and for the Y3K project. In addition to Adam, Andrew, and Arne, I thank the additional co-authors of my 2015 *Molecular Cell* paper on ADCK3 (Krishnadev Oruganty, Brendan Floyd, Catherine Minogue, Jacklyn Saunders, Isabel Johnson, Grant Barber, Russell Wrobel, David Lee, Sheng Li, Natarajan Kannan, Craig Bingman, Josh Coon, and Dave Pagliarini). I thank the other members of the "Q branch", Danielle Lohman and Zack Kemmerer. I thank the entire Y3K team (Alex Hebert, Nick Kwiecien, Alicia Richards, Matt Rush, Arne Ulbrich, Mike Veling, Elyse Frieberger, Alan Higbee, Michael Westphall, Dave Pagliarini, and Josh Coon). And I thank our French collaborators on the *Adck3*$^{-/-}$ mice (Hélène Puccio, Floriana Licitra, and Leila Lredj). Working together with all of these scientists has significantly raised the impact of our work.

I thank the undergraduates that I had the privilege of mentoring: Grant Barber and Isabel Johnson. Through their questions and energy, I became a better scientist. Watching them develop into independent scientists has been gratifying.

I thank my family for their constant support. My sisters, Kathleen and Elizabeth, and my brother, Matthew, have always brought laughter into my day. My mother, Carolyn, has always been steady with caring love, and my father, James, has always been a calm rock of wisdom onto which I could retreat. Their encouragement always gives me energy.

Finally, and most gratefully, I thank my wife, Erin, for her love, understanding, and patience. I joyfully look forward to continuing our life together.

Biochemical Functions of Mitochondrial ADCK3

and Other Coenzyme Q Biosynthesis Proteins

Jonathan Allan Stefely

Under the supervision of Professor David J. Pagliarini

At the University of Wisconsin - Madison

Abstract of dissertation

Mitochondria are energetic organelles with widespread impacts on human health and disease. Numerous gaps in knowledge about mitochondria act as a bottleneck in medical genetics and in the treatment of mitochondrial disease. Toward filling these gaps, I took two approaches: one ‘small’—dissecting subtle chemical features of an individual mitochondrial protein—and one ‘large’—profiling thousands of phenotypes after hundreds of distinct mitochondrial perturbations. Each of these approaches afforded new knowledge about the functions of mitochondrial proteins, expanding our molecular understanding of health and disease.

In the first, molecular-scale approach, I investigated the biochemical function of the human mitochondrial protein ADCK3, which enhances the biosynthesis of coenzyme Q. Using the first crystal structure of ADCK3, which we solved, I systematically identified numerous unique features and showed that they are essential for function in a yeast model system. Using a ligand-binding assay, I determined that subtly altering these features changes the selectivity of ADCK3 nucleotide binding. I also discovered that these same mutations enable autophosphorylation activity, the first demonstration of enzymatic activity for this protein family. More recently, I identified competing enzymatic activities, ATPase activity and

potentially lipid kinase activity, which may play important functional roles. Based on this work, I present new models for ADCK3 function, with an emphasis on implications for the larger protein kinase-like superfamily.

In the second, large-scale approach, which is ongoing, I am collaborating closely with the laboratory of Professor Joshua Coon to functionally profile numerous uncharacterized mitochondrial proteins. Recent advances from our laboratories in culturing yeast and mass spectrometry technology enabled this project. Because we are profiling over 3,000 phenotypes across over 1,000 proteomes, 1,000 lipidomes, and 1,000 metabolomes, we call this effort the "Y3K" project. Early results from this project reveal new gene functions in mitochondrial oxidative phosphorylation and coenzyme Q biosynthesis.

Chapter 1 defines a specific set of gaps in knowledge about mitochondrial biochemistry, those related to mitochondrial coenzyme Q (CoQ) biosynthesis. This review also provides an outlook at how filling these gaps could have widespread clinical impacts. Chapter 2, which was recently published in *Molecular Cell*, begins to fill one of the CoQ-related knowledge gaps by showing that mitochondrial ADCK3 employs an atypical protein kinase-like fold to enable CoQ biosynthesis. Chapter 3 presents unpublished data to support new models for the function of ADCK3 and its widespread UbiB family. Chapter 4 presents additional unpublished data generated by our large-scale "Y3K" project aimed at systematically annotating uncharacterized mitochondrial proteins through global protein-lipid-metabolite profiling. Discussion of the broader implications of each body of work is provided at the end of each chapter.

Table of Contents

Dedication.....i

Acknowledgments ii

Abstract of Dissertation iv

Table of Contents vi

Chapter 1. Defining and filling biochemical gaps in mitochondrial coenzyme Q biosynthesis 1

Chapter 2. Mitochondrial ADCK3 employs an atypical protein kinase-like fold to enable coenzyme Q biosynthesis 40

Chapter 3. Unorthodox functions of an ancient kinase-like family enable isoprenoid lipid biosynthesis 104

Chapter 4. Mitochondrial protein functions revealed by global protein-lipid-metabolite profiles 163

List of Tables and Figures

Chapter 1

Figure 1. Chemical and biological functions of coenzyme Q 20

Figure 2. Current model for the CoQ biosynthesis pathway 21

Figure 3. Models of additional problems in CoQ metabolism 22

Figure 4. CoQ deficiency in human health and disease 23

Table 1. Reactions of eukaryotic CoQ biosynthesis and metabolism 24

Table 2. Structures of eukaryotic CoQ biosynthesis proteins 25

Chapter 2

Figure 1. Unique sequence features of the UbiB family and ADCK3 75

Figure 2. X-ray crystal structure of ADCK3$^{N\Delta254}$ 77

Table 1. ADCK3$^{N\Delta254}$ data collection and refinement statistics 78

Figure 3. ADCK3 adopts an atypical PKL active site that binds nucleotides 79

Figure 4. A single A-to-G mutation of the A-rich loop flips nucleotide selectivity and enables ADCK3 autophosphorylation 81

Figure 5. UbiB-specific features of Coq8p are required for yeast growth and CoQ biosynthesis 83

Figure 6. Pathogenic ADCK3 mutations disrupt protein stability 84

Figure S1. CHAIN analysis of the UbiB family identifies signature motifs 85

Figure S2. ADCK3 adopts an atypical PKL fold 87

Figure S3. Kinase ‘spines’ and nucleotide binding properties of ADCK3 89

Figure S4. Identification of an ADCK3$^{N\Delta250}$ A339G autophosphorylation site and a model for KxGQ domain movement.....91

Figure S5. Effects of Coq8p mutations on yeast growth kinetics 94

Figure S6. Effects of pathogenic mutations on ADCK4 96

Chapter 3

Figure 1. Adck3 is required for the stability of the coenzyme Q biosynthesis complex in mice 138

Figure 2. Coq8p is required specifically for the stability of the CoQ complex in yeast 139

Figure 3. Coq8p autophosphorylates exclusively *in cis* 141

Figure 4. Models for ADCK3 and Coq8p function 143

Figure 5. Coq8p catalyzes ATPase activity with its UbiB-specific KxGQ motif 144

Figure 6. ADCK3 activity is affected by small molecules 145

Figure 7. X-ray crystal structure of ADCK3$^{N\Delta254}$ R611K bound to a nucleotide 147

Figure S1. The phosphoproteome of Adck3$^{-/-}$ mice is perturbed 148

Figure S2. The mitochondrial proteome and phosphoproteome of Δ*coq8* yeast is perturbed 149

Figure S3. Mitochondrial Coq8p binds adenine nucleotides.....151

Figure S4. Autophosphorylation activity of Coq8p and ADCK3 153

Figure S5. Testing the ADCK3 and Coq8p ATPase model 155

Figure S6. Features of CoQ biosynthesis related to the small molecule kinase model of ADCK3 function.....156

Chapter 4

Figure 1. Protein-lipid-metabolite profiling by mass spectrometry 178

Figure 2. Identification of a stable respiratory growth condition 179

Figure 3. Target strain selection 180

Figure 4. Yeast growth rates 181

Figure 5. Respiration-fermentation differences 182

Figure 6. Correlations between perturbation profiles reveal functional relationships 183

Figure 7. Yjr120w affects ATP synthase 185

Figure 8. Molecular insight into CoQ biosynthesis 187

Extended Data Table 1. Y3K target strains 189

Chapter 1

Defining and filling biochemical gaps in mitochondrial coenzyme Q biosynthesis

Jonathan A. Stefely & David J. Pagliarini

Abstract

The discovery of coenzyme Q (CoQ) in the 1950s filled a perplexing biochemical gap in the mitochondrial electron transport chain and provided a foundation for elucidating oxidative phosphorylation. The subsequent boom in bioenergetics research led to the discovery of numerous common diseases linked to mitochondrial dysfunction and CoQ deficiency. Yet, our understanding of human CoQ metabolism still has many gaps, and treatment of CoQ deficiency remains a challenge. Recent efforts to define the mitochondrial proteome placed a new spotlight on numerous uncharacterized proteins and incomplete pathways, including CoQ biosynthesis. In this review, we identify gaps in our current knowledge of mitochondrial CoQ biosynthesis at the biochemical level, highlight recent progress toward filling these gaps, and provide an outlook at the widespread clinical implications of fully defining the cellular machinery of CoQ metabolism.

Introduction

The discovery of coenzyme Q (CoQ) by Crane, Hatefi, Lester, and Widmer (Crane et al., 1957) in the laboratory of David E. Green at the University of Wisconsin-Madison was driven by a well-defined biochemical gap: the mitochondrial electron transport chain (ETC) could not be reconstituted with proteins alone (Crane, 1989, 2007). The lipid coenzyme Q filled this gap, enabled full reconstitution of the ETC *in vitro* (Hatefi et al., 1962; Heller et al., 1961), and became a central component of Mitchell's chemiosmosis theory for oxidative phosphorylation (OxPhos) (Mitchell, 1961). Soon after the discovery of CoQ, it became apparent that CoQ was the same as a lipid called "substance SA" (Festenstein et al., 1955), and subsequently ubiquinone (Morton, 1958a), that was discovered in vitamin A deficient rats (Lowe et al., 1953) by R. A. Morton and colleagues. The chemical structures of CoQ (Lester et al., 1958; Wolf, 1958) and ubiquinone (Morton, 1958a; Morton, 1958b) were determined concurrently and found to be identical.

The discovery of CoQ had implications for biology outside of mitochondria and eukaryotic organisms. CoQ was soon found in prokaryotes (Lester and Crane, 1959) and nearly all eukaryotic cellular membranes (Sastry et al., 1961). Moreover, the general use of lipids for electron transport is even more broadly conserved. Lipids similar to CoQ, such as plastoquinone, were soon found to support photophosphorylation and oxidative phosphorylation across all three superkingdoms of life (Kashket and Brodie, 1963; Redfearn and Friend, 1961).

The chemical structure of CoQ (Figure 1A) enables its biological functions. A long polyisoprene tail anchors CoQ to membranes and makes it one of the most hydrophobic molecules found in living organisms. The number of isoprene units present in this tail varies by organism (10 in human CoQ_{10}, 9 in mouse CoQ_9, 8 in *Escherichia coli* CoQ_8, and 6 in

Saccharomyces cerevisiae CoQ_6) (Lester and Crane, 1959), but its function as membrane anchor remains consistent. The headgroup of CoQ contains a quinone functionality, hence the name CoQ. This quinone headgroup can undergo reversible oxidation-reduction reactions (Figure 1B), which enables its primary function as a coenzyme in the ETC (Figure 1C). CoQ is a requisite gateway for electrons passed from OxPhos complexes I (NADH-CoQ oxidoreductase) and II (succinate-CoQ oxidoreductase) to complex III (CoQ-cytochrome c oxidoreductase) (Figure 1C). The redox chemistry of CoQ also involves protons (Figure 1B), the movement of which generates the proton motive force that drives OxPhos (Mitchell, 1961).

CoQ has additional functions outside of its role in OxPhos (Figure 1D). CoQ is a lipophilic antioxidant (Do et al., 1996; Frei et al., 1990; Green et al., 1961; Stocker et al., 1991), a cofactor for mitochondrial uncoupling proteins (Echtay et al., 2001; Echtay et al., 2000), a regulator of the mitochondrial permeability transition pore (Fontaine et al., 1998), and a membrane stabilizer (Sevin and Sauer, 2014). Furthermore, plastoquinone from chloroplasts can act as a retrograde signal to the nucleus (Petrillo et al., 2014), hinting that CoQ could also play a similar role in mitochondrial-nuclear retrograde signaling.

Given its widespread cellular functions, changes in CoQ production have powerful and complex effects on lifespan, health, and disease. On one hand, genetic defects in human CoQ biosynthesis can cause diseases ranging from isolated myopathy to severe infantile multisystemic disease (Quinzii and Hirano, 2010). Furthermore, CoQ abundance decreases with age (Kalen et al., 1989), a factor that may contribute to the decrease in mitochondrial function that is a hallmark of aging (Lopez-Otin et al., 2013) and is hypothesized to be the primary cause of aging (Wallace, 2005). On the other hand, genetic disruption of CoQ biosynthesis in *C. elegans* (Ewbank et al., 1997; Lakowski and Hekimi, 1996) or mice (Liu et al., 2005) can increase

lifespan. Moreover, a CoQ-deficient diet can extend *C. elegans* lifespan (Larsen and Clarke, 2002). The complex relationship between these contrasting effects is still largely undefined, in part because many gaps still exist in our understanding of CoQ metabolism.

Overview of CoQ biosynthesis

It was not immediately obvious that CoQ is synthesized endogenously by mammals, and the possibility that CoQ could be a vitamin was considered. However, the initial discovery of CoQ in vitamin A deficient rats (Lowe et al., 1953; Morton, 1958a), whose diet was also deficient of CoQ, argued for endogenous CoQ biosynthesis. A series of experiments showing incorporation of radiolabels from small organic precursors into CoQ provided the ultimate proof for endogenous CoQ biosynthesis, as detailed below.

Not only do mammals produce their own CoQ, but nearly every mammalian cell also produces its own CoQ. With the exception of brown adipose tissue, which was recently shown to uptake CoQ from the serum in a receptor-dependent manner (Anderson et al., 2015), CoQ is poorly absorbed into cells and tissues (Miles, 2007). Thus, most cells rely on their own endogenous CoQ biosynthesis.

The majority of eukaryotic CoQ is produced in the inner mitochondrial membrane (Momose and Rudney, 1972), but evidence for extra-mitochondrial CoQ biosynthesis also exists (Kalen et al., 1990; Kalen et al., 1987; Mugoni et al., 2013). This review focuses on mitochondrial CoQ biosynthesis as a general model, but many of the principles and problems discussed here also apply to eukaryotic extra-mitochondrial CoQ biosynthesis and prokaryotic CoQ biosynthesis.

CoQ biosynthesis occurs in 4 stages: (**I**) 4-hydroxybenzoate biosynthesis, (**II**) isoprene biosynthesis, (**III**) tail polymerization and attachment, and (**IV**) headgroup modification (Figure 2 and Table 1), as detailed below. Here, we present this biosynthetic pathway with a revised nomenclature for CoQ intermediates that is independent of the species (independent of the isoprenyl tail length), a historical context to highlight key experiments, and a biochemical framework that we hope will provide an intuitive chemical logic for thinking about problems in CoQ biosynthesis. Gaps in knowledge are emphasized to guide future research.

Reactions and enzymes of CoQ biosynthesis

Stage I. *4-hydroxybenzoate biosynthesis*. In mammals, the CoQ headgroup is derived from the essential amino acid phenylalanine (Figure 2), as demonstrated by incorporation of radiolabeled phenylalanine into the headgroup of CoQ (Bentley, 1961). Tyrosine and 4-hydroxybenzoic acid (4-HB) are even more efficient than phenylalanine as CoQ precursors. Furthermore, 4-HB can outcompete radiolabeled tyrosine for incorporation into CoQ (Olson et al., 1963), suggesting that 4-HB is the direct precursor for the CoQ headgroup. Mammals can convert dietary tyrosine into urinary 4-HB (Booth, 1960), but the enzymes responsible are undefined (Figure 2).

Unlike mammals, bacteria and yeast can produce 4-HB *de novo* through the shikimate pathway (Cox and Gibson, 1964; Gibson, 1962; Lawrence et al., 1974; Morgan, 1962), as reviewed previously (Aussel et al., 2014b; Meganathan, 2001). Nonetheless, 4-HB, once considered to be a bacterial vitamin (Davis, 1950), still enhances the growth of microorganisms, likely by boosting CoQ biosynthesis. Yeast can also use *p*-amino-benozoic acid (pABA) as an

alternative precursor to the CoQ headgroup (Marbois et al., 2010; Pierrel et al., 2010). The amino group from pABA must be subsequently deaminated by an enzyme that has not been identified.

Stage II. *Isoprene biosynthesis*. In mammals, the isoprene units for CoQ biosynthesis are generated through the mevalonate pathway (Figure 2), as demonstrated by incorporation of radiolabeled acetate and radiolabeled mevalonate into the isoprenyl tail of CoQ (Gloor and Wiss, 1959; Gold and Olson, 1966; Olson et al., 1963; Olson et al., 1965).

These early experiments were remarkable, because the biochemistry of the mevalonate pathway was still under investigation at the time CoQ was discovered in 1957. Mevalonate itself had just been discovered (Wright, 1956) and structurally characterized (Wolf, 1957) by a group led by Karl Folkers. The reactions to form β-hydroxy-β-methylglutaryl-CoA (HMG-CoA) from acetyl-CoA had just been elucidated (Rudney, 1957a; Rudney, 1957b) by the group of Harry Rudney. And the active isoprene intermediate itself, Δ^3-isopentenyl pyrophosphate (IPP), along with key intermediates such as 5-pyrophosphomevalonte, had just been discovered by the groups of Konrad Bloch (Chaykin et al., 1958) and Feodor Lynen (Lynen, 1958). This work on steroid biosynthesis set the stage for rapid discovery of acetate, mevalonate, and IPP as CoQ precursors.

Stage III. *Tail polymerization and attachment*. The work of Bloch and Lynen on IPP polymerization in steroid biosynthesis immediately suggested a mechanism by which the polyisoprene tail of CoQ could be produced: head-to-tail polymerization of allylic pyrophosphates (Chaykin et al., 1958) (Lynen, 1958). In the next step, which was also predicted by Lynen (Lynen, 1959), the CoQ polyisoprenyl tail is attached to the headgroup through an electrophilic aromatic substitution (Figure 2).

The prenyltransferase activities for these reactions were identified in mitochondrial lysates isolated from rats (Momose and Rudney, 1972; Winrow and Rudney, 1969) and yeast

(Casey and Threlfall, 1978). The *E. coli* gene *ubiA* was soon linked to the 4-HB:polyprenyltransferase activity (Young et al., 1972), and a crystal structure of this intramembrane enzyme was recently solved (Cheng and Li, 2014). However, the corresponding eukaryotic genes and proteins have been more elusive. After a series of CoQ-deficient yeast mutants were identified (Tzagoloff et al., 1975; Tzagoloff and Dieckmann, 1990), a brute force screen for mutant yeast mitochondria lacking the prenyltransferase activities *in vitro* led to the identification of Coq1p (Ashby and Edwards, 1990) and Coq2p (Ashby et al., 1992) as the responsible enzymes.

Coq1p, the polyprenyl-diphosphate synthetase, independently determines the length of the polyisoprene tail of CoQ (Okada et al., 1996). Coq1p is localized to the matrix side of the inner mitochondrial membrane (Gin and Clarke, 2005). The mammalian Coq1p homologs, Pdss1 and Pdss2, are also localized to the mitochondrial matrix (Pagliarini et al., 2008; Rhee et al., 2013). Similarly, the 4-HB:polyprenyltransferase Coq2p is also localized to the mitochondrial inner membrane, facing the matrix side (He et al., 2014).

In contrast to Coq1p and Coq2p, the IPP biosynthesis machinery is localized to the cytosol. The mechanism by which the highly polar IPP molecule moves from the cytosol to the mitochondrial matrix is unknown. We hypothesize that a transporter for the highly polar pyrophosphate-containing species exists in the inner mitochondrial membrane (Figure 2). Alternatively, IPP could be dephosphorylated to the neutral alcohol by a phosphatase, transported across the membrane, and then re-phosphorylated in the matrix by a kinase.

Similarly, a mitochondrial membrane transporter for the headgroup precursor has not been identified (Figure 2). Furthermore, which headgroup precursor is transported into mitochondria is unknown. If an early headgroup precursor, such as tyrosine, is transported into

mitochondria, then the subsequent enzymes that produce 4-HB are likely mitochondrial, but they have not been identified.

Stage IV. *Headgroup modification*. In the terminal stage of CoQ biosynthesis, the headgroup is modified by a decarboxylation and a series of hydroxylations and methylations (Figure 2). The currently proposed order of these reactions is based on isolation and characterization of CoQ intermediates, initially from large-scale lipid extractions of wild type bacteria (Friis, 1966; Olsen, 1966; Olsen, 1965). Work on *E. coli* by the group of Frank Gibson identified a number of mutant strains that accumulate larger amounts of specific intermediates (Cox et al., 1968), which enabled more rigorous chemical characterization and defined the bacterial CoQ biosynthesis genes (Young et al., 1973). Similarly, CoQ-deficient mutant yeast were identified by the group of Alexander Tzagoloff (Tzagoloff et al., 1975; Tzagoloff and Dieckmann, 1990) and characterized by the groups of Robert Olson (Goewert et al., 1981a; Goewert et al., 1981b) and Catherine Clarke (Tran and Clarke, 2007), which defined a number of the homologous eukaryotic CoQ biosynthesis genes.

The proposed sequence of CoQ headgroup modifications (Figure 2) also follows the chemical logic of electrophilic aromatic substitution (EAS) reactions. First, the 4-hydroxyl of 4-HB acts as an *ortho*-directing group to enhance EAS of the *C*3 and *C*5 positions. Second, the 4-hydoxyl acts as a *para*-directing group to enhance EAS of the *C*1 position. Third, the newly installed 1-hydroxyl group acts as an *ortho*-directing group to enhance EAS of the *C*2 and *C*6 positions. This simple chemical logic of EAS reactions, combined with specific substrate orientation in enzyme active sites, likely affords the regioselectivity needed to produce CoQ. However, these ideas about regioselectivity are largely untested *in vitro.*

The biochemical origin of the CoQ headgroup methyl groups and hydroxyl groups was defined by isotope labeling. Incorporation of radiolabeled methionine into the CoQ headgroup methoxyl groups and methyl group indicated *S*-adenosyl methionine (SAM) as their origin in *E. coli* (Jackman et al., 1967). Incorporation of heavy oxygen ($^{18}O_2$) into the CoQ headgroup methoxyl groups and the *C*1-hydroxyl group indicated molecular oxygen as their origin in aerobically grown *E. coli* (Alexander and Young, 1978b). SAM and O_2 are predicted to be the sources of the methyl groups and hydroxyl groups, respectively, in eukaryotic systems as well. Defining SAM and O_2 as co-factors in CoQ biosynthesis was an important step toward understanding the types of enzymes that might catalyze the reactions. Notably, *E. coli* can also produce CoQ anaerobically with a different set of hydroxylases that likely use H_2O instead of O_2 (Alexander and Young, 1978a). These bacterial anaerobic CoQ biosynthesis hydroxylases have not yet been identified.

C5-hydroxylation. The *C*5-hydroxylation is catalyzed by COQ6 in eukaryotes (Ozeir et al., 2011) and UbiI in prokaryotes (Hajj Chehade et al., 2013). Coq6p is peripherally associated with the matrix face of the inner mitochondrial membrane (Gin et al., 2003). Likewise, mammalian COQ6 is localized to the mitochondrial matrix (Pagliarini et al., 2008; Rhee et al., 2013). Coq6p is predicted to be a flavin-dependent monooxygenase that uses flavin adenine dinucleotide (FAD) as a cofactor and NAD(P)H as a coenzyme for reduction of FAD (Ozeir et al., 2011). The *C*5-hydroxylation requires the ferredoxin Yah1p and the ferredoxin reductase Arh1p (Pierrel et al., 2010), which are predicted to provide electrons to Coq6p in yeast. However, these eukaryotic enzymes have not yet been purified to test these hypotheses *in vitro*. A structure of truncated UbiI revealed a Rossman-like fold with a FAD binding site (Hajj Chehade et al., 2013), but no *in vitro* enzymology was reported.

O-methylation. The *O*-methylations are catalyzed by COQ3 in eukaryotes (Clarke et al., 1991; Goewert et al., 1981b; Gomez et al., 2012; Jonassen and Clarke, 2000; Marbois et al., 1994) and UbiG in prokaryotes (Hsu et al., 1996; Leppik et al., 1976a; Poon et al., 1999; Stroobant et al., 1972). Yeast Coq3p and mammalian COQ3 are localized to the mitochondrial matrix (Hsu et al., 1996; Pagliarini et al., 2008; Rhee et al., 2013). Purified UbiG or mitochondrial extracts containing COQ3 can catalyze both CoQ headgroup *O*-methlylations *in vitro* in a reaction that depends on SAM and a divalent cation (e.g. Zn^{2+} or Co^{2+}) (Hsu et al., 1996; Jonassen and Clarke, 2000; Leppik et al., 1976a; Poon et al., 1999). The molecular basis for the regioselectivity of COQ3, especially how it selectively catalyzes methylation of the *C*6-OH group of DMeQ over the *C*1-OH group, is unknown.

Decarboxylation. The decarboxylation is catalyzed by UbiD in prokaryotes (Cox et al., 1969), but the eukaryotic enzyme has not been identified. A second prokaryotic enzyme, UbiX, is also required for the decarboxylation reaction (Bar-Tana et al., 1980; Gulmezian et al., 2007; Howlett and Bar-Tana, 1980). Partial purification of UbiD demonstrated that it catalyzes decarboxylation of PPHB in a reaction that is enhanced by a small molecule cofactor (Leppik et al., 1976b). Recently, the enzyme UbiX was shown to catalyze prenylation of FMN to form a previously unknown prenylated-FMN (prFMN) cofactor that is required for the decarboxylase activity of UbiD (Lin et al., 2015; White et al., 2015). Evidence for decarboxlyation of the headgroup in mammals was first demonstrated by lack of radioactivity in the final CoQ product when [carbonyl-C^{14}]-*p*-hydroxybenzaldehyde was used as the headgroup precursor (Rudney and Parson, 1963). Polyprenyl vanillic acid (PPVA) (Figure 2) has been isolated from a mutant yeast strain (Goewert et al., 1981a), suggesting that the *C*5-methoxy group is installed before the decarboxylation reaction occurs. The identities of the eukaryotic CoQ headgroup decarboxylase

and the subsequent *C*1-hydroxylase remain major gaps in knowledge of CoQ biosynthesis. An important possibility to consider is that the *C*1-hydroxylation could be part of a catalytic mechanism that leads to decarboxylation. This would be a major deviation from the prokaryotic reaction sequence and mechanism, which could explain why no UbiD homolog appears to be involved in CoQ biosynthesis in eukaryotes.

C1-hydroxylation. The *C*1-hydroxylation is catalyzed by UbiH in prokaryotes (Young et al., 1973), but the eukaryotic enzyme has not been identified. Unlike the *C*5-hydroxylation described above, the eukaryotic *C*1-hydroxylation does not require Arh1p and Yah1p and may not even require FAD (Pierrel et al., 2010), suggesting a different enzyme mechanism. In contrast, prokaryotic UbiH is likely a flavin-dependent monooxygenase, as it shares 30% sequence identity with UbiI, the *C*5-hydroxylase described above (Hajj Chehade et al., 2013).

C2-methylation. The *C2*-methylation is catalyzed by COQ5 in eukaryotes (Barkovich et al., 1997; Dibrov et al., 1997; Nguyen et al., 2014) and UbiE in prokaryotes (Lee et al., 1997; Young, 1971). Yeast Coq5p and mammalian COQ5 are localized to the mitochondrial matrix (Barkovich et al., 1997; Dibrov et al., 1997; Nguyen et al., 2014; Pagliarini et al., 2008; Rhee et al., 2013). Lysates containing Coq5p or UbiE can catalyze DDMQ *C*2-methylation *in vitro* in a reaction that depends on SAM and NADH (Barkovich et al., 1997). Why NADH enhances this reaction has not been defined, but we hypothesize that the NADH helps keep the headgroup in the reduced state, which would enhance electrophilic aromatic substitution (Lederer, 1969). Recently, X-ray structures of Coq5p revealed a typical Rossmann-like fold with a SAM-dependent methyltransferase domain (Dai et al., 2014) (Table 2).

C6-hydroxylation. The *C*6-hydroxylation is catalyzed by COQ7 in eukaryotes (Ewbank et al., 1997; Jonassen et al., 1998; Marbois and Clarke, 1996; Nakai et al., 2001; Stenmark et al.,

2001) and UbiF in prokaryotes (Young, 1971). Coq7p is localized to the inner mitochondrial membrane (Jonassen et al., 1998). Likewise, mammalian COQ7 is largely localized to mitochondria (Pagliarini et al., 2008), but a nuclear form of COQ7 was recently identified in a mitochondrial-nuclear retrograde signaling pathway (Monaghan et al., 2015). Sequence analysis demonstrated that COQ7 belongs to a family of carboxylate-bridged diiron hydroxylases (Stenmark et al., 2001). Stephen Lippard and colleagues demonstrated that COQ7 catalyzes hydroxylation of DMQ *in vitro* in a reaction that involves NADH passing electrons to a carboxylate-bridged diiron center through DMQ (Behan and Lippard, 2010; Lu et al., 2013). Although COQ7 homologs are present in some prokaryotes such as *Rickettsia prowazekki* (Andersson et al., 1998), the *E. coli* enzyme that catalyzes the *C*6-hydroxylation (UbiF) is unrelated (Tran et al., 2006). *E. coli* UbiF is instead predicted to be a flavin-dependent monooxygenase similar to UbiI and UbiH, the *C*5- and *C*1- hydroxylases described above (Hajj Chehade et al., 2013). Why prokaryotes use highly similar enzymes for all three CoQ headgroup hydroxylations, but eukaryotes use different enzyme chemistries, is unknown.

CoQ biosynthesis proteins of unknown molecular function

A number of genes required for CoQ biosynthesis encode proteins of unknown molecular function. In mammals, these CoQ-related mitochondrial orphan proteins (MOPs) include COQ4, ADCK3, ADCK4, COQ9, and COQ10.

COQ4. Yeast Coq4p is peripherally associated with the matrix face of the inner mitochondrial membrane (Belogrudov et al., 2001). Likewise, mammalian COQ4 is localized to mitochondria (Pagliarini et al., 2008). Coq4p has homologs in some proteobacteria, all of which share a conserved motif predicted to bind a divalent cation (Marbois et al., 2009). Coq4p

stabilizes a complex of CoQ biosynthesis proteins that is required for efficient CoQ biosynthesis (Marbois et al., 2005; Marbois et al., 2009), but the underlying mechanism is undefined.

COQ8. Yeast Coq8p, its mammalian co-orthologs ADCK3 and ADCK4, and its prokaryotic ortholog UbiB are members of the ancient UbiB family (Leonard et al., 1998), which comprises a large portion of the protein kinase-like (PKL) superfamily (Kannan et al., 2007). UbiB (Cox et al., 1969; Poon et al., 2000), Coq8p (Do et al., 2001), ADCK3 (Lagier-Tourenne et al., 2008), and ADCK4 (Ashraf et al., 2013) each enhance CoQ biosynthesis. Recently, an X-ray structure of ADCK3 revealed a protein kinase-like fold with numerous unique features that inhibit protein kinase activity (Stefely et al., 2015). Despite the kinase-like structure of ADCK3, whether it actually catalyzes kinase activity *in vivo* remains unknown. Moreover, the endogenous biochemical activity of the entire UbiB family remains undefined. Coq8p, ADCK3, and ADCK4 are associated with the matrix face of the inner mitochondrial membrane (Do et al., 2001; Khadria et al., 2014; Pagliarini et al., 2008; Rhee et al., 2013; Tauche et al., 2008; Xie et al., 2011), where Coq8p is known to stabilize the CoQ biosynthesis complex (He et al., 2014). The presence or absence of Coq8p alters post-translational modifications of Coq3p, Coq5p, and Coq7p *in vivo* (Tauche et al., 2008; Xie et al., 2011), but whether this effect is direct or indirect is unknown. The putative model for the function of Coq8p is that it catalyzes ATP-dependent phosphorylation of Coq3p, Coq5p, and Coq7p to enhance the stability and activity of the CoQ biosynthesis complex, but this idea remains largely untested.

COQ9. Yeast Coq9p and mammalian COQ9 are localized to the matrix face of the inner mitochondrial membrane (Hsieh et al., 2007; Johnson et al., 2005; Pagliarini et al., 2008; Rhee et al., 2013), where they stabilize the CoQ biosynthesis complex (Lohman et al., 2014). Recently, an X-ray structure of Coq9p revealed a lipid-binding pocket that is important for function *in vivo*

(Lohman et al., 2014), but the endogenous lipid ligand remains undefined. Coq9p interacts physically and functionally with Coq7p to enhance the *C*6-hydroxylation reaction (Lohman et al., 2014). Coq9p also appears to enhance the deamination of CoQ intermediates derived from pABA (He et al., 2015).

COQ10. Yeast Coq10p and mammalian Coq10 are localized to mitochondria (Barros et al., 2005; Pagliarini et al., 2008). Coq10p contains a conserved lipid-binding domain that binds CoQ and CoQ intermediates *in vitro* (Allan et al., 2013; Barros et al., 2005). CoQ biosynthesis is less efficient in yeast with *coq10* mutations, and the CoQ produced is less efficiently used for OxPhos (Allan et al., 2013), but the molecular basis for these effects is unknown. Neither Coq10p nor Coq9p has known homologs in *E. coli*. However, the *E. coli* protein UbiJ could be a functional homolog of one of these proteins. UbiJ was recently identified as a CoQ biosynthesis protein and predicted to be a lipid-binding protein (Aussel et al., 2014a).

These CoQ-related mitochondrial orphan proteins (Q-MOPs) could be important for direct chemical transformations in CoQ biosynthesis. Alternatively, they could help solve additional problems in CoQ metabolism, which include missing transporters, regulatory factors, and assembly factors (Figure 3). These additional factors could help bypass some biophysical barriers to CoQ biosynthesis, as briefed below.

Biophysical barriers in CoQ biosynthesis

We group the biophysical barriers to CoQ biosynthesis into two general categories (1) polar precursor problems, and (2) lipophilic quinone inaccessibility.

Polar precursor problems. As described above, the highly polar small molecules IPP, DMAPP, and 4-HB (or another polar headgroup precursor) are used as precursors for building

CoQ in mitochondria. The mitochondrial inner membrane is impermeable to such polar molecules, creating a problem for biosynthetic processes that occur inside and outside of the mitochondrial matrix. Over 5% of the mitochondrial proteome is dedicated to solving this problem by assisting metabolite transport (Schmidt et al., 2010; Wohlrab, 2009). However, the mitochondrial transporters for the isoprene pyrophosphates and 4-HB remain unidentified (Figure 2).

The CoQ biosynthesis proteins, which are encoded by the nuclear DNA, must also be transported into the mitochondrial matrix. Mitochondrial import and protein processing is a complex and regulated process (Schmidt et al., 2010). The specific import and processing pathways of CoQ biosynthesis proteins have not yet been defined (Figure 3A), but these processes are likely important for regulating CoQ biosynthesis.

Lipophilic quinone inaccessibility. A series of experiments by John Markley and colleagues involving chemical reduction kinetics and diagnostic nuclear magnetic resonances showed that a large portion of CoQ exists in the midplane of the lipid bilayer (Ulrich et al., 1985). Even the quinone headgroup is located near the distal end of the phospholipid acyl tails, directly between the lipid leaflets (Figure 3B). Additional NMR studies confirmed these findings and showed that CoQ exists preferentially in the bilayer midplane (Metz, 1995). While these studies have not yet been conducted with CoQ intermediates, we predict that the quinone-containing intermediates (especially DDMQ and DMQ) have similar properties.

The CoQ biosynthesis proteins described above are primarily peripheral membrane proteins, located at the membrane surface. How these peripheral membrane enzymes access substrates located deep in the midplane of the lipid bilayer is unclear (Figure 3B). Reduction of the CoQ headgroup quinone of DDMQ, DMQ, or DMeQ would make it more hydrophilic and

likely bring it closer to the surface of the membrane, but this process would be reversible and may require a dedicated reductase.

The problem of lipophilic intermediates in lipid biosynthesis is not unprecedented. Coenzyme A (CoA) is often used as a hydrophilic handle in lipid biosynthesis (e.g. acyl-CoA intermediates). The CoA thiol group could theoretically be attached directly onto the CoQ headgroup by replacing the *C*4-hydroxyl group. This attachment would require transformation of the *C*4-hydroxyl group into a good leaving group, potentially by ATP-dependent phosphorylation, which would be analogous to the reactions that generate acyl-CoA. Alternatively, phosphorylation of a CoQ headgroup hydroxyl group alone could provide a hydrophilic protecting group to keep the headgroup in the reduced state and located at the surface of the membrane.

The hydrophobicity of the final CoQ product itself also presents challenges for biology. CoQ is known to exist in membranes outside of the mitochondria, but how it gets there is unknown. We predict that a series of CoQ transport proteins exist (Figure 3A). These CoQ transport proteins could also play important roles in transporting extracellular CoQ into the mitochondria, a process that has important implications for treatment of CoQ deficiency.

Clinical implications of defining CoQ biosynthesis

The widespread clinical presentations (Figure 4) and implications of CoQ deficiency have been thoroughly documented in a number of recent reviews (Laredj et al., 2014; Quinzii et al., 2007; Quinzii and Hirano, 2010; Turunen et al., 2004). Primary CoQ deficiency has been linked to mutations in *ADCK3* (Blumkin et al., 2014; Gerards et al., 2010; Horvath et al., 2012; Lagier-Tourenne et al., 2008; Liu et al., 2014; Mollet et al., 2008), *ADCK4* (Ashraf et al., 2013;

Korkmaz et al., 2015), *COQ2* (Diomedi-Camassei et al., 2007; Jakobs et al., 2013; Lopez-Martin et al., 2007; Mitsui, 2013; Quinzii et al., 2006), *COQ4* (Brea-Calvo et al., 2015; Salviati et al., 2012), *COQ6* (Doimo et al., 2014; Heeringa et al., 2011), *COQ7* (Freyer et al., 2015), *COQ9* (Duncan et al., 2009) (Danhauser et al., 2015; Garcia-Corzo et al., 2013), *PDSS1* (Mollet et al., 2007), and *PDSS2* (Gasser et al., 2013; Lopez et al., 2006; Peng et al., 2008) (Figure 4). Secondary CoQ deficiency has been linked to mutations in *ETFDH* (Gempel et al., 2007), *MUT* (Haas et al., 2009), *APTX* (Quinzii et al., 2005), and *BRAF* (Aeby et al., 2007) (Figure 4).

Treatment of CoQ deficiency with exogenous CoQ usually fails, likely due to difficulty with absorption and distribution of CoQ into the deficient mitochondria. Recently, however, a new strategy in the treatment of CoQ deficiency has emerged. This new strategy uses CoQ 'bypass' precursors to sidestep enzymatic defects in CoQ biosynthesis. Mice with a defect in Coq7 were treated with 2,4-dihydroxybenzoic acid (2,4-DHB), which was able to bypass the Coq7-catalyzed *C*6-hydroxylation, elevate CoQ levels, and extend lifespan (Wang et al., 2015). A similar benefit with CoQ 'bypass' precursor treatment was observed in mice with Coq9 mutations (Luna-Sanchez et al., 2015). While this new therapeutic strategy for filling gaps in CoQ biosynthesis provides new hope for patients with CoQ deficiency, it has an important prerequisite: the specific biochemical function of the defective CoQ biosynthesis protein must be known for a biochemical 'bypass' strategy to be developed. This realization further motivates our collective efforts to define the molecular functions of CoQ biosynthesis proteins.

Concluding remarks

In recent years, the known functions of coenzyme Q in human health and disease have expanded significantly, rekindling the drive to fully define its biosynthesis. CoQ now has numerous

defined functions outside of its primary role in the mitochondrial electron transport chain, including regulation of mitochondrial and possibly extra-mitochondrial functions. Likewise, the number of human diseases with important functional links to CoQ biosynthesis has risen. Changes in CoQ metabolism are linked to common diseases such as Parkinson's disease, rare diseases such as a cerebellar ataxia, and even the aging process itself.

Given the importance of CoQ for human biology and the fact that it was discovered nearly 60 years ago, it may be surprising that we still do not fully understand CoQ biosynthesis. This apparent disconnect highlights the challenging nature of studying this biosynthetic process. Challenges presented by this field including unstable proteins, fleeting biosynthetic intermediates, and numerous undefined biochemical components. Fortunately, recent progress in protein biochemistry, X-ray crystallography, mass spectrometry, and systems biology is rising to meet the challenge. The first set of protein structures for eukaryotic CoQ biosynthesis proteins—those of ADCK3, COQ9, and Coq5p (Table 2)—provide a solid molecular foundation for studying their functions. Purification of CoQ biosynthesis proteins is also an important step toward defining important questions about reaction mechanisms and substrate specificities. Furthermore, the recent isolation of a purified human CoQ biosynthesis protein complex (Floyd et al., 2015, manuscript under review) will help to define its integrated reaction mechanisms.

Despite this exciting progress, numerous gaps still exist in our understanding of CoQ biosynthesis. At a basic biochemical level, numerous chemical transformations in CoQ biosynthesis have no associated enzyme, and numerous proteins required for CoQ biosynthesis have no known molecular function. More complex biological knowledge gaps also exist, including questions about how CoQ is transported throughout cells and the body, how CoQ biosynthesis is regulated, and how CoQ is degraded. Furthermore, many clinical knowledge gaps

exist, including questions about the role of CoQ in common diseases and how to treat dysfunctional CoQ metabolism. We hope that this review—by comprehensively defining gaps in knowledge about CoQ biosynthesis at the biochemical level—will facilitate further progress toward understanding CoQ metabolism in human health and disease.

Acknowledgments

We thank members of the Pagliarini laboratory for many critical discussions about CoQ. This work was supported by a Searle Scholars Award, a Shaw Scientist Award and by NIH grants U01GM94622, R01DK098672 and R01GM112057 (to D.J.P.) and a NIH Ruth L. Kirschstein National Research Service Award F30AG043282 (to J.A.S.).

Figures and Tables

Figure 1.

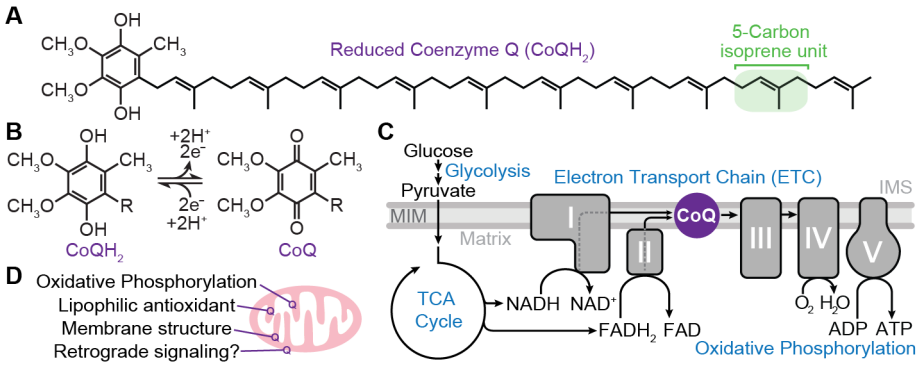

Figure 1. Chemical and biological functions of coenzyme Q

(**A**) Chemical structure of reduced coenzyme Q_{10} ($CoQH_2$).

(**B**) Reduction-oxidation reaction of the CoQ headgroup. 'R' indicates the polyisoprene tail shown above in (A).

(**C**) Overview of mitochondrial metabolism highlighting the central role of CoQ as a requisite electron carrier. I–V, oxidative phosphorylation complexes; IMS, intermembrane space; MIM, mitochondrial inner membrane.

(**D**) Overview of additional functions for CoQ in mitochondrial biology.

Figure 2.

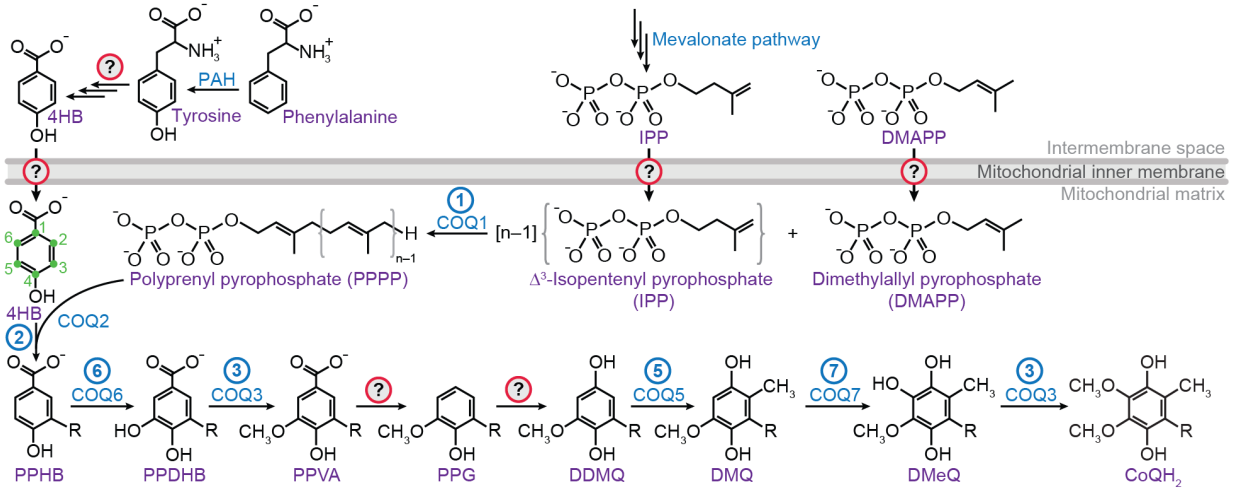

Figure 2. Current model for the CoQ biosynthesis pathway

Scheme of CoQ biosynthesis with currently unidentified proteins indicated by question marks. 'R' indicates the polyisoprenyl side chain (Figure 1A), which would be anchored in the mitochondrial inner membrane. DMAPP, dimethylallyl pyrophosphate; IPP, isopentenyl pyrophosphate; PPPP, polyprenyl pyrophosphate; 4HB, 4-hydroxybenzoic acid; PPHB, polyprenyl-hydroxybenzoic acid; PPDHB, polyprenyl-dihydroxybenzoic acid; PPVA, polyprenyl-vanillic acid; PPG, polyprenyl-guaiacol; DDMQ, demethoxy-demethyl-coenzyme Q; DMQ, demethoxy-coenzyme Q; DMeQ, demethyl-coenzyme Q.

Figure 3.

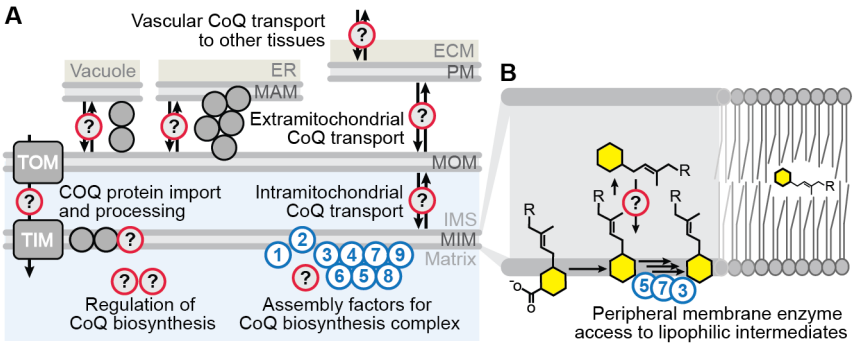

Figure 3. Models of additional problems in CoQ metabolism

(**A**) Model showing questions about CoQ transport and regulation.

(**B**) Model of a biophysical barrier to accessing lipophilic CoQ intermediates.

Figure 4.

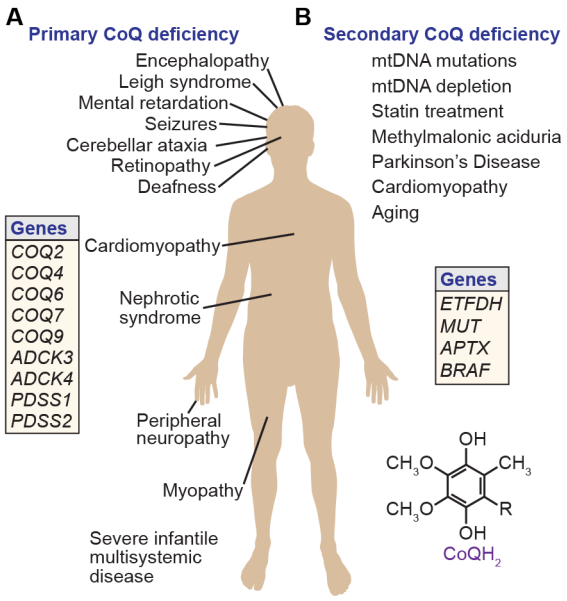

Figure 4. CoQ deficiency in human health and disease

(A) Phenotypes, syndromes, and genes associated with primary CoQ deficiency.

(B) Diseases, conditions, drugs, and genes associated with secondary CoQ deficiency.

Table 1. Reactions of Eukaryotic CoQ Biosynthesis and Metabolism

Reactions	Enzymes	Substrates	Products	Cofactors
Isoprene polymerization	PDSS1, PDSS2, Coq1p	DMAPP and IPP	PPPP	Mg^{2+}
*C*3-Prenylation	COQ2, Coq2p	4-HB and PPPP	PPHB	Mg^{2+}
O-methylations	COQ3, Coq3p	PPDHB or DMeQ	PPVA or CoQ	SAM, Zn^{2+}
*C*2-methylation	COQ5, Coq5p	DDMQ	DMQ	SAM, Mg^{2+}
*C*5-hydroxylation	COQ6, Coq6p	PPHB	PPDHBA	FAD & NAD(P)H
*C*6-hydroxylation	COQ7, Coq7p	DMQ	DMeQ	Diiron center, NADH
*C*1-hydroxylation	**?**	PPG	DDMQ	**?**
Decarboxylation	**?**	PPVA	PPG	prFMN?
Deamination	**?**	**?**	**?**	**?**
Reduction	**?**	**?**	**?**	NADH?
Oxidation	**?**	**?**	**?**	**?**
Phosphorylation	**?**	**?**	**?**	MgATP?

Abbreviations: DMAPP, dimethylallyl pyrophosphate; IPP, isopentenyl pyrophosphate; PPPP, polyprenyl pyrophosphate; 4-HB, 4-hydroxybenzoic acid; PPHB, polyprenyl-hydroxybenzoic acid; PPDHB, polyprenyl-dihydroxybenzoic acid; PPVA, polyprenyl-vanillic acid; PPG, polyprenyl-guaiacol; DDMQ, demethoxy-demethyl-coenzyme Q; DMQ, demethoxy-coenzyme Q; DMeQ, demethyl-coenzyme Q; SAM, *S*-adenosyl methionine; FAD, flavin adenine dinucleotide; NADH, reduced nicotinamide adenine dinucleotide; prFMN, prenylated FMN; MgADP, magnesium divalent cation (Mg^{2+})-adenosine triphosphate complex.

Table 2. Structures of Eukaryotic CoQ Biosynthesis Proteins

Group	Proteins	PDBs	References
COQ1	Coq1p	-	
	PDSS1, PDSS2	-	
COQ2	Coq2p	-	
	COQ2	-	
COQ3	Coq3p	-	
	COQ3	-	
COQ4	Coq4p	-	
	COQ4	-	
COQ5	Coq5p	4OBW, 4OBX	(Dai et al., 2014)
	COQ5	-	
COQ6	Coq6p	-	
	COQ6	-	
COQ7	Coq7p	-	
	COQ7	-	
COQ8	Coq8p	-	
	ADCK3	4PED	(Stefely et al., 2015)
	ADCK4	-	
COQ9	Coq9p	-	
	COQ9	4RHP	(Lohman et al., 2014)
COQ10	Coq10p	-	
	COQ10	-	

References

Aeby, A., Sznajer, Y., Cave, H., Rebuffat, E., Van Coster, R., Rigal, O., and Van Bogaert, P. (2007). Cardiofaciocutaneous (CFC) syndrome associated with muscular coenzyme Q10 deficiency. J Inherit Metab Dis *30*, 827.

Alexander, K., and Young, I.G. (1978a). Alternative hydroxylases for the aerobic and anaerobic biosynthesis of ubiquinone in Escherichia coli. Biochemistry *17*, 4750-4755.

Alexander, K., and Young, I.G. (1978b). Three hydroxylations incorporating molecular oxygen in the aerobic biosynthesis of ubiquinone in Escherichia coli. Biochemistry *17*, 4745-4750.

Allan, C.M., Hill, S., Morvaridi, S., Saiki, R., Johnson, J.S., Liau, W.S., Hirano, K., Kawashima, T., Ji, Z., Loo, J.A.*, et al.* (2013). A conserved START domain coenzyme Q-binding polypeptide is required for efficient Q biosynthesis, respiratory electron transport, and antioxidant function in Saccharomyces cerevisiae. Biochim Biophys Acta *1831*, 776-791.

Anderson, C.M., Kazantzis, M., Wang, J., Venkatraman, S., Goncalves, R.L., Quinlan, C.L., Ng, R., Jastroch, M., Benjamin, D.I., Nie, B.*, et al.* (2015). Dependence of brown adipose tissue function on CD36-mediated coenzyme Q uptake. Cell Rep *10*, 505-515.

Andersson, S.G., Zomorodipour, A., Andersson, J.O., Sicheritz-Ponten, T., Alsmark, U.C., Podowski, R.M., Naslund, A.K., Eriksson, A.S., Winkler, H.H., and Kurland, C.G. (1998). The genome sequence of Rickettsia prowazekii and the origin of mitochondria. Nature *396*, 133-140.

Ashby, M.N., and Edwards, P.A. (1990). Elucidation of the deficiency in two yeast coenzyme Q mutants. Characterization of the structural gene encoding hexaprenyl pyrophosphate synthetase. J Biol Chem *265*, 13157-13164.

Ashby, M.N., Kutsunai, S.Y., Ackerman, S., Tzagoloff, A., and Edwards, P.A. (1992). COQ2 is a candidate for the structural gene encoding para-hydroxybenzoate:polyprenyltransferase. J Biol Chem *267*, 4128-4136.

Ashraf, S., Gee, H.Y., Woerner, S., Xie, L.X., Vega-Warner, V., Lovric, S., Fang, H., Song, X., Cattran, D.C., Avila-Casado, C.*, et al.* (2013). ADCK4 mutations promote steroid-resistant nephrotic syndrome through CoQ10 biosynthesis disruption. J Clin Invest *123*, 5179-5189.

Aussel, L., Loiseau, L., Hajj Chehade, M., Pocachard, B., Fontecave, M., Pierrel, F., and Barras, F. (2014a). ubiJ, a new gene required for aerobic growth and proliferation in macrophage, is involved in coenzyme Q biosynthesis in Escherichia coli and Salmonella enterica serovar Typhimurium. J Bacteriol *196*, 70-79.

Aussel, L., Pierrel, F., Loiseau, L., Lombard, M., Fontecave, M., and Barras, F. (2014b). Biosynthesis and physiology of coenzyme Q in bacteria. Biochim Biophys Acta *1837*, 1004-1011.

Bar-Tana, J., Howlett, B.J., and Hertz, R. (1980). Ubiquinone synthetic pathway in flagellation of Salmonella typhimurium. J Bacteriol *143*, 637-643.

Barkovich, R.J., Shtanko, A., Shepherd, J.A., Lee, P.T., Myles, D.C., Tzagoloff, A., and Clarke, C.F. (1997). Characterization of the COQ5 gene from Saccharomyces cerevisiae. Evidence for a C-methyltransferase in ubiquinone biosynthesis. J Biol Chem *272*, 9182-9188.

Barros, M.H., Johnson, A., Gin, P., Marbois, B.N., Clarke, C.F., and Tzagoloff, A. (2005). The Saccharomyces cerevisiae COQ10 gene encodes a START domain protein required for function of coenzyme Q in respiration. J Biol Chem *280*, 42627-42635.

Behan, R.K., and Lippard, S.J. (2010). The aging-associated enzyme CLK-1 is a member of the carboxylate-bridged diiron family of proteins. Biochemistry *49*, 9679-9681.

Belogrudov, G.I., Lee, P.T., Jonassen, T., Hsu, A.Y., Gin, P., and Clarke, C.F. (2001). Yeast COQ4 encodes a mitochondrial protein required for coenzyme Q synthesis. Arch Biochem Biophys *392*, 48-58.

Bentley, R.R., V. G.; Springer, C. M.; Dialameh, G. H.; Olson, R. E. (1961). The Origin of the Benzoquinone Ring of Coenzyme Q9 in the Rat. Biochem Biophys Res Commun *5*, 443-446.

Blumkin, L., Leshinsky-Silver, E., Zerem, A., Yosovich, K., Lerman-Sagie, T., and Lev, D. (2014). Heterozygous Mutations in the ADCK3 Gene in Siblings with Cerebellar Atrophy and Extreme Phenotypic Variability. JIMD Rep *12*, 103-107.

Booth, A.N.M., M. S.; Robbins, D. J.; Emerson, O. H.; Jones, F. T.; Deeds, F. (1960). Urinary Phenolic Acid Metabolites of Tyrosine. J Biol Chem *235*, 2649-2652.

Brea-Calvo, G., Haack, T.B., Karall, D., Ohtake, A., Invernizzi, F., Carrozzo, R., Kremer, L., Dusi, S., Fauth, C., Scholl-Burgi, S.*, et al.* (2015). COQ4 mutations cause a broad spectrum of mitochondrial disorders associated with CoQ10 deficiency. Am J Hum Genet *96*, 309-317.

Casey, J., and Threlfall, D.R. (1978). Formation of 3-hexaprenyl-4-hydroxybenzoate by matrix-free mitochondrial membrane-rich preparations of yeast. Biochim Biophys Acta *530*, 487-502.

Chaykin, S., Law, J., Phillips, A.H., Tchen, T.T., and Bloch, K. (1958). Phosphorylated Intermediates in the Synthesis of Squalene. Proc Natl Acad Sci U S A *44*, 998-1004.

Cheng, W., and Li, W. (2014). Structural insights into ubiquinone biosynthesis in membranes. Science *343*, 878-881.

Clarke, C.F., Williams, W., and Teruya, J.H. (1991). Ubiquinone biosynthesis in Saccharomyces cerevisiae. Isolation and sequence of COQ3, the 3,4-dihydroxy-5-hexaprenylbenzoate methyltransferase gene. J Biol Chem *266*, 16636-16644.

Cox, G.B., and Gibson, F. (1964). Biosynthesis of Vitamin K and Ubiquinone. Relation to the Shikimic Acid Pathway in Escherichia Coli. Biochim Biophys Acta *93*, 204-206.

Cox, G.B., Gibson, F., and Pittard, J. (1968). Mutant strains of Escherichia coli K-12 unable to form ubiquinone. J Bacteriol *95*, 1591-1598.

Cox, G.B., Young, I.G., McCann, L.M., and Gibson, F. (1969). Biosynthesis of ubiquinone in Escherichia coli K-12: location of genes affecting the metabolism of 3-octaprenyl-4-hydroxybenzoic acid and 2-octaprenylphenol. J Bacteriol *99*, 450-458.

Crane, F.L. (1989). Comments on the discovery of coenzyme Q: a commentary on 'Isolation of a Quinone from Beef Heart Mitochondria'. Biochim Biophys Acta *1000*, 358-361.

Crane, F.L. (2007). Discovery of ubiquinone (coenzyme Q) and an overview of function. Mitochondrion *7 Suppl*, S2-7.

Crane, F.L., Hatefi, Y., Lester, R.L., and Widmer, C. (1957). Isolation of a quinone from beef heart mitochondria. Biochim Biophys Acta *25*, 220-221.

Dai, Y.N., Zhou, K., Cao, D.D., Jiang, Y.L., Meng, F., Chi, C.B., Ren, Y.M., Chen, Y., and Zhou, C.Z. (2014). Crystal structures and catalytic mechanism of the C-methyltransferase Coq5 provide insights into a key step of the yeast coenzyme Q synthesis pathway. Acta Crystallogr D Biol Crystallogr *70*, 2085-2092.

Danhauser, K., Herebian, D., Haack, T.B., Rodenburg, R.J., Strom, T.M., Meitinger, T., Klee, D., Mayatepek, E., Prokisch, H., and Distelmaier, F. (2015). Fatal neonatal encephalopathy and lactic acidosis caused by a homozygous loss-of-function variant in COQ9. Eur J Hum Genet.

Davis, B.D. (1950). p-Hydroxybenzoic acid; a new bacterial vitamin. Nature *166*, 1120-1121.

Dibrov, E., Robinson, K.M., and Lemire, B.D. (1997). The COQ5 gene encodes a yeast mitochondrial protein necessary for ubiquinone biosynthesis and the assembly of the respiratory chain. J Biol Chem *272*, 9175-9181.

Diomedi-Camassei, F., Di Giandomenico, S., Santorelli, F.M., Caridi, G., Piemonte, F., Montini, G., Ghiggeri, G.M., Murer, L., Barisoni, L., Pastore, A.*, et al.* (2007). COQ2 nephropathy: a newly described inherited mitochondriopathy with primary renal involvement. J Am Soc Nephrol *18*, 2773-2780.

Do, T.Q., Hsu, A.Y., Jonassen, T., Lee, P.T., and Clarke, C.F. (2001). A defect in coenzyme Q biosynthesis is responsible for the respiratory deficiency in Saccharomyces cerevisiae abc1 mutants. J Biol Chem *276*, 18161-18168.

Do, T.Q., Schultz, J.R., and Clarke, C.F. (1996). Enhanced sensitivity of ubiquinone-deficient mutants of Saccharomyces cerevisiae to products of autoxidized polyunsaturated fatty acids. Proc Natl Acad Sci U S A *93*, 7534-7539.

Doimo, M., Trevisson, E., Airik, R., Bergdoll, M., Santos-Ocana, C., Hildebrandt, F., Navas, P., Pierrel, F., and Salviati, L. (2014). Effect of vanillic acid on COQ6 mutants identified in patients with coenzyme Q10 deficiency. Biochim Biophys Acta *1842*, 1-6.

Duncan, A.J., Bitner-Glindzicz, M., Meunier, B., Costello, H., Hargreaves, I.P., Lopez, L.C., Hirano, M., Quinzii, C.M., Sadowski, M.I., Hardy, J.*, et al.* (2009). A nonsense mutation in

COQ9 causes autosomal-recessive neonatal-onset primary coenzyme Q10 deficiency: a potentially treatable form of mitochondrial disease. Am J Hum Genet *84*, 558-566.

Echtay, K.S., Winkler, E., Frischmuth, K., and Klingenberg, M. (2001). Uncoupling proteins 2 and 3 are highly active H(+) transporters and highly nucleotide sensitive when activated by coenzyme Q (ubiquinone). Proc Natl Acad Sci U S A *98*, 1416-1421.

Echtay, K.S., Winkler, E., and Klingenberg, M. (2000). Coenzyme Q is an obligatory cofactor for uncoupling protein function. Nature *408*, 609-613.

Ewbank, J.J., Barnes, T.M., Lakowski, B., Lussier, M., Bussey, H., and Hekimi, S. (1997). Structural and functional conservation of the Caenorhabditis elegans timing gene clk-1. Science *275*, 980-983.

Festenstein, G.N., Heaton, F.W., Lowe, J.S., and Morton, R.A. (1955). A constituent of the unsaponifiable portion of animal tissue lipids (lambda max. 272 m mu). Biochem J *59*, 558-566.

Fontaine, E., Ichas, F., and Bernardi, P. (1998). A ubiquinone-binding site regulates the mitochondrial permeability transition pore. J Biol Chem *273*, 25734-25740.

Frei, B., Kim, M.C., and Ames, B.N. (1990). Ubiquinol-10 is an effective lipid-soluble antioxidant at physiological concentrations. Proc Natl Acad Sci U S A *87*, 4879-4883.

Freyer, C., Stranneheim, H., Naess, K., Mourier, A., Felser, A., Maffezzini, C., Lesko, N., Bruhn, H., Engvall, M., Wibom, R.*, et al.* (2015). Rescue of primary ubiquinone deficiency due to a novel COQ7 defect using 2,4-dihydroxybensoic acid. J Med Genet.

Friis, P.D., G. D.; Folkers, K. (1966). Complete Sequence of Biosynthesis from p-Hydroxybenzoic Acid to Ubiquinone. J Am Chem Soc *88*, 4754-4756.

Garcia-Corzo, L., Luna-Sanchez, M., Doerrier, C., Garcia, J.A., Guaras, A., Acin-Perez, R., Bullejos-Peregrin, J., Lopez, A., Escames, G., Enriquez, J.A.*, et al.* (2013). Dysfunctional Coq9 protein causes predominant encephalomyopathy associated with CoQ deficiency. Hum Mol Genet *22*, 1233-1248.

Gasser, D.L., Winkler, C.A., Peng, M., An, P., McKenzie, L.M., Kirk, G.D., Shi, Y., Xie, L.X., Marbois, B.N., Clarke, C.F.*, et al.* (2013). Focal segmental glomerulosclerosis is associated with a PDSS2 haplotype and, independently, with a decreased content of coenzyme Q10. Am J Physiol Renal Physiol *305*, F1228-1238.

Gempel, K., Topaloglu, H., Talim, B., Schneiderat, P., Schoser, B.G., Hans, V.H., Palmafy, B., Kale, G., Tokatli, A., Quinzii, C.*, et al.* (2007). The myopathic form of coenzyme Q10 deficiency is caused by mutations in the electron-transferring-flavoprotein dehydrogenase (ETFDH) gene. Brain *130*, 2037-2044.

Gerards, M., van den Bosch, B., Calis, C., Schoonderwoerd, K., van Engelen, K., Tijssen, M., de Coo, R., van der Kooi, A., and Smeets, H. (2010). Nonsense mutations in CABC1/ADCK3 cause progressive cerebellar ataxia and atrophy. Mitochondrion *10*, 510-515.

Gibson, M.I.G., F.; Doy, C. H.; Morgan, P. (1962). The Branch Point in the Biosynthesis of the Aromatic Amino-Acids. Nature *195*, 1173-1175.

Gin, P., and Clarke, C.F. (2005). Genetic evidence for a multi-subunit complex in coenzyme Q biosynthesis in yeast and the role of the Coq1 hexaprenyl diphosphate synthase. J Biol Chem *280*, 2676-2681.

Gin, P., Hsu, A.Y., Rothman, S.C., Jonassen, T., Lee, P.T., Tzagoloff, A., and Clarke, C.F. (2003). The Saccharomyces cerevisiae COQ6 gene encodes a mitochondrial flavin-dependent monooxygenase required for coenzyme Q biosynthesis. J Biol Chem *278*, 25308-25316.

Gloor, U., and Wiss, O. (1959). On the biosynthesis of ubiquinone (50). Arch Biochem Biophys *83*, 216-222.

Goewert, R.R., Sippel, C.J., Grimm, M.F., and Olson, R.E. (1981a). Identification of 3-methoxy-4-hydroxy-5-hexaprenylbenzoic acid as a new intermediate in ubiquinone biosynthesis by Saccharomyces cerevisiae. Biochemistry *20*, 5611-5616.

Goewert, R.R., Sippel, C.J., and Olson, R.E. (1981b). Identification of 3,4-dihydroxy-5-hexaprenylbenzoic acid as an intermediate in the biosynthesis of ubiquinone-6 by Saccharomyces cerevisiae. Biochemistry *20*, 4217-4223.

Gold, P.H., and Olson, R.E. (1966). Studies on coenzyme Q. The biosynthesis of coenzyme Q9 in rat tissue slices. J Biol Chem *241*, 3507-3516.

Gomez, F., Saiki, R., Chin, R., Srinivasan, C., and Clarke, C.F. (2012). Restoring de novo coenzyme Q biosynthesis in Caenorhabditis elegans coq-3 mutants yields profound rescue compared to exogenous coenzyme Q supplementation. Gene *506*, 106-116.

Green, J., Diplock, A.T., Bunyan, J., Edwin, E.E., and Mc, H.D. (1961). Ubiquinone (coenzyme Q) and the function of vitamin E. Nature *190*, 318-325.

Gulmezian, M., Hyman, K.R., Marbois, B.N., Clarke, C.F., and Javor, G.T. (2007). The role of UbiX in Escherichia coli coenzyme Q biosynthesis. Arch Biochem Biophys *467*, 144-153.

Haas, D., Niklowitz, P., Horster, F., Baumgartner, E.R., Prasad, C., Rodenburg, R.J., Hoffmann, G.F., Menke, T., and Okun, J.G. (2009). Coenzyme Q(10) is decreased in fibroblasts of patients with methylmalonic aciduria but not in mevalonic aciduria. J Inherit Metab Dis *32*, 570-575.

Hajj Chehade, M., Loiseau, L., Lombard, M., Pecqueur, L., Ismail, A., Smadja, M., Golinelli-Pimpaneau, B., Mellot-Draznieks, C., Hamelin, O., Aussel, L.*, et al.* (2013). ubiI, a new gene in Escherichia coli coenzyme Q biosynthesis, is involved in aerobic C5-hydroxylation. J Biol Chem *288*, 20085-20092.

Hatefi, Y., Haavik, A.G., Fowler, L.R., and Griffiths, D.E. (1962). Studies on the electron transfer system. XLII. Reconstitution of the electron transfer system. J Biol Chem *237*, 2661-2669.

He, C.H., Black, D.S., Nguyen, T.P., Wang, C., Srinivasan, C., and Clarke, C.F. (2015). Yeast Coq9 controls deamination of coenzyme Q intermediates that derive from para-aminobenzoic acid. Biochim Biophys Acta *1851*, 1227-1239.

He, C.H., Xie, L.X., Allan, C.M., Tran, U.C., and Clarke, C.F. (2014). Coenzyme Q supplementation or over-expression of the yeast Coq8 putative kinase stabilizes multi-subunit Coq polypeptide complexes in yeast coq null mutants. Biochim Biophys Acta *1841*, 630-644.

Heeringa, S.F., Chernin, G., Chaki, M., Zhou, W., Sloan, A.J., Ji, Z., Xie, L.X., Salviati, L., Hurd, T.W., Vega-Warner, V.*, et al.* (2011). COQ6 mutations in human patients produce nephrotic syndrome with sensorineural deafness. J Clin Invest *121*, 2013-2024.

Heller, J., Szarkowska, L., and Petryszyn, C. (1961). Reduction of coenzyme Q by succinic acid dehydrogenase. Nature *189*, 578-579.

Horvath, R., Czermin, B., Gulati, S., Demuth, S., Houge, G., Pyle, A., Dineiger, C., Blakely, E.L., Hassani, A., Foley, C.*, et al.* (2012). Adult-onset cerebellar ataxia due to mutations in CABC1/ADCK3. J Neurol Neurosurg Psychiatry *83*, 174-178.

Howlett, B.J., and Bar-Tana, J. (1980). Polyprenyl p-hydroxybenzoate carboxylase in flagellation of Salmonella typhimurium. J Bacteriol *143*, 644-651.

Hsieh, E.J., Gin, P., Gulmezian, M., Tran, U.C., Saiki, R., Marbois, B.N., and Clarke, C.F. (2007). Saccharomyces cerevisiae Coq9 polypeptide is a subunit of the mitochondrial coenzyme Q biosynthetic complex. Arch Biochem Biophys *463*, 19-26.

Hsu, A.Y., Poon, W.W., Shepherd, J.A., Myles, D.C., and Clarke, C.F. (1996). Complementation of coq3 mutant yeast by mitochondrial targeting of the Escherichia coli UbiG polypeptide: evidence that UbiG catalyzes both O-methylation steps in ubiquinone biosynthesis. Biochemistry *35*, 9797-9806.

Jackman, L.M., O'Brien, I.G., Cox, G.B., and Gibson, F. (1967). Methionine as the source of methyl groups for ubiquinone and vitamin K: a study using nuclear magnetic resonance and mass spectrometry. Biochim Biophys Acta *141*, 1-7.

Jakobs, B.S., van den Heuvel, L.P., Smeets, R.J., de Vries, M.C., Hien, S., Schaible, T., Smeitink, J.A., Wevers, R.A., Wortmann, S.B., and Rodenburg, R.J. (2013). A novel mutation in COQ2 leading to fatal infantile multisystem disease. J Neurol Sci *326*, 24-28.

Johnson, A., Gin, P., Marbois, B.N., Hsieh, E.J., Wu, M., Barros, M.H., Clarke, C.F., and Tzagoloff, A. (2005). COQ9, a new gene required for the biosynthesis of coenzyme Q in Saccharomyces cerevisiae. J Biol Chem *280*, 31397-31404.

Jonassen, T., and Clarke, C.F. (2000). Isolation and functional expression of human COQ3, a gene encoding a methyltransferase required for ubiquinone biosynthesis. J Biol Chem *275*, 12381-12387.

Jonassen, T., Proft, M., Randez-Gil, F., Schultz, J.R., Marbois, B.N., Entian, K.D., and Clarke, C.F. (1998). Yeast Clk-1 homologue (Coq7/Cat5) is a mitochondrial protein in coenzyme Q synthesis. J Biol Chem *273*, 3351-3357.

Kalen, A., Appelkvist, E.L., Chojnacki, T., and Dallner, G. (1990). Nonaprenyl-4-hydroxybenzoate transferase, an enzyme involved in ubiquinone biosynthesis, in the endoplasmic reticulum-Golgi system of rat liver. J Biol Chem *265*, 1158-1164.

Kalen, A., Appelkvist, E.L., and Dallner, G. (1989). Age-related changes in the lipid compositions of rat and human tissues. Lipids *24*, 579-584.

Kalen, A., Norling, B., Appelkvist, E.L., and Dallner, G. (1987). Ubiquinone biosynthesis by the microsomal fraction from rat liver. Biochim Biophys Acta *926*, 70-78.

Kannan, N., Taylor, S.S., Zhai, Y., Venter, J.C., and Manning, G. (2007). Structural and functional diversity of the microbial kinome. PLoS biology *5*, e17.

Kashket, E.R., and Brodie, A.F. (1963). Oxidative Phosphorylation in Fractionated Bacterial Systems. Viii. Role of Particulate and Soluble Fractions from Escherichia Coli. Biochim Biophys Acta *78*, 52-65.

Khadria, A.S., Mueller, B.K., Stefely, J.A., Tan, C.H., Pagliarini, D.J., and Senes, A. (2014). A Gly-zipper motif mediates homodimerization of the transmembrane domain of the mitochondrial kinase ADCK3. J Am Chem Soc *136*, 14068-14077.

Korkmaz, E., Lipska-Zietkiewicz, B.S., Boyer, O., Gribouval, O., Fourrage, C., Tabatabaei, M., Schnaidt, S., Gucer, S., Kaymaz, F., Arici, M.*, et al.* (2015). ADCK4-Associated Glomerulopathy Causes Adolescence-Onset FSGS. J Am Soc Nephrol.

Lagier-Tourenne, C., Tazir, M., Lopez, L.C., Quinzii, C.M., Assoum, M., Drouot, N., Busso, C., Makri, S., Ali-Pacha, L., Benhassine, T.*, et al.* (2008). ADCK3, an ancestral kinase, is mutated in a form of recessive ataxia associated with coenzyme Q10 deficiency. Am J Hum Genet *82*, 661-672.

Lakowski, B., and Hekimi, S. (1996). Determination of life-span in Caenorhabditis elegans by four clock genes. Science *272*, 1010-1013.

Laredj, L.N., Licitra, F., and Puccio, H.M. (2014). The molecular genetics of coenzyme Q biosynthesis in health and disease. Biochimie *100*, 78-87.

Larsen, P.L., and Clarke, C.F. (2002). Extension of life-span in Caenorhabditis elegans by a diet lacking coenzyme Q. Science *295*, 120-123.

Lawrence, J., Cox, G.B., and Gibson, F. (1974). Biosynthesis of ubiquinone in Escherichia coli K-12: biochemical and genetic characterization of a mutant unable to convert chorismate into 4-hydroxybenzoate. J Bacteriol *118*, 41-45.

Lederer, E. (1969). Some problems concerning biological C-alkylation reactions and phytosterol biosynthesis. Quarterly Reviews, Chemical Society *23*, 453-481.

Lee, P.T., Hsu, A.Y., Ha, H.T., and Clarke, C.F. (1997). A C-methyltransferase involved in both ubiquinone and menaquinone biosynthesis: isolation and identification of the Escherichia coli ubiE gene. J Bacteriol *179*, 1748-1754.

Leonard, C.J., Aravind, L., and Koonin, E.V. (1998). Novel families of putative protein kinases in bacteria and archaea: evolution of the "eukaryotic" protein kinase superfamily. Genome research *8*, 1038-1047.

Leppik, R.A., Stroobant, P., Shineberg, B., Young, I.G., and Gibson, F. (1976a). Membrane-associated reactions in ubiquinone biosynthesis. 2-Octaprenyl-3-methyl-5-hydroxy-6-methoxy-1,4-benzoquinone methyltransferase. Biochim Biophys Acta *428*, 146-156.

Leppik, R.A., Young, I.G., and Gibson, F. (1976b). Membrane-associated reactions in ubiquinone biosynthesis in Escherichia coli. 3-Octaprenyl-4-hydroxybenzoate carboxy-lyase. Biochim Biophys Acta *436*, 800-810.

Lester, R.L., and Crane, F.L. (1959). The natural occurrence of coenzyme Q and related compounds. J Biol Chem *234*, 2169-2175.

Lester, R.L., Crane, F.L., and Hatefi, Y. (1958). Coenzyme Q: a new group of quinones. Journal of the American Chemical Society *80*, 4751-4752.

Lin, F., Ferguson, K.L., Boyer, D.R., Lin, X.N., and Marsh, E.N. (2015). Isofunctional enzymes PAD1 and UbiX catalyze formation of a novel cofactor required by ferulic acid decarboxylase and 4-hydroxy-3-polyprenylbenzoic acid decarboxylase. ACS Chem Biol *10*, 1137-1144.

Liu, X., Jiang, N., Hughes, B., Bigras, E., Shoubridge, E., and Hekimi, S. (2005). Evolutionary conservation of the clk-1-dependent mechanism of longevity: loss of mclk1 increases cellular fitness and lifespan in mice. Genes Dev *19*, 2424-2434.

Liu, Y.T., Hersheson, J., Plagnol, V., Fawcett, K., Duberley, K.E., Preza, E., Hargreaves, I.P., Chalasani, A., Laura, M., Wood, N.W.*, et al.* (2014). Autosomal-recessive cerebellar ataxia caused by a novel ADCK3 mutation that elongates the protein: clinical, genetic and biochemical characterisation. J Neurol Neurosurg Psychiatry *85*, 493-498.

Lohman, D.C., Forouhar, F., Beebe, E.T., Stefely, M.S., Minogue, C.E., Ulbrich, A., Stefely, J.A., Sukumar, S., Luna-Sanchez, M., Jochem, A.*, et al.* (2014). Mitochondrial COQ9 is a lipid-binding protein that associates with COQ7 to enable coenzyme Q biosynthesis. Proc Natl Acad Sci U S A *111*, E4697-4705.

Lopez, L.C., Schuelke, M., Quinzii, C.M., Kanki, T., Rodenburg, R.J., Naini, A., Dimauro, S., and Hirano, M. (2006). Leigh syndrome with nephropathy and CoQ10 deficiency due to decaprenyl diphosphate synthase subunit 2 (PDSS2) mutations. Am J Hum Genet *79*, 1125-1129.

Lopez-Martin, J.M., Salviati, L., Trevisson, E., Montini, G., DiMauro, S., Quinzii, C., Hirano, M., Rodriguez-Hernandez, A., Cordero, M.D., Sanchez-Alcazar, J.A*., et al.* (2007). Missense mutation of the COQ2 gene causes defects of bioenergetics and de novo pyrimidine synthesis. Hum Mol Genet *16*, 1091-1097.

Lopez-Otin, C., Blasco, M.A., Partridge, L., Serrano, M., and Kroemer, G. (2013). The hallmarks of aging. Cell *153*, 1194-1217.

Lowe, J.S., Morton, R.A., and Harrison, R.G. (1953). Aspects of vitamin A deficiency in rats. Nature *172*, 716-719.

Lu, T.T., Lee, S.J., Apfel, U.P., and Lippard, S.J. (2013). Aging-associated enzyme human clock-1: substrate-mediated reduction of the diiron center for 5-demethoxyubiquinone hydroxylation. Biochemistry *52*, 2236-2244.

Luna-Sanchez, M., Diaz-Casado, E., Barca, E., Tejada, M.A., Montilla-Garcia, A., Cobos, E.J., Escames, G., Acuna-Castroviejo, D., Quinzii, C.M., and Lopez, L.C. (2015). The clinical heterogeneity of coenzyme Q10 deficiency results from genotypic differences in the Coq9 gene. EMBO Mol Med *7*, 670-687.

Lynen, F.A., B. W.; Eggerer, H.; Henning, U.; Moslein, E. M. (1959). g,g-Dimethyl-allyl-pyrophosphat und Geranyl-pyrophosphat, biologische Vorstufen des Squalens. Angewandte Chemie *71*, 657-684.

Lynen, F.E., H.; Henning, U.; Kessel, I. (1958). Farnesyl-pyrophosphat und 3-Methyl-d3-butenyl-1-pyrophosphat, die biologischen Vorstufen des Squalens. Angewandte Chemie *70*, 738-742.

Marbois, B., Gin, P., Faull, K.F., Poon, W.W., Lee, P.T., Strahan, J., Shepherd, J.N., and Clarke, C.F. (2005). Coq3 and Coq4 define a polypeptide complex in yeast mitochondria for the biosynthesis of coenzyme Q. J Biol Chem *280*, 20231-20238.

Marbois, B., Gin, P., Gulmezian, M., and Clarke, C.F. (2009). The yeast Coq4 polypeptide organizes a mitochondrial protein complex essential for coenzyme Q biosynthesis. Biochim Biophys Acta *1791*, 69-75.

Marbois, B., Xie, L.X., Choi, S., Hirano, K., Hyman, K., and Clarke, C.F. (2010). para-Aminobenzoic acid is a precursor in coenzyme Q6 biosynthesis in Saccharomyces cerevisiae. J Biol Chem *285*, 27827-27838.

Marbois, B.N., and Clarke, C.F. (1996). The COQ7 gene encodes a protein in saccharomyces cerevisiae necessary for ubiquinone biosynthesis. J Biol Chem *271*, 2995-3004.

Marbois, B.N., Hsu, A., Pillai, R., Colicelli, J., and Clarke, C.F. (1994). Cloning of a rat cDNA encoding dihydroxypolyprenylbenzoate methyltransferase by functional complementation of a Saccharomyces cerevisiae mutant deficient in ubiquinone biosynthesis. Gene *138*, 213-217.

Meganathan, R. (2001). Ubiquinone biosynthesis in microorganisms. FEMS Microbiol Lett *203*, 131-139.

Metz, G.H., K. P.; van Liemt, W. B. S.; Prestegard, J. H.; Lugtenburg, J.; Smith, S. O. (1995). NMR Studies of Ubiquinone Location in Oriented Model Membranes: Evidence for a Single Motionally-Averaged Population. J Am Chem Soc *117*, 564-565.

Miles, M.V. (2007). The uptake and distribution of coenzyme Q10. Mitochondrion *7 Suppl*, S72-77.

Mitchell, P. (1961). Coupling of phosphorylation to electron and hydrogen transfer by a chemi-osmotic type of mechanism. Nature *191*, 144-148.

Mitsui, J.e.a. (2013). Mutations in COQ2 in familial and sporadic multiple-system atrophy. N Engl J Med *369*, 233-244.

Mollet, J., Delahodde, A., Serre, V., Chretien, D., Schlemmer, D., Lombes, A., Boddaert, N., Desguerre, I., de Lonlay, P., de Baulny, H.O.*, et al.* (2008). CABC1 gene mutations cause ubiquinone deficiency with cerebellar ataxia and seizures. Am J Hum Genet *82*, 623-630.

Mollet, J., Giurgea, I., Schlemmer, D., Dallner, G., Chretien, D., Delahodde, A., Bacq, D., de Lonlay, P., Munnich, A., and Rotig, A. (2007). Prenyldiphosphate synthase, subunit 1 (PDSS1) and OH-benzoate polyprenyltransferase (COQ2) mutations in ubiquinone deficiency and oxidative phosphorylation disorders. J Clin Invest *117*, 765-772.

Momose, K., and Rudney, H. (1972). 3-Polyprenyl-4-hydroxybenzoate synthesis in the inner membrane of mitochondria from p-hydroxybenzoate and isopentenylpyrophosphate. A demonstration of isoprenoid synthesis in rat liver mitochondria. J Biol Chem *247*, 3930-3940.

Monaghan, R.M., Barnes, R.G., Fisher, K., Andreou, T., Rooney, N., Poulin, G.B., and Whitmarsh, A.J. (2015). A nuclear role for the respiratory enzyme CLK-1 in regulating mitochondrial stress responses and longevity. Nat Cell Biol *17*, 782-792.

Morgan, P.N.G., M. I.; Gibson, F. (1962). Conversion of Shikimic Acid to Aromatic Compounds. Nature *194*, 1239-1241.

Morton, R.A. (1958a). Ubiquinone. Nature *182*, 1764-1767.

Morton, R.A.G., U.; Schindler, O.; Wilson, G. M.; Chopard-dit-Jean, L. H.; Hemming, F. W.; Isler, O.; Leat, W. M. F.; Pennock, J. F.; Ruegg, R.; Schwieter, U.; Wiss, O. (1958b). Die Struktur des Ubichinons aus Schweineherzen. Helvetica Chimica Acta *41*, 2357-2362.

Mugoni, V., Postel, R., Catanzaro, V., De Luca, E., Turco, E., Digilio, G., Silengo, L., Murphy, M.P., Medana, C., Stainier, D.Y.*, et al.* (2013). Ubiad1 is an antioxidant enzyme that regulates eNOS activity by CoQ10 synthesis. Cell *152*, 504-518.

Nakai, D., Yuasa, S., Takahashi, M., Shimizu, T., Asaumi, S., Isono, K., Takao, T., Suzuki, Y., Kuroyanagi, H., Hirokawa, K.*, et al.* (2001). Mouse homologue of coq7/clk-1, longevity gene in

Caenorhabditis elegans, is essential for coenzyme Q synthesis, maintenance of mitochondrial integrity, and neurogenesis. Biochem Biophys Res Commun *289*, 463-471.

Nguyen, T.P., Casarin, A., Desbats, M.A., Doimo, M., Trevisson, E., Santos-Ocana, C., Navas, P., Clarke, C.F., and Salviati, L. (2014). Molecular characterization of the human COQ5 C-methyltransferase in coenzyme Q10 biosynthesis. Biochim Biophys Acta *1841*, 1628-1638.

Okada, K., Suzuki, K., Kamiya, Y., Zhu, X., Fujisaki, S., Nishimura, Y., Nishino, T., Nakagawa, T., Kawamukai, M., and Matsuda, H. (1996). Polyprenyl diphosphate synthase essentially defines the length of the side chain of ubiquinone. Biochim Biophys Acta *1302*, 217-223.

Olsen, R.K.D., G. D.; Moore, H. W.; Folkers, K.; Parson, W. W.; Rudney, H. (1966). 2-Multiprenylphenols and 2-Decaprenyl-6-methoxyphenol, Biosynthetic Precursors of Ubiquinones. J Am Chem Soc *88*, 5919-5923.

Olsen, R.K.S., J. L.; Daves, G. D.; Moore, H. W.; Folkers, K.; Parson, W. W.; Rudney, H. (1965). 2-Decaprenylphenol, Biosynthetic Precursor of Ubiquinone-10. J Am Chem Soc *87*, 2298-2300.

Olson, R.E., Bentley, R., Aiyar, A.S., Dialameh, G.H., Gold, P.H., Ramsey, V.G., and Springer, C.M. (1963). Benzoate Derivatives as Intermediates in the Biosynthesis of Coenzyme Q in the Rat. J Biol Chem *238*, 3146-3148.

Olson, R.E., Dialamieh, G.H., Bentley, R., Springer, C.M., and Ramsey, V.G. (1965). Studies on Coenzyme Q. Pattern of Labeling in Coenzyme Q9 after Administration of Isotopic Acetate and Aromatic Amino Acids to Rats. J Biol Chem *240*, 514-523.

Ozeir, M., Muhlenhoff, U., Webert, H., Lill, R., Fontecave, M., and Pierrel, F. (2011). Coenzyme Q biosynthesis: Coq6 is required for the C5-hydroxylation reaction and substrate analogs rescue Coq6 deficiency. Chem Biol *18*, 1134-1142.

Pagliarini, D.J., Calvo, S.E., Chang, B., Sheth, S.A., Vafai, S.B., Ong, S.E., Walford, G.A., Sugiana, C., Boneh, A., Chen, W.K.*, et al.* (2008). A mitochondrial protein compendium elucidates complex I disease biology. Cell *134*, 112-123.

Peng, M., Falk, M.J., Haase, V.H., King, R., Polyak, E., Selak, M., Yudkoff, M., Hancock, W.W., Meade, R., Saiki, R.*, et al.* (2008). Primary coenzyme Q deficiency in Pdss2 mutant mice causes isolated renal disease. PLoS Genet *4*, e1000061.

Petrillo, E., Godoy Herz, M.A., Fuchs, A., Reifer, D., Fuller, J., Yanovsky, M.J., Simpson, C., Brown, J.W., Barta, A., Kalyna, M.*, et al.* (2014). A chloroplast retrograde signal regulates nuclear alternative splicing. Science *344*, 427-430.

Pierrel, F., Hamelin, O., Douki, T., Kieffer-Jaquinod, S., Muhlenhoff, U., Ozeir, M., Lill, R., and Fontecave, M. (2010). Involvement of mitochondrial ferredoxin and para-aminobenzoic acid in yeast coenzyme Q biosynthesis. Chem Biol *17*, 449-459.

Poon, W.W., Barkovich, R.J., Hsu, A.Y., Frankel, A., Lee, P.T., Shepherd, J.N., Myles, D.C., and Clarke, C.F. (1999). Yeast and rat Coq3 and Escherichia coli UbiG polypeptides catalyze both O-methyltransferase steps in coenzyme Q biosynthesis. J Biol Chem *274*, 21665-21672.

Poon, W.W., Davis, D.E., Ha, H.T., Jonassen, T., Rather, P.N., and Clarke, C.F. (2000). Identification of Escherichia coli ubiB, a gene required for the first monooxygenase step in ubiquinone biosynthesis. J Bacteriol *182*, 5139-5146.

Quinzii, C., Naini, A., Salviati, L., Trevisson, E., Navas, P., Dimauro, S., and Hirano, M. (2006). A mutation in para-hydroxybenzoate-polyprenyl transferase (COQ2) causes primary coenzyme Q10 deficiency. Am J Hum Genet *78*, 345-349.

Quinzii, C.M., DiMauro, S., and Hirano, M. (2007). Human coenzyme Q10 deficiency. Neurochem Res *32*, 723-727.

Quinzii, C.M., and Hirano, M. (2010). Coenzyme Q and mitochondrial disease. Dev Disabil Res Rev *16*, 183-188.

Quinzii, C.M., Kattah, A.G., Naini, A., Akman, H.O., Mootha, V.K., DiMauro, S., and Hirano, M. (2005). Coenzyme Q deficiency and cerebellar ataxia associated with an aprataxin mutation. Neurology *64*, 539-541.

Redfearn, E.R., and Friend, J. (1961). Oxidation-reduction reactions of plastoquinone in isolated chloroplasts. Nature *191*, 806-807.

Rhee, H.W., Zou, P., Udeshi, N.D., Martell, J.D., Mootha, V.K., Carr, S.A., and Ting, A.Y. (2013). Proteomic mapping of mitochondria in living cells via spatially restricted enzymatic tagging. Science *339*, 1328-1331.

Rudney, H. (1957a). The biosynthesis of beta-hydroxy-beta-methylglutaric acid. J Biol Chem *227*, 363-377.

Rudney, H., and Parson, W.W. (1963). The Conversion of P-Hydroxybenzaldehyde to the Benzoquinone Ring of Ubiquinone in Rhodospirillum Rubrum. J Biol Chem *238*, 3137-3138.

Rudney, H.F., J. J. (1957b). The Biosynthesis of beta-hydroxy-beta-methylglutaryl coenzyme A. J Am Chem Soc *79*, 5580-5581.

Salviati, L., Trevisson, E., Rodriguez Hernandez, M.A., Casarin, A., Pertegato, V., Doimo, M., Cassina, M., Agosto, C., Desbats, M.A., Sartori, G.*, et al.* (2012). Haploinsufficiency of COQ4 causes coenzyme Q10 deficiency. J Med Genet *49*, 187-191.

Sastry, S.P., Jayaraman, J., and Ramasarma, T. (1961). Distribution of coenzyme Q in rat liver cell fractions. Nature *189*, 577.

Schmidt, O., Pfanner, N., and Meisinger, C. (2010). Mitochondrial protein import: from proteomics to functional mechanisms. Nat Rev Mol Cell Biol *11*, 655-667.

Sevin, D.C., and Sauer, U. (2014). Ubiquinone accumulation improves osmotic-stress tolerance in Escherichia coli. Nat Chem Biol *10*, 266-272.

Stefely, J.A., Reidenbach, A.G., Ulbrich, A., Oruganty, K., Floyd, B.J., Jochem, A., Saunders, J.M., Johnson, I.E., Minogue, C.E., Wrobel, R.L.*, et al.* (2015). Mitochondrial ADCK3 employs an atypical protein kinase-like fold to enable coenzyme Q biosynthesis. Mol Cell *57*, 83-94.

Stenmark, P., Grunler, J., Mattsson, J., Sindelar, P.J., Nordlund, P., and Berthold, D.A. (2001). A new member of the family of di-iron carboxylate proteins. Coq7 (clk-1), a membrane-bound hydroxylase involved in ubiquinone biosynthesis. J Biol Chem *276*, 33297-33300.

Stocker, R., Bowry, V.W., and Frei, B. (1991). Ubiquinol-10 protects human low density lipoprotein more efficiently against lipid peroxidation than does alpha-tocopherol. Proc Natl Acad Sci U S A *88*, 1646-1650.

Stroobant, P., Young, I.G., and Gibson, F. (1972). Mutants of Escherichia coli K-12 blocked in the final reaction of ubiquinone biosynthesis: characterization and genetic analysis. J Bacteriol *109*, 134-139.

Tauche, A., Krause-Buchholz, U., and Rodel, G. (2008). Ubiquinone biosynthesis in Saccharomyces cerevisiae: the molecular organization of O-methylase Coq3p depends on Abc1p/Coq8p. FEMS Yeast Res *8*, 1263-1275.

Tran, U.C., and Clarke, C.F. (2007). Endogenous synthesis of coenzyme Q in eukaryotes. Mitochondrion *7 Suppl*, S62-71.

Tran, U.C., Marbois, B., Gin, P., Gulmezian, M., Jonassen, T., and Clarke, C.F. (2006). Complementation of Saccharomyces cerevisiae coq7 mutants by mitochondrial targeting of the Escherichia coli UbiF polypeptide: two functions of yeast Coq7 polypeptide in coenzyme Q biosynthesis. J Biol Chem *281*, 16401-16409.

Turunen, M., Olsson, J., and Dallner, G. (2004). Metabolism and function of coenzyme Q. Biochim Biophys Acta *1660*, 171-199.

Tzagoloff, A., Akai, A., and Needleman, R.B. (1975). Assembly of the mitochondrial membrane system. Characterization of nuclear mutants of Saccharomyces cerevisiae with defects in mitochondrial ATPase and respiratory enzymes. J Biol Chem *250*, 8228-8235.

Tzagoloff, A., and Dieckmann, C.L. (1990). PET genes of Saccharomyces cerevisiae. Microbiol Rev *54*, 211-225.

Ulrich, E.L., Girvin, M.E., Cramer, W.A., and Markley, J.L. (1985). Location and mobility of ubiquinones of different chain lengths in artificial membrane vesicles. Biochemistry *24*, 2501-2508.

Wallace, D.C. (2005). A mitochondrial paradigm of metabolic and degenerative diseases, aging, and cancer: a dawn for evolutionary medicine. Annu Rev Genet *39*, 359-407.

Wang, Y., Oxer, D., and Hekimi, S. (2015). Mitochondrial function and lifespan of mice with controlled ubiquinone biosynthesis. Nat Commun *6*, 6393.

White, M.D., Payne, K.A., Fisher, K., Marshall, S.A., Parker, D., Rattray, N.J., Trivedi, D.K., Goodacre, R., Rigby, S.E., Scrutton, N.S.*, et al.* (2015). UbiX is a flavin prenyltransferase required for bacterial ubiquinone biosynthesis. Nature *522*, 502-506.

Winrow, M.J., and Rudney, H. (1969). The incorporation of p-hydroxybenzoic acid and isopentenyl pyrophphate into ubiquinone precursors by cell-free preparations of rat tissues. Biochem Biophys Res Commun *37*, 833-840.

Wohlrab, H. (2009). Transport proteins (carriers) of mitochondria. IUBMB Life *61*, 40-46.

Wolf, D.E.H., C. H.; Aldrich, P. E.; Skeggs, H. R.; Wright, L. D.; Folkers, K. (1957). Determination of Structure of beta,gamma-dihydroxy-beta-methylvaleric acid. J Am Chem Soc *79*, 1486-1487.

Wolf, D.E.H., C. H.; Trenner, N. R.; Arison, B. H.; Shunk, C. H.; Linn, B. O.; McPherson, J. F.; Folkers, K. (1958). Coenzyme Q. I. Structure Studies on the Coenzyme Q Group. J Am Chem Soc *80*, 4752.

Wright, L.D.C., E. L.; Skeggs, H. R.; MacRae, G. D. E.; Hoffman, C. H.; Wolf, D. E.; Folkers, K. (1956). Isolation of a New Acetate-replacing Factor. J Am Chem Soc *78*, 5273-5275.

Xie, L.X., Hsieh, E.J., Watanabe, S., Allan, C.M., Chen, J.Y., Tran, U.C., and Clarke, C.F. (2011). Expression of the human atypical kinase ADCK3 rescues coenzyme Q biosynthesis and phosphorylation of Coq polypeptides in yeast coq8 mutants. Biochim Biophys Acta *1811*, 348-360.

Young, I.G., Leppik, R.A., Hamilton, J.A., and Gibson, F. (1972). Biochemical and genetic studies on ubiquinone biosynthesis in Escherichia coli K-12:4-hydroxybenzoate octaprenyltransferase. J Bacteriol *110*, 18-25.

Young, I.G., Stroobant, P., Macdonald, C.G., and Gibson, F. (1973). Pathway for ubiquinone biosynthesis in Escherichia coli K-12: gene-enzyme relationships and intermediates. J Bacteriol *114*, 42-52.

Young, I.G.M., L. M.; Stroobant, P.; Gibson, F. (1971). Chacaterization and Genetic Analysis of Mutant Strains of *Escherichia coli* K-12 Accumulating the Ubiquinone Precursors 2-Octaprenyl-6-Methoxy-1,4-Benzoquinone and 2-Octaprenyl-3-Methyl-6-Methoxy-1,4-Benzoquinone. J Bacteriol *105*, 769-778.

Chapter 2

Mitochondrial ADCK3 employs an atypical protein kinase-like fold to enable coenzyme Q biosynthesis

Jonathan A. Stefely[1], Andrew G. Reidenbach[1], Arne Ulbrich, Krishnadev Oruganty, Brendan J. Floyd, Adam Jochem, Jaclyn M. Saunders, Isabel E. Johnson, Catherine E. Minogue, Russell L. Wrobel, Grant E. Barber, David Lee, Sheng Li, Natarajan Kannan, Joshua J. Coon, Craig A. Bingman, & David J. Pagliarini

[1]Co-first author

Author contributions:

J.A.S. was the primary author of this work. J.A.S., A.G.R., and D.J.P. conceived of the project and its design. J.A.S., A.G.R., A.U., K.O, B.J.F., A.J., J.M.S., I.E.J., C.E.M., R.L.W, G.E.B., D.L. and C.A.B. performed experiments and data analysis. S.L., N.K., J.J.C., C.A.B. and D.J.P. aided in experimental design. J.A.S., A.G.R., and D.J.P. wrote the manuscript.

This chapter, in full, was published as an article in *Molecular Cell* (**2015**, *57*, 83–94) by the authors listed above.

Abstract

The ancient UbiB protein kinase-like family is involved in isoprenoid lipid biosynthesis and is implicated in human diseases, but demonstration of UbiB kinase activity has remained elusive for unknown reasons. Here, we quantitatively define UbiB-specific sequence motifs and reveal their positions within the crystal structure of a UbiB protein, ADCK3. We find that multiple UbiB-specific features are poised to inhibit protein kinase activity, including an N-terminal domain that occupies the typical substrate binding pocket and a unique A-rich loop that limits ATP binding by establishing an unusual selectivity for ADP. A single alanine-to-glycine mutation of this loop flips this coenzyme selectivity and enables autophosphorylation, but inhibits coenzyme Q biosynthesis *in vivo*, demonstrating functional relevance for this unique feature. Our work provides mechanistic insight into UbiB enzyme activity and establishes a molecular foundation for further investigation of how UbiB family proteins affect diseases and diverse biological pathways.

Introduction

Protein kinase-like (PKL) superfamily members share an active site that catalyzes adenosine triphosphate (ATP)-dependent phosphorylation (Kannan et al., 2007), but evolution of divergent sequence features and unique accessory domains has enabled adoption of a broad range of biological functions. Crystallographic studies have revealed the unique features of 10 of the 20 known PKL families (Hon et al., 1997; Kang et al., 2008; Knighton et al., 1991; Ku et al., 2007; LaRonde-LeBlanc and Wlodawer, 2004; Mao et al., 2008; Walker et al., 1999; Yamaguchi et al., 2001; Young et al., 2003; Zheng and Jia, 2010); however, members of the UbiB family have remained refractory to purification and biochemical analyses.

UbiB kinases are present in archaea, bacteria and eukaryotes (Leonard et al., 1998), and comprise an estimated one-quarter of all microbial PKLs (Kannan et al., 2007). The founding member of the UbiB family, UbiB from *Escherichia coli*, is required for the aerobic biosynthesis of the redox-active lipid ubiquinone, also known as coenzyme Q (CoQ) (Poon et al., 2000). In eukaryotes, UbiB homologs are found exclusively in mitochondria (Pagliarini et al., 2008) and plastids (Lundquist et al., 2012; Lundquist et al., 2013; Martinis et al., 2013), where they have been implicated in stress responses (Jasinski et al., 2008), copper homeostasis (Schlecht et al., 2014), pigmentation (Lundquist et al., 2013), phospholipid metabolism (Tan et al., 2013), and isoprenoid lipid biosynthesis (Do et al., 2001; Lundquist et al., 2013; Martinis et al., 2013).

The human genome contains five UbiB family genes, *ADCK1–5* (Figure 1A). Mutations in ADCK3 and ADCK4 cause a cerebellar ataxia (Horvath et al., 2012; Lagier-Tourenne et al., 2008; Mollet et al., 2008; Pineda et al., 2010) and a steroid-resistant nephrotic syndrome (Ashraf et al., 2013), respectively, that are each associated with CoQ deficiency. Silencing of ADCK1 expression alters epithelial cell migration (Simpson et al., 2008), and silencing of ADCK2

significantly decreases the viability of cells derived from glioblastoma multiforme (Wiedemeyer et al., 2010) and estrogen receptor-positive breast tumors (Brough et al., 2011). As such, ADCK proteins are promising therapeutic targets that await rigorous biochemical characterization.

ADCK3 (CABC1, COQ8), the focus of this work, has been only minimally characterized at the biochemical level. Phylogenetic analyses defined ADCK3 as an 'atypical kinase' (Manning et al., 2002) and suggested that ADCK3 and ADCK4 are co-orthologs of the yeast protein Coq8p (Lagier-Tourenne et al., 2008). Coq8p is known to stabilize a complex of CoQ biosynthesis proteins in yeast (He, 2014), but the underlying mechanism is undefined. ADCK3 can weakly rescue the respiratory growth defect of Coq8p knockout (*coq8Δ*) yeast, and this rescue partially restores the phosphorylation state of Coq3p, Coq5p and Coq7p *in vivo*; but, whether this effect is direct or indirect is unknown (Xie et al., 2011). ADCK3 is known to reside in the mitochondrial matrix (Pagliarini et al., 2008; Rhee et al., 2013), and we recently demonstrated that ADCK3 contains a transmembrane domain that can drive homodimerization (Khadria et al., 2014).

The primary gaps in knowledge about the UbiB family center around its undefined enzymatic activity. Although UbiB proteins share some sequence features with protein kinases, whether UbiB proteins actually adopt a PKL fold was unknown. Moreover, previous attempts by our lab and others to demonstrate kinase activity for UbiB proteins *in vitro* were unsuccessful for unknown reasons.

Here, to provide molecular insight into the activity of UbiB family proteins, we integrate bioinformatics, crystallography, *in vitro* activity assays, and investigation of *in vivo* CoQ production. By solving a crystal structure of a UbiB family protein, human mitochondrial ADCK3, we show that UbiB proteins adopt an atypical PKL fold with multiple UbiB-specific

features positioned to inhibit protein kinase activity. We demonstrate that mutating one of these unique features relieves enzyme inhibition and enables autophosphorylation *in vitro*, while showing that this same mutation inhibits CoQ production *in vivo*. These results suggest a model wherein inhibition of protein kinase activity is important for the mechanism by which ADCK3 enables CoQ biosynthesis. Our work also suggests a mechanism by which human ADCK3 and ADCK4 mutations disrupt protein stability to cause disease, and provides a foundation for therapeutic targeting of UbiB family proteins.

Results

The UbiB family has numerous unique sequence motifs

The protein kinase-like domain of the UbiB family possesses an N-lobe insert and an N-terminal extension with uncharacterized sequence features (Figure 1A), including a unique and invariant KxGQ motif (Figure 1B). We conducted a statistical analysis of the features that distinguish UbiB proteins from other PKLs, which revealed that the UbiB family also has: an atypical AAAS motif in an alanine-rich (A-rich) loop that replaces the canonical glycine-rich (G-rich) nucleotide-binding loop, an ExD motif in the N-lobe insert, a modified catalytic loop, and a conserved arginine or lysine residue in the F-helix (αF) (Figure 1C and Figure S1A). However, the insolubility of full-length UbiB proteins (Figure S1C) has thus far hampered efforts to determine how these unique sequence elements enable UbiB-specific functions.

Mature mitochondrial ADCK3 is truncated

To generate a tractable system for biochemical analyses, we tested the solubility of various ADCK3 truncation constructs. Mature forms of mitochondrial UbiB proteins are likely processed

to remove their mitochondrial targeting sequences (MTS), and they contain predicted single-pass transmembrane (TM) domains that could limit solubility (Figure 1A). However, the MTS of ADCK3 could not be predicted *in silico*, so we determined it experimentally. Immunoblot and Edman degradation analyses of mitochondrial ADCK3 (Figure 1D) immunoprecipitated from human cells revealed that the mature form of ADCK3 is truncated by 162 residues to yield a 55 kDa protein (Figures 1E and 1F)—a size consistent with the observed yeast Coq8p truncation (Vogtle et al., 2009) and the predicted ADCK4 truncation (Figure 1A). Most of the sequence removed upon import into mitochondria lacks conservation among metazoan orthologs (Figure S1B). While the endogenous form of ADCK3 remained refractory to large-scale purification and crystallization, we were able to purify constructs with N-terminal truncations of 250 residues (ADCK3$^{N\Delta250}$) or 254 residues (ADCK3$^{N\Delta254}$). These constructs retain the PKL domain and the unique N-terminal extension, the combination of which represents the structural core of the UbiB family (Figure 1A). These results, combined with previous localization of ADCK3 to the mitochondrial matrix (Rhee et al., 2013), allowed us to create models for the ADCK3 precursor, the mature mitochondrial form, and the crystallized construct (Figures 1G and 1H).

ADCK3 adopts an atypical protein kinase-like fold

We crystallized and solved the structure of ADCK3$^{N\Delta254}$ at a resolution of 1.6 Å (Figure 2A, Table 1). ADCK3 adopts a core fold similar to that of well-characterized PKLs (Figure S2A), such as protein kinase A (PKA) (Knighton et al., 1991; Zheng et al., 1993) (Figure 2D), whereby the N-lobe folds into a β-sheet and a single α-helix (αC), and the C-lobe folds into a series of α-helices and β-strands. The overall topologies of ADCK3 and PKA are also similar, but ADCK3 contains a long N-terminal extension (GQα1–GQα4), an N-lobe insert between β3 and αC

(GQα5–GQα6), and a C-lobe insert between β9 and αF (Cα1–Cα4) (Figures 2C and 2F)—unique features that likely afford UbiB family-specific functions.

Unexpectedly, the N-terminal extension and the N-lobe insert fold into α-helices that pack together and rest directly over the A-rich loop and the PKL cleft, where they place the signature KxGQ motif into the substrate-binding pocket (Figure 2A). We have named this region of ADCK3, composed of the insert and extension, the 'KxGQ domain' and its component α-helices 'GQα1–GQα6' (Figure 2C). The KxGQ domain completely occludes the cleft that binds peptide substrates in typical protein kinases (Figures 2B and 2E). Moreover, in stark contrast to the architecture of ADCK3, the N-terminal extensions of all other structurally characterized PKL families are positioned far from the active site (Figure S2B–S2K). Even the N-terminal extension and the N-lobe insert of Rio family proteins, which exhibit the highest structural similarity to ADCK3 (Figure S2A), fold away from the nucleotide pocket and leave the PKL cleft open to accept a peptide substrate (Figure S2B).

Within the KxGQ domain of ADCK3, we observed a salt bridge between K276 of the KxGQ motif and E405 of the ExD motif (Figures 3A and 3D). The polar and ionic interactions between Q279, K276, and E405 suggest that they act as a functional triad, which we have named the QKE triad. The QKE triad folds directly into the active site near the A-rich loop and highly conserved PKL residues such as D507 and N493 (Figure 3A). This position of the QKE triad overlaps with that of the substrate phosphoryl acceptor in structures of typical protein kinases. Collectively, this structural analysis of the KxGQ domain and the QKE triad suggests that they could function to inhibit protein kinase activity.

ADCK3 contains an atypical active site

Given that demonstration of kinase activity for a UbiB protein has remained elusive for well over a decade (Leonard et al., 1998), we examined the ADCK3 structure for additional features that could inhibit kinase activity. Comparing the structures of PKA and ADCK3 reveals significant differences within the catalytic loop. In PKA, D166 ($D166^{PKA}$) is orientated toward the terminal phosphate of the ATP substrate, where it is thought to act as a catalytic base for the phosphoryl acceptor. In contrast, the homologous ADCK3 residue, $D488^{ADCK3}$, is oriented in the opposite direction, where it forms a bidentate salt bridge with αF through $R611^{ADCK3}$ (Figure 3C and 3E).

While features such as the QKE triad and the D488:R611 salt bridge could inhibit protein kinase activity, our PKA-ADCK3 superposition also shows that ADCK3 has hallmarks of an active kinase, including a salt bridge between K358 and E411 (Figure 3C), cation-binding residues (N493 and D507) poised for catalysis (Figure 3C), and intact kinase 'spines' (Kornev et al., 2006) (Figures S3A and S3B). These hallmark features allow active kinases to bind MgATP and catalyze phosphoryl transfer. ADCK3's retention of these features suggests that it would be capable of performing catalysis following removal of inhibitory constraints, but neither nucleotide binding nor catalytic properties had yet been demonstrated for a UbiB protein.

ADCK3 exhibits an unusual selectivity for binding ADP over ATP

To test whether ADCK3 can bind ATP, we quantified ligand-induced changes in ADCK3 melting temperature (ΔT_m). In the presence of divalent cations, adenine nucleotides significantly stabilized $ADCK3^{N\Delta 250}$, whereas other nucleotides did not (Figure 3F). Surprisingly, ADCK3 exhibited an unusual selectivity for binding ADP over ATP. PKA, an example of a more typical kinase, binds MgATP and MgADP with similar affinity, with dissociation constants of ~10 μM

(Bhatnagar et al., 1983). ADP binding could inhibit ATP-dependent kinase activity, so we aimed to define the mechanism by which ADCK3 selectively binds ADP over ATP.

The location of the UbiB-specific KxGQ motif near the active site raises the question of whether it mediates nucleotide binding and determines selectivity for ADP. To measure the effects of ADCK3 point mutations on nucleotide binding, we quantified ΔT_m values over a range of ligand concentrations to generate ligand-binding curves, which allowed us to determine apparent dissociation constants ($K_{d,\,app}$) and maximum ΔT_m values ($\Delta T_{m,\,max}$) (Figure S3C–S3E). As expected, mutation of canonical PKL ATP-binding residues dramatically decreased ATP and ADP binding; however, mutation of the KxGQ motif had minimal effects (Figure 3B), suggesting that it is not part of the core nucleotide-binding pocket.

To further examine the structural basis for nucleotide binding, we used deuterium exchange mass spectrometry (DXMS) (Figure 3G and 3H). DXMS revealed that ADCK3 has a stable hydrophobic core anchored by the F-helix, while the KxGQ domain and portions of the unique C-lobe are more mobile. Dramatic decreases in deuterium exchange rates in the presence of nucleotides were observed for the conserved DFG motif, which coordinates a cation that mediates nucleotide binding (see D507 in Figure 3C), and for the unique A-rich loop. This direct involvement of the UbiB-specific A-rich loop in nucleotide binding nominated it as a possible structural determinant of selectivity for ADP.

The A-rich loop of ADCK3 is a structural determinant of coenzyme selectivity

Comparing the conformation of the A-rich loop of ADCK3 to the G-rich loop of PKA reveals significant differences (Figure 4A). The sterics and conformational flexibility of $G52^{PKA}$ allow a backbone amide of the G-rich loop to hydrogen bond with the γ-phosphate of ATP. The A-rich

loop of ADCK3 adopts a different conformation, and the homologous backbone amide is not ideally positioned to bind ATP. Furthermore, in superimposed structures of ADCK3 and PKA, $A339^{ADCK3}$ clashes with the nucleotide bound to PKA.

To test the hypothesis that the A-rich loop of ADCK3 is a determinant of coenzyme selectivity, we mutated its alanine residues to glycine residues, thereby converting it into a more typical G-rich loop. An A339G mutation of ADCK3 significantly enhanced affinity for MgATP without affecting MgADP binding. As such, the A339G mutation affords a 6-fold increase in selectivity for ATP over ADP (K_d^{MgADP}/K_d^{MgATP}) (Figures 4B and S4A). Like the A339G mutation, an A337G,A339G double mutation also enhanced selectively for ATP (Figures 4C and S4A). However, in contrast, an A337G mutation alone did not flip coenzyme selectivity. These results demonstrate that $A339^{ADCK3}$ is a major structural determinant of coenzyme selectivity and suggest that it could also be an important determinant of ADCK3 enzyme activity.

A single A-to-G mutation of the A-rich loop enables autophosphorylation

The G-rich loop of typical protein kinases is important for MgATP binding, peptide substrate binding, and catalysis (Bossemeyer, 1994; Hemmer et al., 1997). To test the idea that the ADCK3 A339G mutation might similarly enable protein kinase activity, we examined the ability of ADCK3 A-rich loop mutants to autophosphorylate. The A339G and A337G,A339G double mutations both enabled autophosphorylation (Figure 4D), which we found to be dependent on time and ATP concentration (Figures 4E–G). MgATP-dependent phosphorylation of the N-terminal serine residue of ADCK3 A339G was also observed by liquid chromatography high-resolution tandem mass spectrometry (LC-MS/MS) (Figure S4B–D). Autophosphorylation was inhibited by an A339G,D507N double mutation (Figure 4H), which also inhibited MgATP

binding (Figure 4I), demonstrating that the phosphorylation is ADCK3-dependent and not due to a contaminating kinase. Furthermore, the autophosphorylation was Mg^{2+}-dependent (Figure 4H), a typical feature of kinase activity. Under these reaction conditions, we also observed non-specific phosphorylation of all three ADCK3 variants with MnATP, a result that has been observed previously in reactions with MnATP (Schieven and Martin, 1988). Collectively, these results demonstrate that ADCK3 A339 inhibits protein kinase activity *in vitro*.

Mutation of the conserved KxGQ motif enhances autophosphorylation

The activity of the ADCK3 A339G mutant enabled us to test our structure-based hypothesis that the KxGQ domain inhibits protein kinase activity. In the A339G background, KxGQ motif mutations markedly enhanced autophosphorylation activity (Figure 4J). Interestingly, the enhanced autophosphorylation activity was not observed with KxGQ motif single mutants. Under these conditions, the A339G mutation appears to be necessary for autophosphorylation activity *in vitro*.

In vivo, accessory factors could induce conformational changes of the A-rich loop and the KxGQ domain to enhance activity. Based on our structure, we generated two hypothetical models for how the KxGQ domain could move (Figure S4E). To begin testing these models, we used normal mode analysis (NMA) to examine computationally predicted conformational changes. Subtle harmonic movements of the KxGQ domain were observed by NMA, providing evidence for slight opening of the KxGQ domain as a "3-hinge door" (Figure S4F). Flexibility of "hinge 1," the region between GQα3 and GQα4, would be needed for any opening of the KxGQ domain according to this model—a feature that is supported experimentally by the observation of high B-factors (Figure S4J) and high deuterium exchange rates (Figure 4H) for this region. These

techniques cannot provide an indication of how far the KxGQ domain could open; however, collectively, the results suggest that movement of this region is feasible. Even without significant movement of the KxGQ domain, computational analyses predict a small pocket that could potentially accommodate a small phosphoryl acceptor substrate (Figure S4G–I).

UbiB-specific features are required for coenzyme Q biosynthesis

To test the direct functional relevance of novel UbiB family sequence elements, we performed *in vivo* structure-function analyses with Coq8p. Using our ADCK3 structure, we generated a homology model of Coq8p (Figure S5A and S5B), which allowed us to design Coq8p mutations and examine their structural effects. We then expressed Coq8p variants in *coq8Δ* yeast, which exhibit a respiratory growth defect on non-fermentable carbon sources caused by CoQ deficiency. Mutation of conserved nucleotide pocket residues eliminated respiratory growth, both on solid media with non-fermentable carbon sources (Figure 5A) and in liquid media with depleted glucose (Figure S5C). Using high-resolution LC-MS, we demonstrated that these growth phenotypes closely mirrored decreases in CoQ abundance (Figure 5B). Together, this panel of assays enables rapid and precise measurement of the phenotypic effects of mutations to conserved Coq8p and ADCK3 residues.

We next used these yeast assays to define essential residues in the A-rich loop and the KxGQ domain. Importantly, the mutation homologous to ADCK3 A339G, Coq8p A197G, caused a significant decrease in CoQ abundance (Figure 5B), despite its activation of ADCK3 protein kinase activity *in vitro*, demonstrating the functional relevance of this conserved alanine residue. Mutation of the serine residue of the AAAS motif also markedly decreased respiratory growth (Figure 5A) and CoQ abundance (Figure 5B), further emphasizing the importance of the

A-rich loop. Finally, mutations of the QKE triad eliminated respiratory growth and CoQ production (Figure 5A and 5B), demonstrating an essential role for the QKE triad in the core function of UbiB proteins.

Pathogenic ADCK3 and ADCK4 mutations disrupt protein stability

Our ADCK3 structure provides an opportunity to investigate the molecular basis of human diseases associated with UbiB family members. ADCK3 mutations that cause a cerebellar ataxia map to multiple regions of the protein, including the KxGQ domain (Figure 6A), further validating the central importance of this unique region of the protein (Horvath et al., 2012; Lagier-Tourenne et al., 2008; Mollet et al., 2008; Pineda et al., 2010). We used our structure to predict the deleterious effects of ADCK3 mutations (Figure 6B), most of which show decreased protein thermal stability or affinity for nucleotide (Figure 6C and 6D). By generating a homology model of ADCK4, we were likewise able to infer the deleterious effects of mutations in this kinase that cause a kidney disease (Ashraf et al., 2013) (Figure S6).

Discussion

Insights into the enzyme activity of the UbiB family

Since the classification of UbiB family protein sequences as protein kinase-like (Leonard et al., 1998), it has been assumed that UbiB family members are protein kinases. However, until now, to our knowledge, the structure, ligand-binding properties, and activity of a UbiB protein had not been described. Our results demonstrate that a UbiB family protein, ADCK3, does in fact adopt a PKL fold and bind adenine nucleotides in a divalent cation-dependent manner, strengthening the hypothesis that UbiB proteins are *bona fide* kinases.

This work also provides rationale for why demonstration of UbiB protein kinase activity has been so elusive. Our structural and biochemical investigations show that multiple UbiB-specific features inhibit ADCK3 protein kinase activity. With a single A-to-G mutation of the A-rich loop, we were able to release one of these inhibitory mechanisms and demonstrate kinase activity for a UbiB family protein.

Our work also shows that the QKE triad is essential for function *in vivo* and provides insight into the biochemical function of the conserved KxGQ domain. If UbiB proteins catalyze phosphorylation of proteins, as previously hypothesized (Martinis et al., 2013; Xie et al., 2011), then the KxGQ domain is likely to be an autoinhibitory domain because it fills the space normally occupied by peptide or protein substrates in typical protein kinases. This idea is supported by the enhanced autophosphorylation activity of KxGQ mutants in the A339G background. However, our analyses raise a competing hypothesis: ADCK3 may phosphorylate a small molecule, with the KxGQ domain functioning as a substrate-binding domain. This idea is supported by the observation of a potential small molecule binding pocket that could be accessed with minimal conformational changes and would be even more accessible with subtle movements of the KxGQ domain, such as those predicted by our normal mode analysis. The observed phosphorylation of an N-terminal serine is concordant with the protein kinase hypothesis, but this moderately hydrophobic N-terminal sequence could also mimic an elongated small molecule, such as a lipid.

A final hypothesis related to our observation of UbiB-specific inhibitory mechanisms is that ADCK3 is a pseudokinase. However, the retention of all residues necessary for catalysis, and the requirement of these residues for *in vivo* function, suggest that this is unlikely, as all

characterized pseudokinases are missing one or more essential catalytic residues (Zeqiraj and van Aalten, 2010).

Implications for our understanding of the PKL superfamily

Our investigation of UbiB family proteins has widespread implications for our understanding of the ubiquitous PKL superfamily. One UbiB-specific feature, the A-rich loop, is a striking deviation from common G-rich nucleotide binding motifs. G-rich motifs are not only widespread in the PKL superfamily; they are also found in the Rossmann fold (Rossmann et al., 1974) and the p-loop (Walker A motif) (Saraste et al., 1990). Generally, these G-rich motifs enable coordination of nucleotide phosphates by backbone amides. The second glycine in the G-rich loop (Gx**G**xxG) was known to be critical for ATP binding and protein kinase catalysis by PKA (Bossemeyer, 1994; Hemmer et al., 1997), but it was not known what effects this residue had on nucleotide selectivity. Our work demonstrates that the analogous A-rich loop of ADCK3 confers an unusual selectivity for ADP over ATP. Moving forward, it may be important to test the hypothesis that UbiB proteins can use ADP as a phosphoryl donor. An ADP-dependent glucokinase has been described (Ito et al., 2001), but no PKL superfamily members are known to be ADP-dependent kinases.

Insight into the biosynthesis of isoprenoid lipids

Many UbiB family proteins are required for the biosynthesis of isoprenoid lipids, such as coenzyme Q, plastoquinone, phylloquinone (vitamin K), plastochromanol, and α-tocopherol (vitamin E) (Cardazzo et al., 1998; Do et al., 2001; Lundquist et al., 2013; Martinis et al., 2013; Poon et al., 2000). Our work provides a molecular foundation for investigating this requirement.

We show that UbiB-specific features, such as the A-rich loop and KxGQ motif, are required for the ability of Coq8p to enable mitochondrial CoQ biosynthesis. Furthermore, our structure-activity investigations suggest that inhibition of protein kinase activity is important for the mechanism by which UbiB proteins enhance coenzyme Q biosynthesis.

Ongoing work in our laboratory seeks to understand why this inhibition of UbiB protein kinase activity is important for isoprenoid lipid metabolism. The yeast ortholog of ADCK3, Coq8p, has an established role in stabilizing a membrane-associated complex of proteins that comprises the CoQ biosynthetic machinery (He et al., 2014), and we currently favor two competing hypotheses for how Coq8p could mechanistically fulfill this role. One hypothesis is that Coq8p is a protein kinase that phosphorylates other proteins in the CoQ complex to stabilize their interactions. If this is true, then our work suggests that this protein kinase activity must be carefully regulated to enable proper phosphorylation of the CoQ complex. However, as detailed above, our work raises the alternative possibility that UbiB proteins are small molecule kinases. If this is true, then Coq8p might phosphorylate a prenyl lipid, which has been suggested to be a part of the mature CoQ biosynthetic complex (He et al., 2014). We recently demonstrated that another CoQ-related protein, COQ9, binds phosphorylated lipids and isoprenoid lipids (Lohman et al., 2014). COQ9 and ADCK3 comprise a single polypeptide in the protozoan, *Tetrahymena thermophila,* suggesting that these proteins might work together to stabilize the CoQ biosynthetic complex or to seed its formation on the inner mitochondrial membrane.

Implications for human diseases involving UbiB family proteins

Mutations of ADCK3 are responsible for a neurodegenerative disease (Horvath et al., 2012; Lagier-Tourenne et al., 2008; Mollet et al., 2008; Pineda et al., 2010), and mutations of a closely

related homolog, ADCK4, are responsible for a steroid resistant nephrotic syndrome (Ashraf et al., 2013). The results presented here provide a structural framework for understanding how these ADCK mutations cause human disease.

Other ADCK proteins, such as ADCK2, have been linked to cancer cell viability (Brough et al., 2011; Wiedemeyer et al., 2010), suggesting inhibition of ADCK proteins as a potential therapeutic strategy. Kinases are proven chemotherapeutic targets for small molecule inhibitors, but off-target kinase inhibition can be problematic. Encouragingly, our analyses reveal that the architecture of the UbiB family nucleotide-binding pocket, especially the placement of the KxGQ motif, is likely sufficiently distinct to enable the development of specific inhibitors. Furthermore, ADCK2 has unique sequence features that distinguish it from the other human ADCKs, which should assist development of ADCK2-specific inhibitors. Our structure of ADCK3 provides a foundation for building homology models of ADCK2 for structure-based inhibitor design.

Collectively, our investigation of how ADCK3 uses a significant variation on the PKL fold to enable ubiquinone biosynthesis has broad implications on our understanding of kinase enzyme regulation, catalysis, and substrate recognition. These results also provide a framework for further biochemical analysis and therapeutic targeting of the widespread UbiB family.

Experimental Procedures

Prediction of targeting sequences and transmembrane domains

Mitochondrial targeting sequences (MTSs) were predicted with MitoProt II (Claros and Vincens, 1996). The Coq8p MTS was previously defined by observation of the N-terminus of mature

Coq8p (Vogtle et al., 2009). Transmembrane domains were predicted with Phobius (Kall et al., 2007).

Statistical analysis of unique sequence motifs (CHAIN analysis)

MAPGAPS (Neuwald, 2009), a program to hierarchically align sequences using a profile-profile alignment method, was used to align close to 150,000 sequences belonging to the PKL superfamily, as done previously (Kannan and Neuwald, 2005). Redundant sequences at a sequence identity cutoff of 90% were removed from the alignment. The curated alignment was used to delineate uniquely conserved residue patterns in the UbiB family using the program CHAIN (Neuwald, 2007; Neuwald et al., 2003). CHAIN analysis uses a Bayesian partitioning scheme to delineate residue patterns most distinguishing a set of foreground sequences against a set of background sequences. The input to CHAIN is an aligned set of 'foreground' sequences and a set of 'background' sequences that are evolutionarily more diverse. For CHAIN analyses, UbiB sequences were used as the foreground. Two different background sets were used: (a) all other PKL proteins, or (b) multiple ePK-like kinases (ELKs), including those of the CAK family (aminoglycoside, choline, and ethanolamine kinases), the MTRK family, the FruK family, PKL maltose kinases, and the RevK family. Default parameters were used to generate residue patterns with the highest log-likelihood of being 'contrastingly conserved' in the foreground in comparison to the background.

Cloning of ADCK3 constructs and mutants

ADCK3 was obtained from a human cDNA source using the Flexi® cloning method (Blommel et al., 2009), amplified, inserted into the pEU-His Flexivector, and verified by DNA sequencing.

ADCK3 was transferred to pVP68K (Blommel et al., 2009) to create a vector for bacterial expression. This pVP68K plasmid encodes ADCK3 fused to an 8His-cytoplasmically-targeted maltose-binding protein (MBP) with a linker including a tobacco etch virus (TEV) protease recognition site (8His-MBP-[TEV]-ADCK3). PIPE cloning (Klock and Lesley, 2009) was used to introduce truncations and mutations into the ADCK3 gene. PCR was performed using Pfu-Ultra II polymerase (Stratagene, La Jolla, CA). All oligonucleotides were purchased from IDT (Coralville, IA). Upon PCR completion, the template was destroyed by DpnI digestion. The DpnI-digested PCR product was purified using a kit (Qiagen, Valencia, CA) and the eluted DNA was used to transform *E. coli* 10G chemically competent cells (Lucigen, Middleton, WI). Plasmids were isolated from transformants and DNA sequencing was used to identify those containing the correct mutation and/or truncation. For mammalian expression of ADCK3-FLAG, the full-length ADCK3 coding region was cloned into pcDNA3.1 using Gibson Assembly cloning (New England Biolabs).

Mammalian cell culture and affinity purification

HEK293 cells were grown in Dulbecco's modified Eagle's medium (DMEM, LifeTechnologies) supplemented with 10% fetal bovine serum and 1% penicillin-streptomycin (LifeTechnologies), and were subcultured by trypsinization. On day one, 7 million cells were plated in a 15 cm dish and allowed to grow overnight. On day two, cells were transiently transfected with a mix of 20 μg pcDNA3.1 ADCK3-FLAG plasmid, 75 μg linear polyethylenimine (PEI, PolySciences), and 900 μL Opti-MEM (LifeTechnologies). On day four, cells were washed with and harvested into phosphate-buffered saline (PBS), and cell pellets were frozen at −80 °C. Cell pellets were lysed in 200 μL PBS containing 0.5% IGEPAL CA-630 (NP-40, Sigma), protease inhibitors (10 μM

benzamide HCl, 1 μg/mL 1,10-phenanthroline and 0.5 μg/mL each of pepstatin A, chymostatin, antipain, leupeptin, aprotinin; Sigma), phosphatase inhibitors (500 μM imidazole, 250 μM NaF, 300 μM sodium molybdate, 250 μM sodium orthovanadate, 1 mM sodium tartrate; Sigma), and deacetylase inhibitors (10 mM each sodium butyrate and nicotinamide; Sigma). Insoluble materials were pelleted (16,000 *g*, 10 min, 4 °C) and the supernatant was mixed with 30 μL pre-washed anti-FLAG magnetic beads (Sigma M8823) for 2 h at 4 °C. Following incubation, beads were washed three times in PBS containing 0.05% IGEPAL CA-630 and once in PBS. Proteins were eluted in 60 μL PBS containing 0.2 mg/mL FLAG-peptide for 30 min at room temperature.

Subcellular localization via confocal microscopy

On the day prior to transfection, cells were plated at a density of 75,000 cells/well onto poly-D-lysine-coated coverslips in 6-well dishes. Cells were transiently transfected with a mix of 1 μg pcDNA3.1 ADCK3-FLAG, 0.5 μg plasmid encoding green fluorescent protein with an N-terminal mitochondrial localization sequence (Hanson et al., 2004) (MLS-GFP), 7.5 μg PEI, and 200 μL Opti-MEM. After 24 hours, the cells were fixed (4% paraformaldehyde in PBS), permeabilized (0.2% Triton X-100 in PBS), blocked (1% BSA in PBS), and probed with mouse anti-FLAG M2 1° antibody (F1804, Sigma, 1:2000 (v/v) in 1% BSA in PBS) and Alexa Fluor 594-conjugated goat anti-mouse 2° antibody (LifeTechnologies, 1:2000 (v/v) in 1% BSA in PBS) in 1% BSA in PBS. Hoechst dye (1 μg/mL) was used to label nuclear DNA. Slides were placed in mounting medium (1:1, v/v, glycerol/PBS). Images were captured using the Nikon A1R system, Plan Apo VC 60X oil immersion optics, with sequential laser excitation using 561 nm (Alexa Fluor), 488 nm (GFP), and 408 nm (Hoechst) lasers. Images were collected and assembled into a Z-stack using the NIS-Elements software.

Analysis of ADCK3-FLAG by N-terminal sequencing

ADCK3-FLAG isolated by FLAG affinity purification was further resolved by SDS-PAGE (NuPAGE 4–12% Bis-Tris gel; 50 mM MES, 50 mM Tris, 1 mM EDTA, 0.1% SDS (w/v); 150 V, 7 h, 4 °C) and transferred by electroblot to a polyvinylidene fluoride membrane (Sequi-Blot PVDF membrane, 0.2 μm pore size; 25 mM Tris, 192 mM glycine, 20% (v/v) methanol; 100 V, 1 h, 4 °C). A Novex Sharp Pre-Stained Protein Standard was used as a molecular weight marker. The PVDF membrane was stained (0.1% (w/v) Coomassie brilliant blue R-250, 40% (v/v) methanol, 10% (v/v) acetic acid), destained (40% (v/v) methanol, 10% (v/v) acetic acid), and rinsed (90% (v/v) methanol, 5% (v/v) acetic acid). A small piece of the PVDF containing the protein band was cut out of the membrane, washed (H_2O), and loaded into the instrument for analysis (494 Procise Protein Sequencer, 140C Analyzer, Applied Biosystems, Iowa State University Protein Facility).

Expression and purification of ADCK3$^{N\Delta254}$ for crystallization

For selenomethionine-labeled protein expression, the 8His-MBP-[TEV]-ADCK3$^{N\Delta254}$ construct was transformed into the *E. coli* strain B834-pRARE2 (pRARE2 (Burgess-Brown et al., 2008) was isolated from Rosetta 2 cells (Novagen) and transformed into the B834 strain (Lucigen)). Protein expression was performed as described (Gromek et al., 2013) with modification of the final incubation temperature after IPTG induction to 12 °C for 24 hours. Cells were isolated and frozen at –80 °C until further use. For protein purification, cells were thawed, resuspended in lysis buffer (20 mM Tris-HCl, pH 7.2, 300 mM NaCl, 2 mM DTT, 20% (v/v) glycerol, 0.25 mM PMSF, 1 μM protease inhibitor E-64 (Sigma), rLysozyme (Novagen), and Benzonase

(Novagen)), and lysed by sonication (15 min, 4 °C). The lysate was centrifuged (30 min, 75,600 *g*, 4 °C). PEI (0.1% v/v) was added and the lysate was centrifuged again (30 min, 75,600 *g*, 4 °C). A nickel ion metal affinity chromatography (IMAC) column (His Trap FF Crude Ni Sepharose column; GE Lifesciences) was equilibrated with 5 column volumes (CVs) of binding buffer (300 mM NaCl, 35 mM Imidazole, 20 mM Tris-HCl pH 7.2, 20% (v/v) glycerol, 2 mM DTT, and 0.25 mM PMSF). The supernatant containing soluble cell lysate was filtered (0.8 µm syringe filter) and loaded onto the IMAC (1.0 mL/min). The column was washed with binding buffer (4 CVs) and wash buffer (25 mM imidazole, 300 mM NaCl, 20 mM Tris-HCl pH 7.2, 20% v/v glycerol, 2 mM DTT, and 0.25 mM PMSF) (5 CVs). 8His-MBP-[TEV]-ADCK3$^{N\Delta254}$ was eluted with elution buffer (500 mM imidazole, 300 mM NaCl, 20 mM Tris-HCl pH 7.2, 20% v/v glycerol, 2 mM DTT, and 0.25 mM PMSF) (5 CVs). Protein purity was assessed by SDS-PAGE and the appropriate fractions were pooled and dialyzed into cleavage buffer (150 mM NaCl, 20 mM Tris-HCl pH 7.2, 10% v/v glycerol, 2 mM DTT, and 0.25 mM PMSF) using a dialysis cassette (1 kDa MWCO) (Thermo) or dialysis tubing (12–14 kDa MWCO) (Fisher). To cleave MBP from ADCK3$^{N\Delta254}$, Δ238TEV protease (Blommel and Fox, 2007) was added to the sample (1:100, TEV/fusion protein, mass/mass) and incubated (~12 h, 20 °C). After cleavage was complete, as assessed by SDS-PAGE, the sample was filtered (0.8 µm syringe filter). A second IMAC purification was performed to separate the 8His-MBP from ADCK3$^{N\Delta254}$. An IMAC column was equilibrated with binding buffer (4 CVs). The sample was loaded onto the column (3 mL/min) and the column was washed with binding buffer (4 CVs). A gradient elution was performed (0–350 mM imidazole in binding buffer over 15 CV). Fractions containing ADCK3$^{N\Delta254}$ were assessed by SDS-PAGE, pooled, and concentrated using a polyethersulfone (PES) membrane concentrator (10 kDa MWCO) (Thermo). ADCK3$^{N\Delta254}$ was further purified by

gel filtration (HiPrep 16/60 Sephacryl S-200 High Resolution column; GE Healthcare) with an isocratic elution (10 mM HEPES pH 7, 100 mM NaCl, 0.3 mM TCEP; flow rate of 0.5 mL/min). Fractions containing ADCK3$^{N\Delta254}$ were monitored by SDS-PAGE, pooled, and concentrated using a PES membrane concentrator (10 kDa MWCO) prior to crystallization.

Crystallization

Crystals of selenomethionine-labeled ADCK3$^{N\Delta254}$ were obtained by applying the high throughput screening and optimization platform developed at the Center for Eukaryotic Structural Genomics (Markley et al., 2009). Crystallization screens were set with a TTP Labtech Mosquito robot, and a Tecan Genesis was used for optimization solutions. All operations were tracked using SESAME LIMS (Zolnai et al., 2003). The best crystals were obtained by microseeding into 5 μL of 5 mg/mL selenomethionyl ADCK3$^{N\Delta254}$, 12.5% PEG 3350, 150 mM $(NH_4)_2SO_4$, 5 mM $MgCl_2$, 50 mM NaHEPES pH 7.5.

X-ray data collection and structure determination

Hundreds of samples were screened for diffraction quality at the LS-CAT and GM/CA beamlines at the Advanced Photon Source. Most crystals were split and were extremely sensitive to cryopreservation. Single-wavelength anomalous diffraction data at 0.9786Ā was collected on a MAR300 CCD detector at LS-CAT beamline 21-ID-G on an exceptional specimen cryopreserved using Paratone-N. Diffraction data was collected at 100K, and was reduced with HKL2000 (Otwinowski and Minor, 1997). The selenium substructure was determined with HySS (Grosse-Kunstleve and Adams, 2003) and phased using Phenix Autosolve (Terwilliger et al., 2009) with a phasing figure of merit of 0.394. The model was iteratively improved using

ARP/wARP (Langer et al., 2008)-Refmac (Murshudov et al., 1997), Phenix (Afonine et al., 2012) refinement and Coot (Emsley et al., 2010) with 5% of reflections consistently held in a cross-validation set. Traditional $2mF_o–DF_c$, $mF_o–DF_c$ and composite simulated annealing omit maps were calculated throughout the refinement procedure. The final model was continuous from residues 258–644. Electron density for four residues at both the amino- and carboxy-termini was not observed. Electron density for residues 301–330 is relatively poor, probably indicating substantial disorder in this portion of the protein. 98% of the residues are in favored backbone conformations, 2% are in allowed and two residues are in disallowed space (Chen et al., 2010). Residue N323 is in the disorderly loop and has poor density. S340 is in excellent density. The presumed ATP and substrate binding pockets were filled with ordered solvent.

Dali Server Structure Analysis

The ADCK3 structure was used as a query protein structure to search the Protein Structure Database with DaliLite v. 3 through the Dali server (Holm et al., 2008).

Homology modeling

Homology models of ADCK4 and Coq8p were created using the SWISS-MODEL server (Bordoli et al., 2009). The ADCK3 structure was used as a template. The models were assessed with the ProQ2 server (Ray et al., 2012) and the PDBSum server (de Beer et al., 2014), which includes a PROCHECK analysis.

Expression and purification of ADCK3$^{N\Delta250}$ for DSF experiments and activity assays

8His-MBP-[TEV]-ADCK3$^{N\Delta250}$ was overexpressed in *E. coli* by autoinduction (Fox and Blommel, 2009). Cells were isolated and frozen at –80 °C until further use. For protein purification, cells were thawed, resuspended in Lysis Buffer (50 mM KH_2PO_4, 20 mM Tris-HCl (pH 7.2), 300 mM NaCl, 10% glycerol, 5 mM BME, 0.25 mM PMSF, 1 mg/mL lysozyme, peptide protease inhibitors (500 ng/mL leupeptin hemisulfate, pepstatin A, chymostatin, aprotinin, and antipain dihydrochloride (Sigma)), pH 7.2) and incubated (1 h, 4 °C). The cells were lysed by sonication (4 °C, 6 V, 60 s x 5). The lysate was clarified by centrifugation (15,000 *g*, 30 min, 4 °C). The cleared lysate was mixed with cobalt IMAC resin (Talon resin) and incubated (4 °C, 1 h). The resin was pelleted by centrifugation (700 *g*, 5 min, 4 °C) and washed twice with wash buffer (50 mM KH_2PO_4, 20 mM Tris-HCl (pH 7.2), 300 mM NaCl, 10% glycerol, 5 mM BME, 0.25 mM PMSF, 10 mM imidazole, peptide protease inhibitors, pH 7.2) (10 resin bed volumes). The resin was resuspended in wash buffer (1 bed volume), transferred to a polypropylene chromatography column, and allowed to settle by gravity. The resin was washed again with wash buffer (5 bed volumes). His-tagged protein was eluted with elution buffer (50 mM KH_2PO_4, 20 mM Tris-HCl (pH 7.2), 300 mM NaCl, 10% glycerol, 5 mM BME, 0.25 mM PMSF, 100 mM imidazole, pH 7.2). The eluted protein was concentrated with a MW-cutoff spin filter (50 kDa MWCO) and exchanged into storage buffer (50 mM KH_2PO_4, 20 mM Tris-HCl (pH 7.2), 300 mM NaCl, 10% glycerol, 5 mM BME, 0.25 mM PMSF, pH 7.2). The concentration of 8His-MBP-[TEV]-ADCK3$^{N\Delta250}$ was determined by its absorbance at 280 nm (ε = 96,720 $M^{-1}cm^{-1}$) (MW = 89.9 kDa). The fusion protein was incubated with Δ238TEV protease (1:50, TEV/fusion protein, mass/mass) (1 h, 20 °C). The TEV protease reaction mixture was mixed with cobalt IMAC resin (Talon resin), incubated (4 °C, 1 h), transferred to a

polypropylene chromatography column, and allowed to settle by gravity. The unbound ADCK3$^{N\Delta250}$ was allowed to flow through the column and was collected. This flow through was concentrated with a MW-cutoff spin filter (30 kDa MWCO) and exchanged into storage buffer. The concentration of ADCK3$^{N\Delta250}$ was determined by its absorbance at 280 nm (ε = 28,880 $M^{-1}cm^{-1}$) (MW = 45.6 kDa). The protein was aliquoted, frozen in $N_{2(l)}$, and stored at –80 °C. Fractions from the protein preparation were analyzed by SDS-PAGE.

Differential Scanning Fluorimetry (DSF)

The general DSF method has been described previously (Niesen et al., 2007). Mixtures (20 µL total volume) of ADCK3$^{N\Delta250}$ (1 µM), SYPRO Orange dye (Life Tech.) (5X), NaCl (150 mM), HEPES (100 mM, pH 7.5), and ligands (e.g. MgATP) were prepared in Micro Amp Optical 96 (0.2 mL) Well Reaction Plates (Applied Biosystems). Plates were sealed with Optical Adhesive Covers (Applied Biosystems). The fluorescence of the mixture was measured as the temperature was increased from 15 to 99 °C using an Applied Biosystems ViiA7 Real Time PCR System. The samples were heated initially at a rate of 2 °C/s until the temperature reached 15 °C. The samples were then heated at a rate of 0.017 °C/s until the temperature reached 99 °C. Fluorescence measurements were collected continuously from 15 to 99 °C using excitation filter x1 (470 ± 15 nm) and emission filter m4 (623 ± 14 nm). The fluorescence data was analyzed with Protein Thermal Shift software (Applied Biosystems) to determine T_m values. ΔT_m values were determined by subtracting the T_m of the protein without ligand from the T_m of the protein with ligand ($\Delta T_m = T_{m,\ ligand} - \Delta T_{m,\ no\ ligand}$). Student's t-test was used to determine statistical significance.

To determine ADCK3 ligand-binding selectivity, DSF was used to determine ΔT_m values for ADCK3$^{N\Delta250}$ with a series of potential small molecule ligands (ribose, adenine, adenosine, AMP, ADP, ATP, GDP, GTP, CDP, CTP, UDP, and UTP) ([small molecule] = 1 mM). These ligands were combined with $MgCl_2$ (4 mM), $MnCl_2$ (4 mM), $CaCl_2$ (4 mM), or no cation. In a single experiment, three ΔT_m measurements were made for each condition. These experiments were conducted at least three times for each condition.

To determine apparent K_d values for Mg-ATP and Mg-ADP, DSF experiments were conducted with ADCK3$^{N\Delta250}$ and a range of nucleotide concentrations (0–10 mM ADP or ATP). [$MgCl_2$] was held constant at 20 mM. At least two ΔT_m measurements were made for each [ligand]. The average ΔT_m values (for each [ligand]) were plotted against the [ligand] to give ligand-binding curves, which were fit with a single-site ligand binding saturation curve (SigmaPlot Software) to generate apparent K_d values and maximum ΔT_m values. These experiments were conducted at least three times for each ADCK3$^{N\Delta250}$ variant and nucleotide combination.

Deuterium exchange mass spectrometry (DXMS)

For DXMS experiments, ADCK3$^{N\Delta250}$ was purified essentially as described above (protein preparation for DSF experiments), except that the following "low solute" buffers were used: (i) lysis buffer: 10 mM Tris-HCl (pH 7.2), 150 mM NaCl, 5% glycerol, 1 mM BME, 0.25 mM PMSF, 1 mg/mL lysozyme, peptide protease inhibitors, pH 7.2; (ii) wash buffer: 10 mM Tris-HCl (pH 7.2), 150 mM NaCl, 5% glycerol, 1 mM BME, 0.25 mM PMSF, 10 mM imidazole, peptide protease inhibitors, pH 7.2; (iii) elution buffer: 10 mM Tris-HCl (pH 7.2), 150 mM

NaCl, 5% glycerol, 1 mM BME, 100 mM imidazole, pH 7.2; (iv) storage buffer: 10 mM Tris-HCl (pH 7.2), 150 mM NaCl, 5% glycerol, 1 mM BME, pH 7.2.

Prior to conducting the H/D exchange experiments, quench conditions that produced an optimal pepsin fragmentation pattern were established as previously described (Hsu et al., 2009; Li et al., 2011). Briefly, 3 μL of stock solution of $ADCK3^{N\Delta250}$ (1.1 mg/mL in 10 mM Tris-HCl, pH 7.2, 5% Glycerol, 1 mM DTT and 150 mM NaCl) was diluted with 9 μL of H_2O Buffer, and then mixed with 18 mL of quench solution (0.08, 0.8, 1.6, 3.2 and 6.4 M GuHCl in 0.8% formic acid, 16.6% glycerol) on ice. The ADCK3 samples were then subjected to proteolysis, and the resulting peptides were separated and analyzed by mass spectrometry. The optimal peptide coverage maps of ADCK3 were obtained using 3.2 M GuHCl.

For deuterium exchange experiments, a stock solution of 50 μM $ADCK3^{N\Delta250}$ was prepared in a buffer containing 8.3 mM Tris, pH 7.2, 150 mM NaCl in H_2O. Apo-ADCK3, ADCK3-ATPγS and ADCK3-ADP were prepared at same protein concentration at final salt concentration of 2.5 mM $MnCl_2$, with or without 2 mM ATPγS or ADP, and incubated at room temperature for 20 min then cooled to 0 °C. The HDX experiments were initiated by diluting 2 μL of stock solution (ADCK3, ADCK3-Mn, ADCK3-Mn-ATPγS or ADCK3-Mn-ADP) with 10 μL of D_2O buffer (8.3 mM Tris, 150 mM NaCl, in D_2O, pD_{READ} 7.2) at 0 °C. At 10, 100, 1000, 10000, and 100000 s, the exchange reactions were quenched by adding 18 μL of optimized quench (3.2 M GuHCl, 0.8% formic acid, 16.6% glycerol) at 0 °C and then samples were frozen at –80 °C. In addition, nondeuterated control samples (incubated in H_2O buffer mentioned above) and equilibrium-deuterated back exchange control samples (incubated in D_2O buffer containing 0.5% formic acid overnight at 25 °C) were prepared.

The frozen samples were later thawed at 4 °C and passed over an online pepsin column (16 μL bed volume (Sigma)) at a flow rate of 20 μL/min. The resulting peptides were collected on a C18 trap (Michrom MAGIC C18AQ 0.2x2) and separated using a C18 reversed phase column (Michrom MAGIC C18AQ 0.2x50). A linear gradient of 8–48% B over 30 min (A: 0.05% TFA in H_2O; B: 80% acetonitrile, 0.01% TFA, and 20 % (H_2O) was performed at a flow rate of 2 μL/min with column effluent directed into an Orbitrap Elite mass spectrometer (Thermo Fisher Scientific). The instrument was operated in positive ESI mode with a sheath gas flow of 8 units, a spray voltage of 4.5 kV, a capillary temperature of 200 °C, and a S-lens RF of 67%. MS data was acquired in both profile and data-dependent mode. The resolution of the survey scan was set at 60,000, at m/z 400 with a target value of $1x10^6$ ions and 3 microscans. The maximum injection time for MS/MS was varied between 25 ms and 200 ms. Dynamic exclusion was 30 s and early expiration was disabled. The isolation window for MS/MS fragmentation was set to 2, and the five most abundant ions were selected for product ion analysis. Proteome Discoverer software (Thermo Fisher Scientific) was used to identify the sequence of the peptide ions. The centroids of the isotopic envelopes of nondeuterated, partially deuterated and equilibrium-deuterated peptides were measured using DXMS Explorer (Sierra Analytics Inc., Modesto, CA) and then converted to corresponding deuteration level.

In vitro Kinase Autophosphorylation Assays

Unless otherwise indicated, $ADCK3^{N\Delta250}$ A339G (3 μM) was mixed with [γ-^{32}P]ATP (0.2 μCi/μL, 100 μM $[ATP]_{total}$) and $MgCl_2$ (20 mM) in an aqueous buffer (100 mM HEPES, 150 mM NaCl, pH 7.5) and incubated (37 °C, 100 min, 500 rpm) (final concentrations for reaction components). For the divalent cation screen, $MgCl_2$, $MnCl_2$, or $CaCl_2$ was used at 20 mM.

Reactions were quenched with 4xLDS buffer (106 mM TrisHCl, 141 mM Tris base, 2% LDS, 10% glycerol, 0.51 mM EDTA, 0.175 mM Phenol Red, 0.22 mM Coomassie Brilliant Blue G-250, pH 8.5). [γ-^{32}P]ATP was separated from ADCK3 by SDS-PAGE (10% Bis-Tris gel, MES buffer, 150 V, 1.5 h). The gel was stained with Coomassie Brilliant Blue, dried under vacuum, and imaged by digital photography. A storage phosphor screen was exposed to the gel (~5 days) and then imaged with a Typhoon (GE) to generate the phosphorimages.

Analysis of ADCK3 Autophosphorylation by Phosphoproteomic Mass Spectrometry

ADCK3$^{N\Delta250}$ (WT or A339G) (10 μM) was mixed with ATP (1 mM) and $MgCl_2$ (20 mM) in an aqueous buffer (200 mM HEPES, 300 mM NaCl, pH 7.5) and incubated (37 °C, 2 h, 500 rpm). Control reactions were conducted in parallel without ATP. Reactions were frozen in $N_{2(l)}$ after completion.

Protein was brought up in 1 M urea, 50 mM Tris (pH 8), 50 mM HEPES (pH 7.5), and 75 mM NaCl at a concentration of 100 μg/μL. Protein was reduced with 5 mM dithiothreitol (incubation at 58 °C for 45 min) and alkylated with 15 mM iodoacetamide (incubation in the dark, at ambient temperature, for 45 min). Alkylation was quenched by adding an additional 5 mM dithiothreitol at ambient temperature and incubated for 15 min. Protein was enzymatically digested with sequencing-grade trypsin (Promega, Madison, WI) at a ratio of 1:28 (enzyme:protein) and the resulting mixtures were incubated at ambient temperature overnight. An additional aliquot of trypsin was added to each sample the next morning (1:56 enzyme:protein ratio) and the resulting mixtures were incubated at room temperature for one hour. Digests were quenched by bringing the pH ~2 with trifluoroacetic acid and immediately desalted using C18 solid-phase extraction columns (SepPak, Waters, Milford, MA). For

phosphosite localization of the N-terminal ADCK3$^{N\Delta250}$ A339G phosphopeptide, 20 µg of peptides from the ADCK3$^{N\Delta250}$ A339G plus MgATP sample were labeled with TMT-0, as described previously (Guarani et al., 2014). All protein samples were analyzed by nano reverse-phase liquid chromatography coupled to an Orbitrap Fusion (Thermo). Non-labeled samples were analyzed using discovery-based data-independent acquisition. To achieve peptide localization of the N-terminal ADCK3$^{N\Delta250}$ A339G peptide, we performed a targeted analysis on *m/z* 806.37 (sSPFLSEANAER^{2+}), alternating between higher-energy collisional dissociation (HCD) and collisional-activated dissociation (CAD). Data was processed using the in-house software suite COMPASS (Wenger et al., 2011). OMSSA (Geer et al., 2004) (version 2.1.8) searches were performed against a target-decoy database (*Uniprot (Escherichia coli),* www.uniprot.org, 16 July 2014, containing the appropriate ADCK3 WT/mutant protein sequence). Searches were conducted using a 150 ppm precursor mass tolerance and a 0.015 Da product mass tolerance. A maximum of 3 missed tryptic cleavages were allowed. The fixed modification specified was carbamidomethylation of cysteine residues, and the variable modifications specified were oxidation of methionine and phosphorylation of threonine, serine, and tyrosine residues. Results were filtered to 1% FDR at the unique peptide level using the COMPASS software suite.

Calculation of predicted tunnels

The program CAVER Analyst (Chovancova et al., 2012) was used to examine tunnels that could allow small molecules to travel to the active site from outside the protein. Water molecules near the predicted location of the gamma phosphate of ATP were used as the starting point for computation of tunnels to the surface of the protein.

Normal mode analysis (NMA)

Conformational changes of the ADCK3 structure were analyzed by normal mode analysis through the *ElNémo* webserver (Suhre and Sanejouand, 2004). Numerous normal modes were investigated, and the mode with the most obvious movement of the KxGQ domain (mode 10) was selected for display. Changes in angles between KxGQ domain helices were measured in PyMOL generated images.

Cloning of Coq8p constructs and mutants

The *Saccharomyces cerevisiae* gene *coq8* was amplified by Accuprime Pfu polymerase (Invitrogen, USA) with primers generating an MluI site (forward) and KpnI (reverse). Both the *coq8* amplicon and the yeast expression vector p426 GPD (Mumberg et al., 1995) were digested with MluI and KpnI and subsequently ligated and transformed into DH5α *E. coli*. Plasmid minipreps were performed and recombinants were confirmed by sequencing. *Coq8* mutants were generated via standard site-directed mutagenesis (50 ng template, 0.2 mM dNTPs, 0.2 μM each primer, 3% (v/v) DMSO, 0.625 U Pfu Ultra AD). After an initial 2 minute denaturation at 95 °C, cycled 26 times: 95 °C for 15 s, 60 °C for 30 s, and 68 °C for 7 minutes. Reactions were incubated with DpnI (10 U) to destroy template DNA. Plasmids were transformed into DH5α *E. coli*. Plasmid minipreps were performed and mutations were confirmed by sequencing.

Yeast growth assays

Saccharomyces cerevisiae (W303 background strain) yeast were transformed as previously described (Gietz and Woods, 2002). *Coq8Δ* yeast transformed with p426 GPD plasmids

encoding for Coq8p variants were grown on uracil drop-out (Ura^-) synthetic media plates containing glucose (2%, w/v). Individual colonies of yeast were used to inoculate Ura^- media (20 g/L glucose) starter cultures (3 mL), which were incubated (30 °C, ~12 h, 230 rpm).

To assay yeast growth on agar plates, serial dilutions of yeast from a starter culture were prepared in Ura^- media lacking glucose. 10^4, 10^3, 10^2, or 10 yeast cells were dropped onto Ura^- agar media plates containing either glucose (2%, w/v) or glycerol (3%, v/v) and incubated (30 °C, 2 d).

To assay yeast growth in liquid media, yeast from a starter culture were swapped into Ura^- media with glucose (0.1%, w/v) and glycerol (3%, v/v) at an initial density of $5x10^6$ cells/mL. The cultures were incubated in a sterile 96 well plate with an optical, breathable cover seal (shaking at 1140 rpm). Optical density readings were obtained every 30 min.

Yeast coenzyme Q (CoQ_6) quantitation by LC-MS

$2.5x10^6$ yeast cells (as determined by OD_{600} of a starter culture) were used to inoculate a 25 mL culture of Ura^- media (10 g/L glucose), which was incubated (30 °C, 230 rpm) for 23 h. At 23 h, the yeast cultures were ~4 h past the diauxic shift and the media was depleted of glucose. The OD_{600} of the culture was measured and used to determine the volume of culture needed to isolate $1x10^8$ yeast cells. $1x10^8$ yeast cells were pelleted by centrifugation (3,000 *g*, 3 min, 4 °C), the supernatant was discarded, and the yeast pellet was frozen at –20 °C.

A frozen pellet of yeast (10^8 yeast cells) was thawed on ice and mixed with phosphate-buffered saline (200 μL) and glass beads (0.5 mm diameter, 100 μL). The yeast were lysed by vortexing with the glass beads (30 s). Coenzyme Q_{10} (CoQ_{10}) was added as an internal standard (10 μM, 10 μL), and the lysate was vortexed (30 s). Hexanes/2-propanol (10:1, v/v) (500 μL)

was added and vortexed (2 x 30 s). The samples were centrifuged (3,000 *g*, 1 min, 4 °C) to complete phase separation. 400 µL of the organic phase was transferred to a clean tube and dried under $N_{2(g)}$. The organic residue was reconstituted in ACN/IPA/H_2O (65:30:5, v/v/v) (100 µL) by vortexing (30 s) and transferred to a glass vial for LC-MS analysis.

LC-MS analysis was performed on an Ascentis Express C18 column (150 mm x 2.1 mm x 2.7 µm particle size, Supelco, Bellefonte, PA) using an Accela LC Pump (500 µL/min flow rate, Thermo Scientific, San Jose, CA). Mobile phase A consisted of 10 mM ammonium acetate in ACN/H_2O (70:30, v/v) containing 250 µL/L acetic acid. Mobile phase B consisted of 10 mM ammonium acetate in IPA/ACN (90:10, v/v) with the same additives. Initially, mobile phase B was held at 50% for 2 min and then increased to 95% over 3 min where it was held for 5 min. The column was re-equilibrated for 4 min before the next injection. Ten µL of sample were injected by an HTC PAL autosampler (Thermo Scientific, San Jose, CA). The LC system was coupled to a Q Exactive mass spectrometer (Build 2.3 SP2) by a HESI II heated ESI source kept at 350 °C (Thermo Scientific, San Jose, CA). The inlet capillary was kept at 350 °C, sheath gas was set to 60 units, and auxiliary gas to 15 units. The MS was operated in negative mode (2.5 kV) from 3 to 4.85 min with a mass range of 500–600 Th and an AGC target of $2x10^5$ and in positive mode (3 kV) from 4.7 to 7.5 min with a mass range spanning 550 to 900 Th and an AGC target of $1x10^6$. Resolving power was always set at 17,500. Quantitation was performed by integrating the peak areas of the $[M+H]^+$ ion of CoQ_6 at 591.44 Th and the $[M-H]^-$ ion of HAB at 544.42 Th using the Xcalibur software suite (2.2 SP1.48, Thermo Scientific, San Jose, CA) and normalizing peak areas to the CoQ_{10} internal standard. Student's t-test was used to determine statistical significance.

Accession Numbers

The coordinates and structure factors have been deposited in the Protein Data Bank with accession code 4PED.

Acknowledgments

We thank the following members of the UW-Madison-based Mitochondrial Protein Partnership for technical and managerial assistance: Emily Beebe, Tina Misenheimer, Nichole Reinen, Ronnie Frederick, Katarzyna Gromek, Don Drott, David Aceti, John Primm, Brian Fox, and John Markley. We thank Brendan Dolan for microscopy work, Michael Westphall for mass spectrometry support, G.N. Phillips, Jr. for guidance and support in all crystallographic endeavors, Bob Smith and Samir Joshi for crystallomics assistance, and Craig Ogata, Ruslan Sanishvili, Joe Brunzelle and Elena Kondrashkina for beamline support. This work was supported by a Searle Scholars Award, a Shaw Scientist Award and by NIH grants U01GM94622, R01DK098672 and R01GM112057 (to D.J.P.), NIH Ruth L. Kirschstein National Research Service Award F30AG043282 (to J.A.S.), and NIH Chemistry-Biology Interface Training Grant T32GM008505 (to A.G.R.). Use of the Advanced Photon Source was supported by the U.S. DOE (DE-AC02-06CH11357). LS-CAT was supported by the Michigan Economic Development Corporation (085P1000817). GM/CA @ APS has received funds from the NIH NCI (Y1-CO-1020) and NIGMS (Y1-GM-1104).

Figures and Table

Figure 1.

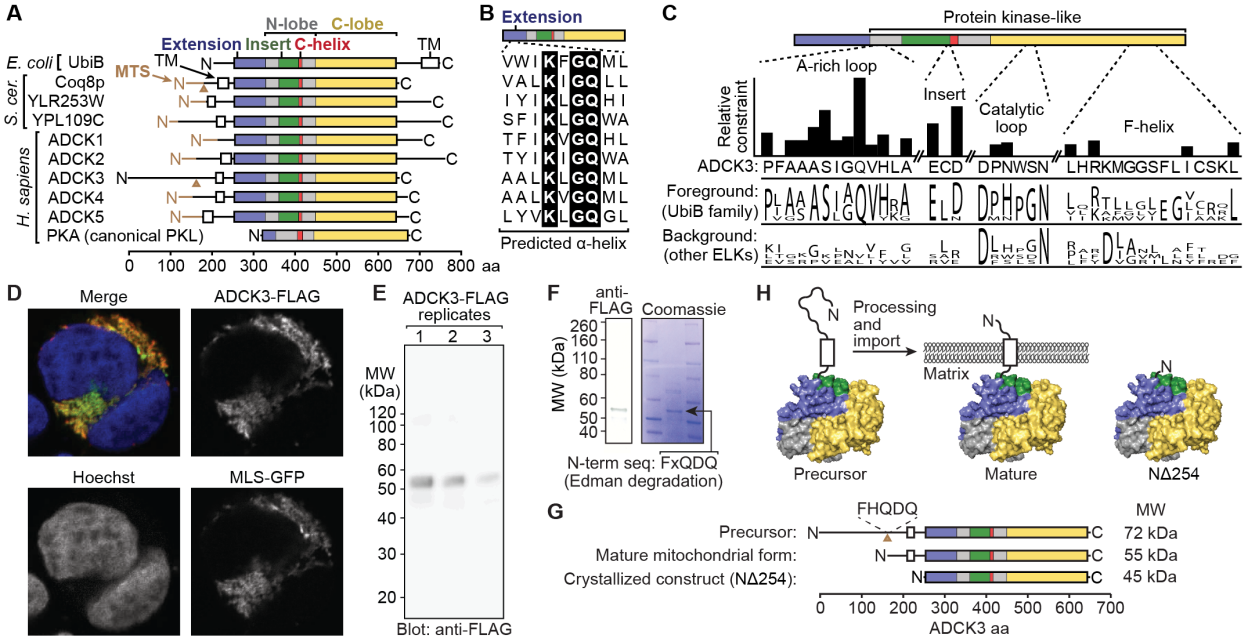

Figure 1. Unique sequence features of the UbiB family and ADCK3

(**A**) Domain structures of UbiB family proteins (human, yeast, and *E. coli*) and PKA (human). Brown triangles represent observed N-termini of mature Coq8p and mature ADCK3 (see D–G).

(**B**) Alignment of a predicted α-helix in the N-terminal extension of UbiB family proteins as listed in (A).

(**C**) Signature motifs identified by a statistical analysis of the UbiB family (foreground) compared to other ePK-like kinase (ELK) sequences (background) with associated sequence logos. Histogram bar height (on an approximately logarithmic scale) represents the selective constraint imposed on unique foreground residue (a measure of "uniqueness"). See also Figure S1A.

(**D**) Confocal microscopy of HEK293 cells transfected with ADCK3-FLAG and MLS-GFP (mitochondrial marker). Nuclear DNA is visualized by Hoechst stain.

(**E**) Anti-FLAG immunoblot of ADCK3-FLAG immunopreciptated from HEK293 cells (3 biological replicates).

(**F**) N-terminal sequence (FxQDQ) of a Coomassie-stained band of mature, IP'd ADCK3-FLAG at ~55 kDa as determined by Edman degradation ('x' indicates an unclear residue), and a parallel lane analyzed by anti-FLAG immunoblot.

(**G**) Domain structures of precursor, mature, and crystallized ADCK3. The location of the observed mitochondrial ADCK3-FLAG N-terminus (FHQDQ) in the full-length protein is indicated, along with the predicted molecular weights of all three proteins. See also Figure S2.

(**H**) Cartoon models of precursor, mature and crystallized ADCK3. The NΔ254 model is based on our crystal structure (see Figure 2).

Figure 2.

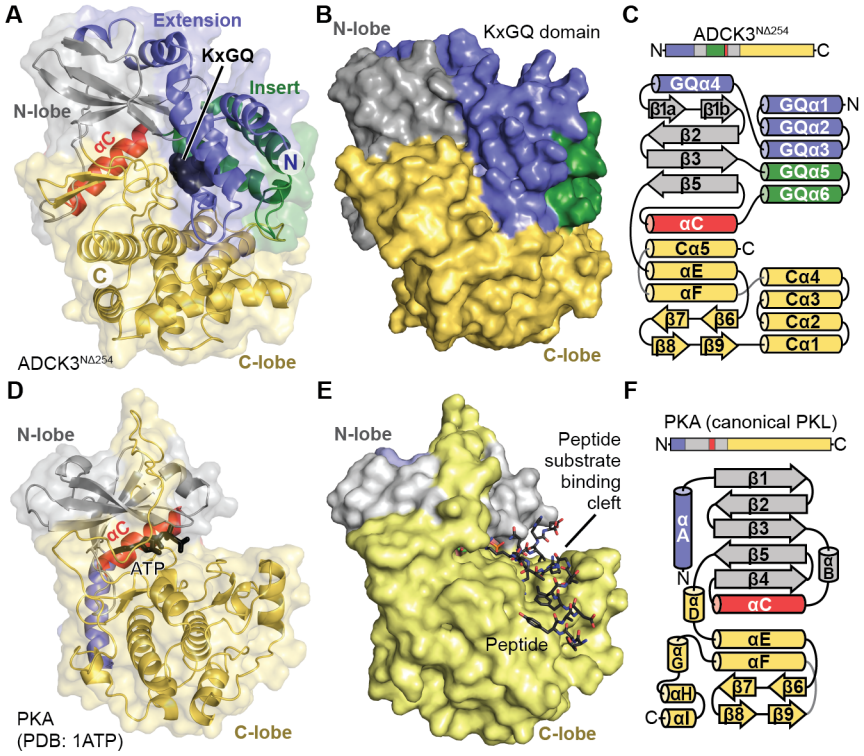

Figure 2. X-ray crystal structure of ADCK3$^{N\Delta254}$

(**A**) Overall structure of ADCK3$^{N\Delta254}$ with domains colored as in Figure 1A and the KxGQ motif residues represented with black spheres.

(**B**) Surface representation of ADCK3$^{N\Delta254}$ with domains colored as in (A).

(**C**) Topology map of ADCK3$^{N\Delta254}$ colored as in (A).

(**D**) Overall structure of PKA (PDB: 1ATP) (Zheng et al., 1993) with domains colored as in Figure 1A and bound ATP represented with black sticks.

(**E**) Surface representation of PKA with a peptide substrate analog represented as sticks and domains colored as in (D).

(**F**) Topology map of PKA colored as in (D).

See also Figure S2.

Table 1. Hs.ADCK3$^{N\Delta254}$ Data collection and refinement statistics

	ADCK3$^{N\Delta254}$
Data collection	
Space group	C 1 2 1
Cell dimensions	
a, *b*, *c* (Å)	148.671, 54.557, 45.009
α, *β*, *γ* (°)	90, 94, 90
Resolution (Å)	39.63–1.639 (1.697–1.639)*
R_{sym} or R_{merge}	0.0954 (0.862)
$I/\sigma I$	22.9 (1.9)
Completeness (%)	93.2 (79.5)
Redundancy	7.6 (5.6)
Refinement	
Resolution (Å)	39.63–1.639
No. reflections	324414 (24751)
$R_{work/}$ R_{free}	0.1649/0.2110
No. atoms	
Protein	3213
Ligand/ion	10
Water	267
B-factors	
Protein	19.3
Ligand/ion	26.9
Water	25.4
R.m.s. deviations	
Bond lengths (Å)	0.012
Bond angles (°)	1.43

*Highest resolution shell is shown in parenthesis.

Figure 3.

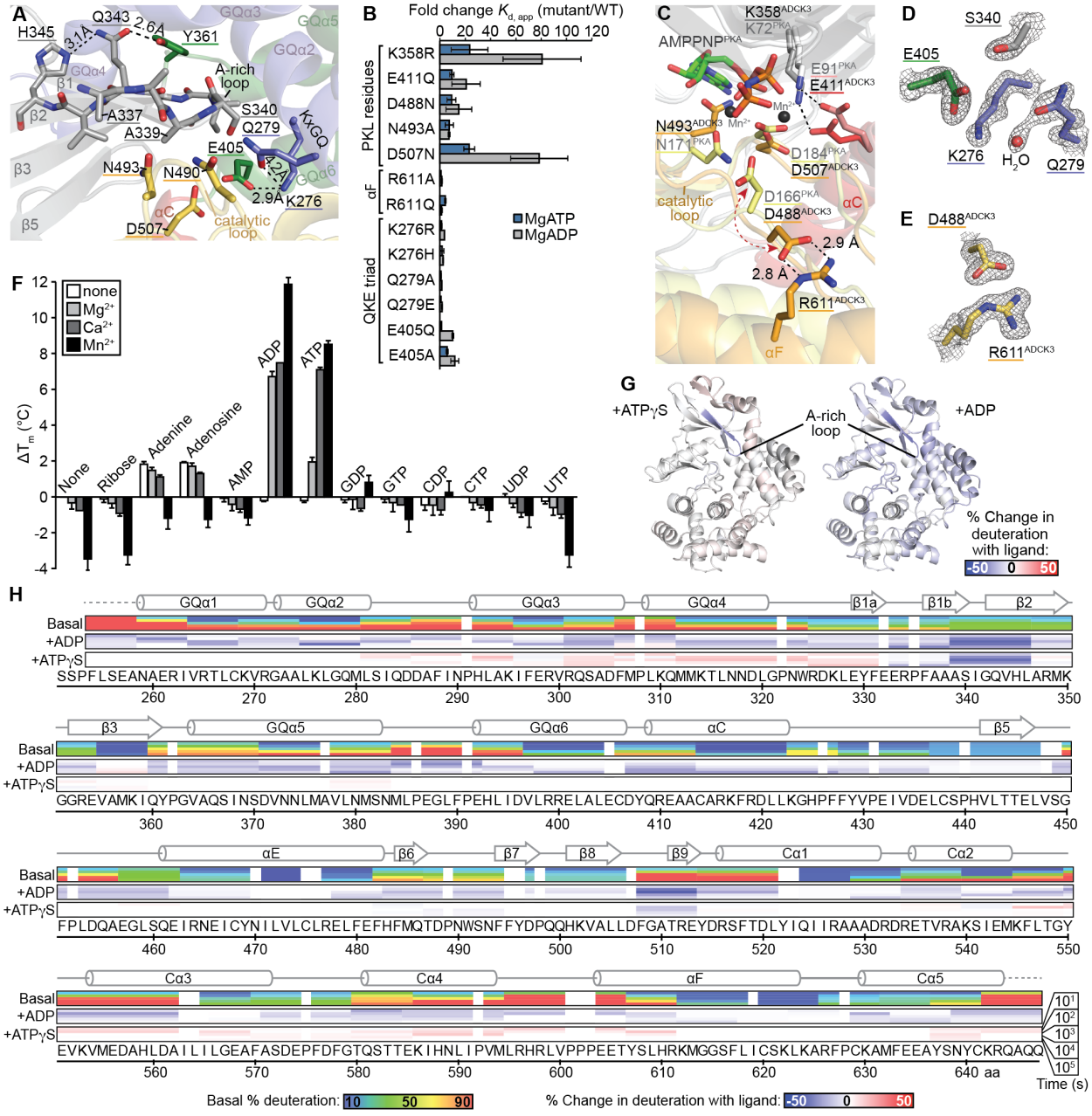

Figure 3. ADCK3 adopts an atypical PKL active site that binds nucleotides

(**A**) Structure of the A-rich loop and the QKE triad of ADCK3$^{N\Delta254}$ colored as in Figure 2.

(**B**) Fold changes in apparent $K_d^{Mg\text{-}ATP}$ and $K_d^{Mg\text{-}ADP}$ for ADCK3$^{N\Delta250}$ mutants compared to wild type as assessed by differential scanning fluorimetry (DSF) (mean ± s.d., n = 3).

(**C**) Superposition of the nucleotide binding pockets of ADCK3$^{N\Delta254}$ (darker colors and black text) and PKA (PDB: 2QCS) (Kim et al., 2007) (lighter colors and gray text) colored as in Figure 2. The nucleotide (AMPPNP) (green) and cations (black spheres) are from the PKA structure. Red arrows highlight the unusual conformation of D488^{ADCK3}.

(**D**) Simulated annealing composite omit maps ($2mF_o–DF_c$) contoured at 1.4σ (gray mesh) of the QKE triad and the serine of the AAAS motif.

(**E**) Simulated annealing composite omit map ($2mF_o–DF_c$) of D488 and R611 contoured at 1.8σ (gray mesh).

(**F**) ΔT_m of ADCK3$^{N\Delta250}$ due to addition of various ligands and cations (mean ± s.d., n = 3 independent ΔT_m determinations).

(**G**) Average differences (over 5 time points) in deuterium exchange of ADCK3$^{N\Delta250}$ due to the presence of ATPγS or ADP mapped onto the structure of ADCK3$^{N\Delta254}$.

(**H**) Ribbon maps of ADCK3 showing deuterium exchange levels in three separate conditions (Basal, Mn^{2+} only; +ADP, MnADP; +ATPγS, MnATPγS) at five separate time points. Conditions with MnADP and MnATPγS are shown as changes in deuteration compared to the basal levels for each time point. Incubation times with D_2O are shown at the bottom right.

See also Figure S3.

Figure 4.

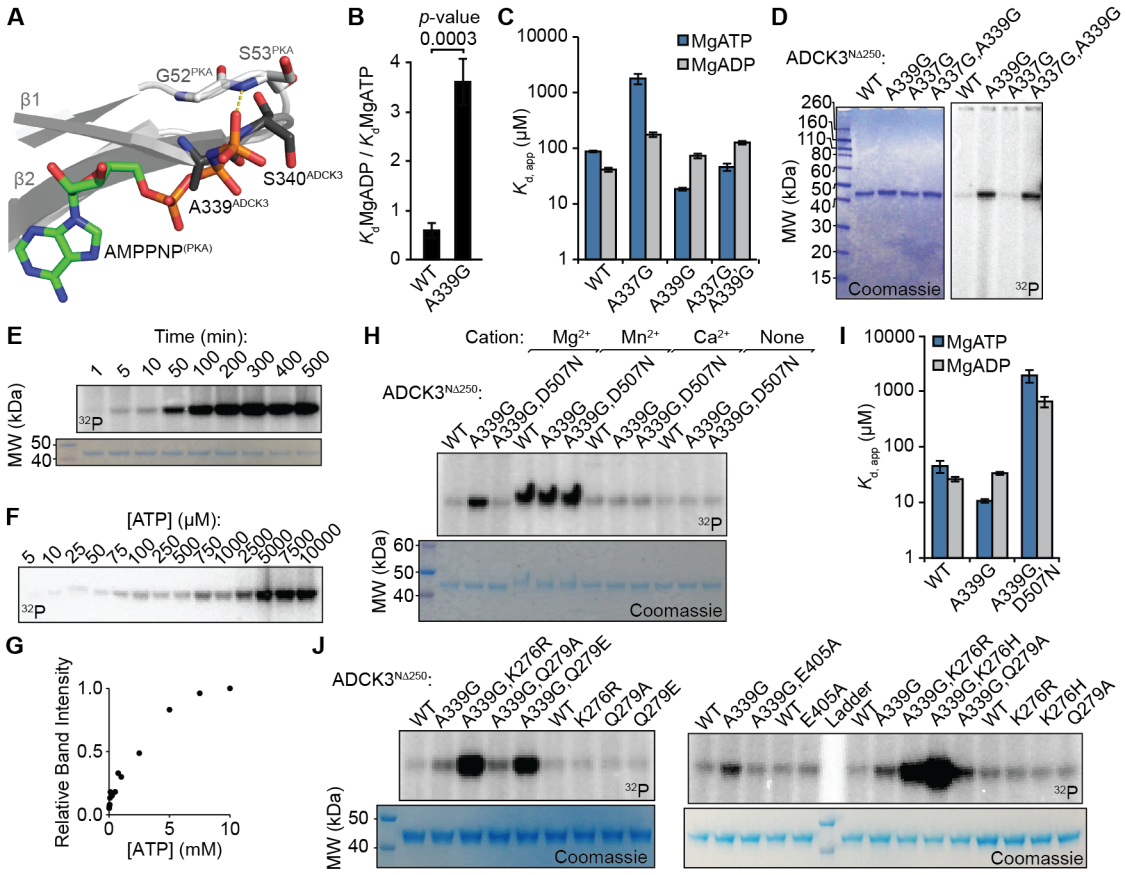

Figure 4. A single A-to-G mutation of the A-rich loop flips nucleotide selectivity and enables ADCK3 autophosphorylation

(**A**) Comparison of the G-rich loop of PKA (PDB: 2QCS) and the A-rich loop of ADCK3$^{N\Delta254}$ (dark gray). AMPPNP (green) is from the PKA structure. The overall structural superposition is the same as in Figure 3C.

(**B**) Nucleotide selectivity of ADCK3$^{N\Delta250}$ A339G compared to wild type (WT). Apparent K_d values were assessed by DSF (mean ± s.d., n = 3; 3 independent K_d measurements were made for each of 3 different protein preparations of WT and A339G).

(**C and I**) $K_d^{Mg\text{-}ATP}$ and $K_d^{Mg\text{-}ADP}$ for ADCK3$^{N\Delta250}$ variants as assessed by DSF (mean ± s.d., n = 3 independent K_d determinations).

(**D, E, F, H, J**) SDS-PAGE analysis of *in vitro* [γ-^{32}P]ATP autophosphorylation reactions with ADCK3$^{N\Delta250}$ variants. MgATP was used for all reactions except those noted in (H).

(**E**) Time course of ADCK3$^{N\Delta250}$ A339G autophosphorylation.

(**F**) Dependence of ADCK3$^{N\Delta250}$ A339G autophosphorylation on ATP concentration.

(**G**) Relative quantification of radioactivity from ^{32}P-ADCK3$^{N\Delta250}$ A339G bands in (F).

See also Figure S4.

Figure 5.

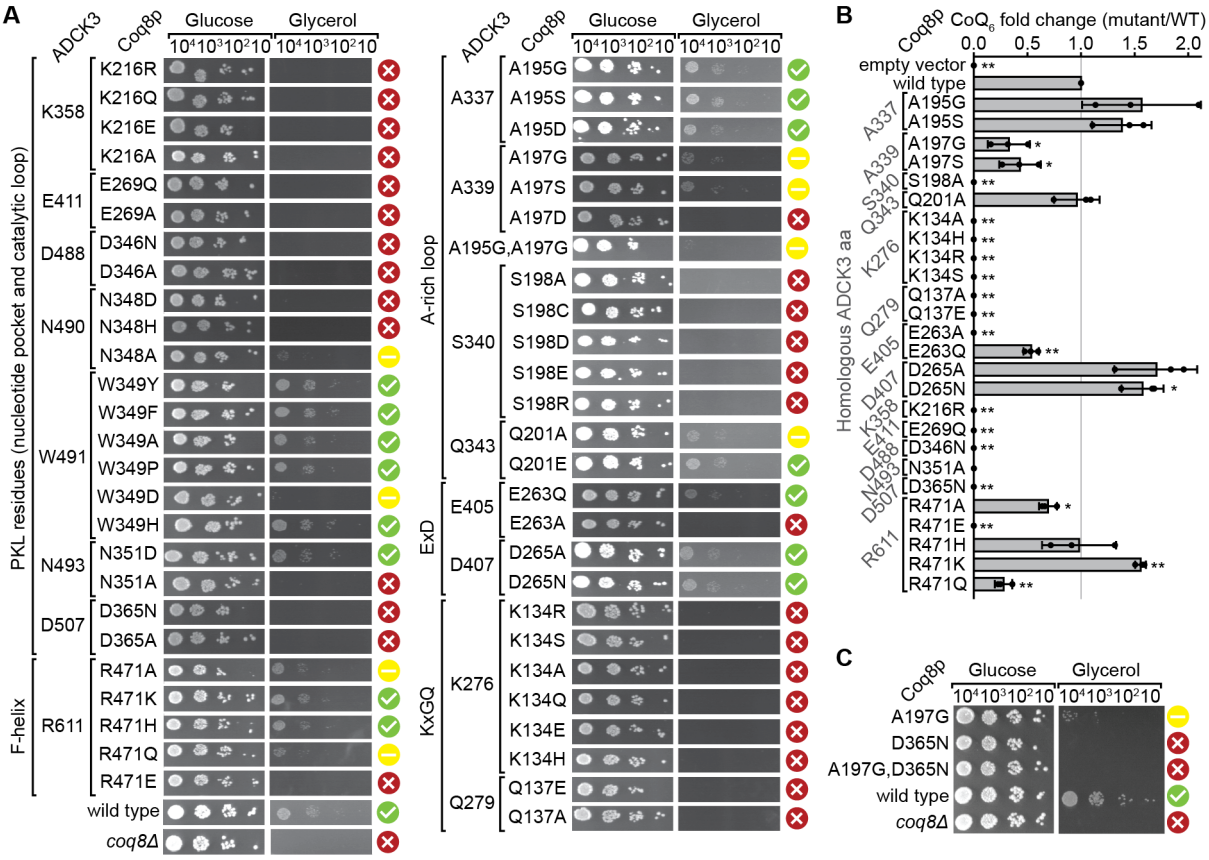

Figure 5. UbiB-specific features of Coq8p are required for yeast growth and CoQ biosynthesis

(**A and C**) Serial dilutions of yeast transformed with the indicated Coq8p variants grown on agar plates with glucose or glycerol. Homologous ADCK3 residues are indicated to the left of the Coq8p residues. Red 'X' symbols indicate no growth on glycerol, yellow dash symbols indicate moderate or low growth on glycerol, and green check mark symbols indicate wild type-like growth on glycerol.

(**B**) Fold changes in CoQ_6 abundance of yeast with Coq8p point mutations compared to wild type Coq8p as determined by LC-MS (mean with 95% c.i., n = 3 biological replicates).

See also Figure S5.

Figure 6.

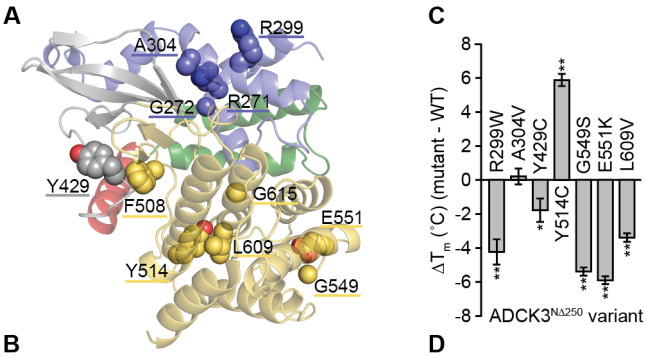

Mutation	Predicted effects on ADCK3 structure
R271C	Loss of interactions with V300 and Y361
G272V	Steric clash with I341 and S340
G272D	Steric clash with I341 and S340
R299W	Loss of interactions with S303 and E261
A304V	Steric clash with P335 and A338
A304T	Steric clash with P335 and A338
Y429C	Loss of interactions with E446 & R419
F508S	Altered DFG motif conformation
Y514C	Loss of H-bond with E605 backbone
G549S	Steric clash with I542
E551K	Loss of H-bond with T548 backbone
L609V	Altered F-helix conformation
G615D	Altered F-helix conformation

Figure 6. Pathogenic ADCK3 mutations disrupt protein stability

(**A**) Residues mutated in patients with cerebellar ataxia mapped onto the ADCK3$^{N\Delta254}$ structure as spheres. Domains are colored as in Figure 2.

(**B**) Predicted structural effects of pathogenic ADCK3 mutations.

(**C**) Fold changes in ΔT_m of ADCK3$^{N\Delta250}$ mutants compared to wild type as assessed by DSF (mean ± s.d., n = 3 independent ΔT_m determinations).

(**D**) Fold changes in apparent $K_d^{Mg\text{-}ADP}$ for ADCK3$^{N\Delta250}$ mutants compared to wild type as assessed by DSF (mean ± s.d., n = 3 independent $K_{d,\,app}$ determinations). *p-value < 0.05, **p-value < 0.01.

Figure S1, related to Figure 1

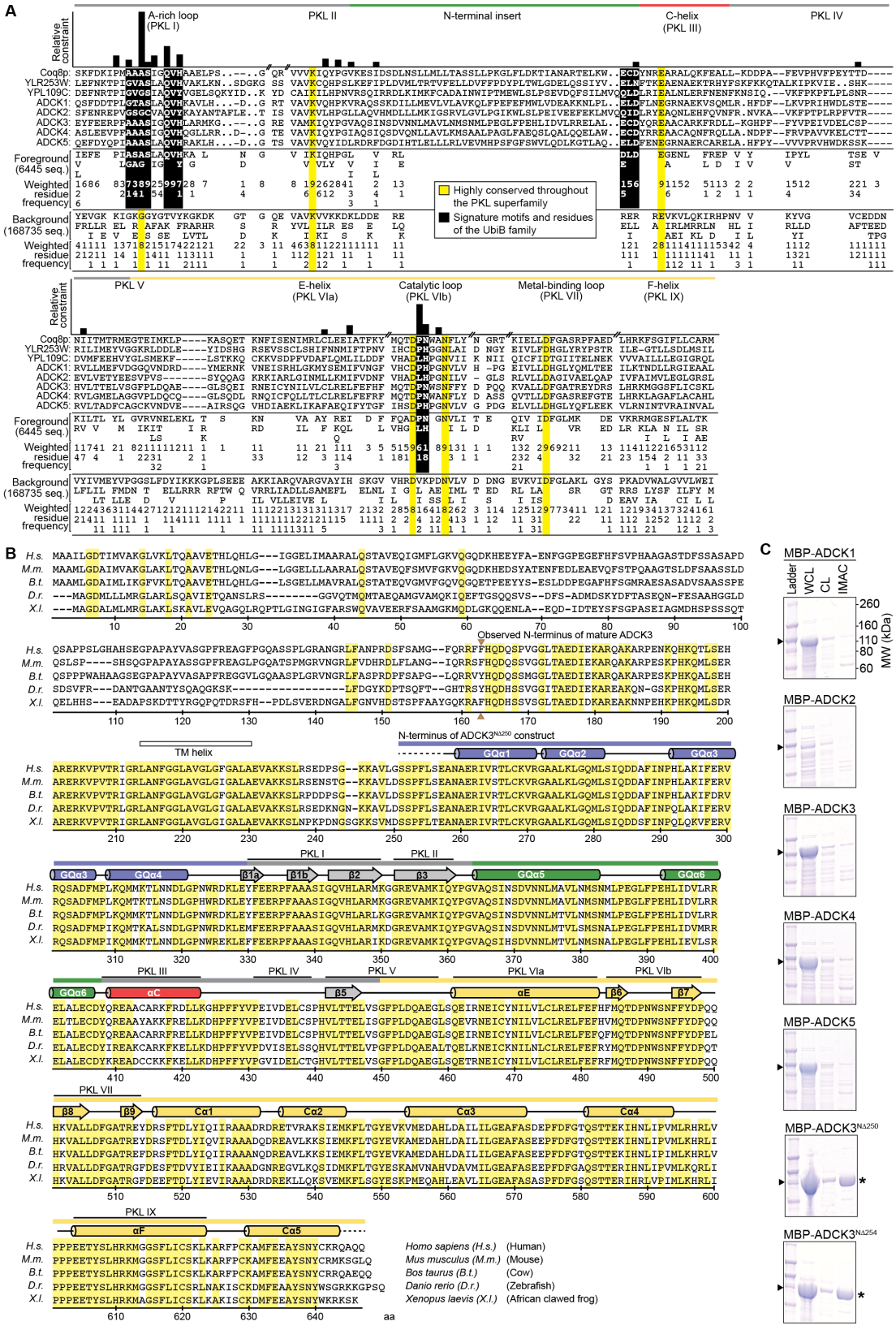

Figure S1, related to Figure 1. CHAIN analysis of the UbiB family identifies signature motifs

(A) CHAIN analysis of UbiB family proteins (foreground) against a background of all other PKL proteins (over 175,000 sequences total). The histogram bar height (the log-likelihood ratio of the 'uniqueness' of the conserved pattern) represents the selective constraint imposed on unique foreground residues. The number of sequences in each set (foreground and background) is shown in parentheses. Residue frequencies are indicated with integer tenths (e.g., '9' indicates that the above residue occurs in 90–99% of the (weighted) sequences). Weighting adjusts for families that are overrepresented in the alignment. ADCK3 domains are indicated with a bar (colored as in Figure 1) above the histogram.

(B) Amino acid sequence alignment of ADCK3 from five metazoan species. The scale corresponds to the amino acid number for human ADCK3. Yellow highlights indicate invariant residues. Secondary structure as observed in our ADCK3$^{N\Delta254}$ crystal structure is depicted above the sequence, along with annotation of PKL subdomains. A predicted single-pass transmembrane domain is marked by a white bar.

(C) SDS-PAGE analysis of parallel attempts to purify maltose-binding protein (MBP)-tagged human ADCK proteins. Triangles indicate the position of the MBP-ADCK construct, and asterisks highlight purified proteins. WCL, whole cell lysate; CL, cleared lysate; IMAC, concentrated protein after immobilized metal affinity chromatography.

Figure S2, related to Figure 2

A

PDB ID	Z score	RMSD (Å)	Protein
4JIN	11.8	3.1	Rio1 kinase
1ZTF	11.7	3.2	Rio1 kinase
3RE4	11.4	3.6	Rio1 kinase
1ZP9	11.3	3.4	Rio1 kinase
1ZTH	11.2	3.2	Rio1 kinase
1ZP9	11.1	3.4	Rio1 kinase
4GYG	10.9	3.5	Rio2 kinase
4GYI	10.7	3.6	Rio2 kinase
2PHK	10.7	3.4	Phosphorylase kinase
1QL6	10.6	3.5	Phosphorylase kinase
1PHK	10.5	3.4	Phosphorylase kinase
1CSN	10.3	3.3	Casein kinase
4BTM	10.2	3.2	Tau-Tubulin kinase
4BTJ	10.2	3.2	Tau-Tubulin kinase
3RAW	10.1	3.4	CLK3
1Z57	10.1	3.3	CLK1
3NR9	10.1	3.6	CLK2
2CSN	10.1	3.1	Casein kinase
3LM5	10.1	3.3	Ser/Thr Protein Kinase 17B
4FIE	10.1	3.3	PAK 4
3LLT	10.0	3.3	PFLAMMER
3LM0	10.0	3.4	Ser/Thr Protein Kinase 17B
2WU7	10.0	3.5	CLK3
4AZE	9.9	3.5	DSTPR
3SV0	9.9	3.0	Casein kinase-like
1EH4	9.9	3.1	Casein kinase
3E7E	9.9	3.5	Mitotic checkpoint kinase
1CKJ	9.9	3.0	Casein kinase
2VAG	9.9	3.2	CLK1
1CKI	9.9	3.0	Casein kinase
4KS8	9.9	3.3	PAK 6
2Y7J	9.9	3.6	Phosphorylase kinase
2QCS	9.9	3.0	PKA
1JBP	9.9	3.0	PKA
3QAL	9.9	3.0	PKA
⋮ (Numerous additional hits not shown) ⋮			

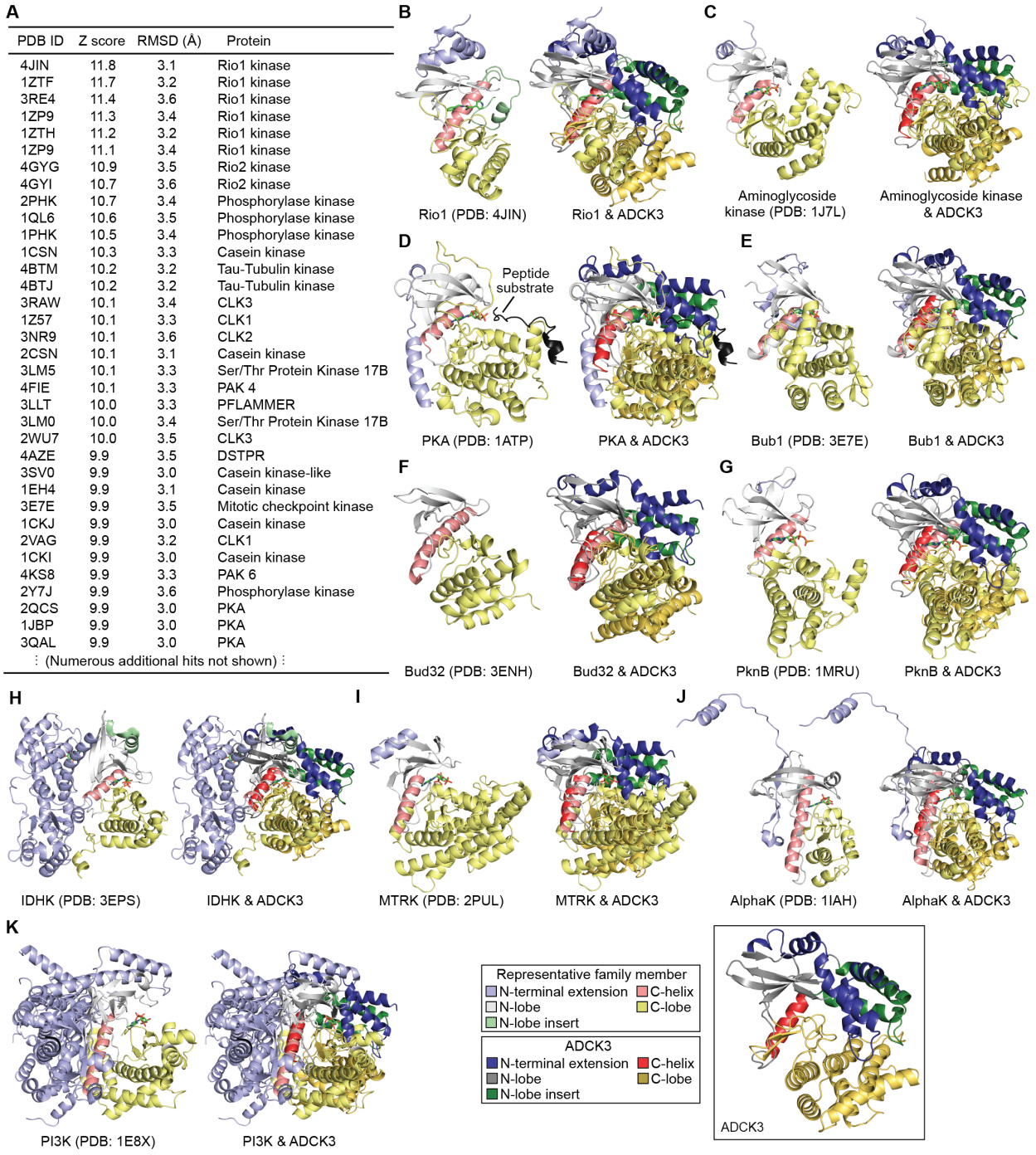

Figure S2, related to Figure 2. ADCK3 adopts an atypical PKL fold

(A) Structures in the PDB with the most three-dimensional similarity to ADCK3. Similar structures were identified with the Dali server and are listed in descending order of structural similarity (as indicated by the Z score). Root-mean-square deviation (RMSD) is also shown.

(B)–(K) Superposition of ADCK3 with representative members of other PKL families: (B) Rio1 (PDB: 4JIN) (Rio family), (C) aminoglycoside kinase (PBD: 1J7L) (CAK family), (D) PKA (PDB: 1ATP) (ePK family), (E) Bub1 (PDB: 3E7E) (Bub1 family), (F) Bud32 (PDB: 3ENH) (Bud32 family), (G) PknB (PDB: 1MRU) (PknB family), (H) AceK (PBD: 3EPS) (IDHK family), (I) MTRK (PDB: 2PUL) (MTRK family), (J) AlphaK (PDB: 1IAH) (AlphaK family), (K) PI3K (PBD: 1E8X) (PI3K family).

Figure S3, related to Figure 3

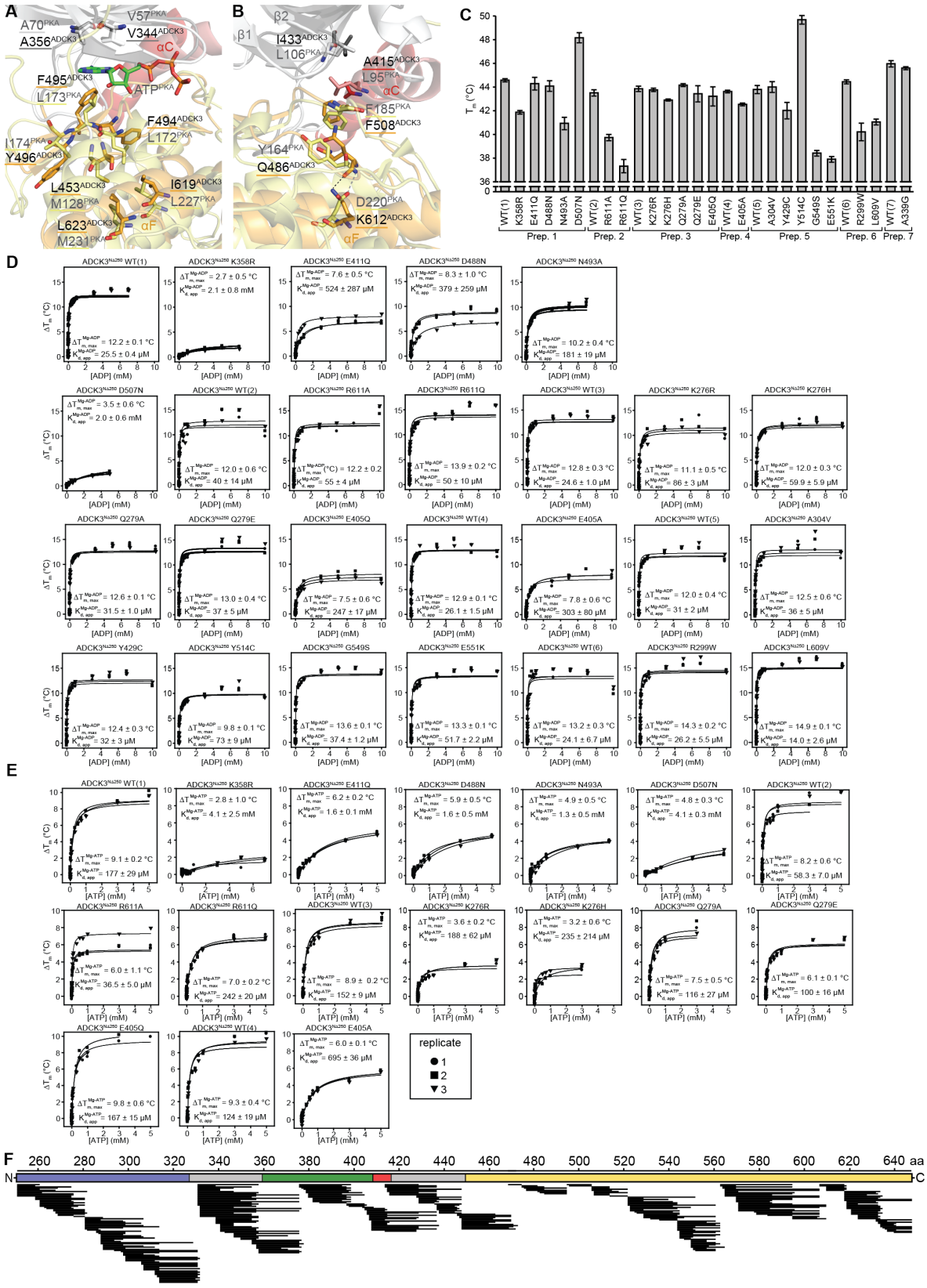

Figure S3, related to Figure 3. Kinase 'spines' and nucleotide binding properties of ADCK3

(A) Superposition of ADCK3$^{N\Delta254}$ (darker colors and black text) and PKA (PDB: 1ATP) (lighter colors and gray text) colored as shown in Figure 2 with C-spine residues represented as stick models. The ATP shown is from the PKA structure.

(B) Superposition of ADCK3$^{N\Delta254}$ and PKA (PDB: 1ATP) with R-spine residues represented as stick models, colored as in Figure 2.

(C) T_m of ADCK3$^{N\Delta250}$ variants (mean ± s.d., n = 3 independent T_m determinations). Protein preparation groups (Prep. 1–7) indicate sets of proteins that were purified in parallel on the same day.

(D) MgADP binding curves for ADCK3$^{N\Delta250}$ variants. Binding curves from three independent experiments are shown.

(E) MgATP binding curves for ADCK3$^{N\Delta250}$ variants. Binding curves from three independent experiments are shown.

(F) Peptide coverage map from the DXMS analysis of ADCK3$^{N\Delta250}$. Black lines represent individually observed peptides.

Figure S4, related to Figure 4

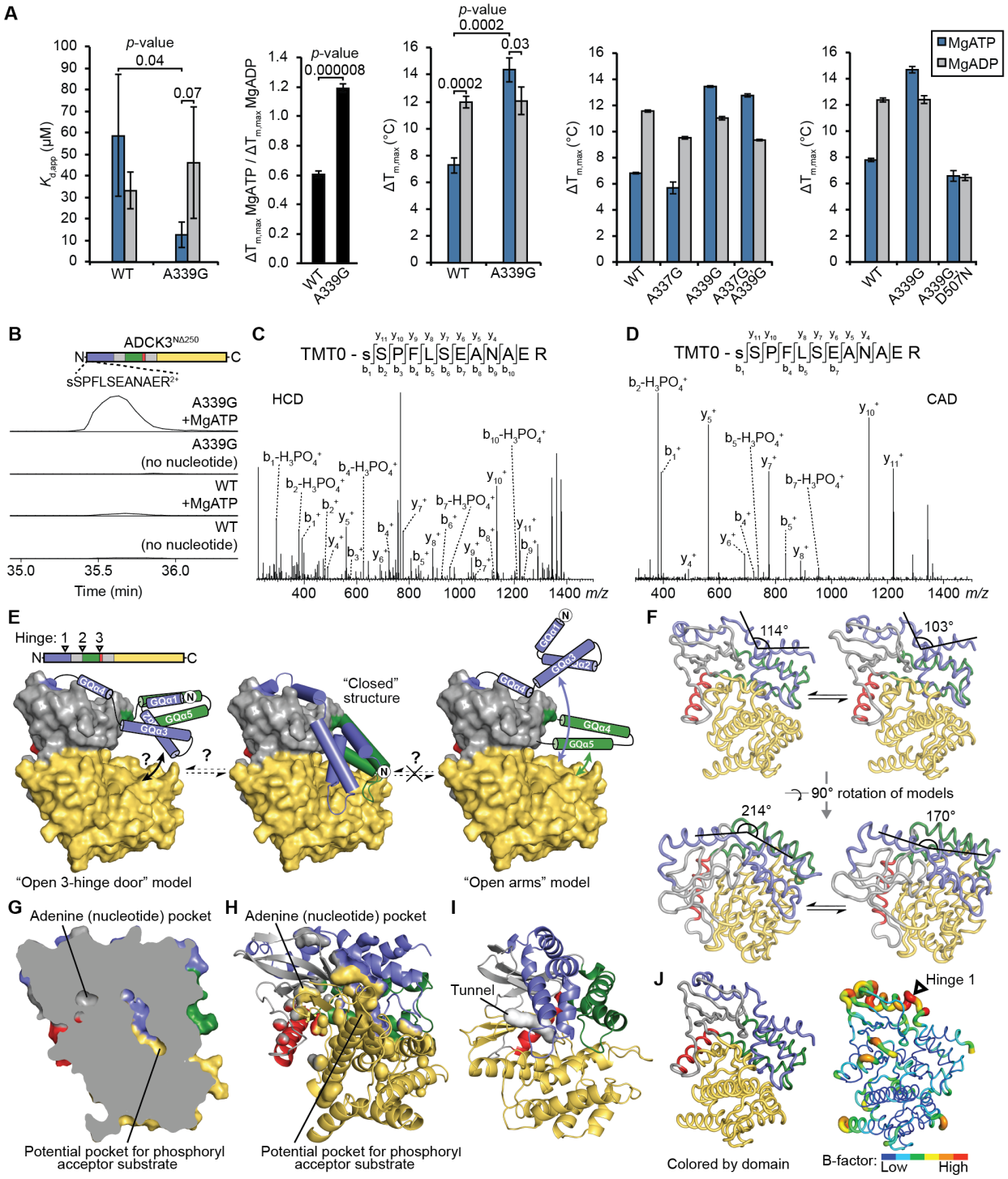

Figure S4, related to Figure 4. Identification of an ADCK3$^{N\Delta250}$ A339G autophosphorylation site and a model for KxGQ domain movement

(A) $K_{d,}^{MgATP}$, K_d^{MgADP}, and $\Delta T_{m,max}$ for ADCK3$^{N\Delta250}$ variants as assessed by DSF (Left three graphs: mean ± s.d., n = 3, 3 independent K_d measurements were made for each of 3 different protein preparations of WT and A339G. Right two graphs: mean ± s.d., n = 3 independent $\Delta T_{m,max}$ determinations).

(B) Extracted ion chromatograms (XICs) reflecting the MS^1 precursor intensities of peptide sSPFLSEANAER^{2+} (*m/z* 694.30) (s, phospho-serine; S, serine) over time in LC-MS/MS analyses of tryptically digested ADCK3$^{N\Delta250}$ (WT or A339G) from *in vitro* autophosphorylation reactions with MgATP or no nucleotide. XICs have been normalized to LC-MS/MS total ion current and are the result of a 5-point boxcar average.

(C) and (D) MS^2 spectra attained by targeted LC-MS/MS analysis of TMT0-labeled peptide sSPFLSEANAER^{2+} (*m/z* 806.37), fragmented using both (C) higher-energy collisional dissociation (HCD) and (D) collisional-activated dissociation (CAD). The spectra presented represent the average of all respective MS^2 spectra collected while the peptide was eluting.

(E) Hypothetical models for KxGQ domain movement away from the active site.

(F) Movement of the KxGQ domain based on normal mode analysis. Angles were measured at the harmonic extremes of a single normal mode.

(G) and (H) Molecular surface representations of cavities in the ADCK3 structure calculated with a 1.4 Å probe radius using PyMOL. Two cavities near the active site are shown in (G), and all cavities are shown in (H).

(I) Surface representation of a tunnel (white) between the active site of ADCK3 (cartoon colored as in Figure 2) and the protein surface, as identified with the program CAVER.

(J) B factor putty model of ADCK3$^{N\Delta254}$ (right) generated in PyMOL with a ribbon map of ADCK3 (left) colored as in Figure 2 for reference.

Figure S5, related to Figure 5

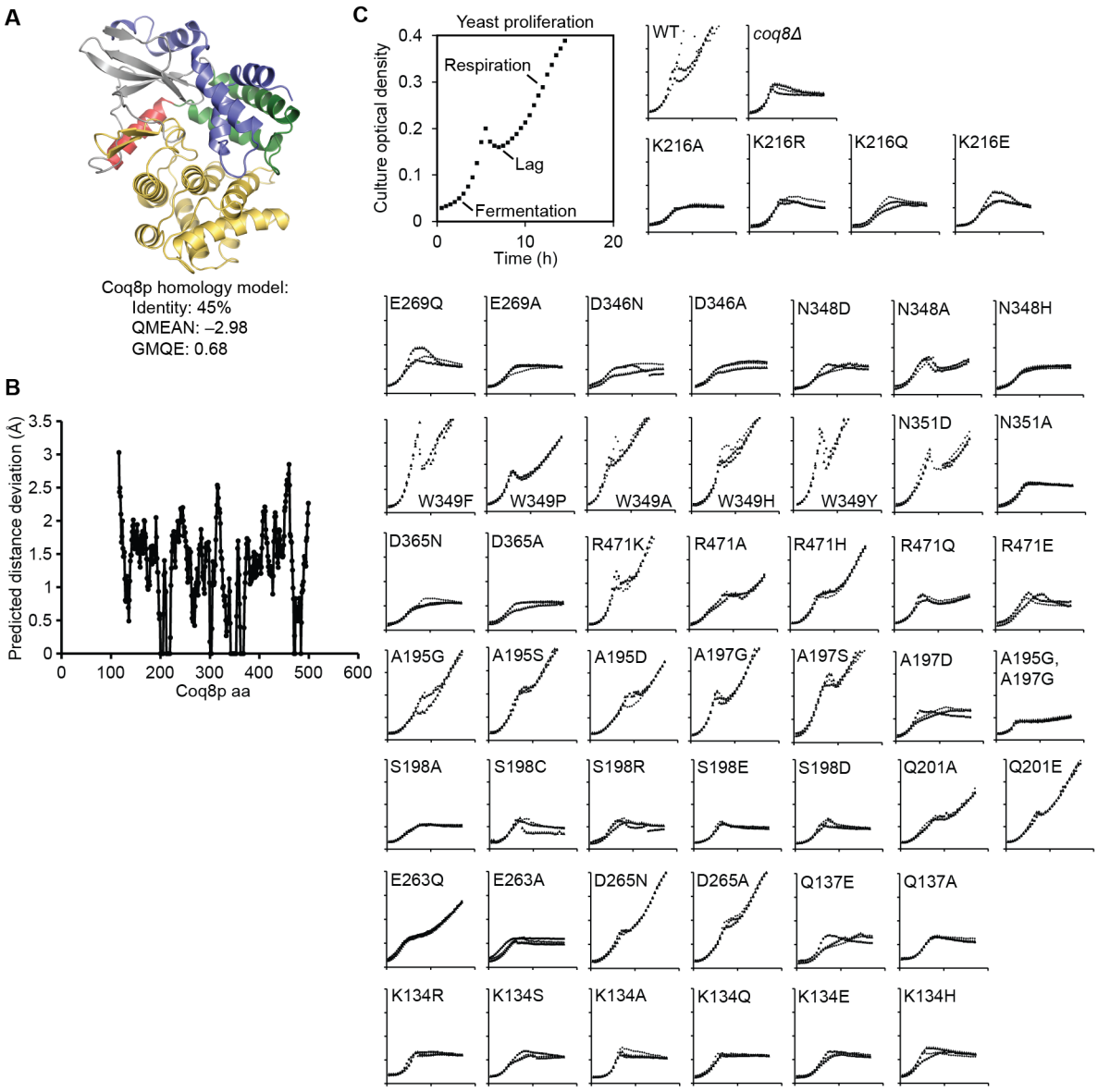

Figure S5, related to Figure 5. Effects of Coq8p mutations on yeast growth kinetics

(A) Homology structure model of Coq8p with percent sequence identity and global model assessment scores (QMEAN and GMQE) shown below the model.

(B) Predicted distance deviations of individual amino acid residues in the Coq8p homology model as assessed by ProQ2.

(C) Liquid media growth assays of yeast transformed with indicated Coq8p variants grown in YEP media with 0.1% glucose and 3% glycerol. A representative wild type growth result is shown in the top left corner. All other graphs are shown on the same scales for both axes.

Figure S6, related to Figure 6

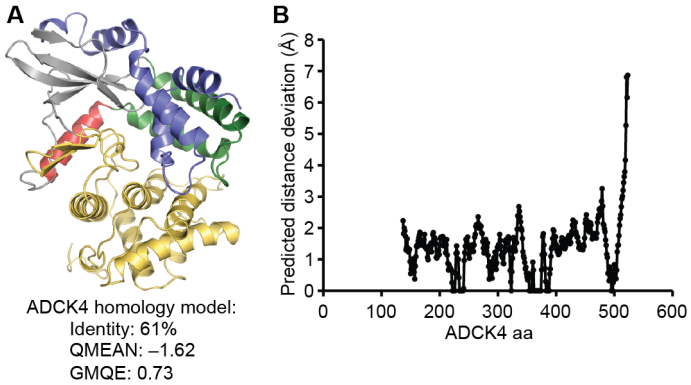

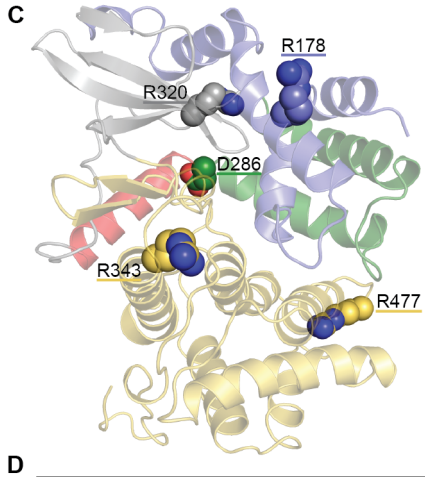

D

ADCK4 mutation	Homologous ADCK3 residue	Predicted effects on ADCK4 structure
R178W	R299	Loss of polar interactions with S182 and E140
D286G	D407	Loss of polar interactions with C-helix
R320W	H441	Loss of polar interaction with Q248 (N-terminal insert)
R343W	R464	Loss of polar interactions with F-helix
R477Q	R598	Loss of polar interactions in C-terminal lobe

Figure S6, related to Figure 6. Effects of pathogenic mutations on ADCK4

(A) Homology structure model of ADCK4 with percent sequence identity and global model assessment scores (QMEAN and GMQE) shown below the model.

(B) Predicted distance deviations of individual amino acid residues in the ADCK4 homology model as assessed by ProQ2.

(C) Residues mutated in patients with a steroid-resistant nephrotic syndrome mapped onto the ADCK4 structure model as spheres. Domains are colored as in Figure 2.

(D) Predicted structural effects of ADCK4 mutations.

References

Afonine, P.V., Grosse-Kunstleve, R.W., Echols, N., Headd, J.J., Moriarty, N.W., Mustyakimov, M., Terwilliger, T.C., Urzhumtsev, A., Zwart, P.H., and Adams, P.D. (2012). Towards automated crystallographic structure refinement with phenix.refine. Acta Crystallogr. D *68*, 352–367.

Ashraf, S., Gee, H.Y., Woerner, S., Xie, L.X., Vega-Warner, V., Lovric, S., Fang, H., Song, X., Cattran, D.C., Avila-Casado, C.*, et al.* (2013). ADCK4 mutations promote steroid-resistant nephrotic syndrome through CoQ10 biosynthesis disruption. J. Clin. Invest. *123*, 5179–5189.

Bhatnagar, D., Roskoski, R., Jr., Rosendahl, M.S., and Leonard, N.J. (1983). Adenosine cyclic 3',5'-monophosphate dependent protein kinase: a new fluorescence displacement titration technique for characterizing the nucleotide binding site on the catalytic subunit. Biochemistry *22*, 6310–6317.

Blommel, P.G., and Fox, B.G. (2007). A combined approach to improving large-scale production of tobacco etch virus protease. Protein expression and purification *55*, 53–68.

Blommel, P.G., Martin, P.A., Seder, K.D., Wrobel, R.L., and Fox, B.G. (2009). Flexi vector cloning. Methods Mol. Biol. *498*, 55–73.

Bordoli, L., Kiefer, F., Arnold, K., Benkert, P., Battey, J., and Schwede, T. (2009). Protein structure homology modeling using SWISS-MODEL workspace. Nat. Protoc. *4*, 1–13.

Bossemeyer, D. (1994). The glycine-rich sequence of protein kinases: a multifunctional element. Trends Biochem. Sci. *19*, 201–205.

Brough, R., Frankum, J.R., Sims, D., Mackay, A., Mendes-Pereira, A.M., Bajrami, I., Costa-Cabral, S., Rafiq, R., Ahmad, A.S., Cerone, M.A.*, et al.* (2011). Functional viability profiles of breast cancer. Cancer Discov. *1*, 260–273.

Burgess-Brown, N.A., Sharma, S., Sobott, F., Loenarz, C., Oppermann, U., and Gileadi, O. (2008). Codon optimization can improve expression of human genes in Escherichia coli: A multi-gene study. Protein Expr. Purif. *59*, 94–102.

Cardazzo, B., Hamel, P., Sakamoto, W., Wintz, H., and Dujardin, G. (1998). Isolation of an Arabidopsis thaliana cDNA by complementation of a yeast abc1 deletion mutant deficient in complex III respiratory activity. Gene *221*, 117–125.

Chen, V.B., Arendall, W.B., Headd, J.J., Keedy, D.A., Immormino, R.M., Kapral, G.J., Murray, L.W., Richardson, J.S., and Richardson, D.C. (2010). MolProbity: all-atom structure validation for macromolecular crystallography. Acta Crystallogr. D *66*, 12–21.

Chovancova, E., Pavelka, A., Benes, P., Strnad, O., Brezovsky, J., Kozlikova, B., Gora, A., Sustr, V., Klvana, M., Medek, P*., et al.* (2012). CAVER 3.0: a tool for the analysis of transport pathways in dynamic protein structures. PLoS Comput. Biol. *8*, e1002708.

Claros, M.G., and Vincens, P. (1996). Computational method to predict mitochondrially imported proteins and their targeting sequences. Eur. J. Biochem. *241*, 779–786.

de Beer, T.A., Berka, K., Thornton, J.M., and Laskowski, R.A. (2014). PDBsum additions. Nucleic Acids Res. *42*, D292–296.

Do, T.Q., Hsu, A.Y., Jonassen, T., Lee, P.T., and Clarke, C.F. (2001). A defect in coenzyme Q biosynthesis is responsible for the respiratory deficiency in Saccharomyces cerevisiae abc1 mutants. J. Biol. Chem. *276*, 18161–18168.

Emsley, P., Lohkamp, B., Scott, W.G., and Cowtan, K. (2010). Features and development of Coot. Acta Crystallogr. D *66*, 486–501.

Fox, B.G., and Blommel, P.G. (2009). Autoinduction of protein expression. Curr. Protoc. Protein Sci. *Chapter 5*, Unit 5 23.

Geer, L.Y., Markey, S.P., Kowalak, J.A., Wagner, L., Xu, M., Maynard, D.M., Yang, X., Shi, W., and Bryant, S.H. (2004). Open mass spectrometry search algorithm. J. Proteome Res. *3*, 958–964.

Gietz, R.D., and Woods, R.A. (2002). Transformation of yeast by lithium acetate/single-stranded carrier DNA/polyethylene glycol method. Meth. Enzymol. *350*, 87–96.

Gromek, K.A., Meddaugh, H.R., Wrobel, R.L., Suchy, F.P., Bingman, C.A., Primm, J.G., and Fox, B.G. (2013). Improved expression and purification of sigma 1 receptor fused to maltose binding protein by alteration of linker sequence. Protein Expr. Purif. *89*, 203–209.

Grosse-Kunstleve, R.W., and Adams, P.D. (2003). Substructure search procedures for macromolecular structures. Acta Crystallogr. D *59*, 1966–1973.

Guarani, V., Paulo, J., Zhai, B., Huttlin, E.L., Gygi, S.P., and Harper, J.W. (2014). TIMMDC1/C3orf1 functions as a membrane-embedded mitochondrial complex I assembly factor through association with the MCIA complex. Mol. Cell. Biol. *34*, 847–861.

Hanson, G.T., Aggeler, R., Oglesbee, D., Cannon, M., Capaldi, R.A., Tsien, R.Y., and Remington, S.J. (2004). Investigating mitochondrial redox potential with redox-sensitive green fluorescent protein indicators. J. Biol. Chem. *279*, 13044–13053.

He, C.H., Xie, L.X., Allan, C.M., Tran, U.C., and Clarke, C.F. (2014). Coenzyme Q supplementation or over-expression of the yeast Coq8 putative kinase stabilizes multi-subunit Coq polypeptide complexes in yeast coq null mutants. Biochim. Biophys. Acta *1841*, 630–644.

Hemmer, W., McGlone, M., Tsigelny, I., and Taylor, S.S. (1997). Role of the glycine triad in the ATP-binding site of cAMP-dependent protein kinase. J. Biol. Chem. *272*, 16946–16954.

Holm, L., Kaariainen, S., Rosenstrom, P., and Schenkel, A. (2008). Searching protein structure databases with DaliLite v.3. Bioinformatics *24*, 2780–2781.

Hon, W.C., McKay, G.A., Thompson, P.R., Sweet, R.M., Yang, D.S., Wright, G.D., and Berghuis, A.M. (1997). Structure of an enzyme required for aminoglycoside antibiotic resistance reveals homology to eukaryotic protein kinases. Cell *89*, 887–895.

Horvath, R., Czermin, B., Gulati, S., Demuth, S., Houge, G., Pyle, A., Dineiger, C., Blakely, E.L., Hassani, A., Foley, C*., et al.* (2012). Adult-onset cerebellar ataxia due to mutations in CABC1/ADCK3. J. Neurol. Neurosurg. Psych. *83*, 174–178.

Hsu, S., Kim, Y., Li, S., Durrant, E.S., Pace, R.M., Woods, V.L., Jr., and Gentry, M.S. (2009). Structural insights into glucan phosphatase dynamics using amide hydrogen-deuterium exchange mass spectrometry. Biochemistry *48*, 9891–9902.

Ito, S., Fushinobu, S., Yoshioka, I., Koga, S., Matsuzawa, H., and Wakagi, T. (2001). Structural basis for the ADP-specificity of a novel glucokinase from a hyperthermophilic archaeon. Structure *9*, 205–214.

Jasinski, M., Sudre, D., Schansker, G., Schellenberg, M., Constant, S., Martinoia, E., and Bovet, L. (2008). AtOSA1, a member of the Abc1-like family, as a new factor in cadmium and oxidative stress response. Plant Physiol. *147*, 719–731.

Kall, L., Krogh, A., and Sonnhammer, E.L. (2007). Advantages of combined transmembrane topology and signal peptide prediction--the Phobius web server. Nucleic Acids Res. *35*, W429–432.

Kang, J., Yang, M., Li, B., Qi, W., Zhang, C., Shokat, K.M., Tomchick, D.R., Machius, M., and Yu, H. (2008). Structure and substrate recruitment of the human spindle checkpoint kinase Bub1. Mol. Cell *32*, 394–405.

Kannan, N., and Neuwald, A.F. (2005). Did protein kinase regulatory mechanisms evolve through elaboration of a simple structural component? J. Mol. Biol. *351*, 956–972.

Kannan, N., Taylor, S.S., Zhai, Y., Venter, J.C., and Manning, G. (2007). Structural and functional diversity of the microbial kinome. PLoS Biol. *5*, e17.

Khadria, A.S., Mueller, B.K., Stefely, J.A., Tan, C.H., Pagliarini, D.J., and Senes, A. (2014). A Gly-Zipper Motif Mediates Homodimerization of the Transmembrane Domain of the Mitochondrial Kinase ADCK3. J. Am. Chem. Soc. *136* (40), 14068–14077.

Kim, C., Cheng, C.Y., Saldanha, S.A., and Taylor, S.S. (2007). PKA-I holoenzyme structure reveals a mechanism for cAMP-dependent activation. Cell *130*, 1032–1043.

Klock, H.E., and Lesley, S.A. (2009). The Polymerase Incomplete Primer Extension (PIPE) method applied to high-throughput cloning and site-directed mutagenesis. Meth. Mol. Biol. *498*, 91–103.

Knighton, D.R., Zheng, J.H., Ten Eyck, L.F., Ashford, V.A., Xuong, N.H., Taylor, S.S., and Sowadski, J.M. (1991). Crystal structure of the catalytic subunit of cyclic adenosine monophosphate-dependent protein kinase. Science *253*, 407–414.

Kornev, A.P., Haste, N.M., Taylor, S.S., and Eyck, L.F. (2006). Surface comparison of active and inactive protein kinases identifies a conserved activation mechanism. Proc. Natl. Acad. Sci. USA *103*, 17783–17788.

Ku, S.Y., Yip, P., Cornell, K.A., Riscoe, M.K., Behr, J.B., Guillerm, G., and Howell, P.L. (2007). Structures of 5-methylthioribose kinase reveal substrate specificity and unusual mode of nucleotide binding. J. Biol. Chem. *282*, 22195–22206.

Lagier-Tourenne, C., Tazir, M., Lopez, L.C., Quinzii, C.M., Assoum, M., Drouot, N., Busso, C., Makri, S., Ali-Pacha, L., Benhassine, T.*, et al.* (2008). ADCK3, an ancestral kinase, is mutated in a form of recessive ataxia associated with coenzyme Q10 deficiency. Am. J. Hum. Genet. *82*, 661–672.

Langer, G., Cohen, S.X., Lamzin, V.S., and Perrakis, A. (2008). Automated macromolecular model building for X-ray crystallography using ARP/wARP version 7. Nat. Protoc. *3*, 1171–1179.

LaRonde-LeBlanc, N., and Wlodawer, A. (2004). Crystal structure of A. fulgidus Rio2 defines a new family of serine protein kinases. Structure *12*, 1585–1594.

Leonard, C.J., Aravind, L., and Koonin, E.V. (1998). Novel families of putative protein kinases in bacteria and archaea: evolution of the "eukaryotic" protein kinase superfamily. Genome Res. *8*, 1038–1047.

Li, S., Tsalkova, T., White, M.A., Mei, F.C., Liu, T., Wang, D., Woods, V.L., Jr., and Cheng, X. (2011). Mechanism of intracellular cAMP sensor Epac2 activation: cAMP-induced conformational changes identified by amide hydrogen/deuterium exchange mass spectrometry (DXMS). J. Biol. Chem. *286*, 17889–17897.

Lohman, D.C., Forouhar, F., Beebe, E.T., Stefely, M.S., Minogue, C.E., Ulbrich, A., Stefely, J.A., Sukumar, S., Luna-Sanchez, M., Jochem, A.*, et al.* (2014). Mitochondrial COQ9 is a lipid-binding protein that associates with COQ7 to enable coenzyme Q biosynthesis. Proc. Natl. Acad. Sci. USA. doi: 10.1073/pnas.1413128111.

Lundquist, P.K., Davis, J.I., and van Wijk, K.J. (2012). ABC1K atypical kinases in plants: filling the organellar kinase void. Trends Plant Sci. *17*, 546–555.

Lundquist, P.K., Poliakov, A., Giacomelli, L., Friso, G., Appel, M., McQuinn, R.P., Krasnoff, S.B., Rowland, E., Ponnala, L., Sun, Q.*, et al.* (2013). Loss of plastoglobule kinases ABC1K1 and ABC1K3 causes conditional degreening, modified prenyl-lipids, and recruitment of the jasmonic acid pathway. Plant Cell *25*, 1818–1839.

Manning, G., Whyte, D.B., Martinez, R., Hunter, T., and Sudarsanam, S. (2002). The protein kinase complement of the human genome. Science *298*, 1912–1934.

Mao, D.Y., Neculai, D., Downey, M., Orlicky, S., Haffani, Y.Z., Ceccarelli, D.F., Ho, J.S., Szilard, R.K., Zhang, W., Ho, C.S.*, et al.* (2008). Atomic structure of the KEOPS complex: an ancient protein kinase-containing molecular machine. Mol. Cell *32*, 259–275.

Markley, J.L., Aceti, D.J., Bingman, C.A., Fox, B.G., Frederick, R.O., Makino, S., Nichols, K.W., Phillips, G.N., Jr., Primm, J.G., Sahu, S.C.*, et al.* (2009). The Center for Eukaryotic Structural Genomics. J. Struct. Funct. Genomics *10*, 165–179.

Martinis, J., Glauser, G., Valimareanu, S., and Kessler, F. (2013). A chloroplast ABC1-like kinase regulates vitamin E metabolism in Arabidopsis. Plant Physiol. *162*, 652–662.

Mollet, J., Delahodde, A., Serre, V., Chretien, D., Schlemmer, D., Lombes, A., Boddaert, N., Desguerre, I., de Lonlay, P., de Baulny, H.O.*, et al.* (2008). CABC1 gene mutations cause ubiquinone deficiency with cerebellar ataxia and seizures. Am. J. Hum. Genet. *82*, 623–630.

Mumberg, D., Muller, R., and Funk, M. (1995). Yeast vectors for the controlled expression of heterologous proteins in different genetic backgrounds. Gene *156*, 119–122.

Murshudov, G.N., Vagin, A.A., and Dodson, E.J. (1997). Refinement of macromolecular structures by the maximum-likelihood method. Acta Crystallogr. D *53*, 240–255.

Neuwald, A.F. (2007). The CHAIN program: forging evolutionary links to underlying mechanisms. Trends Biochem. Sci. *32*, 487–493.

Neuwald, A.F. (2009). Rapid detection, classification and accurate alignment of up to a million or more related protein sequences. Bioinformatics *25*, 1869–1875.

Neuwald, A.F., Kannan, N., Poleksic, A., Hata, N., and Liu, J.S. (2003). Ran's C-terminal, basic patch, and nucleotide exchange mechanisms in light of a canonical structure for Rab, Rho, Ras, and Ran GTPases. Genome Res. *13*, 673–692.

Niesen, F.H., Berglund, H., and Vedadi, M. (2007). The use of differential scanning fluorimetry to detect ligand interactions that promote protein stability. Nat. Protoc. *2*, 2212–2221.

Otwinowski, Z., and Minor, W. (1997). Processing of X-ray diffraction data collected in oscillation mode. Meth. Enzymol. *276*, 307–326.

Pagliarini, D.J., Calvo, S.E., Chang, B., Sheth, S.A., Vafai, S.B., Ong, S.E., Walford, G.A., Sugiana, C., Boneh, A., Chen, W.K.*, et al.* (2008). A mitochondrial protein compendium elucidates complex I disease biology. Cell *134*, 112–123.

Pineda, M., Montero, R., Aracil, A., O'Callaghan, M.M., Mas, A., Espinos, C., Martinez-Rubio, D., Palau, F., Navas, P., Briones, P.*, et al.* (2010). Coenzyme Q(10)-responsive ataxia: 2-year-treatment follow-up. Mov. Disord. *25*, 1262–1268.

Poon, W.W., Davis, D.E., Ha, H.T., Jonassen, T., Rather, P.N., and Clarke, C.F. (2000). Identification of Escherichia coli ubiB, a gene required for the first monooxygenase step in ubiquinone biosynthesis. J. Bacteriol. *182*, 5139–5146.

Ray, A., Lindahl, E., and Wallner, B. (2012). Improved model quality assessment using ProQ2. BMC bioinformatics *13*, 224.

Rhee, H.W., Zou, P., Udeshi, N.D., Martell, J.D., Mootha, V.K., Carr, S.A., and Ting, A.Y. (2013). Proteomic mapping of mitochondria in living cells via spatially restricted enzymatic tagging. Science *339*, 1328–1331.

Rossmann, M.G., Moras, D., and Olsen, K.W. (1974). Chemical and biological evolution of nucleotide-binding protein. Nature *250*, 194–199.

Saraste, M., Sibbald, P.R., and Wittinghofer, A. (1990). The P-loop--a common motif in ATP- and GTP-binding proteins. Trends Biochem. Sci. *15*, 430–434.

Schieven, G., and Martin, G.S. (1988). Nonenzymatic phosphorylation of tyrosine and serine by ATP is catalyzed by manganese but not magnesium. J. Biol. Chem. *263*, 15590–15593.

Schlecht, U., Suresh, S., Xu, W., Aparicio, A.M., Chu, A., Proctor, M.J., Davis, R.W., Scharfe, C., and St Onge, R.P. (2014). A functional screen for copper homeostasis genes identifies a pharmacologically tractable cellular system. BMC genomics *15*, 263.

Simpson, K.J., Selfors, L.M., Bui, J., Reynolds, A., Leake, D., Khvorova, A., and Brugge, J.S. (2008). Identification of genes that regulate epithelial cell migration using an siRNA screening approach. Nat. Cell Biol. *10*, 1027–1038.

Suhre, K., and Sanejouand, Y.H. (2004). ElNemo: a normal mode web server for protein movement analysis and the generation of templates for molecular replacement. Nucleic Acids Res. *32*, W610–614.

Tan, T., Ozbalci, C., Brugger, B., Rapaport, D., and Dimmer, K.S. (2013). Mcp1 and Mcp2, two novel proteins involved in mitochondrial lipid homeostasis. J. Cell Sci. *126*, 3563–3574.

Terwilliger, T.C., Adams, P.D., Read, R.J., Mccoy, A.J., Moriarty, N.W., Grosse-Kunstleve, R.W., Afonine, P.V., Zwart, P.H., and Hung, L.W. (2009). Decision-making in structure solution

using Bayesian estimates of map quality: the PHENIX AutoSol wizard. Acta Crystallogr. D *65*, 582–601.

Vogtle, F.N., Wortelkamp, S., Zahedi, R.P., Becker, D., Leidhold, C., Gevaert, K., Kellermann, J., Voos, W., Sickmann, A., Pfanner, N.*, et al.* (2009). Global analysis of the mitochondrial N-proteome identifies a processing peptidase critical for protein stability. Cell *139*, 428–439.

Walker, E.H., Perisic, O., Ried, C., Stephens, L., and Williams, R.L. (1999). Structural insights into phosphoinositide 3-kinase catalysis and signalling. Nature *402*, 313–320.

Wenger, C.D., Phanstiel, D.H., Lee, M.V., Bailey, D.J., and Coon, J.J. (2011). COMPASS: a suite of pre- and post-search proteomics software tools for OMSSA. Proteomics *11*, 1064–1074.

Wiedemeyer, W.R., Dunn, I.F., Quayle, S.N., Zhang, J., Chheda, M.G., Dunn, G.P., Zhuang, L., Rosenbluh, J., Chen, S., Xiao, Y.*, et al.* (2010). Pattern of retinoblastoma pathway inactivation dictates response to CDK4/6 inhibition in GBM. Proc. Natl. Acad. Sci. USA *107*, 11501–11506.

Xie, L.X., Hsieh, E.J., Watanabe, S., Allan, C.M., Chen, J.Y., Tran, U.C., and Clarke, C.F. (2011). Expression of the human atypical kinase ADCK3 rescues coenzyme Q biosynthesis and phosphorylation of Coq polypeptides in yeast coq8 mutants.
Biochim. Biophys. Acta *1811*, 348–360.

Yamaguchi, H., Matsushita, M., Nairn, A.C., and Kuriyan, J. (2001). Crystal structure of the atypical protein kinase domain of a TRP channel with phosphotransferase activity. Mol. Cell *7*, 1047–1057.

Young, T.A., Delagoutte, B., Endrizzi, J.A., Falick, A.M., and Alber, T. (2003). Structure of Mycobacterium tuberculosis PknB supports a universal activation mechanism for Ser/Thr protein kinases. Nat. Struct. Mol. Biol. *10*, 168–174.

Zeqiraj, E., and van Aalten, D.M. (2010). Pseudokinases-remnants of evolution or key allosteric regulators? Curr. Opin. Struct. Biol. *20*, 772–781.

Zheng, J., and Jia, Z. (2010). Structure of the bifunctional isocitrate dehydrogenase kinase/phosphatase. Nature *465*, 961–965.

Zheng, J., Trafny, E.A., Knighton, D.R., Xuong, N.H., Taylor, S.S., Ten Eyck, L.F., and Sowadski, J.M. (1993). 2.2 A refined crystal structure of the catalytic subunit of cAMP-dependent protein kinase complexed with MnATP and a peptide inhibitor. Acta Crystallogr. D *49*, 362–365.

Zolnai, Z., Lee, P.T., Li, J., Chapman, M.R., Newman, C.S., Phillips, G.N., Jr., Rayment, I., Ulrich, E.L., Volkman, B.F., and Markley, J.L. (2003). Project management system for structural and functional proteomics: Sesame. J. Struct. Funct. Genomics *4*, 11–23.

Chapter 3

Unorthodox functions of an ancient kinase-like family enable isoprenoid lipid biosynthesis

Jonathan A. Stefely, Andrew G. Reidenbach, Catherine E. Minogue, Alexander S. Hebert, Xiao Guo, Craig A. Bingman, Arne Ulbrich, Isabel E. Johnson, Danielle C. Lohman, Adam Jochem, Floriana Licitra, Leila Laredj, Hélène Puccio, Joshua J. Coon, & David J. Pagliarini

Author contributions:

J.A.S. was the primary author of this chapter. J.A.S. and D.J.P. conceived of the project and its design. F.L., L.L., and H.P. created the *Adck3*$^{-/-}$ mouse and characterized its physiology. J.A.S., A.G.R., and C.E.M. conducted proteomic analysis of the *Adck3*$^{-/-}$ mice. J.A.S. and A.S.H. conducted proteomic analysis of the Δ*coq8* yeast. A.J. conducted cloning experiments. J.A.S conducted *in vitro* kinase assays and ligand binding assays with Coq8p and ADCK3. J.A.S. and X.G. conducted experiments to identify the Coq8p autophosphorylation sites. J.A.S. and I.E.J. conducted ATPase assays with Coq8p and ADCK3. C.A.B. solved the ADCK3-nucleotide structure. J.A.S. analyzed the conformational changes of the ADCK3-nucleotide structure. J.A.S., A.U., and D.C.L. conducted lipid-binding assays. J.A.S., A.G.R., C.E.M., A.S.H., X.G., C.A.B., A.U., I.E.J., D.C.L., A.J., F.L., L.L., H.P., J.J.C., and D.J.P. performed data analysis.

Abstract

The ancient protein kinase-like (PKL) UbiB family enables diverse biological functions, including the biosynthesis of isoprenoid lipids such as coenzyme Q (CoQ). Like many putative protein kinases, UbiBs are assumed to function by catalyzing protein phosphorylation, yet this idea remains largely untested. Here we show that two UbiB proteins, mammalian Adck3 and its yeast ortholog Coq8p, are specifically required for maintaining the abundance of CoQ biosynthesis proteins. To test the molecular basis for this function, we show that Coq8p autophosphorylates *in cis*. However, Coq8p does not catalyze phosphorylation of other proteins *in trans*, arguing against the putative model that Coq8p is a protein kinase. In testing alternative models for Coq8p function, we show that Coq8p has unexpectedly robust ATPase activity that depends on UbiB-specific residues required for function *in vivo*. Furthermore, we identify small molecules that bind to Coq8p and impact ADCK3 enzyme activity *in vitro*. Finally, we solve an ADCK3-nucleotide co-crystal structure that shows nucleotide-dependent conformational switches that could impact small molecule binding or protein-protein interactions, yet the invariant KxGQ motif is still positioned to inhibit protein kinase activity. Collectively, these findings argue for an unorthodox PKL function, in which ADCK3 acts as a small molecule kinase or an ATPase.

Introduction

The protein kinase-like (PKL) superfamily supports and regulates diverse biological functions, generally by catalyzing transfer of a phosphoryl group from ATP to a substrate (Kannan et al., 2007; Manning et al., 2002). The canonical function for most PKLs is catalysis of protein phosphorylation. Increasingly, however, non-canonical PKL functions are coming to light. For example, the PI3K family of PKLs includes small molecule kinases (Walker et al., 1999), but it also includes *bona fide* protein kinases such as mTOR (Brown et al., 1994; Brown et al., 1995; Sabatini et al., 1994; Yang et al., 2013), making it difficult to distinguish these activities. Other PKLs, such as Ire1, have protein kinase activity, but can function through nucleotide-induced oligomerization independent of kinase activity (Korennykh et al., 2009; Lee et al., 2008; Papa et al., 2003). Similarly, pseudokinases, which represent 10% of the human kinome, lack kinase activity, but can function through nucleotide-induced conformational changes (Boudeau et al., 2006; Zeqiraj and van Aalten, 2010). Differentiating these diverse mechanisms of PKL action remains a central challenge.

The UbiB family of PKLs is widespread, comprising an estimated one quarter of all microbial PKLs (Kannan et al., 2007), and conserved, ranging from bacteria to humans (Leonard et al., 1998). The diverse biological functions of UbiB proteins include roles in isoprenoid lipid biosynthesis (Do et al., 2001; Poon et al., 2000), phospholipid metabolism (Tan et al., 2013), stress responses (Jasinski et al., 2008), plant pigmentation (Lundquist et al., 2013), copper homeostasis (Schlecht et al., 2014), epithelial cell migration (Simpson et al., 2008), and the viability of cells derived from glioblastoma mulitforme (Wiedemeyer et al., 2010) and estrogen receptor-positive breast tumors (Brough et al., 2011). However, the molecular basis for these

functions remains unknown, largely because the endogenous biochemical activities of UbiB proteins are undefined.

Mutations in two of the five human UbiB family '*ADCK*' genes, *ADCK3* and *ADCK4*, can cause coenzyme Q (CoQ) deficiency. *ADCK3* mutations cause a cerebellar ataxia (Horvath et al., 2012; Lagier-Tourenne et al., 2008; Mollet et al., 2008; Pineda et al., 2010), while *ADCK4* mutations cause a steroid resistant nephrotic syndrome (Ashraf et al., 2013). ADCK3 and ADCK4 are known to localize to the mitochondrial matrix (Pagliarini et al., 2008; Rhee et al., 2013), where CoQ biosynthesis occurs, but whether they function exclusively in CoQ biosynthesis or have wider biological functions is unknown.

Mutation of the yeast ortholog of *ADCK3* and *ADCK4*, *coq8*, also causes CoQ deficiency (Do et al., 2001). Coq8p stabilizes a complex of CoQ biosynthesis proteins (He et al., 2014). The prevailing model to explain this effect assumes that Coq8p is a protein kinase that phosphorylates proteins in the CoQ biosynthesis complex. Consistently, the presence or absence of *coq8* modulates post-translational modification of Coq3p, Coq5p, and Coq7p *in vivo* (Xie et al., 2011), but whether this effect is direct or indirect is unknown. The ability of Coq8p to directly catalyze phosphorylation of proteins *in vitro* has not yet been tested.

Toward understanding the molecular basis for ADCK3 function, we previously solved a crystal structure of ADCK3, which revealed an atypical protein kinase-like fold with numerous features positioned to inhibit protein kinase activity (Stefely et al., 2015). Mutating one of these features enabled autophosphorylation *in vitro*, but decreased CoQ biosynthesis *in vivo*, suggesting that inhibition of protein kinase activity is functionally important. However, this work had some limitations. First, the *in vitro* studies were conducted with a truncated enzyme lacking a transmembrane helix that could impact enzyme activity (Khadria et al., 2014). Second, the

crystal structure of ADCK3 was solved in the apo form. Whether nucleotide binding could release the inhibitory features through conformational changes was unknown.

Here, we show that *Adck3*$^{-/-}$ mice and Δ*coq8* yeast are specifically deficient for CoQ biosynthesis complex proteins. To begin understanding the molecular basis for this effect, we purified the full-length mitochondrial form of Coq8p and examined its activity *in vitro*. We show that Coq8p can autophosphorylate *in cis*, but it does not catalyze phosphorylation of proteins *in trans*. Furthermore, a nucleotide-ADCK3 co-crystal structure maintains features positioned to inhibit protein kinase activity. These results argue against the protein kinase model for Coq8p function and demand a revised model. We present two alternative models for Coq8p function—the small molecule kinase model and the ATPase model—and evidence that supports these non-canonical models over the protein kinase model.

Results and Discussion

Adck3 Specifically Enhances Coenzyme Q Biosynthesis in Mice

To begin investigating the function of Adck3 in mice, we generated an *Adck3*$^{-/-}$ mouse line (Hélène Puccio and colleagues, unpublished results). *Adck3*$^{-/-}$ mice exhibit a progressive gait ataxia, similar to that observed in human patients with *ADCK3* mutations, a specific defect in cerebellar Purkinje cells, and CoQ deficiency (Hélène Puccio and colleagues, unpublished results).

Toward understanding the molecular basis for the phenotype changes in the *Adck3*$^{-/-}$ mice, we quantified changes in protein abundances by unbiased, mass spectrometry (MS)-based proteomics (Figure 1). The cerebellum of *Adck3*$^{-/-}$ mice is significantly deficient for the CoQ biosynthesis complex proteins Coq5, Coq7, and Coq9 (Figure 1A). The decrease in these CoQ

proteins stands out from among a background of smaller, less significant perturbations, suggesting that the function of Adck3 is relatively specific for maintaining the CoQ biosynthesis complex. Skeletal muscle and heart tissue showed similarly specific decreases in the levels of CoQ biosynthesis proteins Coq3, Coq5, Coq6, Coq7, and Coq9 (Figures 1B and 1C), suggesting that Adck3 plays a similar functional role in tissues outside of the cerebellum. Kidney tissue also showed a significant decrease in the abundances of CoQ biosynthesis proteins, but the magnitude of the decreases in the kidney was lower than in the other tissue types (Figure 1D).

Skeletal muscle, heart, and kidney tissue each showed a significant increase in the abundance of the protein sulfide quinone reductase-like (Sqrdl), but no significant change in Sqrdl abundance was observed in the cerebellum. This suggests a difference in the adaptive response to Adck3 deficiency across tissues, but the specific functional importance of Sqrdl elevation remains to be investigated. Notably, we also previously observed a perturbation of Sqrdl protein abundance in mice with a *Coq9* mutation (Lohman et al., 2014), suggesting a more general association between Sqrdl and CoQ biosynthesis.

Because Adck3 is hypothesized to be a protein kinase, we characterized changes in the phosphoproteome of *Adck3*$^{-/-}$ mice by unbiased MS. Numerous significant changes in phosphopeptide abundances were observed in the cerebellum and skeletal muscle of *Adck3*$^{-/-}$ mice (Figure S1). Many of the perturbations are likely indirect, downstream effects of the Adck3 deficiency because the perturbed phosphopeptides are not from mitochondrial proteins. Moreover, a previous phosphoproteomic study of yeast gene knockout strains demonstrated that most observed changes are indirect (Bodenmiller et al., 2010). A significant decrease in a phosphopeptide containing Coq9 pS81 was observed in the *Adck3*$^{-/-}$ mouse cerebellum (Figure S1A). Whether this observation is due to a decrease in phosphorylation stoichiometry or due to

the observed decrease in Coq9 protein abundance (Figure 1A) is difficult to determine by unbiased MS-based proteomics. In skeletal muscle, two Coq9 phosphopeptides were observed (pS81 and pY88), but they did not show significant changes across the two genotypes (Figure S1B). Despite detecting and quantifying over 7,500 phosphopeptides in the cerebellum and over 6,000 phosphopeptides in the skeletal muscle, we did not detect phosphopeptides from Coq3, Coq5, or Coq7, the hypothesized Adck3 protein substrates (Xie et al., 2011).

Coq8p Specifically Enhances Coenzyme Q Biosynthesis in Yeast

The yeast *Saccharomyces cerevisiae* is a widely used model organism for studying CoQ biosynthesis. To see if the selectivity for CoQ biosynthesis we observed with the *Adck3*$^{-/-}$ mice is conserved in yeast, we conducted a MS-based proteomics study of yeast lacking the *Adck3* homolog (Δ*coq8* yeast). *Coq8* mRNA levels are known to increase during the metabolic transition from fermentation to respiration (DeRisi et al., 1997), termed the diauxic shift. We took advantage of this transition to look at the dynamics of Coq8p function. Samples of WT and Δ*coq8* yeast were isolated before, during, and after the diauxic shift (Figure 2A), and each time point was analyzed by MS-based proteomics and phosphoproteomics.

CoQ biosynthesis proteins increased during the diauxic shift in WT yeast (Figure 2B), but this increase was blunted and not maintained in the Δ*coq8* yeast (Figure 2C). The Δ*coq8* yeast also showed deficiency of some CoQ biosynthesis proteins at all three time points investigated (Figure 2D). Examining changes across the entire proteome showed a significant and specific impact on CoQ biosynthesis complex proteins (Coq3p–Coq7p and Coq9p) during and after the diauxic shift (Figures 2E–2G). Collectively, these results demonstrate that Coq8p plays a

dynamic and specific role in CoQ production in yeast, supporting the stability of the CoQ biosynthesis complex when yeast are in respiratory growth.

Because Coq8p is hypothesized to be a protein kinase, we also quantified changes in the phosphoproteome of WT and Δ*coq8* yeast across all three time points (Figure 2A). Numerous significant changes in phosphopeptides were observed in Δ*coq8* yeast before (Figure S2A), during (Figure S2B), and after (Figure S2C) the diauxic shift. Dramatic changes in phosphopeptides were observed for many mitochondrial proteins (Figures S2A–S2C), including proteins of the mitochondrial ribosome (Figure S2D), oxidative phosphorylation (Figure S2D), and central carbon metabolism (Figure S2E). In total, we identified and quantified over 6,000 yeast phosphopeptides across the diauxic shift in both genotypes, generating a comprehensive resource for investigation of dynamic protein phosphorylation in yeast. However, despite our deep coverage of the yeast phosphoproteome, we did not observe any phosphopeptides from CoQ biosynthesis proteins.

The surprisingly selective impact of Adck3 and Coq8p on proteins of the CoQ biosynthesis complex focused our efforts to define the underlying biochemical activity of ADCK3 and Coq8p. To begin, we first tested the hypothesis that Coq8p is a protein kinase that catalyzes phosphorylation of CoQ biosynthesis proteins *in vitro*.

Coq8p Catalyzes Autophosphorylation Exclusively *in cis*

We purified the full-length mitochondrial form of Coq8p ($Coq8^{N\Delta41}$) by removing a 41 amino acid residue mitochondrial targeting sequence (Figure S3A), which had been previously identified (Vogtle et al., 2009). Compared to $ADCK3^{N\Delta250}$ (Stefely et al., 2015), $Coq8^{N\Delta41}$ contains two additional predicted α-helices on the N-terminal extension (Figures S3B). One of

these α-helices is homologous to the ADCK3 transmembrane domain, which could impact enzyme activity (Khadria et al., 2014) (Figure S3C). To enable direct biochemical comparisons, we also purified protein kinase A (PKA), the canonical protein kinase, in parallel with $Coq8^{N\Delta41}$ (Figure S3A).

To test the nucleotide binding properties of $Coq8^{N\Delta41}$ and PKA, we quantified ligand-induced changes in protein melting temperature (ΔT_m). Both $Coq8^{N\Delta41}$ and PKA preferentially bound adenine nucleotides (Figure S3D). $Coq8^{N\Delta41}$ preferentially bound MgADP over MgATP, whereas PKA showed a slight preference for MgATP. As we previously observed with $ADCK3^{N\Delta250}$, a single A-to-G mutation of the A-rich loop of $Coq8^{N\Delta41}$ flips nucleotide selectivity (Figures S3E and S3F). The $Coq8^{N\Delta41}$ A197G mutant prefers to bind MgATP over MgADP, whereas PKA shows a similar affinity for MgATP and MgADP (Figures S3G and S3H). These results show that the unique nucleotide binding features that we observed with human ADCK3 are conserved in yeast Coq8p.

Mutating the A-rich loop (A197G) of $Coq8^{N\Delta41}$ also enhances autophosphorylation activity, which we found to be dependent on cation binding residue D365 (Figure 3A), Mg^{2+} (Figure 3B), and time (Figure 3C). A double mutation of both the A-rich loop (A197G) and the lysine of the invariant KxGQ motif (K134H) further enhanced autophosphorylation activity (Figures 3A–3C and 3F), similar to those of $ADCK3^{N\Delta250}$ (Stefely et al., 2015).

LC-MS/MS analysis revealed the amino acid residues autophosphorylated by $Coq8^{N\Delta41}$ (WT, A179G, and A197G,K134H) (Figure S4A). The most abundant phosphorylation sites that were mutation-responsive included pS83, pS114, pT122, pS126, pS156, and pS198 (Figure 3D). These autophosphorylated residues all localize to the UbiB-specific KxGQ domain (Figure 3E), which is positioned in the pocket where the peptide substrate of most protein kinases would

normally bind. With moderate conformational changes of the KxGQ domain, these residues could be accessible for autophosphorylation *in cis* or *in trans*.

To determine whether Coq8$^{N\Delta41}$ autophosphorylates *in cis* or *in trans*, we conducted reactions with combinations of active (A197G,K134H) and inactive (D365N) enzymes (Figure 3G). By using tagged and untagged versions of the enzymes, we were able to separate the active and inactive enzymes by size with SDS-PAGE. The maltose binding protein (MBP) tag did not disrupt autophosphorylation activity (Figure 3G). In reactions with both inactive and active enzymes, only the active enzyme was autophosphorylated, demonstrating that Coq8$^{N\Delta41}$ autophosphorylates exclusively *in cis* (Figure 3G). Similar results were obtained with WT Coq8$^{N\Delta41}$ (Figure S4B) and ADCK3$^{N\Delta250}$ A339G (Figure S4C).

The lack of autophosphorylation *in trans* raised the question of whether Coq8$^{N\Delta41}$ can catalyze phosphorylation of any protein *in trans*. While PKA catalyzed robust phosphorylation of the general protein kinase substrate myelin basic protein, neither WT Coq8$^{N\Delta41}$ nor A197G,K134H Coq8$^{N\Delta41}$ catalyzed protein phosphorylation *in trans* (Figure S4D). Similarly, PKA catalyzed robust phosphorylation of a mixture of CoQ biosynthesis proteins (COQ3–COQ7 and COQ9), but, again, neither WT Coq8$^{N\Delta41}$ nor A197G,K134H Coq8$^{N\Delta41}$ catalyzed protein phosphorylation *in trans* (Figure S4D).

Alternative Models for ADCK3 Function

Multiple observations from present and past (Stefely et al., 2015) work argue against the model that ADCK3 and Coq8p function as protein kinases to enable CoQ biosynthesis (Figure 4A): (1) The ADCK3 KxGQ domain occludes the typical peptide substrate binding pocket. (2) Mutations of UbiB-specific structural features enhance autophosphorylation activity *in vitro*, but

decrease CoQ production *in vivo*. (3) ADCK3 and Coq8p catalyze autophosphorylation exclusively *in cis*. (4) Neither ADCK3 nor Coq8p catalyzes phosphorylation of proteins *in trans*. Thus, new models for ADCK3 function are needed.

The new models for ADCK3 function must incorporate the following features, which our present and past (Stefely et al., 2015) work supports: (1) Adenine nucleotide binding is essential for function *in vivo*. (2) A conserved active site structure that catalyzes phosphoryl transfer is also essential for function *in vivo*. (3) The KxGQ motif, which is unique to the UbiB family and invariant in UbiB proteins, is also essential for function *in vivo*. (4) ADCK3 and Coq8p specifically stabilize the CoQ biosynthesis complex to enable CoQ biosynthesis. We support two new models for ADCK3 function that could account for these features: The small molecule kinase model (Figure 4B) and the ATPase model (Figure 4C).

Coq8p Catalyzes ATPase Activity with its KxGQ motif

To begin testing these new models we examined Coq8$^{N\Delta41}$ for ATPase activity. PKA and WT Coq8$^{N\Delta41}$ both catalyzed ATPase activity (Figure 5A). The A197G mutation, which enhances MgATP binding *in vitro* (Figure S3E), increased the ATPase activity. However, the A197G,K134H double mutant decreased the ATPase activity, to a level near that of the D365N mutant, which does not bind nucleotides. The decrease in ATPase activity seen with the A197G,K134H double mutant is in stark contrast to the way that it dramatically increases autophosphorylation activity. A similar decrease in ATPase activity was also seen with the K134H mutant, which also increases autophosphorylation activity (Figure 3F). These results show that Coq8$^{N\Delta41}$ ATPase activity is enhanced by the lysine of the KxGQ motif. Importantly, we previously showed that the KxGQ motif does not significantly impact nucleotide binding

(Stefely et al., 2015), suggesting that K134 impacts catalysis through a different mechanism, possibly by binding the water molecule that hydrolyzes ATP. We also previously showed that the K134H mutation completely eliminates CoQ production *in vivo* (Stefely et al., 2015), suggesting that the ATPase activity is more closely related to the endogenous activity of Coq8p than the *in vitro* autophosphorylation activity.

Previous structural analysis of ADCK3 showed that the lysine of the KxGQ motif coordinates a well-ordered water molecule (Figure 5B). This water molecule essentially superimposes with the phosphoryl acceptor hydroxyl group of typical protein kinases, making it a prime candidate for the water molecule that is phosphorylated by ATP in the observed ATPase reaction. In the ATPase model, this phosphorylation of water would be the relevant endogenous activity. Alternatively, in the small molecule kinase model, this water molecule could mimic a small molecule substrate hydroxyl group that is normally coordinated by the KxGQ motif (Figure 5B).

A third possibility is that the lysine of the KxGQ motif is actually phosphorylated through a 'lysine kinase' activity (Figure 5B). Phospholysine (pLys) would be extremely labile, even more so than phosphohistidine (pHis), and subsequent hydrolysis of pLys could be observed as a net ATPase reaction (Figure 5C). We have examined Coq8p and ADCK3 for lysine kinase activity under basic and neutral pH conditions. While we have not yet observed any evidence for pLys (or pHis) formation, these investigations are ongoing. This work is complicated by the fact that no lysine kinase has been reported, so no positive control is available for testing our experimental conditions.

The discovery of $Coq8^{N\Delta41}$ ATPase activity also raises the question of how ATPase activity could impact the CoQ biosynthesis complex. We recently discovered that ADCK3-

FLAG co-purifies from human tissue culture cells with numerous COQ proteins (Floyd et al., 2015, under review). Changes in ADCK3 nucleotide binding could act as a metabolic sensor to regulate CoQ biosynthesis by modulating protein-protein interactions. To test this idea, we are currently examining protein-protein interactions with the panel of mutants characterized above, which have a range of effects on nucleotide binding, autophosphorylation activity, and ATPase activity, with or without various nucleotides (ATP, ADP, and ATPγS) (Figure S5). We are also examining this same panel of mutants in yeast (Figure S5).

Small Molecules Impact ADCK3 Enzyme Activity

Water is likely the smallest molecule that can be phosphorylated by ADCK3. However, as described above, it could mimic another small molecule substrate in the active site. CoQ biosynthesis intermediates contain a number of phosphorylatable hydroxyl groups that make them potential substrates for ADCK3 (Figure S6A). Phosphorylation of a CoQ intermediate could help keep it at the surface of the lipid bilayer where it would be more accessible to the peripheral membrane enzymes of CoQ biosynthesis. The CoQ intermediate demethoxy-demethyl-coenzyme Q (DDMQ) is a particularly appealing candidate for phosphorylation because it would be highly hydrophobic in its oxidized state. Furthermore, the methylation of DDMQ catalyzed by COQ5 is predicted to require the reduced form of DDMQ, and a phosphoryl group could act as a protecting group to help keep DDMQ in the reduced state. Thus, ADCK3 could act as a lipid kinase to assist the COQ5 methylation reaction by catalyzing phosphorylation of DDMQ (Figure S5A). Consistent with a functional connection between ADCK3 and COQ5, the bacterial homolog of *ADCK3* (*ubiB*) is usually found in operons with the bacterial homolog of *COQ5* (*ubiE*) (Figure S5B).

To test the idea that ADCK3 can catalyze phosphorylation of a CoQ biosynthesis intermediate, we used small molecule analogs of CoQ intermediate headgroups because the full intermediates are not commercially available. We also used a kinase assay based on detection of the ADP product rather than detection of the phosphorylated product because phosphorylated CoQ intermediates are likely to be unstable and difficult to detect. Conversion of ATP to ADP catalyzed by ADCK3$^{N\Delta250}$ A339G was selectively enhanced by addition of 1,4-dihydroxy-2,6-dimethoxybenzene, a DDMQ headgroup analog (Figure 6A). This enhancement of ADP production was observed consistently across multiple protein preparations of ADCK3$^{N\Delta250}$ A339G (Figure 6B). The enhancement of ADP production could be indicative of substrate phosphorylation (Figure 6C), but it could also be accounted for by an increase in ATPase activity or autophosphorylation activity. Work to distinguish these possibilities is ongoing. Regardless, the observation that a DDMQ analog impacts ADCK3 enzyme activity is likely a functionally important result.

In an attempt to observe phosphorylation of DDMQ, we conducted lipid kinase reactions with lipid extracts from Δ*ubiE E. coli*, which are known to accumulate DDMQ, and Δ*ubiF E. coli*, which are known to accumulate the closely related species demethoxy coenzyme Q (DMQ) (Young, 1971). In these reactions we observed a significant amount of background diacylglycerol kinase (DAGK) activity, which catalyzes formation of phosphatidic acid (PA) and lysophosphatidic acid (LPA), likely due to a small amount of contaminating DAGK enzyme from *E. coli*. However, we also observed formation of a third product that depends on the presence of ADCK3$^{N\Delta250}$ A339G (Figure 6D). Efforts to identify the product by LC-MS/MS are ongoing.

To more generally test the idea that an ADCK3 protein-lipid interaction is important for function, we conducted liposome-protein co-floatation assays. ADCK3$^{N\Delta250}$ and Coq8$^{N\Delta41}$ both bound to liposomes as efficiently as COQ9 (Figure 6E), which is a known lipid-binding protein (Lohman et al., 2014). Coq8$^{N\Delta41}$ appears to bind liposomes better than ADCK3$^{N\Delta250}$, likely because of the additional hydrophobic α-helix present on its N-terminus. The presence of MgATP and ADCK3$^{N\Delta250}$ or Coq8$^{N\Delta41}$ also appears to decrease binding of COQ9 to liposomes (Figure 6E), which could be due to a functional interaction. Consistent with the idea that ADCK3 and COQ9 may interact functionally, an ADCK3-COQ9 fusion protein is present in *Tetrahymena thermophila* (Figure S6C).

To identify the specific lipids that bind to Coq8$^{N\Delta41}$, we conducted an affinity co-purification-mass spectrometry experiment using COQ9 as a positive control and PKA as a negative control (Figure S6D). The glycerophospholipids phosphatidylethanolamine (PE) and phosphatidylglycerol (PG) co-purified non-specifically with all proteins tested, a general phenomenon that has been observed previously (Maeda et al., 2013). In contrast, the *E. coli* CoQ biosynthesis intermediate octaprenylphenol (OPP) (Figure 6G) co-purified with Coq8$^{N\Delta41}$ and COQ9$^{N\Delta79}$, but not with PKA (Figure 6F). While COQ9 is already known to be a lipid binding protein, this result suggests that a physical interaction between Coq8$^{N\Delta41}$ and an intermediate in CoQ biosynthesis may likewise be functionally important. Interestingly, OPP is the CoQ intermediate that accumulates in Δ*ubiB E. coli* (Cox et al., 1969; Poon et al., 2000), which lack the bacterial homolog of Coq8p.

Nucleotide binding alters the structure of ADCK3

To further test the three models for ADCK3 function (Figure 4), we crystallized an ADCK3$^{N\Delta254}$ mutant (R611K) in the presence of the non-hydrolyzable ATP-analog adenosine 5'-(β,γ-imido)triphosphate (AMPPNP) and solved an X-ray structure of the ADCK3-nucleotide co-crystal at a resolution of 2.1 Å. We used the R611K variant because we were unable to obtain ADCK3-nucleotide co-crystals with the wild type enzyme. The R611K mutation was designed to modify slightly the F-helix of the protein, based on our previous work (Stefely et al., 2015).

The overall structure of nucleotide-bound ADCK3 is largely similar to that of the apo enzyme, but some important conformational changes exist (Figure 7A). Comparing the active site residues of apo ADCK3 (Figure 7B) to those of nucleotide-bound ADCK3 (Figure 7C) reveals a moderate outward expansion to accommodate the nucleotide (Figure 7D). As predicted by our *in vitro* ligand binding results, the A-rich loop makes a direct contact with the nucleotide through a hydrogen bond involving S340 of the AAAS motif (Figure 7C). The A339G mutation likely changes the conformation of the A-rich loop to flip nucleotide selectivity, but the specifics of this difference await discovery of an ADCK3-ADP co-crystal structure. Importantly, the location of the KxGQ motif in the active site remains largely unchanged. The KxGQ motif is still positioned to occlude the typical peptide substrate binding pocket (Figure 7C).

Given the maintenance of structural features positioned to inhibit protein kinase activity, we looked for features concordant with the alternative ADCK3 models (Figure 4). Nucleotide binding significantly alters the QKE triad. A tight salt bridge between E405 of the KxGQ insert and K276 of the KxGQ extension in the apo structure (Figure 7E) is weakened in favor of a new salt bridge between K276 and Q279 (Figure 7F). While this change in the active site may appear subtle, it translates into a large 10 Å displacement of the loop between GQα5 and GQα6, which

we have named the ‘Q switch’. This 10 Å distance deviation is comparable with the GTP-GDP differences observed in the switch II region of the GTPase H-ras (Milburn et al., 1990). Conformational changes of GTPases and ATPases often alter protein-protein interactions, and the nucleotide-dependent changes in the conformation of ADCK3 appear large enough to have such an effect. Another important change impacts the putative substrate binding site. While the conformational changes of the KxGQ domain as a whole are likely too small to allow a peptide substrate to enter the active site, the moderate opening of the active site could enhance binding of a small-molecule substrate, as we previously predicted with computational modeling (Stefely et al., 2015). These structural observations alone cannot distinguish the ATPase and small molecule kinase models. However, they provide further evidence for one of these two alternative models over the protein kinase model.

Conclusion

Our results demonstrate that ADCK3 and Coq8p selectively function in CoQ biosynthesis by maintaining the stability of CoQ biosynthesis complex proteins *in vivo*. Structural features and the lack of protein kinase activity *in trans* argue against the protein kinase model for ADCK3 function. The discordance between KxGQ mutations enhancing *cis* autophosphorylation *in vitro* but inhibiting function *in vivo* also argues against the protein kinase model. The concordantly deleterious impact of KxGQ mutations on ATPase activity and CoQ production *in vivo* argues that the ATPase activity is more closely related to the endogenous activity of ADCK3 and Coq8p. ATPase activity can also be thought of as small molecule kinase activity, with water as the substrate. Work to determine whether water or another small molecule is the *bona fide* endogenous substrate of ADCK3 is ongoing. Collectively, this work provides evidence against

the previously assumed model that UbiB family proteins are protein kinases and supports an alternative model in which UbiB family proteins catalyze phosphorylation of a small molecule. More broadly, this work provides further evidence that PKLs can function through unorthodox mechanisms distinct from protein kinase activity.

Experimental Procedures

Mouse Tissue Homogenization for Proteomics and Lipidomics

The follow procedures for homogenization of mouse tissues were performed at 4 °C (in a cold room) as quickly as possible. Less than 5 minutes of time elapsed between removing the tissues from storage at -80 °C and freezing the homogenates in liquid nitrogen.

Cerebellum. A mouse cerebellum was removed from storage at -80 °C and halved by a single cut following the median plane (through the cerebellar vermis). The left cerebellar hemisphere and left half of the cerebellar vermis were homogenized in Proteomics Lysis Buffer [urea (8 M), tris, pH 8 (40 mM), NaCl (30 mM), $CaCl_2$ (1 mM), phosphatase inhibitors (PhosSTOP, Roche), protease inhibitors (cOmplete, Mini, Roche)] in a Tenbroeck glass homogenizer (pre-cooled on ice) (15 manual strokes). The homogenate was immediately transferred to a plastic microcentrifuge tube (pre-cooled on ice), flash frozen in liquid nitrogen, and stored at -80 °C. The right cerebellar hemisphere and right half of the cerebellar vermis were homogenized in Lipidomics Homogenization Buffer [phosphate (11.8 mM), NaCl (137 mM), KCl (2.7 mM), pH 7.2, phosphatase inhibitors (PhosSTOP, Roche), protease inhibitors (cOmplete, Mini, Roche)] in a Dounce homogenizer (pre-cooled on ice) (20 strokes with a loose-fitting pestle and 20 strokes with a tight-fitting pestle). The homogenate was immediately

aliquotted into plastic microcentrifuge tubes (pre-cooled on ice), flash frozen in liquid nitrogen, and stored at -80 °C.

Quadriceps. A mouse quadriceps was removed from storage at -80 °C and cut into three pieces (~40 mg each). One piece of the tissue was homogenized in Proteomics Lysis Buffer (1 mL) in a Potter-Elvehjem homogenizer (pre-cooled on ice) (20 strokes, 700 rpm). The homogenate was immediately transferred to a plastic microcentrifuge tube (pre-cooled on ice), flash frozen in liquid nitrogen, and stored at -80 °C. A second piece of the tissue was homogenized in Lipidomics Homogenization Buffer (1 mL) in a Potter-Elvehjem homogenizer (pre-cooled on ice) (20 strokes, 700 rpm). The homogenate was immediately aliquotted into plastic microcentrifuge tubes (pre-cooled on ice), flash frozen in liquid nitrogen, and stored at -80 °C.

Heart. A mouse heart was removed from storage at -80 °C and cut into two pieces. One piece of the tissue was homogenized in Proteomics Lysis Buffer (1 mL) in a Potter-Elvehjem homogenizer (pre-cooled on ice) (12 strokes, 1000 rpm). The homogenate was immediately transferred to a plastic microcentrifuge tube (pre-cooled on ice), flash frozen in liquid nitrogen, and stored at -80 °C. A second piece of the tissue was homogenized in Lipidomics Homogenization Buffer (1 mL) in a Potter-Elvehjem homogenizer (pre-cooled on ice) (12 strokes, 1000 rpm). The homogenate was immediately aliquotted into plastic microcentrifuge tubes (pre-cooled on ice), flash frozen in liquid nitrogen, and stored at -80 °C.

Kidney. A mouse kidney was removed from storage at -80 °C and cut into two pieces. One piece of the tissue was homogenized in Proteomics Lysis Buffer (1 mL) in a Potter-Elvehjem homogenizer (pre-cooled on ice) (12 strokes, 1000 rpm). The homogenate was immediately transferred to a plastic microcentrifuge tube (pre-cooled on ice), flash frozen in

liquid nitrogen, and stored at -80 °C. A second piece of the tissue was homogenized in Lipidomics Homogenization Buffer (1 mL) in a Potter-Elvehjem homogenizer (pre-cooled on ice) (12 strokes, 1000 rpm). The homogenate was immediately aliquotted into plastic microcentrifuge tubes (pre-cooled on ice), flash frozen in liquid nitrogen, and stored at -80 °C.

Mouse Proteomics and Phosphoproteomics

Sample preparation. Homogenate was thawed at 4 °C and lysed on ice using probe sonication. Protein content was evaluated using a BCA assay (Thermo Fisher Scientific, San Jose, CA). Proteins were reduced with 5 mM dithiothreitol (58 °C, 30 min) and alkylated with 15 mM iodoacetamide (incubation in the dark at ambient temperature, 30 min). Alkylation was quenched by adding additional 5 mM dithiothreitol (ambient temperature, 15 minutes). Proteins were enzymatically digested in a two-step process. First, proteinase LysC (Wako Chemicals, Richmond, VA) was added to each sample at a ratio of 1:100 (enzyme:protein) and the resulting mixtures were incubated (37 ºC, 3 h). Next, samples were diluted to a final concentration of 1.5 M urea (pH 8) with a solution of 50 mM Tris and 5 mM $CaCl_2$. Sequencing-grade trypsin (Promega, Madison, WI) was added to each sample at a ratio of 1:50 (enzyme:protein) and the resulting mixtures were incubated at ambient temperature overnight. The following morning each sample was incubated with an additional aliquot of sequencing-grade trypsin at ratio of 1:100 (enzyme:protein) for approximately 1.5 hours. Digests were quenched by bringing the pH ~2 with trifluoroacetic acid and immediately desalted using C18 solid-phase extraction columns (SepPak, Waters, Milford, MA).

Desalted material was labeled with TMT 8-plex isobaric labels (Thermo-Pierce, Rockford, IL). Prior to quenching the TMT reactions, ~5 μg of material from each TMT channel

was combined into a test mix and analyzed by LC-MS/MS to evaluate labeling efficiency and obtain optimal ratios for sample recombination. Following quenching, tagged peptides were combined in equal amounts by mass (~1000 μg per channel for phosphorylation analyses, ~500 μg per channel for protein analyses) and desalted. All experiments had ≥ 98% labeling efficiency, calculated by the number N-terminal labeled peptides divided by the total number of peptide identifications.

Sample fractionation. Labeled peptides were fractionated by strong cation exchange (SCX) using a polysulfoethylaspartamide column (9.4×200 mm; PolyLC) on a Surveyor LC quaternary pump (Thermo Scientific). Each dried and mixed TMT sample was re-suspended in buffer A, injected onto the column, and subjected to the following gradient for separation: 100% buffer A from 0–2 min, 0–15% buffer from 2–5 min, and 15–100% buffer B from 5–35 min. Buffer B was held at 100% for 10 minutes and then the column was washed extensively with buffer C and water prior to recalibration. Flow rate was held at 3.0 mL/min throughout the separation. Buffer compositions were as follows: buffer A [5 mM KH_2PO_4, 30% acetonitrile (pH 2.65)], buffer B [5 mM KH_2PO_4, 350 mM KCl, 30% acetonitrile (pH 2.65)] buffer C [50 mM KH_2PO_4, 500 mM KCl (pH 7.5)]. Twelve fractions were collected over the first 50 minute elution period and were immediately frozen, lyophilized, and desalted. A small portion of each, 5%, was extracted and used for protein analysis. The remaining material was retained for phosphopeptide enrichment.

Phosphopeptide Enrichment. Phosphopeptides were enriched using immobilized metal affinity chromatography (IMAC) with magnetic beads (Qiagen, Valencia, CA). Following equilibration with water, the magnetic beads were incubated with 40 mM EDTA (pH 8.0) for 1 hour, with shaking. Next, the beads were washed four times with water and incubated with 30

mM $FeCl_3$ for 1 hour, with shaking. Beads were then washed four times with 80% acetonitrile/0.15% TFA. Each of the 12 fractions were re-suspended in 80% acetonitrile/0.15% TFA and incubated with the magnetic beads for 45 minutes, with shaking. Following this incubation, all unbound peptides were collected for subsequent acetyl lysine enrichment. Bound peptides were washed three times with 80% acetonitrile/0.15% TFA and eluted with 50% acetonitrile, 0.7% NH_4OH. Eluted peptides were immediately acidified with 4% FA, frozen, and lyophilized. Each phospho peptide fraction was re-suspended in 20 µL 0.2% FA for LC-MS/MS analysis.

LC-MS/MS analysis. All experiments were performed using a NanoAcquity UPLC system (Waters, Milford, MA) coupled to an Orbitrap Elite mass spectrometer (Thermo Fisher Scientific, San Jose, CA). Reverse-phase columns were made in-house by packing a fused silica capillary (75 µm i.d., 360 µm o.d, with a laser-pulled electrospray tip) with 1.7 µm diameter, 130 Å pore size Bridged Ethylene Hybrid C18 particles (Waters) to a final length of 30 cm. The column was heated to 60 °C for all experiments. Samples were loaded onto the column for 12 minutes in 95:5 buffer A [water, 0.2% formic acid, and 5% DMSO]:buffer B [acetonitrile, 0.2% formic acid, and 5% DMSO] at a flow-rate of 0.30 µL/min. Peptides were eluted using the following gradient: an increase to 7% B over 1 min, followed by a 42 min linear gradient from 7% to 18% B, followed by a 28 min linear gradient from 18% to 27% B, followed by a final 1 min ramp to 75% B which was held for 3 minutes. The column was equilibrated with 5% buffer B for an additional 25 min. Precursor peptide cations were generated from the eluent through the utilization of a nanoESI source.

Mass spectrometry instrument methods consisted of MS^1 survey scans (1e6 target value; 60,000 resolution; 300 Th – 1500 Th) that were used to guide fifteen subsequent data-dependent

MS/MS scans (3Th isolation window, HCD fragmentation, normalized collision energy of 35; 5e4 target value, 30,000 resolution). Dynamic exclusion duration was set to 30 s, with a maximum exclusion list of 500 and an exclusion width of 0.55 Th below and 2.55 Th above the selected average mass. Maximum injection times were set to 50 ms for all MS^1 scans, 150 ms for MS/MS scans in whole protein analyses, and 200 ms for MS/MS scans in phospho enrichment analyses.

Data Analysis. Data was processed using the in-house software suite COMPASS (Wenger et al., 2011). OMSSA (Geer et al., 2004) (version 2.1.8) searches were performed against a target-decoy database (*Uniprot (mouse),* www.uniprot.org, August 7th, 2013). Searches were conducted using a 150 ppm precursor mass tolerance and a 0.015 Da product mass tolerance. A maximum of 3 missed tryptic cleavages were allowed. The fixed modifications specified were carbamidomethylation of cysteine residues, TMT 8-plex on peptide N-termini, and TMT 8-plex on lysine residues. The variable modifications specified were oxidation of methionine and TMT 8-plex on tyrosine residues. Additional variable modifications were specified for phospho-peptide analyses (phosphorylation of threonine, serine, and tyrosine residues). TMT quantification of identified peptides was performed within COMPASS as described previously (Phanstiel et al., 2011). Peptides identified within each of 12 fractions were grouped into proteins according to previously reported rules (Nesvizhskii and Aebersold, 2005) using COMPASS. Phosphopeptide localization was performed using *Phosphinator* software within COMPASS, as described previously (Phanstiel et al., 2011). This program both localized phosphorylation sites and combined quantitative data for phospho-isoforms across all 12 fractions. All phosphosites had to be localized for a given phospho-peptide to be included in subsequent quantitative analysis. Protein quantification was performed by summing all of the

reporter ion intensities within each channel for all peptides uniquely mapping back to a given protein. All quantitative data was normalized at the protein level, $\log_2$ transformed and mean normalized. Fold-changes were then calculated by averaging protein-normalized values for each condition and calculating the difference of averages. For each comparison, a *p*-value was calculated using Student's t-test (assuming equal variance) and then correcting for multiple hypotheses (Storey method).

Yeast Cultures

Saccharomyces cerevisae wild type strain DS10 was obtained from the laboratory of Elizabeth A. Craig ("WT JH27a DS10", *his3-11,15 leu2-3,112 lys1 lys2 Δtrp1 ura3-52*). Δ*coq8* DS10 yeast were created by replacing the *coq8* gene with a *ura3* selectable marker using standard methods for PCR amplification and homologous recombination (Baudin et al., 1993). The insertion of the *ura3* marker at the *coq8* locus was confirmed by a PCR assay and DNA sequencing.

Single colonies of yeast were used to inoculate starter cultures in YPD media (4 mL), which were incubated (30 °C, 230 rpm, 12 h). Synthetic complete media (500 mL) with glucose (10 g/L) was inoculated with $5x10^6$ yeast cells from a starter culture and incubated (30 °C, 230 rpm). Yeast cell pellets were isolated at three time points during the culture (as shown in Figure 2A) by centrifugation (1,000 *g*, 3 min, 4 °C) and frozen in $N_{2(l)}$. Cell culture density was determined by measuring the optical density at 600 nm (OD_{600}) and converting this value to [cells], as described previously (Hebert et al., 2013). Media glucose concentration was determined with a Glucose (HK) Assay Kit (Sigma), as described previously (Hebert et al., 2013).

Yeast Proteomics and Phosphoproteomics

Yeast proteomics and phosphoproteomics were conducted essentially as described above for the mouse proteomics and phosphoproteomics except 6-plex TMT was used instead of 8-plex TMT. Three sets of 6-plex TMT runs were conducted, each with a biological replicate of the 6 conditions (each 6-plex TMT set contained samples from WT and Δ*coq8* yeast across the three time points).

Cloning of Coq8p, ADCK3, and PKA constructs

Cloning of ADCK3$^{N\Delta250}$ into pVP68K has been described previously (Stefely et al., 2015). Here, to generate ADCK3$^{N\Delta250}$-Flag-3xHA with PIPE cloning methods (Klock et al., 2008), separate ADCK3$^{N\Delta250}$ and Flag-3xHA amplicons were generated and combined prior to transformation. The 3xHA was amplified from plasmid pJR13019 (Chen et al., 2012), obtained from the laboratory of Jared Rutter. pET15b PKA Cat (Narayana et al., 1997) was obtained as a gift from Susan Taylor (Addgene plasmid #14921), and PKA was sub-cloned into the vector pVP68K (Blommel et al., 2009). Coq8 was also cloned into pVP68K and the N-terminal 41 amino acid residues were removed by standard PIPE cloning methods. PIPE reactions were DpnI digested and transformed into DH5alpha competent *E. coli* cells. Plasmids were isolated from transformants and DNA sequencing was used to identify those containing the correct constructs. Constructs were then transformed into RIPL competent *E. coli* cells for protein expression.

Helical Wheel Projections

The helical wheel projections of Coq8p and ADCK3 were generated using a web-based program developed by Don Armstrong and Raphael Zidovetski (UC-Riverside).

Expression and purification of Coq8$^{N\Delta41}$ for in vitro assays

8His-MBP-[TEV]-Coq8$^{N\Delta41}$ was overexpressed in *E. coli* by autoinduction (Fox and Blommel, 2009). Cells were isolated by centrifugation, frozen in $N_{2(l)}$, and stored at –80 °C until further use. For protein purification, cells were thawed on ice, resuspended in Lysis Buffer (50 mM HEPES (pH 7.5), 150 mM NaCl, 5% glycerol, 1 mM BME, 0.25 mM PMSF, 1 mg/mL lysozyme, pH 7.5) and incubated (1 h, 4 °C). The cells were lysed by sonication (4 °C, 6 V, 60 s x 4). The lysate was clarified by centrifugation (15,000 *g*, 30 min, 4 °C). The cleared lysate was mixed with cobalt IMAC resin (Talon resin) and incubated (4 °C, 1 h). The resin was pelleted by centrifugation (700 *g*, 5 min, 4 °C) and washed four times with Wash Buffer (50 mM HEPES (pH 7.5), 150 mM NaCl, 5% glycerol, 1 mM BME, 0.25 mM PMSF, 10 mM imidazole, pH 7.5) (10 resin bed volumes). His-tagged protein was eluted with Elution Buffer (50 mM HEPES (pH 7.5), 150 mM NaCl, 5% glycerol, 1 mM BME, 100 mM imidazole, pH 7.5). The eluted protein was concentrated with a MW-cutoff spin filter (50 kDa MWCO) and exchanged into storage buffer (50 mM HEPES (pH 7.5), 150 mM NaCl, 5% glycerol, 1 mM BME, pH 7.5). The concentration of 8His-MBP-[TEV]-Coq8$^{N\Delta41}$ was determined by its absorbance at 280 nm (ε = 109,210 $M^{-1}cm^{-1}$) (MW = 96.2 kDa). The fusion protein was incubated with Δ238TEV protease (ref) (1:50, TEV/fusion protein, mass/mass) (1 h, 20 °C). The TEV protease reaction mixture was mixed with cobalt IMAC resin (Talon resin) and incubated (4 °C, 1 h). The unbound Coq8$^{N\Delta41}$ was isolated and concentrated with a MW-cutoff spin filter (30 kDa MWCO) and exchanged into storage buffer. The concentration of Coq8$^{N\Delta41}$ was determined by its absorbance at 280 nm (ε = 41,370 $M^{-1}cm^{-1}$) (MW = 52 kDa). The protein was aliquoted, frozen in $N_{2(l)}$, and stored at –80 °C. Fractions from the protein preparation were analyzed by SDS-PAGE.

Expression and purification of PKA for in vitro assays

8-His-MBP-PKA and PKA (mouse PKA, Prkaca) were isolated as described above for $Coq8^{N\Delta41}$. The concentration of 8His-MBP-[TEV]-PKA was determined by its absorbance at 280 nm (ε = 121,700 $M^{-1}cm^{-1}$) (MW = 84.8 kDa). The concentration of PKA was determined by its absorbance at 280 nm (ε = 53,860 $M^{-1}cm^{-1}$) (MW = 40.5 kDa).

Differential Scanning Fluorimetry (DSF)

The general DSF method has been described previously (Niesen et al., 2007). Mixtures (20 µL total volume) of $Coq8^{N\Delta41}$ (2 µM) or PKA (1 µM) were prepared with SYPRO Orange dye (Life Tech.) (2X), NaCl (150 mM), HEPES (100 mM, pH 7.5), and ligands (e.g. MgATP). Otherwise, the general DSF method, ligand screen, and dissociation constant experiments were conducted as described for $ADCK3^{N\Delta250}$ (Stefely et al., 2015).

***In vitro* Kinase Autophosphorylation Assays**

Unless otherwise indicated, $Coq8^{N\Delta41}$ (4 µM), MBP-$Coq8^{N\Delta41}$ (4 µM), or PKA (4 µM) was mixed with [γ-^{32}P]ATP (0.25 µCi/µL, 100 µM $[ATP]_{total}$) and $MgCl_2$ (20 mM) in an aqueous buffer (100 mM HEPES, 150 mM NaCl, 0.1 mg/mL BSA, 0.5 mM DTT, pH 7.5) and incubated (30 °C, 60 min, 500 rpm) (final concentrations for reaction components). For the divalent cation screen, $MgCl_2$ and $CaCl_2$ were used at 20 mM. Reactions were quenched with 4xLDS buffer (106 mM TrisHCl, 141 mM Tris base, 2% LDS, 10% glycerol, 0.51 mM EDTA, 0.175 mM Phenol Red, 0.22 mM Coomassie Brilliant Blue G-250, pH 8.5). [γ-^{32}P]ATP was separated from $Coq8^{N\Delta41}$ by SDS-PAGE (10% Bis-Tris gel, MES buffer, 150 V, 1.5 h). The gel was stained with Coomassie Brilliant Blue, dried under vacuum, and imaged by digital photography. A storage phosphor

screen was exposed to the gel (~5 days) and then imaged with a Typhoon (GE) to generate the phosphorimages.

ADCK3$^{N\Delta250}$ autophosphorylation assays were conducted as described previously (Stefely et al., 2015).

Analysis of Coq8p Autophosphorylation by Phosphoproteomic Mass Spectrometry

Coq8$^{N\Delta41}$ (WT, A197G, D365N, or A197G,K134H) (20 μM) was mixed with nucleotide (ATP, ADP, or none) (1 mM) in an aqueous buffer (100 mM HEPES, 150 mM NaCl, 20 mM $MgCl_2$, 0.1 mg/mL BSA, 0.5 mM DTT, pH 7.5) and incubated (30 °C, 60 min, 500 rpm). All 12 reactions were conducted in parallel. Reactions were flash frozen in $N_{2(l)}$ after completion.

A sample of each autophosphorylation reaction (100 μL) was mixed with lysis buffer (300 μL) (8 M urea, 40 mM Tris (pH = 8.0), 30 mM NaCl, 2 mM $MgCl_2$, 1 mM $CaCl_2$, 1 x phosphatase inhibitor cocktail tablet, and 1 x protease inhibitor tablet). Dithiothreitol (DTT) was added (to 2 mM) and incubated (37 °C, 30 min) to reduce disulfide bonds. Alkylation of cysteines was achieved by adding iodoacetimide (to 7 mM) and incubating in the dark (room temp., 30 min). The alkylation reaction was quenched by adding DTT (to 7 mM) and incubating (room temp., 15 min). Protein was digested with lys-C (37 °C, 4 hours) (1:100, enzymse:protein mass ratio). The sample was diluted to 1.5 M urea with 50 mM Tris (pH = 8.0) and 1 mM $CaCl_2$ solution. Trypsin (1:100, enzyme:protein) was added to further digest the proteins. After overnight incubation at 37 °C, another aliquot of trypsin (1:100, enzyme:protein mass ratio) was added and incubated (1 hour). The digestion was quenched by adding 10% trifluoroacetic acid to bring the pH below 2. The peptides were desalted with Sep-Pak Vac 1cc tC18 cartridges (Waters). Immobilized metal affinity chromatography (IMAC) with magnetic agarose beads

(Qiagen) was used to enrich for phosphopeptides (Phanstiel et al., 2011). Both non-phospho and phospho fractions were analyzed by reverse phase nano LC coupled to an Orbitrap Elite (Thermo). All MS raw data were analyzed with COMPASS (Wenger et al., 2011). A precursor mass tolerance of 150 ppm and a product ion mass tolerance of 0.01 Da, and up to 3 missed cleavages with trypsin were applied to searching. Carbamidomethylation of cysteines was set as fixed modification, while oxidation of methionines, phosphorylation with neutral loss on serine and threonine residues, and intact phosphorylation on tyrosine residues were set as variable modifications. Peptides were grouped into parsimonious protein groups by Protein Hoarder at 1% FDR at the unique protein group level.

***In vitro* Protein Kinase Assays**

PKA (4 μM) or $Coq8^{N\Delta41}$ (4 μM) and protein substrates (myelin basic protein (Millipore 13-104, 6 μM), none, or a mixture of COQ proteins) were mixed with [γ-^{32}P]ATP (0.3 μCi/μL, 100 μM $[ATP]_{total}$) in an aqueous buffer (100 mM HEPES, 150 mM NaCl, 20 mM $MgCl_2$, 0.1 mg/mL BSA, 0.5 mM DTT, pH 7.5) and incubated (30 °C, 40 min, 500 rpm) (final concentrations for reaction components). The mixture of COQ proteins (COQ3–COQ7 and COQ9) was prepared using a cell-free expression system as described (Floyd et al., 2015, manuscript submitted). Reactions were quenched with 4xLDS buffer (106 mM TrisHCl, 141 mM Tris base, 2% LDS, 10% glycerol, 0.51 mM EDTA, 0.175 mM Phenol Red, 0.22 mM Coomassie Brilliant Blue G-250, pH 8.5). [γ-^{32}P]ATP was separated from phosphorylated proteins by SDS-PAGE (10% Bis-Tris gel, MES buffer, 150 V, 1.5 h). The gel was stained with Coomassie Brilliant Blue, dried under vacuum, and imaged by digital photography. A storage phosphor screen was exposed to the gel (~5 days) and then imaged with a Typhoon (GE) to generate the phosphorimages.

ATPase Assays

$Coq8^{N\Delta41}$ (10 μM) or PKA (10 μM) was mixed with nucleotide (ATP, ADP, or AMP) (10 μM or 500 μM) in an aqueous buffer (100 mM HEPES, 150 mM NaCl, 10 mM $MgCl_2$, 0.1 mg/mL BSA, 0.5 mM DTT, pH 7.5) and incubated (22 °C, 10 min). The reactions were quenched by addition of a malachite green-based phosphate detection reagent (Cytoskeleton). Absorbance at 650 nm was quantified. A standard curve of inorganic phosphate was used to determine the amount of phosphate produced in each reaction.

ADP Detection Enzyme Assays

$ADCK3^{N\Delta250}$ (4 μM) was mixed with potential small molecule substrates (1 mM, see Figure 6A for molecules tested) and ATP (100 μM) in an aqueous buffer (100 mM HEPES, 150 mM NaCl, 20 mM $MgCl_2$, 0.1 mg/mL BSA, 0.5 mM DTT, pH 7.5) and incubated (37 °C, 30 min). Relative amounts of ADP produced in the reactions were determined with a luminescence-based commercially available assay (ADPglo, Promega).

In Vitro Lipid Kinase Assays

$ADCK3^{N\Delta250}$ (4 μM), PKA (Promega, 0.2 U/μL), or DAGK (Sigma D3065, 1:1000 dilution of undefined stock) was mixed with *ΔubiE* or *ΔubiF* extract micelles (lipids extracted from *E. coli* with hexanes/IPA (10:1, v/v) and reconstituted in 10 mM Triton X-100) and [γ-^{32}P]ATP (0.3 μCi/μL, 100 μM $[ATP]_{total}$) in an aqueous buffer (100 mM HEPES, 150 mM NaCl, 20 mM $MgCl_2$, 0.1 mg/mL BSA, 0.5 mM DTT, pH 7.5) and incubated (37 °C, 30 min, 500 rpm) (final concentrations for reaction components, reaction volume of 20 μL). The reactions were quenched with $CHCl_3$/MeOH (1:1, v/v, 200 μL) and acetic acid (1 M, 50 μL). The samples were

mixed by vortexing, centrifuged, and the lower organic phase was isolated. Lipids in the extracts were separated by thin layer chromatography (TLC, SiO_2, $CHCl_3$/MeOH/30% NH_4OH/H_2O, 50:40:8:2, v/v/v/v) and dried. A storage phosphor screen was exposed to the TLC plate (~5 days) and then imaged with a Typhoon (GE) to generate the phosphorimages.

Liposome-Protein Co-Floatation Assays

E. coli ΔubiE were cultured in Terrific Broth (24 h, 37 °C, 230 rpm) and isolated by centrifugation. Lipids were extracted from a portion of *E. coli* pellet (~1.2 g wet weight) with $CHCl_3$/MeOH (1:1, v/v), reduced with excess $NaBH_4$, quenched with AcOH, and re-extracted with $CHCl_3$/MeOH (1:1, v/v). The lipids were dried under $Ar_{(g)}$ to afford 12 mg of dry lipid mass. The lipids were reconstituted in $CHCl_3$/MeOH (1:1, v/v, 1 mL) and stored under $Ar_{(g)}$.

To form the *ΔubiE* extract liposomes, 2.2 mg of *ΔubiE* lipids were mixed with NBD-PC (17.4 μL, 1 mM), dried under $Ar_{(g)}$, and reconstituted in an aqueous buffer (20 mM Tris, 150 mM NaCl, 1 mM DTT). Liposomes were formed by sonication (22 °C, 30 min, bath sonicator).

$Coq8^{N\Delta41}$ (1 μM), $ADCK3^{N\Delta250}$ (1 μM), or $COQ9^{N\Delta79}$ (1 μM) (10 μL protein mixture) was mixed with MgATP (5 mM $MgCl_2$, 1 mM ATP) (5 μL nucleotide mixture) and liposomes (135 μL) and incubated (30 °C, 20 min, 230 rpm). After incubation, the reactions were moved onto ice and mixed with 75% (w/v) sucrose buffer (100 μL) (all sucrose buffers in 20 mM Tris, 150 mM NaCl, 1 mM DTT). Overlaid 25% sucrose (200 μL) and 0% sucrose (50 μL) in a micro ultracentrifuge tube. Centrifuged (240,000 *g*, 4 °C, 1 h), and subsequently isolated 150 μL from the top of the gradient and 150 μL from the bottom of the gradient. Both the top and the bottom fractions were analyzed by SDS-PAGE with sliver staining. Flotation of the liposomes was assessed by tracking the fluorescence of NBD-PC.

In Silico Bacterial Operon Analysis

The DOOR 2.0 database (Mao et al., 2014) was searched for operons containing homologs of the *E. coli ubiB* gene. UbiB-containing operons from numerous pathogenic microbes were extracted. Unannotated genes were examined by BLAST sequence analysis to identify homologs in *E. coli*, and genes with clear homolog to *E. coli ubiE* or *ubiJ* are annotated as such in the figure.

Co-Purification and LC-MS/MS analysis of Coq8p Ligands from *E. coli*

E. coli ΔubiE and *ΔubiF* were cultured in Terrific Broth (24 h, 37 °C, 230 rpm) and isolated by centrifugation. An *E. coli* lysate with overexpressed His_8-MBP-$Coq8^{N\Delta41}$ was mixed with *ΔubiE* lysate and *ΔubiF* lysate (1 h, 4 °C). Subsequently, His_8-MBP-$Coq8^{N\Delta41}$ and co-purifying ligands were isolated by cobalt IMAC as described above for protein purification of His_8-MBP-$Coq8^{N\Delta41}$. The elution from the first IMAC was isolated directly without further concentration and snap frozen in $N_{2(l)}$.

A sample of His_8-MBP-tagged protein (40 nmol, 310 µL, 129 µM) in "Elution Buffer" (50 mM HEPES, 150 mM NaCl, 5% glycerol, 1 mM BME, 100 mM imidazole, pH 7.5) was mixed with CoQ_6 (internal standard, 0.1 nmol, 10 µL, 10 µM) by vortexing (30 s, 4 °C). $CHCl_3$/MeOH (1:1, v/v) (5 mL) was added and vortexed (2 x 30 s). HCl (1 M, 400 µL) was added and vortexed (30 s). $NaCl_{(aq)}$ (saturated, 1 mL) was added and vortexed (30 s). The samples were centrifuged (1,800 *g*, 4 min, 4 °C) to complete phase separation. The lower organic phase was transferred to a clean tube and dried under $Ar_{(g)}$. The organic residue was reconstituted in ACN/IPA/H_2O (65:30:5, v/v/v) (200 µL) by vortexing (60 s) and transferred to a glass autosampler vial.

Lipids from 10 µL of extract were separated by LC on an Ascentis Express C18 column (150 mm x 2.1 mm x 2.7 µm particle size, Supelco, Bellefonte, PA) using an Accela HPLC pump (Thermo Scientific, San Jose, CA) at a flow-rate of 0.4 mL/min. Mobile phase A was 70/30 acetonitrile/water containing 10 mM ammonium acetate and 0.025 % acetic acid and B was 90/10 isopropanol/acetonitrile containing the same additives. At the beginning of the gradient, the flow was maintained at 20% B for 1 min, then ramped to 30% at 4 min, to 50% at 5 min, to 85% at 20 min, to 99% at 21 min, held there until 25 min, returned to 20% B at 25.5 min, and finally the column was re-equilibrated to 30 min before beginning the next injection sequence. The auto sampler (HTC PAL, Thermo Scientific) vigorously mixed each sample before injection to ensure homogeneity.

The MS conditions were as follows: a Q Exactive mass spectrometer (Thermo Scientific, Build 2.5) was operated in fast polarity switching mode, acquiring both positive and negative mode MS and MS/MS spectra. The mass ranges were 300–1600 Th in positive mode and 200–1600 Th in negative ion mode. Tandem MS acquisition was data dependent, fragmenting the two most abundant precursors from each MS scan with a 10 s exclusion duration. The MS was equipped with a HESI II spray source kept at 350 °C and ± 4 kV. The inlet capillary was kept at 350 °C and sheath and auxiliary gases were set to 35 and 15 units. Resolving power was 17,500 for all scans, AGC target was $1x10^6$ for MS scans and $1x10^5$ for MS/MS scans, the isolation width was 1 Th for MS/MS scans, normalized collision energy was stepped at 20, 30, and 40 units, and maximum injection time was set to 100 ms for MS scans and 50 ms for MS/MS scans. Quantitation was performed by integrating MS^1 elution profiles of lipids using the Xcalibur software suite (Thermo Scientific, Version 3.0).

Acknowledgments

We thank Bob Smith for crystallomics assistance, and Craig Ogata, Ruslan Sanishvili, Joe Brunzelle and Elena Kondrashkina for beamline support. This work was supported by a Searle Scholars Award, a Shaw Scientist Award and by NIH grants U01GM94622, R01DK098672 and R01GM112057 (to D.J.P.), NIH Ruth L. Kirschstein National Research Service Award F30AG043282 (to J.A.S.), and NIH Chemistry-Biology Interface Training Grant T32GM008505 (to A.G.R.). Use of the Advanced Photon Source was supported by the U.S. DOE (DE-AC02-06CH11357). LS-CAT was supported by the Michigan Economic Development Corporation (085P1000817). GM/CA @ APS has received funds from the NIH NCI (Y1-CO-1020) and NIGMS (Y1-GM-1104).

Figures

Figure 1.

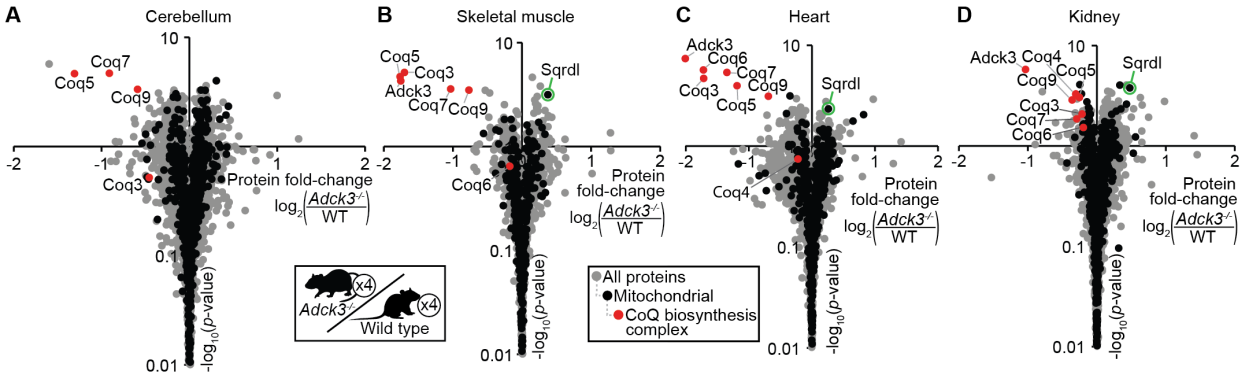

Figure 1. Adck3 is Required for the Stability of the Coenzyme Q Biosynthesis Complex in Mice

(**A**) Fold changes in cerebellum protein abundances (mean $\log_2(Adck3^{-/-}/\text{WT})$, n = 4) versus statistical significance ($-\log_{10}(p\text{-value})$) as quantified by LC-MS/MS. Mitochondrial proteins are shown in black, and all observed CoQ biosynthesis complex proteins are shown in red.

(**B**) Fold changes in skeletal muscle (quadriceps) protein abundances, otherwise as in (A).

(**C**) Fold changes in heart protein abundances, otherwise as in (A).

(**D**) Fold changes in kidney protein abundances, otherwise as in (A).

See also Figure S1.

Figure 2.

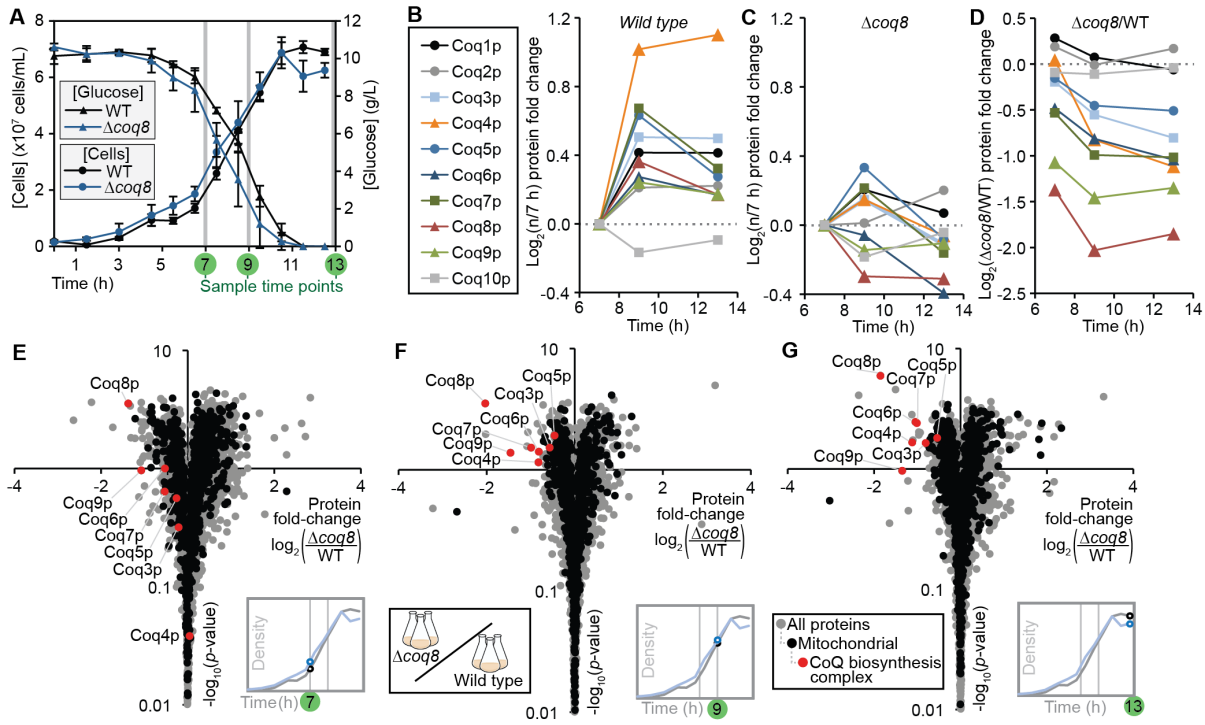

Figure 2. Coq8p is Required Specifically for the Stability of the CoQ Complex in Yeast

(**A**) Yeast culture (Δ*coq8* and WT) densities (mean ± SD, n = 3) and glucose concentrations (mean ± SD, n = 3) versus time. Samples were harvested for proteomics analysis at the indicated time points (7 h, 9 h, and 13 h).

(**B**) Fold changes in CoQ biosynthesis protein abundances in WT yeast ($\log_2$(abundance at indicated time point/abundance at 7 h time point), mean, n = 3) versus time as determined by LC-MS/MS.

(**C**) Fold changes in CoQ biosynthesis protein abundances in Δ*coq8* yeast ($\log_2$(abundance at indicated time point/abundance at 7 h time point), mean, n = 3) versus time as determined by LC-MS/MS.

(**D**) Fold changes in CoQ biosynthesis protein abundances ($\log_2$(Δ*coq8*/WT), mean, n = 3) at each of the 3 sample time points shown in (A).

(**E**) Fold changes in protein abundances (mean $\log_2$(Δ*coq8*/WT), n = 3) at the 7 h time point versus statistical significance (–$\log_{10}$(*p*-value)) as quantified by LC-MS/MS. Mitochondrial proteins are shown in black, and all observed CoQ biosynthesis complex proteins are shown in red.

(**F**) Fold changes in protein abundances at the 9 h time point, otherwise as in (E).

(**G**) Fold changes in protein abundances at the 13 h time point, otherwise as in (E).

See also Figure S2.

Figure 3.

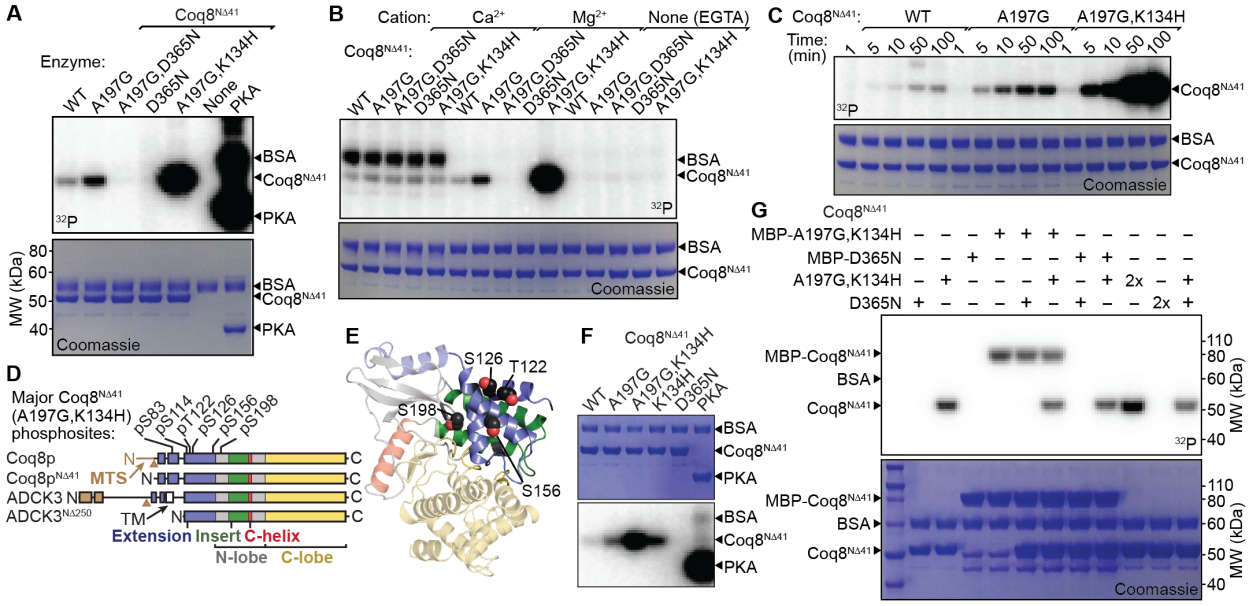

Figure 3. Coq8p Autophosphorylates Exclusively *in cis*

(**A**) SDS-PAGE analysis of *in vitro* Mg[γ-^{32}P]ATP autophosphorylation reactions with Coq8^{NΔ41} variants or protein kinase A (PKA). Bovine serum albumin (BSA) was included in the reaction buffer.

(**B**) Divalent cation dependence of Coq8^{NΔ41} autophosphorylation as determined by SDS-PAGE analysis of *in vitro* [γ-^{32}P]ATP reactions.

(**C**) Time course of Coq8^{NΔ41} autophosphorylation as determined by SDS-PAGE analysis of *in vitro* Mg[γ-^{32}P]ATP reactions.

(**D**) Coq8^{NΔ41} (A197G,K134H) autophosphorylation sites identified by LC-MS/MS.

(**E**) Coq8^{NΔ41} (A197G,K134H) autophosphorylation sites identified by LC-MS/MS mapped onto a homology model of Coq8p generated from our ADCK3 crystal structure.

(**F**) SDS-PAGE analysis of *in vitro* Mg[γ-^{32}P]ATP autophosphorylation reactions with Coq8^{NΔ41} variants.

(**G**) SDS-PAGE analysis of *in vitro* Mg[γ-^{32}P]ATP autophosphorylation reactions with the indicated combinations of Coq8$^{N\Delta41}$ variants and maltose binding protein (MBP) tagged Coq8$^{N\Delta41}$ variants.

See also Figures S3 and S4.

Figure 4.

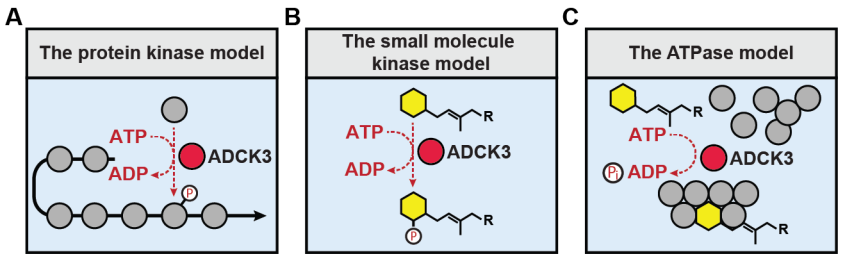

Figure 4. Models for ADCK3 and Coq8p function

(**A**) The protein kinase model, in which ADCK3 catalyzes phosphorylation of a protein that enhances CoQ biosynthesis. ADCK3 is shown as a red circle. CoQ biosynthesis proteins are shown as gray circles.

(**B**) The small molecule kinase model, in which ADCK3 catalyzes phosphorylation of a small molecule, such as an intermediate in CoQ biosynthesis or a co-factor required for CoQ biosynthesis.

(**C**) The ATPase model, in which ADCK3 catalyzes hydrolysis of ATP to ADP to enable assembly of the CoQ biosynthesis complex with its substrates.

Figure 5.

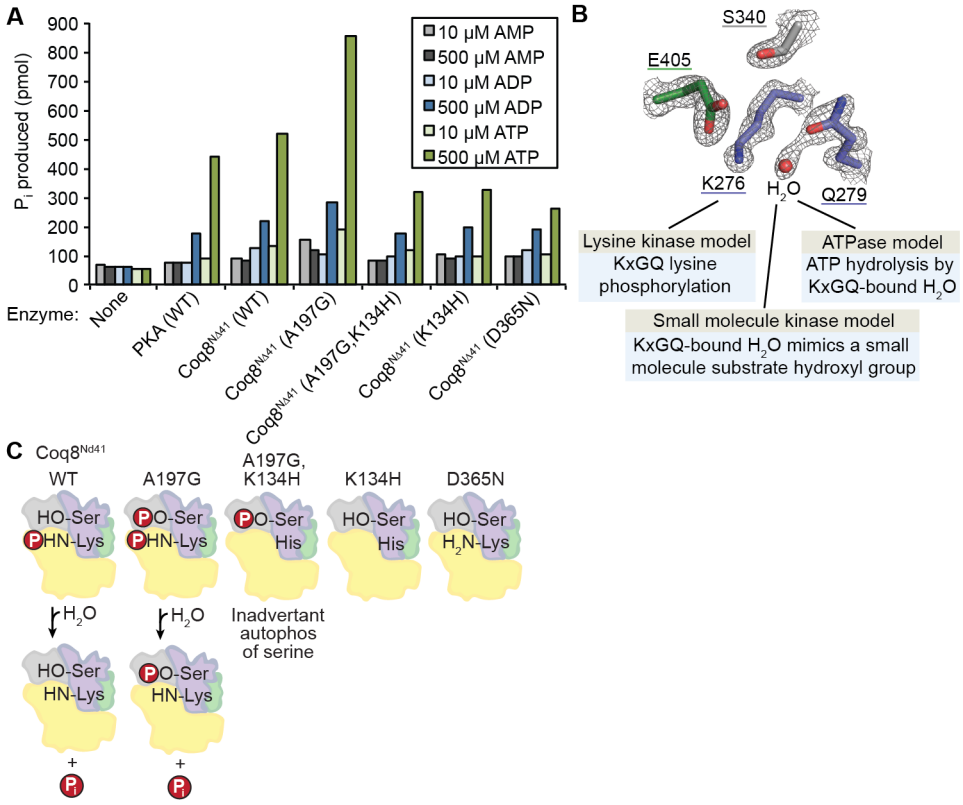

Figure 5. Coq8p Catalyzes ATPase Activity with its UbiB-Specific KxGQ motif

(**A**) Inorganic phosphate produced by *in vitro* reactions with the indicated enzymes and nucleotides as determined with a malachite green assay.

(**B**) Three models that could account for the observed dependence of ATPase activity on the lysine of the KxGQ motif. The water molecule bound by the KxGQ motif in the ADCK3 structure is shown.

(**C**) A model for how lysine kinase activity could be observed as ATPase activity.

Figure 6.

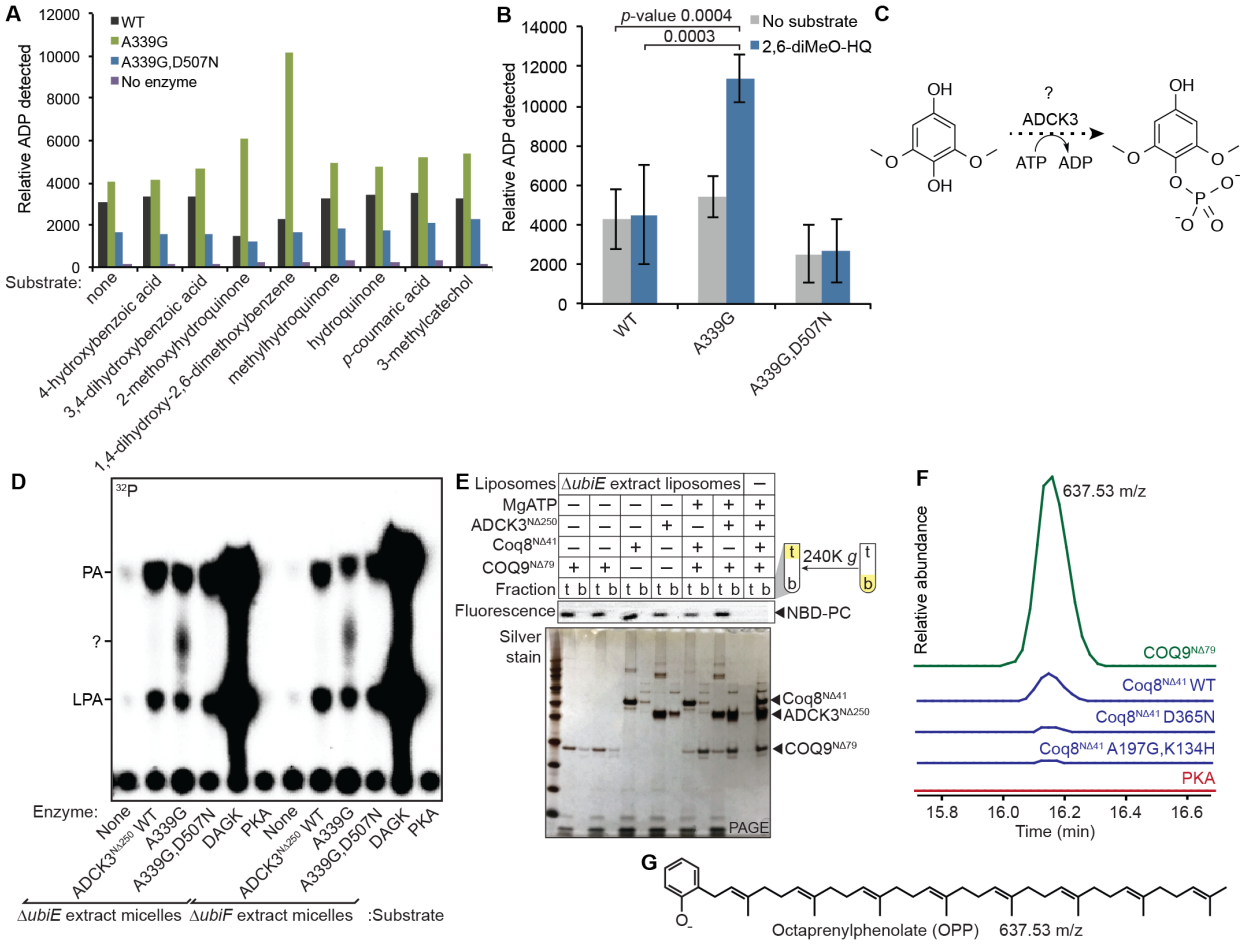

Figure 6. ADCK3 Activity is Affected By Small Molecules

(**A**) Relative amount of ADP (as observed by luminescence with an enzyme-linked assay) generated in reactions with the indicated ADCK3$^{N\Delta250}$ variants and small molecule substrates.

(**B**) Relative amount of ADP (mean ± SD, n = 4) (as observed by luminescence with an enzyme linked assay) generated in reactions with the indicated ADCK3$^{N\Delta250}$ variants and 1,4-dihydroxy-2,6-dimethoxybenzene (2,6-dimethoxy-hydroquinone).

(**C**) Hypothesized ATP-dependent phosphorylation of 1,4-dihydroxy-2,6-dimethoxybenzene catalyzed by ADCK3.

(**D**) TLC analysis of *in vitro* Mg[γ-^{32}P]ATP reactions with ADCK3$^{N\Delta250}$ variants, PKA, or diacylglycerol kinase (DAGK) and micelles (Triton X-100) with lipids extracted from bacteria (Δ*ubiE* or Δ*ubiF*).

(**E**) SDS-PAGE analysis of a liposome-protein co-floatation assay with the indicated proteins and liposomes generated from Δ*ubiE* extract lipids. The liposomes included a fluorescent lipid marker (NBD-PC). Top (t) and bottom (b) fractions after the spin are indicated.

(**F**) Extracted ion chromatograms (XICs) reflecting the MS^1 precursor intensities of a species with m/z 637.53 over elution time as observed by negative mode LC-MS/MS.

(**G**) Structure of octaprenylphenolate (OPP) (molecular weight: 637.53 g/mol).

Figure 7.

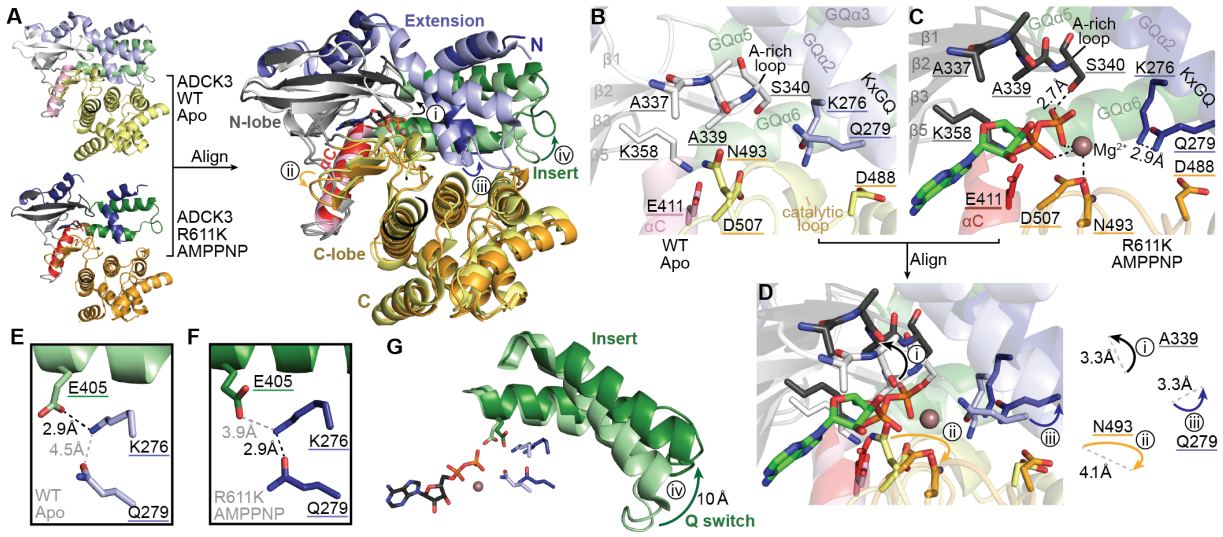

Figure 7. X-ray crystal structure of ADCK3$^{N\Delta254}$ R611K bound to a nucleotide

(**A**) Overall structure of ADCK3$^{N\Delta254}$ R611K bound to the nucleotide adenosine 5'-(β,γ-imido)triphosphate (AMPPNP) superimposed with that of apo ADCK3$^{N\Delta254}$ (WT) (PDB: 4PED). Conformational changes in the (i) A-rich loop, (ii) catalytic loop, (iii) KxGQ extension, and (iv) KxGQ insert are highlighted. The general domain color scheme is maintained throughout this figure, with the apo structure in lighter colors.

(**B**) Structure of active site residues of ADCK3$^{N\Delta254}$ (apo).

(**C**) Structure of active site residues of ADCK3$^{N\Delta254}$ R611K bound to a nucleotide. The nucleotide is modeled as ADP because the γ-phosphate was not able to be resolved.

(**D**) Superposition of the active sites of apo and nucleotide-bound ADCK3$^{N\Delta254}$. Distance differences between the two conformations are shown to the right.

(**E**) Structure of the QKE triad of ADCK3$^{N\Delta254}$ (apo).

(**F**) Structure of the QKE triad of ADCK3$^{N\Delta254}$ R611K bound to a nucleotide.

(**G**) Superposition of the KxGQ inserts of apo and nucleotide-bound ADCK3$^{N\Delta254}$. The distance difference between the GQα5-GQα6 loops (the Q switch) is shown to the right.

Figure S1, related to Figure 1

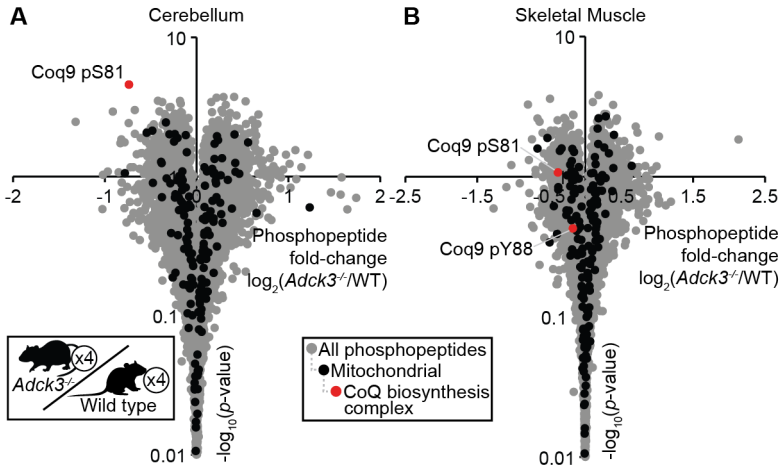

Figure S1, related to Figure 1. The phosphoproteome of Adck3$^{-/-}$ mice is perturbed

(**A**) Fold changes in cerebellum phosphopeptide abundances (mean $\log_2$(*Adck3*$^{-/-}$/WT), n = 4) versus statistical significance (–$\log_{10}$(*p*-value)) as quantified by LC-MS/MS. Mitochondrial phosphopeptides are shown in black, and all observed phosphopeptides from CoQ biosynthesis complex proteins are shown in red.

(**B**) Fold changes in skeletal muscle (quadriceps) phosphopeptide abundances, otherwise as in (A).

Figure S2, related to Figure 2

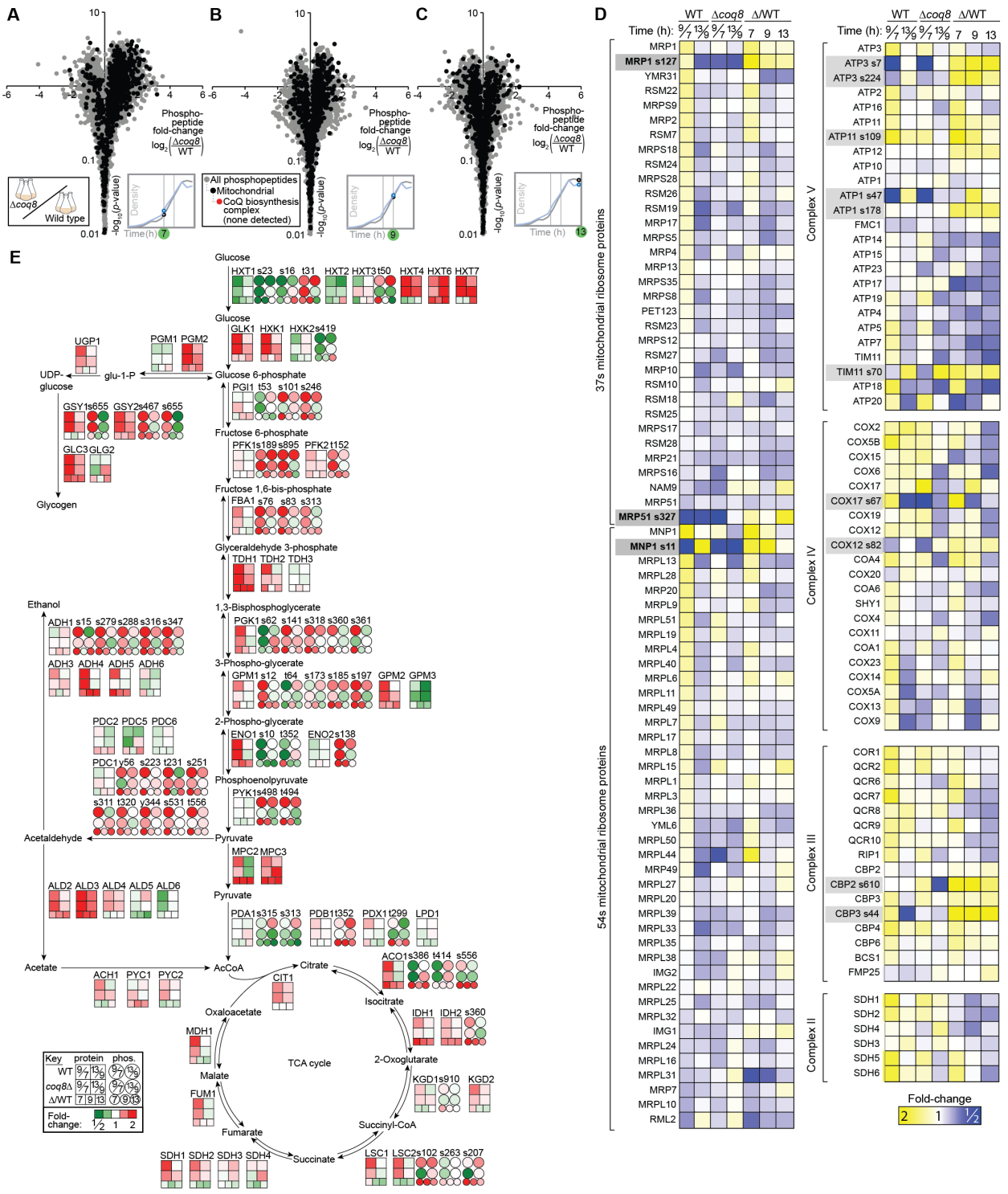

Figure S2, related to Figure 2. The mitochondrial proteome and phosphoproteome of Δ*coq8* yeast is perturbed

(**A**) Fold changes in phosphopeptide abundances (mean $\log_2$(Δ*coq8*/WT), n = 3) at the 7 h time point versus statistical significance ($-\log_{10}$(*p*-value)) as quantified by LC-MS/MS. Mitochondrial phosphopeptides are shown in black, and all observed phosphopeptides from CoQ biosynthesis complex proteins are shown in red. Details of the corresponding yeast growth curve and sample time points are shown in Figure 2A.

(**B**) Fold changes in phosphopeptide abundances at the 9 h time point, otherwise as in (A).

(**C**) Fold changes in protein abundances at the 13 h time point, otherwise as in (A).

(**D**) Heat map of fold changes in the abundances of proteins and phosphopeptides (mean, n = 3) from the mitochondrial ribosome and oxidative phosphorylation complexes as determined by LC-MS/MS.

(**E**) Heat maps of fold changes in the abundances of proteins and phosphopeptides (mean, n = 3) from central carbon metabolism pathways as determined by LC-MS/MS. Boxes indicate proteins, and circles indicate phosphopeptides from the protein shown immediately to the left.

Figure S3, related to Figure 3

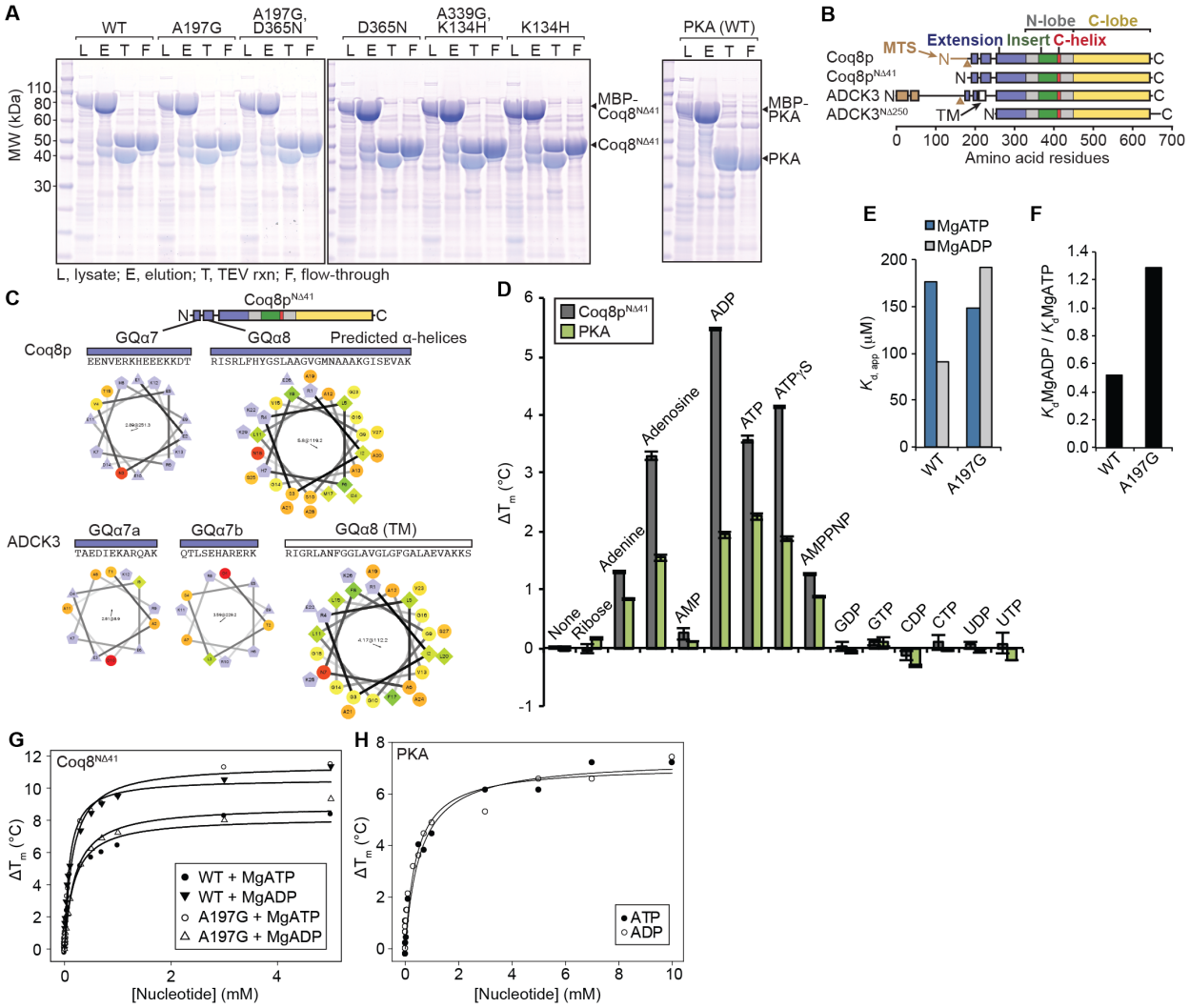

Figure S3, related to Figure 3. Mitochondrial Coq8p binds adenine nucleotides

(**A**) SDS-PAGE analysis of fractions from an isolation of recombinant Coq8$^{N\Delta41}$ (WT and variants) and PKA (WT).

(**B**) Domain structures of Coq8p, ADCK3, and truncated constructs. The white box represents a single-pass transmembrane domain of ADCK3. Brown triangles represent observed N-termini of mature Coq8p and mature ADCK3. MTS, mitochondrial targeting sequence.

(**C**) Helical wheel projections of predicted α-helices from the N-terminus of the Coq8$^{N\Delta41}$ construct and the homologous region of ADCK3 (see domain structures in (A)).

(**D**) ΔT_m of $Coq8^{N\Delta41}$ or PKA due to addition of various ligands (mean ± SD, n = 3) in the presence of Mg^{2+} as assessed by differential scanning fluorimetry (DSF).

(**E**) K_d^{MgATP} and K_d^{MgADP} for $Coq8^{N\Delta41}$ (WT and A197G) variants as assessed by DSF.

(**F**) Nucleotide selectivity of $Coq8^{N\Delta41}$ A197G compared to WT. Apparent K_d values were assessed by DSF.

(**G**) Nucleotide binding curves for $Coq8^{N\Delta41}$ (WT and A197G).

(**H**) Nucleotide binding curves for PKA in the presence of MgATP or MgADP.

Figure S4, related to Figure 3

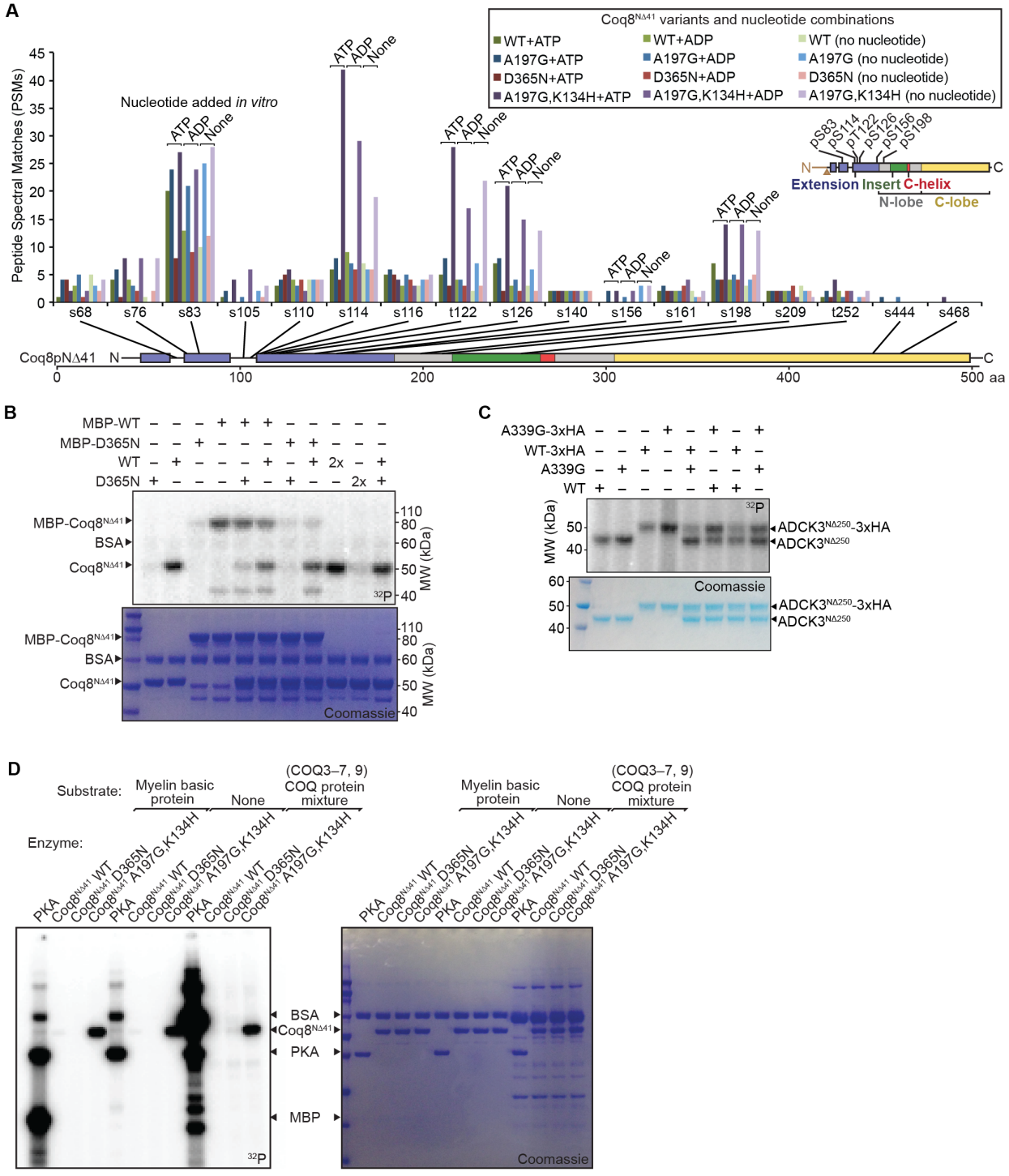

Figure S4, related to Figure 3. Autophosphorylation activity of Coq8p and ADCK3

(**A**) Number of PSMs observed for Coq8$^{N\Delta41}$ phosphopeptides detected by LC-MS/MS analysis of *in vitro* MgATP autophosphorylation reactions.

(**B**) SDS-PAGE analysis of *in vitro* Mg[γ-^{32}P]ATP autophosphorylation reactions with the indicated combinations of Coq8$^{N\Delta41}$ variants and maltose binding protein (MBP) tagged Coq8$^{N\Delta41}$ variants.

(**C**) SDS-PAGE analysis of *in vitro* Mg[γ-^{32}P]ATP autophosphorylation reactions with the indicated combinations of ADCK3$^{N\Delta250}$ variants and 3xHA-tagged ADCK3$^{N\Delta250}$ variants.

(**D**) SDS-PAGE analysis of *in vitro* Mg[γ-^{32}P]ATP kinase reactions with PKA or Coq8$^{N\Delta41}$ (WT, D365N, or A197G,K134H) and potential substrate proteins (myelin basic protein or a mixture of CoQ biosynthesis proteins, COQ3–COQ7 and COQ9).

Figure S5, related to Figure 5

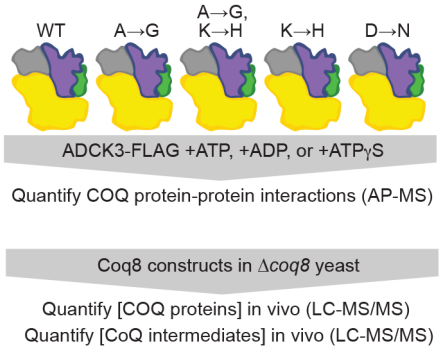

Figure S5, related to Figure 5. Testing the ADCK3 and Coq8p ATPase model.

(**A**) Design of a set of experiments in progress to test the ATPase model for Coq8p and ADCK3 function.

Figure S6.

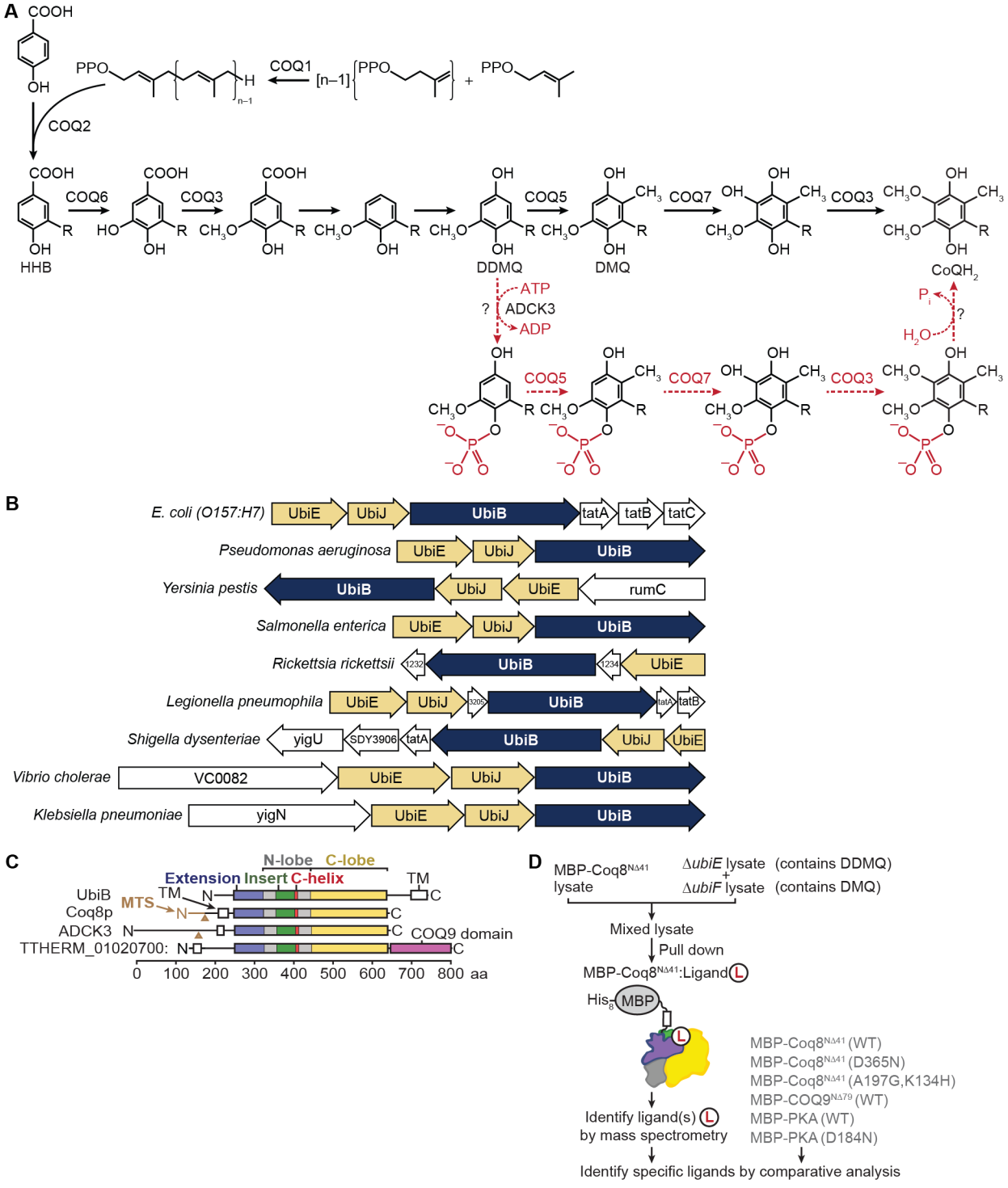

Figure S6, related to Figure 6. Features of CoQ biosynthesis related to the small molecule kinase model of ADCK3 function

(**A**) Eukaryotic CoQ biosynthesis pathway, including hypothesized phosphorylation of a lipid intermediate. HHB, hexaprenyl-hydroxy-benozoic acid; DDMQ, demethoxy-demethyl-coenzyme Q; DMQ, demethoxy-coenzyme Q.

(**B**) Operons containing the gene *ubiB* from numerous bacteria. The *ubiB* gene is shown in dark blue, and the additional CoQ biosynthesis genes *ubiE* and *ubiJ* are shown in gold.

(**C**) Domain structures of *E. coli* UbiB, yeast Coq8p, human ADCK3, and a UbiB family homolog from *Tetrahymena thermophila* that contains a fused COQ9 protein domain.

(**D**) Experimental design for identification of small molecules that co-purify with $Coq8^{N\Delta41}$ and $COQ9^{N\Delta79}$.

References

Ashraf, S., Gee, H.Y., Woerner, S., Xie, L.X., Vega-Warner, V., Lovric, S., Fang, H., Song, X., Cattran, D.C., Avila-Casado, C.*, et al.* (2013). ADCK4 mutations promote steroid-resistant nephrotic syndrome through CoQ10 biosynthesis disruption. The Journal of clinical investigation *123*, 5179-5189.

Baudin, A., Ozier-Kalogeropoulos, O., Denouel, A., Lacroute, F., and Cullin, C. (1993). A simple and efficient method for direct gene deletion in Saccharomyces cerevisiae. Nucleic acids research *21*, 3329-3330.

Blommel, P.G., Martin, P.A., Seder, K.D., Wrobel, R.L., and Fox, B.G. (2009). Flexi vector cloning. Methods in molecular biology *498*, 55-73.

Bodenmiller, B., Wanka, S., Kraft, C., Urban, J., Campbell, D., Pedrioli, P.G., Gerrits, B., Picotti, P., Lam, H., Vitek, O.*, et al.* (2010). Phosphoproteomic analysis reveals interconnected system-wide responses to perturbations of kinases and phosphatases in yeast. Sci Signal *3*, rs4.

Boudeau, J., Miranda-Saavedra, D., Barton, G.J., and Alessi, D.R. (2006). Emerging roles of pseudokinases. Trends Cell Biol *16*, 443-452.

Brough, R., Frankum, J.R., Sims, D., Mackay, A., Mendes-Pereira, A.M., Bajrami, I., Costa-Cabral, S., Rafiq, R., Ahmad, A.S., Cerone, M.A.*, et al.* (2011). Functional viability profiles of breast cancer. Cancer discovery *1*, 260-273.

Brown, E.J., Albers, M.W., Shin, T.B., Ichikawa, K., Keith, C.T., Lane, W.S., and Schreiber, S.L. (1994). A mammalian protein targeted by G1-arresting rapamycin-receptor complex. Nature *369*, 756-758.

Brown, E.J., Beal, P.A., Keith, C.T., Chen, J., Shin, T.B., and Schreiber, S.L. (1995). Control of p70 s6 kinase by kinase activity of FRAP in vivo. Nature *377*, 441-446.

Chen, Y.C., Taylor, E.B., Dephoure, N., Heo, J.M., Tonhato, A., Papandreou, I., Nath, N., Denko, N.C., Gygi, S.P., and Rutter, J. (2012). Identification of a protein mediating respiratory supercomplex stability. Cell Metab *15*, 348-360.

Cox, G.B., Young, I.G., McCann, L.M., and Gibson, F. (1969). Biosynthesis of ubiquinone in Escherichia coli K-12: location of genes affecting the metabolism of 3-octaprenyl-4-hydroxybenzoic acid and 2-octaprenylphenol. Journal of bacteriology *99*, 450-458.

DeRisi, J.L., Iyer, V.R., and Brown, P.O. (1997). Exploring the metabolic and genetic control of gene expression on a genomic scale. Science *278*, 680-686.

Do, T.Q., Hsu, A.Y., Jonassen, T., Lee, P.T., and Clarke, C.F. (2001). A defect in coenzyme Q biosynthesis is responsible for the respiratory deficiency in Saccharomyces cerevisiae abc1 mutants. The Journal of biological chemistry *276*, 18161-18168.

Fox, B.G., and Blommel, P.G. (2009). Autoinduction of protein expression. Current protocols in protein science / editorial board, John E Coligan [et al] *Chapter 5*, Unit 5 23.

Geer, L.Y., Markey, S.P., Kowalak, J.A., Wagner, L., Xu, M., Maynard, D.M., Yang, X., Shi, W., and Bryant, S.H. (2004). Open mass spectrometry search algorithm. Journal of proteome research *3*, 958-964.

He, C.H., Xie, L.X., Allan, C.M., Tran, U.C., and Clarke, C.F. (2014). Coenzyme Q supplementation or over-expression of the yeast Coq8 putative kinase stabilizes multi-subunit Coq polypeptide complexes in yeast coq null mutants. Biochimica et biophysica acta *1841*, 630-644.

Hebert, A.S., Merrill, A.E., Stefely, J.A., Bailey, D.J., Wenger, C.D., Westphall, M.S., Pagliarini, D.J., and Coon, J.J. (2013). Amine-reactive neutron-encoded labels for highly plexed proteomic quantitation. Molecular & cellular proteomics : MCP *12*, 3360-3369.

Horvath, R., Czermin, B., Gulati, S., Demuth, S., Houge, G., Pyle, A., Dineiger, C., Blakely, E.L., Hassani, A., Foley, C.*, et al.* (2012). Adult-onset cerebellar ataxia due to mutations in CABC1/ADCK3. Journal of neurology, neurosurgery, and psychiatry *83*, 174-178.

Jasinski, M., Sudre, D., Schansker, G., Schellenberg, M., Constant, S., Martinoia, E., and Bovet, L. (2008). AtOSA1, a member of the Abc1-like family, as a new factor in cadmium and oxidative stress response. Plant physiology *147*, 719-731.

Kannan, N., Taylor, S.S., Zhai, Y., Venter, J.C., and Manning, G. (2007). Structural and functional diversity of the microbial kinome. PLoS biology *5*, e17.

Khadria, A.S., Mueller, B.K., Stefely, J.A., Tan, C.H., Pagliarini, D.J., and Senes, A. (2014). A Gly-zipper motif mediates homodimerization of the transmembrane domain of the mitochondrial kinase ADCK3. Journal of the American Chemical Society *136*, 14068-14077.

Klock, H.E., Koesema, E.J., Knuth, M.W., and Lesley, S.A. (2008). Combining the polymerase incomplete primer extension method for cloning and mutagenesis with microscreening to accelerate structural genomics efforts. Proteins *71*, 982-994.

Korennykh, A.V., Egea, P.F., Korostelev, A.A., Finer-Moore, J., Zhang, C., Shokat, K.M., Stroud, R.M., and Walter, P. (2009). The unfolded protein response signals through high-order assembly of Ire1. Nature *457*, 687-693.

Lagier-Tourenne, C., Tazir, M., Lopez, L.C., Quinzii, C.M., Assoum, M., Drouot, N., Busso, C., Makri, S., Ali-Pacha, L., Benhassine, T.*, et al.* (2008). ADCK3, an ancestral kinase, is mutated in a form of recessive ataxia associated with coenzyme Q10 deficiency. American journal of human genetics *82*, 661-672.

Lee, K.P., Dey, M., Neculai, D., Cao, C., Dever, T.E., and Sicheri, F. (2008). Structure of the dual enzyme Ire1 reveals the basis for catalysis and regulation in nonconventional RNA splicing. Cell *132*, 89-100.

Leonard, C.J., Aravind, L., and Koonin, E.V. (1998). Novel families of putative protein kinases in bacteria and archaea: evolution of the "eukaryotic" protein kinase superfamily. Genome research *8*, 1038-1047.

Lohman, D.C., Forouhar, F., Beebe, E.T., Stefely, M.S., Minogue, C.E., Ulbrich, A., Stefely, J.A., Sukumar, S., Luna-Sanchez, M., Jochem, A.*, et al.* (2014). Mitochondrial COQ9 is a lipid-binding protein that associates with COQ7 to enable coenzyme Q biosynthesis. Proceedings of the National Academy of Sciences of the United States of America *111*, E4697-4705.

Lundquist, P.K., Poliakov, A., Giacomelli, L., Friso, G., Appel, M., McQuinn, R.P., Krasnoff, S.B., Rowland, E., Ponnala, L., Sun, Q.*, et al.* (2013). Loss of plastoglobule kinases ABC1K1 and ABC1K3 causes conditional degreening, modified prenyl-lipids, and recruitment of the jasmonic acid pathway. The Plant cell *25*, 1818-1839.

Maeda, K., Anand, K., Chiapparino, A., Kumar, A., Poletto, M., Kaksonen, M., and Gavin, A.C. (2013). Interactome map uncovers phosphatidylserine transport by oxysterol-binding proteins. Nature *501*, 257-261.

Manning, G., Whyte, D.B., Martinez, R., Hunter, T., and Sudarsanam, S. (2002). The protein kinase complement of the human genome. Science *298*, 1912-1934.

Mao, X., Ma, Q., Zhou, C., Chen, X., Zhang, H., Yang, J., Mao, F., Lai, W., and Xu, Y. (2014). DOOR 2.0: presenting operons and their functions through dynamic and integrated views. Nucleic acids research *42*, D654-659.

Milburn, M.V., Tong, L., deVos, A.M., Brunger, A., Yamaizumi, Z., Nishimura, S., and Kim, S.H. (1990). Molecular switch for signal transduction: structural differences between active and inactive forms of protooncogenic ras proteins. Science *247*, 939-945.

Mollet, J., Delahodde, A., Serre, V., Chretien, D., Schlemmer, D., Lombes, A., Boddaert, N., Desguerre, I., de Lonlay, P., de Baulny, H.O.*, et al.* (2008). CABC1 gene mutations cause ubiquinone deficiency with cerebellar ataxia and seizures. American journal of human genetics *82*, 623-630.

Narayana, N., Cox, S., Shaltiel, S., Taylor, S.S., and Xuong, N. (1997). Crystal structure of a polyhistidine-tagged recombinant catalytic subunit of cAMP-dependent protein kinase complexed with the peptide inhibitor PKI(5-24) and adenosine. Biochemistry *36*, 4438-4448.

Nesvizhskii, A.I., and Aebersold, R. (2005). Interpretation of shotgun proteomic data: the protein inference problem. Molecular & cellular proteomics : MCP *4*, 1419-1440.

Niesen, F.H., Berglund, H., and Vedadi, M. (2007). The use of differential scanning fluorimetry to detect ligand interactions that promote protein stability. Nature protocols *2*, 2212-2221.

Pagliarini, D.J., Calvo, S.E., Chang, B., Sheth, S.A., Vafai, S.B., Ong, S.E., Walford, G.A., Sugiana, C., Boneh, A., Chen, W.K.*, et al.* (2008). A mitochondrial protein compendium elucidates complex I disease biology. Cell *134*, 112-123.

Papa, F.R., Zhang, C., Shokat, K., and Walter, P. (2003). Bypassing a kinase activity with an ATP-competitive drug. Science *302*, 1533-1537.

Phanstiel, D.H., Brumbaugh, J., Wenger, C.D., Tian, S., Probasco, M.D., Bailey, D.J., Swaney, D.L., Tervo, M.A., Bolin, J.M., Ruotti, V.*, et al.* (2011). Proteomic and phosphoproteomic comparison of human ES and iPS cells. Nat Methods *8*, 821-827.

Pineda, M., Montero, R., Aracil, A., O'Callaghan, M.M., Mas, A., Espinos, C., Martinez-Rubio, D., Palau, F., Navas, P., Briones, P.*, et al.* (2010). Coenzyme Q(10)-responsive ataxia: 2-year-treatment follow-up. Movement disorders : official journal of the Movement Disorder Society *25*, 1262-1268.

Poon, W.W., Davis, D.E., Ha, H.T., Jonassen, T., Rather, P.N., and Clarke, C.F. (2000). Identification of Escherichia coli ubiB, a gene required for the first monooxygenase step in ubiquinone biosynthesis. Journal of bacteriology *182*, 5139-5146.

Rhee, H.W., Zou, P., Udeshi, N.D., Martell, J.D., Mootha, V.K., Carr, S.A., and Ting, A.Y. (2013). Proteomic mapping of mitochondria in living cells via spatially restricted enzymatic tagging. Science *339*, 1328-1331.

Sabatini, D.M., Erdjument-Bromage, H., Lui, M., Tempst, P., and Snyder, S.H. (1994). RAFT1: a mammalian protein that binds to FKBP12 in a rapamycin-dependent fashion and is homologous to yeast TORs. Cell *78*, 35-43.

Schlecht, U., Suresh, S., Xu, W., Aparicio, A.M., Chu, A., Proctor, M.J., Davis, R.W., Scharfe, C., and St Onge, R.P. (2014). A functional screen for copper homeostasis genes identifies a pharmacologically tractable cellular system. BMC genomics *15*, 263.

Simpson, K.J., Selfors, L.M., Bui, J., Reynolds, A., Leake, D., Khvorova, A., and Brugge, J.S. (2008). Identification of genes that regulate epithelial cell migration using an siRNA screening approach. Nature cell biology *10*, 1027-1038.

Stefely, J.A., Reidenbach, A.G., Ulbrich, A., Oruganty, K., Floyd, B.J., Jochem, A., Saunders, J.M., Johnson, I.E., Minogue, C.E., Wrobel, R.L.*, et al.* (2015). Mitochondrial ADCK3 employs an atypical protein kinase-like fold to enable coenzyme Q biosynthesis. Molecular cell *57*, 83-94.

Tan, T., Ozbalci, C., Brugger, B., Rapaport, D., and Dimmer, K.S. (2013). Mcp1 and Mcp2, two novel proteins involved in mitochondrial lipid homeostasis. Journal of cell science *126*, 3563-3574.

Vogtle, F.N., Wortelkamp, S., Zahedi, R.P., Becker, D., Leidhold, C., Gevaert, K., Kellermann, J., Voos, W., Sickmann, A., Pfanner, N.*, et al.* (2009). Global analysis of the mitochondrial N-proteome identifies a processing peptidase critical for protein stability. Cell *139*, 428-439.

Walker, E.H., Perisic, O., Ried, C., Stephens, L., and Williams, R.L. (1999). Structural insights into phosphoinositide 3-kinase catalysis and signalling. Nature *402*, 313-320.

Wenger, C.D., Phanstiel, D.H., Lee, M.V., Bailey, D.J., and Coon, J.J. (2011). COMPASS: a suite of pre- and post-search proteomics software tools for OMSSA. Proteomics *11*, 1064-1074.

Wiedemeyer, W.R., Dunn, I.F., Quayle, S.N., Zhang, J., Chheda, M.G., Dunn, G.P., Zhuang, L., Rosenbluh, J., Chen, S., Xiao, Y.*, et al.* (2010). Pattern of retinoblastoma pathway inactivation dictates response to CDK4/6 inhibition in GBM. Proceedings of the National Academy of Sciences of the United States of America *107*, 11501-11506.

Xie, L.X., Hsieh, E.J., Watanabe, S., Allan, C.M., Chen, J.Y., Tran, U.C., and Clarke, C.F. (2011). Expression of the human atypical kinase ADCK3 rescues coenzyme Q biosynthesis and phosphorylation of Coq polypeptides in yeast coq8 mutants. Biochimica et biophysica acta *1811*, 348-360.

Yang, H., Rudge, D.G., Koos, J.D., Vaidialingam, B., Yang, H.J., and Pavletich, N.P. (2013). mTOR kinase structure, mechanism and regulation. Nature *497*, 217-223.

Young, I.G.M., L. M.; Stroobant, P.; Gibson, F. (1971). Characterization and Genetic Analysis of Mutant Strains of *Escherichia coli* K-12 Accumulating the Ubiquinone Precursors 2-Octaprenyl-6-Methoxy-1,4-Benzoquinone and 2-Octaprenyl-3-Methyl-6-Methoxy-1,4-Benzoquinone. Journal of bacteriology *105*, 769-778.

Zeqiraj, E., and van Aalten, D.M. (2010). Pseudokinases-remnants of evolution or key allosteric regulators? Current opinion in structural biology *20*, 772-781.

Chapter 4

Mitochondrial protein functions revealed by global protein-lipid-metabolite profiles

Jonathan A. Stefely, Nicholas W. Kwiecien, Alexander S. Hebert, Matthew J. P. Rush, Arne Ulbrich, Alicia L. Richards, Elyse Freiberger, Michael T. Veling, Xiao Guo, Adam Jochem, Alan J. Higbee, Michael S. Westphall, David J. Pagliarini, and Joshua J. Coon

Author contributions:

J.A.S. was the primary author of this chapter. J.A.S, A.S.H., D.J.P., and J.J.C. conceived of the project and its design. J.A.S. selected target strains, cultured yeast, and prepared samples for mass spectrometry analysis (proteomics input quantitation, metabolite extractions, and lipid extractions). A.J. assisted with yeast cultures and conducted genetic experiments. J.A.S. and A.S.H. identified a stable respiratory growth condition. A.S.H, A.L.R., and E.F. conducted LC-MS/MS proteomics. M.J.P.R. and A.J.H. conducted GC-MS metabolomics. A.U. conducted LC-MS/MS lipidomics. N.W.K created and applied software to transform raw mass spectrometry data into biomolecule quantities, perturbation profile correlations, and graphs. M.S.W., D.J.P., and J.J.C. aided in experimental design. J.A.S., A.J., X.G., M.T.V., and D.J.P. conducted follow-up biological and biochemical studies. J.A.S., N.W.K., A.S.H., M.J.P.R., A.U., A.L.R., E.F., M.T.V., A.J., M.S.W., D.J.P., and J.J.C. analyzed data and interpreted results.

Abstract

Perturbing an organism and characterizing its phenotypes can elucidate gene function or disease pathogenesis. A central challenge in this process is to quantify phenotypes with enough breadth to capture the diagnostic features. Here, using single gene deletion yeast strains as a eukaryotic model system, we quantify 3,000 biochemical phenotypes by generating 3,000 mass spectrometry profiles, covering 1,000 proteomes, 1,000 lipidomes, and 1,000 metabolomes. The scope and depth of our phenotyping approach provides functional insight at numerous levels, ranging from quantitative assessment of specific molecules to systems-level correlations between perturbation profiles. Through this work, we predict functions for previously uncharacterized mitochondrial proteins. We validate a subset of our functional annotations, including genes required for mitochondrial oxidative phosphorylation and mitochondrial lipid metabolism. Our results provide molecular insight into mitochondrial diseases and, more broadly, establish a high-throughput approach for defining gene function.

Introduction

Technical advances in genetics have enabled rapid and widespread identification of new genes and new disease variants in many organisms (Mardis, 2011). However, functional annotation of these genes and the proteins they encode lags behind. Incomplete annotation of the human genome limits our understanding of disease and is recognized as a bottleneck in medicine, limiting bench-to-bedside translation of the human genome sequence into new therapies (Green et al., 2011).

Our initial annotation efforts focus on characterizing genes that affect mitochondria, dynamic organelles associated with over 150 human diseases (Koopman et al., 2012; Nunnari and Suomalainen, 2012; Vafai and Mootha, 2012). Nearly 300 of the ~1,100 proteins that localize to mammalian mitochondria have no known function (Pagliarini et al., 2008; Pagliarini and Rutter, 2013), and many additional mitochondrial proteins are poorly annotated. Systematic strategies for functional annotation of mitochondrial proteins are needed to fill these gaps.

The yeast *Saccharomyces cerevisiae* is a widely used model organism for elucidating eukaryotic gene function. Phenotype analysis of single gene deletion yeast strains led to the discovery of genes that affect competitive fitness, drug resistance, morphology, DNA damage, and respiration (Giaever et al., 2002; Steinmetz et al., 2002; Winzeler et al., 1999). However, many single gene deletions do not affect readily quantifiable biological phenotypes because cellular compensation can restore homeostasis. In landmark studies, genome-wide mRNA expression profiling provided a deeper look at the cellular response to environmental changes (DeRisi et al., 1997) and genetic perturbations (Hughes et al., 2000; Kemmeren et al., 2014). However, in the most comprehensive yeast mRNA profiling study to date, only 47% of mutant strains had mRNA profiles that deviated significantly from those of wild type yeast (Kemmeren

et al., 2014). Rapidly quantifying phenotypes with enough depth to identify changes diagnostic for a specific gene function remains a challenge.

High-resolution mass spectrometry (MS)-based proteomics, which enables unbiased quantitation of thousands of proteins, is one of the deepest and most specific phenotyping methods available (Aebersold and Mann, 2003). However, proteomics is traditionally low throughput. Recently, we accelerated MS proteome analysis to a rate of one yeast proteome per hour (Hebert et al., 2014; Richards et al., 2015), thereby rivaling the speed, depth, and accuracy of mRNA profiling methods. Here, we analyze 1,000 yeast cultures with high-throughput MS proteomics, lipidomics, and metabolomics to reveal molecular insight into numerous mitochondrial functions.

Results and Discussion

Global mass spectrometry profiling of yeast

This work relied on 4 critical features: distinct metabolic states, reproducible culture conditions, diverse mitochondrial perturbations, and high-throughput mass spectrometry (Fig. 1).

The functions of yeast mitochondria are affected dramatically by the concentration of glucose in the growth media, so we required two distinct culture conditions—fermentation and respiration—to comprehensively cover mitochondrial functions. Most yeast studies use an early log-phase fermentation culture condition with high glucose (20 g/L), which is stable and reproducible (Kemmeren et al., 2014), but it represses mitochondrial respiration. Growing high glucose cultures into and past the diauxic shift activates mitochondrial respiration, but a host of dynamic changes occur as other media components are depleted and the cells enter stationary phase (Casanovas et al., 2015; Picotti et al., 2009). The variability introduced by this highly

dynamic growth phase makes it impractical for large-scale investigations. Completely replacing glucose with a non-fermentable sugar is incompatible with the growth of respiratory-deficient yeast strains. To overcome these problems, we developed a culture system with a small amount of glucose (1 g/L), which enables respiratory-deficient strains to proliferate, and a larger amount of a non-fermentable sugar (30 g/L glycerol), which is used for respiratory metabolism after the glucose is consumed. This respiration culture condition, like the traditional fermentation culture system, affords a steady growth phase and a stable biological state, as reflected by a proteome that is stable over multiple hours (Fig. 2). This proteome stability provides a critical window for reproducible sample harvesting.

Our approach also required diverse perturbations to sample mitochondrial functions broadly. Accordingly, we analyzed single gene deletion yeast strains spanning numerous cellular processes (Fig. 3). The 184 deletion strains we profiled covered 124 characterized (reference) genes, 60 uncharacterized (orphan) genes, 150 genes conserved in humans, and 63 homologs of genes implicated in human disease (Extended Data Table 1). To enable statistical analysis of phenotypes, three biological replicates of each strain were grown under both fermentation and respiration culture conditions (Fig. 1). The mutant strains showed a wide range of growth rates (Fig. 4), reflecting the diversity of perturbations.

All 1,000 cultures were analyzed by high-throughput MS-based proteomics, lipidomics, and metabolomics. We achieved an average coverage of ~3,000 yeast proteins, which represents ~70% of the expressed yeast proteome. The efficiency of our proteomics platform has approached that of mRNA microarray profiling, both in terms of time and cost. We also used a recently developed high-resolution GC-MS instrument for our metabolomics analysis, which was able to detect reproducibly 150 metabolites. Similarly, using high-resolution LC-MS, we profiled

40 lipids in each strain. In total, our analysis covered over 3,000 biochemical phenotypes. The accuracy of our methods is supported by observation of expected differences between our two culture conditions, such as elevated levels of oxidative phosphorylation (OxPhos) proteins, TCA cycle metabolites, and the mitochondrial lipid cardiolipin in the respiration cultures (Fig. 5).

Perturbation profile correlations reveal functional relationships

This work generated a data set with approximately 3 million biomolecule measurements. Proteome-wide plots of protein abundance perturbations for pairs of mutants showed strong linear correlations for mutants of related function (Fig. 6). For example, the proteome perturbation profiles of Δ*coq8* and Δ*coq9* yeast had a Pearson correlation coefficient of 0.86 (Fig. 6a), reflecting the fact that both Coq8p and Coq9p are required for CoQ biosynthesis. Importantly, only low degrees of correlation were observed for unrelated gene pairs, such as Δ*coq8* and Δ*sco1* (Fig. 6a), demonstrating the specificity of this type of analysis. Conducting the correlation analysis across all strains in the study revealed numerous functionally related groups, including both reference and orphan genes (Fig. 6b, c). For example, the uncharacterized strain Δ*yjr120w* was correlated to OxPhos mutants such as Δ*coq9* and Δ*atp2* (Fig. 6). Similar correlations were observed for perturbation profiles of metabolites and lipids (Fig. 6b, c), again including both reference and orphan gene correlations. These results suggest that protein-lipid-metabolite perturbation profile correlation analysis can be a powerful method for prediction of gene function. To make this analysis easily accessible, we created a software program to view these correlation analyses, as well as the underlying data sets of perturbation profiles, which will be freely available online.

Functional insight into oxidative phosphorylation

To begin evaluating the functional predictions generated by our correlation analyses, we tested the aforementioned prediction that Δ*yjr120w* is involved in OxPhos. Examining the specific proteins perturbed in Δ*yjr120w* yeast compared to wild type yeast showed significant decreases in ATP synthase proteins, especially Atp2p (Fig. 7a). Compared to all other mutants in the study, the large decrease in Atp2p abundance is unique to the Δ*yjr120w* and Δ*atp2* strains (Fig. 7b). A close functional relationship between *yjr120w* and *atp2* is further suggested by the genetic location of *yjr120w* directly upstream of *atp2* (*yjr121w*) (Fig. 7c). Consistently, overexpression of *atp2* from a plasmid rescues the respiratory growth defect of Δ*yjr120w* yeast (Fig. 7d, e), demonstrating a functional relationship between *atp2* and *yjr120w in vivo*. A decrease in *atp2* mRNA in the Δ*yjr120w* strain is likely a component of the underlying molecular mechanism (Fig. 7f). These results validate the idea that systems-level perturbation profile correlation analysis can predict gene function at the level of biological processes and pathways, and that deep biochemical phenotyping can provide additional functional information at the molecular level.

Functional insight into coenzyme Q biosynthesis

All 10 known CoQ biosynthesis genes exhibited highly correlated perturbation profiles in our study (Fig. 6). This created strong signatures that allowed us to dig deeper into the uncharacterized features of CoQ biosynthesis, which include missing enzymes (Fig. 8a), missing regulatory factors, and proteins of unknown molecular function (see Chapter 1). By quantifying the abundances of CoQ and the CoQ biosynthesis intermediate PPHB across all strains in the study, we discovered a number of strains that directly impact CoQ biosynthesis (Fig. 8b–e).

The Δ*oct1* strain has significant CoQ deficiency and an abnormal accumulation of PPHB, a signature shared with the Δ*coq3–9* strains (Fig. 8b-e). Coq3p–Coq9p are proteins of the CoQ biosynthesis complex (He et al., 2014). Oct1p is the yeast mitochondrial intermediate peptidase (MIP) (Quiros et al., 2015). By cleaving an octapeptide from the N-terminus of its substrates (Isaya et al., 1992), Oct1p can stabilize and activate mitochondrial proteins (Vogtle et al., 2011). Coq2p and Coq8p are predicted Oct1p substrates (Branda and Isaya, 1995), and Coq4p, Coq6p, and Coq9p also have potential Oct1p recognition sequences. Unprocessed Coq proteins could destabilize or inactivate the CoQ biosynthesis complex, leading to the observed CoQ deficiency. Consistently, the abundances of Coq8p and Coq9p are decreased in the Δ*oct1* strain. These results suggest a new function for Oct1p in regulation of CoQ biosynthesis.

The Δ*fzo1* strain also has significant CoQ deficiency and an abnormal accumulation of PPHB (Fig. 8b-e). Disruption of the mammalian homolog of Fzo1p, MFN2, was recently shown to cause CoQ deficiency (Mourier et al., 2015). Our results show that this function is conserved in yeast. Fzo1p is a GTPase localized to the mitochondrial outer membrane, and it enables mitochondrial fusion (Hales and Fuller, 1997; Hermann et al., 1998). Interestingly, deficiency of another mitochondrial fusion mediator, Mgm1p (Sesaki et al., 2003), also causes significant CoQ deficiency and an abnormal accumulation of PPHB (Fig. 8b, d). Thus, our results suggest a broader role for mitochondrial fusion in CoQ biosynthesis. Defects in mitochondrial fission and fusion affect a broad range of common disorders and rare diseases (Archer, 2013), and our results suggest that CoQ deficiency may be part of the underlying pathogenesis. Specifically, mutations to the human Fzo1p homolog MFN2 cause Charcot-Marie-Tooth disease 2A (Zuchner et al., 2004), and mutations to the human Mgm1p homolog OPA1 cause autosomal dominant

optic atrophy (Alexander et al., 2000; Delettre et al., 2000). Our results suggest that boosting CoQ biosynthesis could be a therapeutic strategy for patients with these diseases.

The Δ*ybr230w-a*, Δ*hem25*, Δ*vps39*, and Δ*hfd1* strains also showed significant CoQ perturbations (Fig. 8b-e). Ybr230w-a is a paralog of Coq8p that likely arose from the yeast whole genome duplication (Kellis et al., 2004). Consistent with a role for Ybr230w in CoQ biosynthesis, we observed a specific protein-protein interaction between Ybr230w and Coq9p-FLAG in an unbiased affinity enrichment mass spectrometry (AE-MS) experiment (data not shown). Hem25p is likely a mitochondrial metabolite transporter that enhances heme biosynthesis (Guernsey et al., 2009). The specific molecule that Hem25p transports is unclear, so it could play a role in the biosynthesis of both CoQ and heme. Hem25p is also the homolog of human SLC25A38, which is linked to sideroblastic anemia. Vps39p was recently shown to facilitate lipid exchange between mitochondria and the endomembrane system (Elbaz-Alon et al., 2014), which could impact the metabolism of CoQ or its lipid precursors. Hfd1p is a lipid dehydrogenase located to the mitochondrial outer membrane (Nakahara et al., 2012), which could also impact the metabolism of CoQ or its precursors. Hfd1p is also linked to Sjogren-Larsson syndrome. Collectively, we discovered a number of connections between mitochondrial proteins and CoQ metabolism, including proteins already implicated in human disease. Efforts to define the molecular basis for how these proteins impact CoQ biosynthesis are in progress.

Functional insight into endoplasmic reticulum-mitochondria communication

Like genes of CoQ biosynthesis, genes involved in endoplasmic reticulum (ER)-mitochondria connections also exhibited strong perturbation signatures that allowed us to investigate uncharacterized features. In particular, the Δ*iml2* strain showed a significant and

specific decrease in the ER protein Emc3p, a recently identified member of a conserved ER membrane protein complex (EMC) (Jonikas et al., 2009). Iml2p is an uncharacterized protein localized to the outer mitochondrial membrane, where it could potentially interact with the ER. The Iml2p protein itself was significantly elevated in Δ*mmm1*, Δ*mdm12*, and Δ*mdm10* yeast, mutants of the ER-mitochondria encounter structure (ERMES) (Kornmann et al., 2009), further suggesting a role in ER-mitochondria communication. We also observed strong correlations between EMC proteins and the mitochondrial outer membrane proteins Om14p and Om45p, suggesting that they might also function in ER-mitochondria connections. Further biochemical investigation of these predicted functions is in progress.

Conclusion

Our development of high-throughput deep phenotyping by mass spectrometry, through quantitative assessment of protein-lipid-metabolite perturbation profiles, should assist numerous fields of scientific inquiry. First, our investigation of yeast mitochondrial processes can be expanded to the entire yeast genome. Second, our phenotyping approach will be useful for investigating human cell lines with genetic perturbations such as RNA interference, gene overexpression, and CRISPR gene disruption. Third, our approach will be useful for systematic investigation of phenotype changes in normal and diseased human tissues, such as tumors. Fourth, we predict that our approach, which has defined perturbation profiles for specific biochemical pathways, can also be used to help define the biological targets of drugs or chemical probes.

In our first demonstration of this experimental approach, we defined new functions for a number of mitochondrial proteins. Yjr120w is now annotated as a gene important for ATP

synthase. We discovered new connections between CoQ biosynthesis and Oct1p, Fzo1p, Mgm1p, Hem25p, Ybr230w, Hfd1p, and Vps39p. Our work also implicates a number of mitochondrial outer membrane proteins in ER-mitochondria communication. Many of the genes we annotated are homologs of human mitochondrial disease genes. This work strengthens the biochemical foundation for investigating these diseases.

Experimental Procedures

Yeast Strains. The parental (wild type) strain for this study was the haploid MATalpha BY4742 strain. Single-gene deletion derivatives of BY4742 were obtained either through the gene deletion consortium (Giaever, Nature, 2002, 418, 387) (purchased from Thermo Scientific) or, if necessary (see below), re-made in-house using a *KanMX* deletion cassette to match those in the consortium collection. See Extended Data Table 1 for a list of individual strains.

A number of quality control measures were instituted for the deletion yeast strains. First, all deletion strains were grown on agar plates with G418 (Geniticin), which are selective for strains containing a *KanMX* cassette. Second, because many of the strains used in this study have impaired mitochondrial respiration, we characterized respiratory competency and compared these phenotypes to those reported in the literature. Third, we examined our proteomics data for evidence of the gene deletion. Strains with a specific and significant decrease (p-value < 0.05 and $\log_2(\Delta gene/wt) < -2$) in the protein encoded by the deleted gene were considered confirmed by MS proteomics. The gene deletions of strains that did not meet these quality controls were examined by a PCR assay and, if necessary, were re-made in-house.

Yeast Culture Media. Single lots of yeast extract ("Y") (Research Products International, RPI), peptone ("P") (RPI), agar (Fisher), dextrose ("D") (RPI), glycerol ("G") (RPI), and G418 (RPI) were used for all experiments. YP and YPG solutions were sterilized by automated autoclave. G418 and dextrose were prepared as separate solutions, sterilized by filtration (0.22 μm pore size, VWR), and added separately to autoclaved YP or YPG. YPD+G418 plates contained yeast extract (10 g/L), peptone (20 g/L), agar (15 g/L), dextrose (20 g/L), and G418 (200 mg/L). YPD plates contained yeast extract (10 g/L), peptone (20 g/L), agar (15 g/L), and dextrose (20 g/L).

YPG plates contained yeast extract (10 g/L), peptone (20 g/L), agar (15 g/L), and glycerol (30 g/L). YPD media contained yeast extract (10 g/L), peptone (20 g/L), and dextrose (20 g/L). YPGD media contained yeast extract (10 g/L), peptone (20 g/L), glycerol (30 g/L) and dextrose (1 g/L).

Yeast Cultures. Yeast from a glycerol stock stored at −80 °C were streaked onto a YPD+G418 plate and incubated (30 °C, ~60 h). An individual colony of yeast was used to inoculate a starter culture (3 mL YPD) and incubated (30 °C, 230 rpm, 10–15 h). The concentration of cells in the culture was determined by measuring the optical density of the culture at 600 nm (OD_{600}) and converting this value to [cells] with the following equation: [cells] (cells/mL) = $8x10^6(OD_{600})$ – 55000 (Hebert, MCP, 2013). YPD or YPGD media (100 mL media at ambient temperature in a sterile 250 mL Erlenmeyer flask) was inoculated with $2.5x10^6$ yeast cells and incubated (30 °C, 230 rpm). Samples of the YPD cultures were harvested 12 h after inoculation, a time point that corresponds to early fermentive (logarithmic) growth. Samples of YPGD cultures were harvested 25 h after inoculation, a time point that corresponds to early respiratory growth.

Numerous quality control measures were instituted for the yeast cultures. First, as described in this manuscript, we determined that both the fermentive and the respiratory time points occur within stable growth phases, thus moderate variations in harvest time should not significantly affect the results. Second, we measured the OD_{600} of the cultures at both time points to ensure that they fell within an acceptable range. Third, we included a wild type culture with each set of deletion strain cultures (19 deletion strains and 1 wild type strain) in order to identify deviant sets of cultures. If the wild type strain in a set deviated significantly from the mean wild type values, the entire set was regrown. To evaluate deviation from the mean, we examined wild

type OD_{600} upon harvest and wild type proteome profiles. Any set with a deviant wild type sample was completely regrown.

For high-resolution growth curve analyses, the concentration of glucose in the media was determined by centrifuging a sample of the culture (0.5 mL) (15,000 x g, 4 min, 4 °C) to pellet the cells, isolating and freezing the cell-free media (supernatant) in $N_{2(l)}$, and determining the glucose concentration with a Glucose (HK) Assay Kit (Sigma).

Sample Preparation for LC-MS/MS Proteomics. $1x10^8$ yeast cells were harvested by centrifugation (3,000 *g*, 3 min, 4 °C), the supernatant was removed, and the cell pellet was flash frozen in liquid nitrogen. The pellets were stored at −80 °C prior to lysis.

Sample Preparation for LC-MS Lipid Quantitation. $1x10^8$ yeast cells were harvested by centrifugation (3,000 *g*, 3 min, 4 °C), the supernatant was removed, and the cell pellet was flash frozen in liquid nitrogen. The pellets were stored at −80 °C prior to extraction. Frozen pellets of yeast ($1x10^8$ cells) were thawed on ice and mixed with glass beads (0.5 mm diameter, 100 µL). $CHCl_3$/MeOH (1:1, v/v, 4 °C) (900 µL) (with 27.8 nM CoQ_{10} and 27.8 nM PE(15:0/15:0)) was added and vortexed (2 x 30 s). HCl (1 M, 200 µL, 4 °C) was added and vortexed (2 x 30 s). The samples were centrifuged (5,000 *g*, 2 min, 4 °C) to complete phase separation. 400 µL of the organic phase was transferred to a clean tube and dried under $Ar_{(g)}$. The organic residue was reconstituted in ACN/IPA/H_2O (65:30:5, v/v/v) (100 µL) by vortexing (2 x 20 s) and transferred to an amber glass vial for LC-MS analysis.

Sample Preparation for MS Metabolomics. $1x10^8$ yeast cells yeast cells were isolated by rapid vacuum filtration onto a nylon filter membrane (0.45 mm pore size, Millipore) using a Glass Microanalysis Filter Holder (Millipore), briefly washed with phosphate buffered saline (1 mL), and immediately submerged into acetonitrile/methanol/H_2O (2:2:1, v/v/v, 1.5 mL, pre-cooled to –20 °C) in a plastic tube. The time from sampling yeast from the culture to submersion in cold extraction solvent was less than 30 s. Tubes with the extraction solvent, nylon filter, and yeast were incubated at –20 °C for ~1 hour, and then stored at –80 °C prior to analysis.

Acknowledgments

This work was supported by a Searle Scholars Award, a Shaw Scientist Award and by NIH grants U01GM94622 and R01GM112057 (to D.J.P.), NIH Ruth L. Kirschstein National Research Service Award F30AG043282 (to J.A.S.).

Figures

Figure 1.

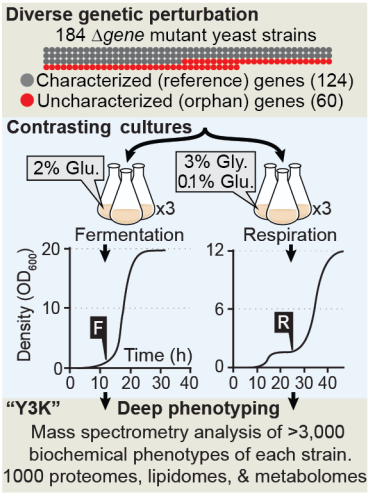

Figure 1 | Protein-lipid-metabolite profiling by mass spectrometry. Overall approach for yeast cultures and phenotyping by mass spectrometry.

Figure 2.

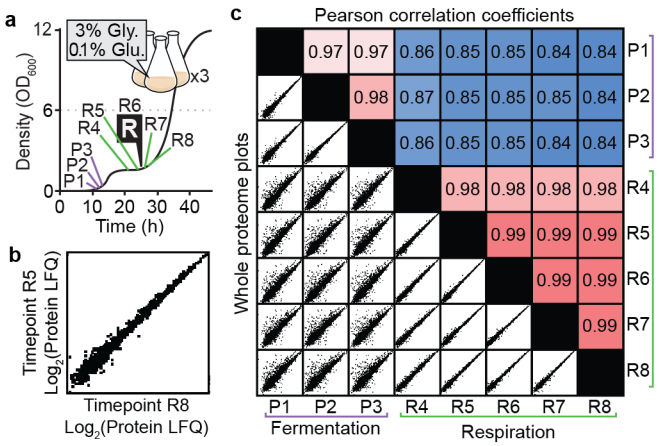

Figure 2 | Identification of a stable respiratory growth condition. a, Growth curve for respiration culture condition (3% glycerol (w/v), 0.1% glucose (w/v)) indicating the time points of 8 sample harvests (R1–R8). The R6 time point at 25 h was chosen for the larger Y3K study. **b**, Whole-proteome plot of $\log_2$ label-free quantitation (LFQ) values for each protein quantified in the R5 and R8 time points. **c**, Pairwise whole proteome plot comparisons (as in (b)) across all eight time points (lower left) and linear regression analysis of each comparison (upper right).

Figure 3.

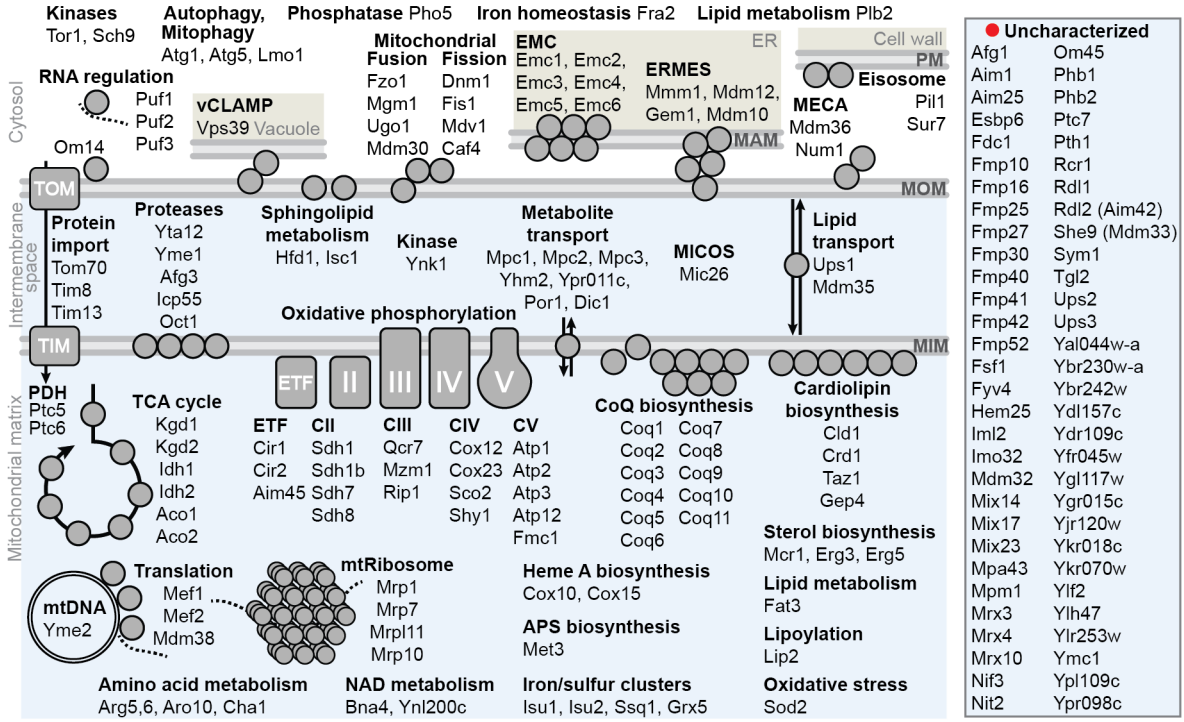

Figure 3 | Target strain selection. Proteins encoded by the individual genes knocked out of the 184 yeast strains investigated in this study, shown in the context of core biological pathways. MAM, mitochondria-associated membrane; MOM, mitochondrial outer membrane; MIM, mitochondrial inner membrane; ERMES, ER-mitochondria encounter structure.

Figure 4.

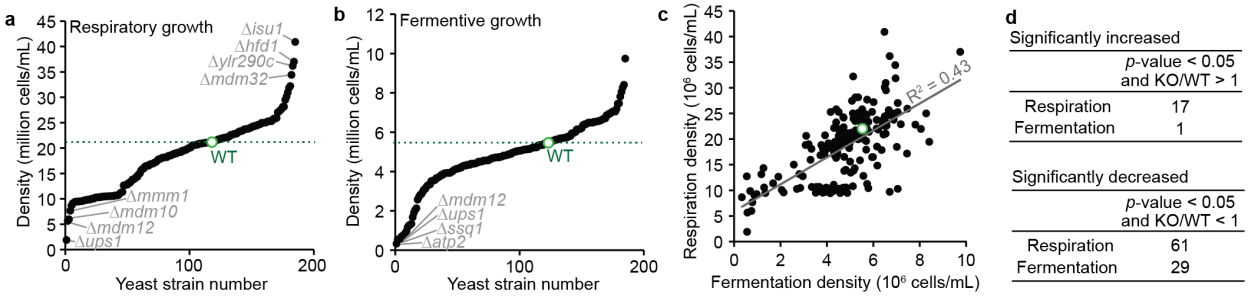

Figure 4 | Yeast growth rates. **a**, Density of yeast cultures in the respiratory growth condition (mean, n = 3). **b**, Density of yeast cultures in the fermentation growth condition (mean, n = 3). **c**, Correlation of yeast culture densities in fermentation vs respiration growth condition (mean, n = 3). **d**, Tables of significant changes in yeast culture densities.

Figure 5.

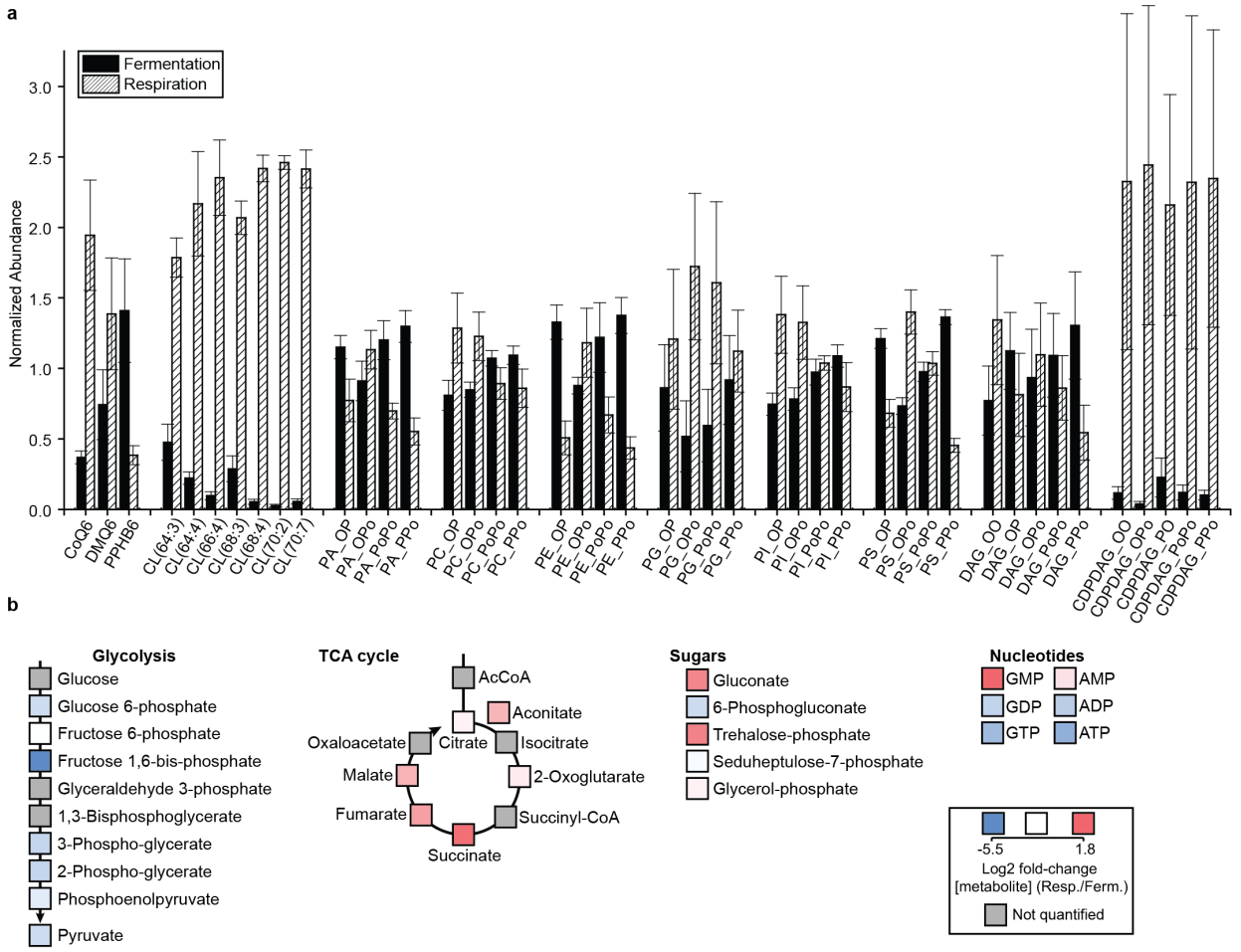

Figure 5 | Respiration-fermentation differences. a, Normalized abundances of lipid species in wild type yeast under fermentation or respiration (mean ± sd, n = 3). DMQ6, Demethoxy-coenzyme Q_6; PPHB, 3-polyprenyl-4-hydroxybenzoic acid; CL, cardiolipin; PA, phosphatidic acid; PC, phosphatidylcholine; PE, phosphatidylethanolamine; PG, phosphatidylglycerol; PI, phosphatidylinositol; PS, phosphatidylserine; DAG, diacylglycerol; CDP-DAG, cytidine diphosphate-diacylglycerol; O, oleic acid; P, palmitic acid; Po, palmitoleic acid. **b**, Heat map of metabolites in central carbon metabolism highlighting changes between respiration and fermentation.

Figure 6.

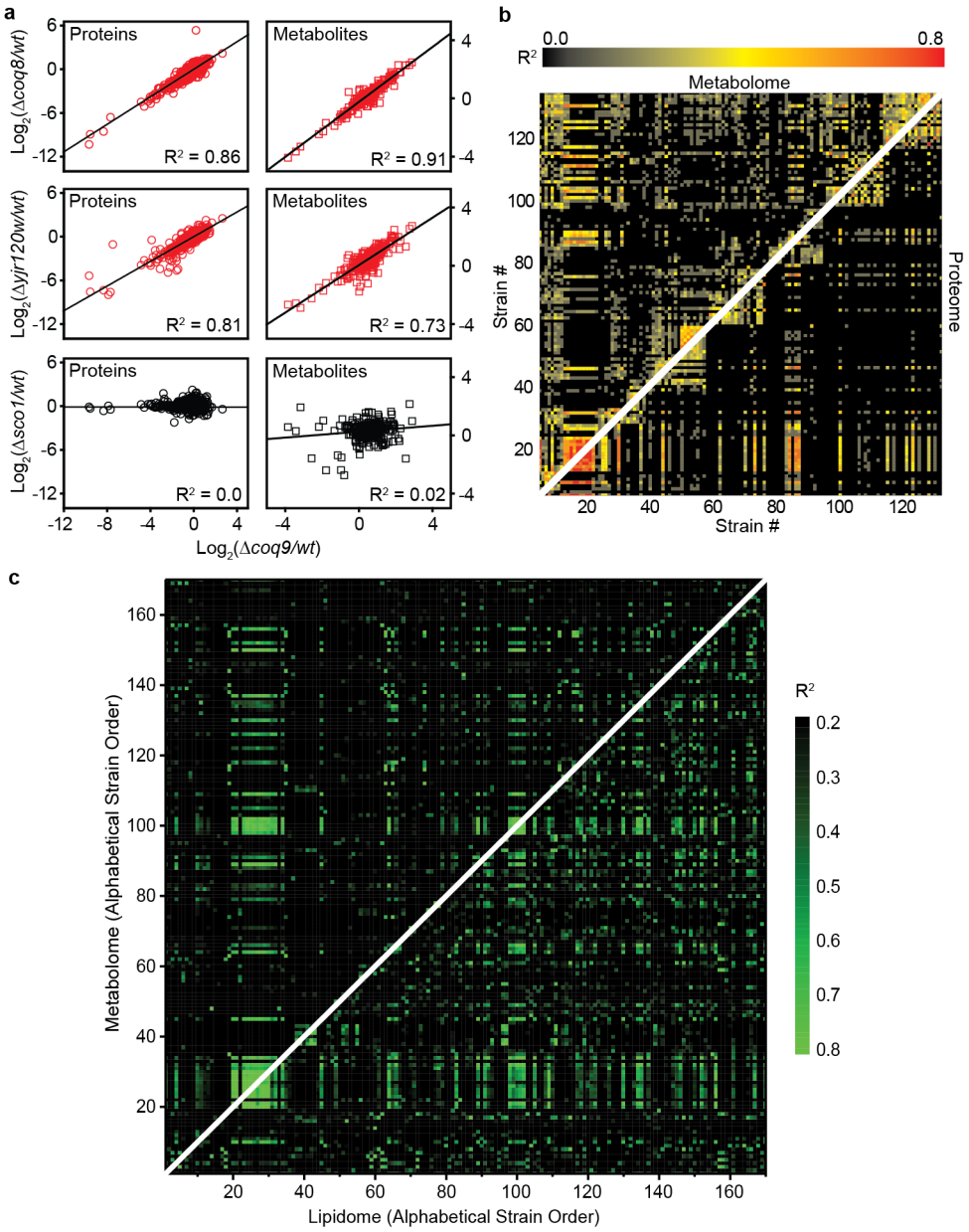

Figure 6 | Correlations between perturbation profiles reveal functional relationships. All three panels in this figure show data for the respiration culture condition. Parallel data has been collected for the fermentation condition (data not shown). **a**, Pairwise whole-proteome and whole-metabolome correlation plots comparing Δ*gene* strains, annotated with Pearson correlation coefficients. Proteins (o) and metabolites (□) are plotted as $\log_2(\Delta gene/wt)$ of label

free quantitation (LFQ) values (mean, n = 3). **b**, Heat map of correlation coefficients for each pairwise Δ*gene*/*wt* vs Δ*gene*/*wt* comparison. Whole metabolome correlations are shown in the top left triangle, and whole proteome correlations are shown in the bottom right triangle. **c**, Heat map of correlation coefficients for each pairwise Δ*gene*/*wt* vs Δ*gene*/*wt* comparison. Whole metabolome correlations are shown in the top left triangle, and whole lipidome correlations are shown in the bottom right triangle.

Figure 7.

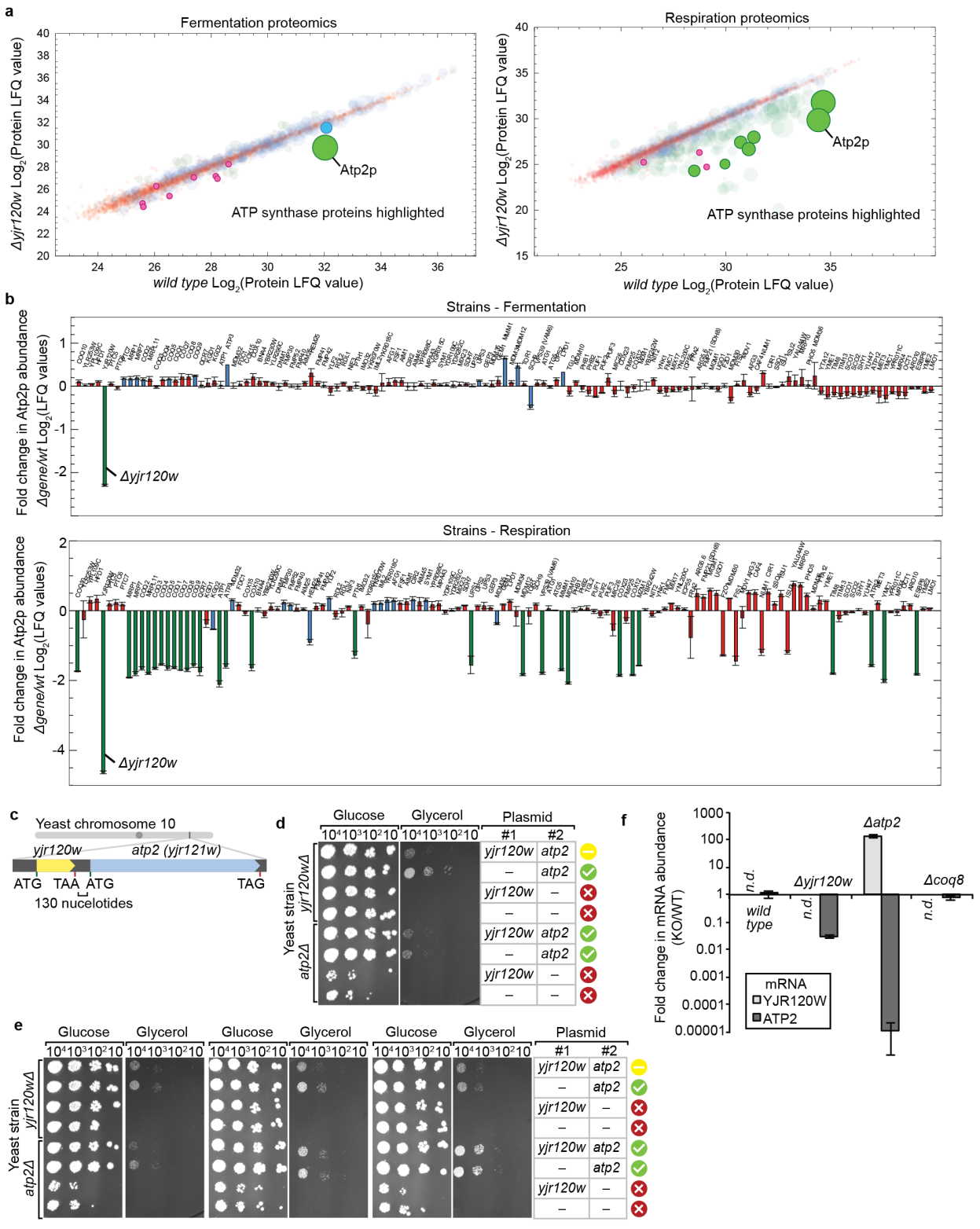
a
Fermentation proteomics
Δyjr120w Log2(Protein LFQ value)
wild type Log2(Protein LFQ value)
Atp2p
ATP synthase proteins highlighted
Respiration proteomics
Δyjr120w Log2(Protein LFQ value)
wild type Log2(Protein LFQ value)
Atp2p
ATP synthase proteins highlighted
b
Strains - Fermentation
Fold change in Atp2p abundance
Δgene/wt Log2(LFQ values)
Δyjr120w
Strains - Respiration
Fold change in Atp2p abundance
Δgene/wt Log2(LFQ values)
Δyjr120w
c
Yeast chromosome 10
yjr120w
atp2 (yjr121w)
ATG TAA ATG
TAG
130 nucelotides
d
Glucose
Glycerol
Plasmid
#1
#2
Yeast strain
yjr120wΔ
atp2Δ
yjr120w
atp2
e
Glucose
Glycerol
Plasmid
#1
#2
Yeast strain
yjr120wΔ
atp2Δ
yjr120w
atp2
f
Fold change in mRNA abundance (KO/WT)
n.d.
wild type
Δyjr120w
Δatp2
Δcoq8
mRNA
YJR120W
ATP2

Figure 7 | Yjr120w affects ATP synthase. a, Comparisons of the proteomes of Δ*yjr120w* and wild type yeast in fermentation and respiration. **b**, Changes in Atp2p protein abundance ($\log_2$(Δ*gene*/*wt*)) in fermentation and respiration across knockout strains in the study. **c**, Genomic organization of *yjr120w* and *atp2*. **d**, Serial dilutions of yeast transformed with the indicated plasmids grown on agar plates with glucose or glycerol. Red X symbols indicate no growth on glycerol, yellow dash symbols indicate moderate or low growth on glycerol, and green check mark symbols indicate WT-like growth on glycerol. **e**, Three additional replicates of that shown in (d). **f**, Fold changes (Δ*gene*/*wt*) in *yjr120w* and *atp2* gene expression (normalized to a control mRNA, *ubc6*).

Figure 8.

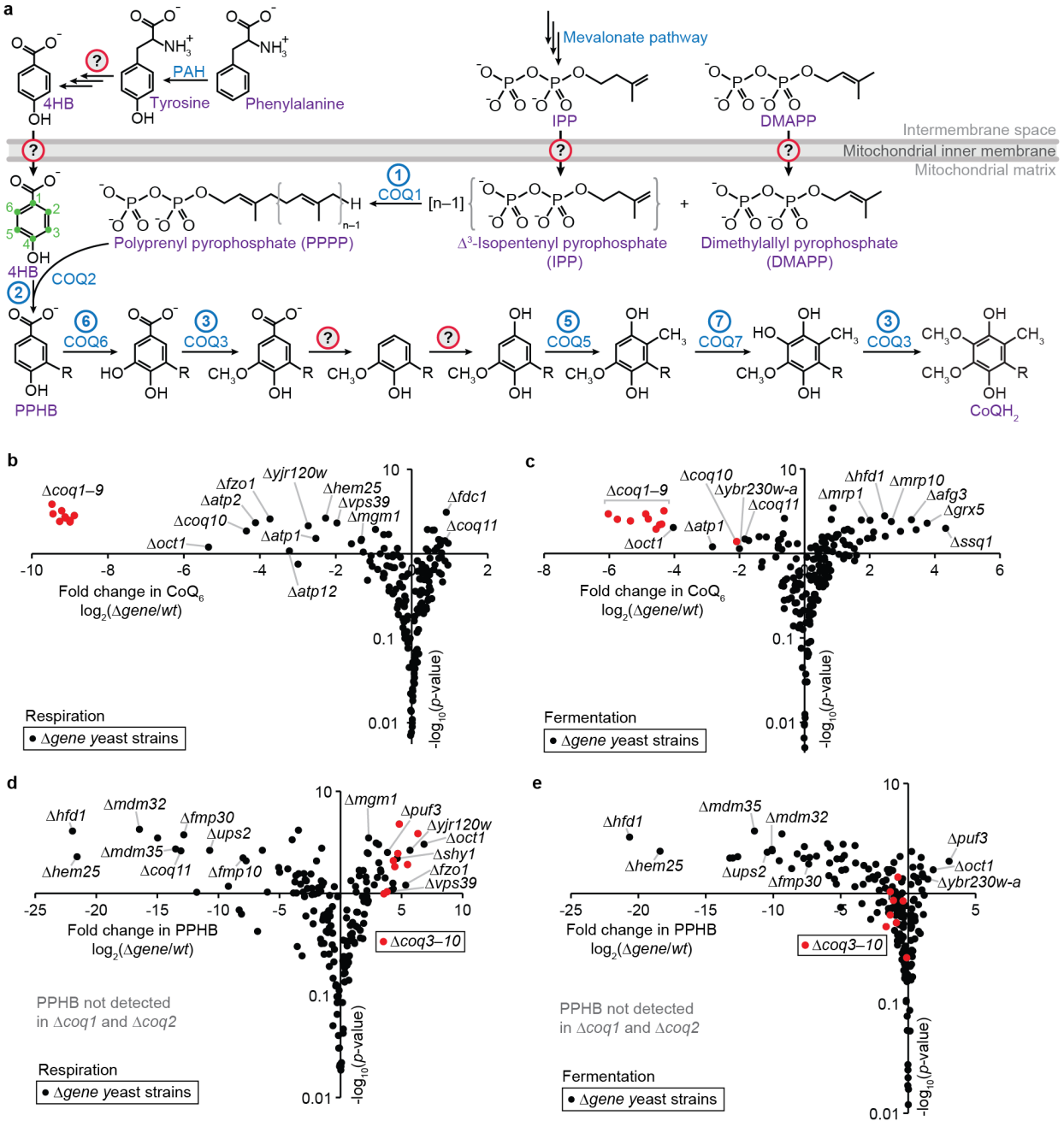

Figure 8 | Molecular insight into CoQ biosynthesis. a, Scheme of CoQ biosynthesis, highlighting missing enzymes and missing transporters. 4-HB, 4-hydroxybenzoic acid; PPHB, 3-polyprenyl-4-hydroxybenzoic acid. **b-c**, Fold changes in CoQ_6 abundance (mean $\log_2(\Delta gene/wt)$, n = 3) versus statistical significance ($-\log_{10}(p\text{-value})$) as quantified by LC-MS for respiration (**b**)

and fermentation (**c**). **d-e**, Fold changes in PPHB abundance (mean $\log_2(\Delta gene/wt)$, n = 3) versus statistical significance ($-\log_{10}(p\text{-value})$) as quantified by LC-MS for respiration (**d**) and fermentation (**e**).

Extended Data Table 1. Y3K target strains

Deleted gene (systematic)	Deleted gene (standard)	Human homolog(s)	D.J.P. Archive #	Associated human disease(s)
YLR304C	ACO1	ACO2	Sc-III-A3	Infantile cerebellar-retinal degeneration; optic atrophy 8.
YJL200C	ACO2	ACO2	Sc-IV-E6	Infantile cerebellar-retinal degeneration; optic atrophy 8.
YEL052W	AFG1	LACE1	Sc-III-B2	
YER017C	AFG3	AFG3L2	Sc-II-C9	Autosomal dominant spinocerebellar ataxia (SCA28)
YAL046C	AIM1	BOLA3	Sc-III-B4	multiple mitochondrial dysfunctions syndrome-2
YJR100C	AIM25	PLSCR3	Sc-II-I9	
YPR004C	AIM45	ETFA	Sc-III-B6	Glutaric acidemia IIA
YER069W	ARG5,6	NAGS	Sc-II-F2	N-acetylglutamate synthase deficiency
YDR380W	ARO10	None	Sc-III-I9	
YGL180W	ATG1	ULK1, ULK2, ULK3	Sc-III-D9	
YPL149W	ATG5	ATG5	Sc-III-E1	
YBL099W	ATP1	ATP5A1	Sc-II-B6	Fatal neonatal mitochondrial encephalopathy
YJL180C	ATP12	ATPAF2	Sc-III-I4	Mitochondrial complex V deficiency, nuclear type 1
YJR121W	ATP2	ATP5B	Sc-IV-F7	
YBR039W	ATP3	ATP5C1	Sc-II-B7	
YBL098W	BNA4	KMO	Sc-II-I2	Therapeutic target for Huntingtons disease
YKR036C	CAF4	None	Sc-III-H1	
YCL064C	CHA1	SDS	Sc-IV-H7	
YGR207C	CIR1	ETFB	Sc-III-H3	Glutaric acidemia IIB
YOR356W	CIR2	ETFDH	Sc-III-B5	Glutaric acidemia IIC, secondary CoQ deficiency.
YGR110W	CLD1	ABHD4	Sc-IV-C2	
YBR003W	COQ1	PDSS1, PDSS2	Sc-II-A7	CoQ deficiency.
YOL008W	COQ10	COQ10	Sc-II-A6	
YLR290C	COQ11	NDUFA9	Sc-II-I4	Leigh syndrome (NDUFA9)
YNR041C	COQ2	COQ2	Sc-II-A8	CoQ deficiency, multiple system atrophy.
YOL096C	COQ3	COQ3	Sc-II-A5	
YDR204W	COQ4	COQ4	Sc-II-A4	CoQ deficiency.
YML110C	COQ5	COQ5	Sc-II-A3	

Extended Data Table 1. Y3K target strains (continued)

Deleted gene (systematic)	Deleted gene (standard)	Human homolog(s)	D.J.P. Archive #	Associated human disease(s)
YGR255C	COQ6	COQ6	Sc-IV-E2	Coenzyme Q10 deficiency, primary, 6
YOR125C	COQ7	COQ7	Sc-II-C2	CoQ deficiency.
YGL119W	COQ8	COQ8	Sc-II-C3	CoQ deficiency, ARCA2, SRNS
YLR201C	COQ9	COQ9	Sc-II-A2	CoQ deficiency.
YPL172C	COX10	COX10	Sc-II-I1	Leigh, De Toni-Fanconi-Debre, Charcot-Marie-Tooth type 1A, HNPP
YLR038C	COX12	COX6B1, COX6B2	Sc-II-H5	CIV deficiency.
YHR116W	COX23	CHCHD7	Sc-III-F1	
YDL142C	CRD1	CRLS1	Sc-IV-C1	Possible cause of Leigh syndrome
YLR348C	DIC1	SLC25A10	Sc-IV-G9	
YLL001W	DNM1	DNM1L	Sc-II-I5	Encephalopathy
YCL045C	EMC1	EMC1	Sc-IV-F8	
YJR088C	EMC2	EMC2	Sc-IV-F9	
YKL207W	EMC3	EMC3	Sc-IV-G1	
YGL231C	EMC4	EMC4	Sc-IV-G2	
YIL027C	EMC5	MMGT1	Sc-IV-G3	
YLL014W	EMC6	EMC6	Sc-IV-G4	
YLR056W	ERG3	SC5D	Sc-IV-G8	Lathosterolosis
YMR015C	ERG5	CYP26A1 (?)	Sc-IV-E9	
YNL125C	ESBP6	SLC16A12 (?)	Sc-IV-A1	Cataract, juvenile, with microcornea and glucosuria
YKL187C	FAT3	None	Sc-IV-F5	
YDR539W	FDC1	None	Sc-II-H8	
YIL065C	FIS1	FIS1	Sc-III-G8	
YIL098C	FMC1	C7orf55	Sc-III-F7	
YER182W	FMP10	THEM4	Sc-IV-H2	
YDR070C	FMP16	None	Sc-IV-H1	
YBR269C	FMP21 (SDH8)	SDHAF4	Sc-II-F3	
YLR077W	FMP25	RCBTB2 (?)	Sc-III-F2	
YLR454W	FMP27	BCOX1	Sc-IV-H3	
YPL103C	FMP30	NAPEPLD	Sc-II-I6	
YPL222W	FMP40	SELO	Sc-II-I8	
YNL168C	FMP41	FAHD1	Sc-III-A2	
YMR221C	FMP42	SLC43A3	Sc-II-E6	
YER004W	FMP52	HTATIP2	Sc-II-I7	
YGL220W	FRA2	BOLA2	Sc-III-G4	
YOR271C	FSF1	SFXN5	Sc-III-B3	
YHR059W	FYV4	None	Sc-IV-B6	

Extended Data Table 1. Y3K target strains (continued)

Deleted gene (systematic)	Deleted gene (standard)	Human homolog(s)	D.J.P. Archive #	Associated human disease(s)
YBR179C	FZO1	MFN1, MFN2	Sc-III-G6	Charcot-Marie-Tooth disease type 2A2
YAL048C	GEM1	MIRO1, MIRO2	Sc-III-D1	
YHR100C	GEP4	None	Sc-IV-B2	
YPL059W	GRX5	GLRX5	Sc-IV-A7	autosomal recessive pyridoxine-refractory sideroblastic anemia
YDL119C	HEM25	SLC25A38	Sc-III-A1	autosomal congenital sideroblastic anemia
YMR110C	HFD1	ALDH3A1, ALDH3A2	Sc-II-E4	Sjogren-Larsson syndrome
YER078C	ICP55	XPNPEP3	Sc-III-F9	Nephronophthisis-like neuropathy 1
YNL037C	IDH1	IDH3G, IDH3B	Sc-IV-C5	Retinitis pigmentosa 46
YOR136W	IDH2	IDH3A	Sc-IV-C6	
YJL082W	IML2	TTC39C (?)	Sc-III-A9	
YGR031W	IMO32	ABHD11	Sc-III-A6	ABHD11 gene is deleted in Williams syndrome
YER019W	ISC1	SMPD2	Sc-IV-B4	
YPL135W	ISU1	ISCU1, ISCU2	Sc-III-H5	Myopathy with lactic acidosis
YOR226C	ISU2	ISCU1, ISCU2	Sc-III-H6	Myopathy with lactic acidosis
YIL125W	KGD1	OGDH	Sc-II-E8	oxoglutaric aciduria
YDR148C	KGD2	DLST	Sc-II-E3	
YLR239C	LIP2	LIPT2	Sc-IV-F3	
YLL007C	LMO1	None	Sc-IV-A3	
YKL150W	MCR1	CYB5R2 (?)	Sc-IV-E8	
YAL010C	MDM10	None	Sc-III-E2	
YOL009C	MDM12	None	Sc-III-D5	
YLR368W	MDM30	None	Sc-III-G7	
YOR147W	MDM32	None	Sc-II-C1	
YKL053C-A	MDM35	TRIAP1	Sc-III-C9	
YPR083W	MDM36	None	Sc-III-H7	
YOL027C	MDM38	LETM1	Sc-IV-E5	Wolf-Hirschhorn syndrome
YJL112W	MDV1	None	Sc-III-G9	
YLR069C	MEF1	GFM1	Sc-IV-C7	Combined oxidative phosphorylation deficiency 1
YJL102W	MEF2	GFM2	Sc-IV-C8	neurodevelopmental disorder with diabetes

Extended Data Table 1. Y3K target strains (continued)

Deleted gene (systematic)	Deleted gene (standard)	Human homolog(s)	D.J.P. Archive #	Associated human disease(s)
YJR010W	MET3	PAPSS2	Sc-III-I5	Brachyolmia 4 with mild epiphyseal and metaphyseal changes
YOR211C	MGM1	OPA1	Sc-II-F5	Autosomal dominant optic atrophy
YGR235C	MIC26	APOO	Sc-III-E9	
YDR031W	MIX14	CHCHD5	Sc-IV-G7	
YMR002W	MIX17	CHCHD2, CHCHD10	Sc-II-H6	Mitochondrial myopathy, ALS2, spinal muscular atrophy.
YBL107C	MIX23	None	Sc-III-C3	
YLL006W	MMM1	None	Sc-III-D2	
YNL249C	MPA43	FGGY	Sc-III-B9	ALS
YGL080W	MPC1	MPC1	Sc-IV-H4	
YHR162W	MPC2	MPC2	Sc-IV-H5	
YGR243W	MPC3	MPC2	Sc-IV-H6	
YJL066C	MPM1	None	Sc-IV-F6	
YDR347W	MRP1	None	Sc-II-B3	
YDL045W-A	MRP10	CHCHD1	Sc-III-G2	
YNL005C	MRP7	MRPL27	Sc-II-B4	
YDL202W	MRPL11	None	Sc-II-B5	
YDR282C	MRX10	RMND1	Sc-III-C2	Infantile encephaloneuromyopathy, Combined oxidative phosphorylation deficiency 11
YBL095W	MRX3	THEM4 (?)	Sc-IV-F1	
YPL168W	MRX4	None	Sc-III-I8	
YDR493W	MZM1	LYRM7	Sc-III-F3	CIII deficiency.
YGL221C	NIF3	NIF3L1	Sc-III-A4	
YJL126W	NIT2	NIT1	Sc-III-F5	
YDR150W	NUM1	None	Sc-III-H2	
YKL134C	OCT1	MIPEP	Sc-II-C4	
YBR230C	OM14	None	Sc-IV-G5	
YIL136W	OM45	None	Sc-IV-G6	
YGR132C	PHB1	PHB	Sc-III-E3	Breast cancer susceptibility
YGR231C	PHB2	PHB2	Sc-III-E4	
YBR093C	PHO5	MINPP1 (?)	Sc-III-G3	
YGR086C	PIL1	None	Sc-IV-B3	
YMR006C	PLB2	PLA2G4F	Sc-IV-B9	
YNL055C	POR1	VDAC3, VDAC2, VDAC1	Sc-IV-A8	Encephalopathy, mitochondrial

Extended Data Table 1. Y3K target strains (continued)

Deleted gene (systematic)	Deleted gene (standard)	Human homolog(s)	D.J.P. Archive #	Associated human disease(s)
YOR090C	PTC5	PDP2	Sc-II-A9	
YCR079W	PTC6	PPM1K (?)	Sc-II-B1	
YHR076W	PTC7	PPTC7	Sc-II-B2	
YHR189W	PTH1	PTRH1	Sc-III-A5	
YJR091C	PUF1	PUM2, PUM1	Sc-III-E6	
YPR042C	PUF2	PUM2, PUM1	Sc-III-E7	
YLL013C	PUF3	PUM2, PUM1	Sc-III-E8	
YDR529C	QCR7	UQCRB	Sc-II-E9	CIII deficiency
YBR005W	RCR1	None	Sc-IV-E3	
YOR285W	RDL1	TSTD1 (?)	Sc-II-H7	
YOR286W	RDL2 (AIM42)	TSTD1	Sc-II-G3	
YEL024W	RIP1	UQCRFS1	Sc-IV-A6	
YHR205W	SCH9	RPS6KB1, RPS6KB2	Sc-III-D7	
YBR024W	SCO2	SCO1	Sc-III-I1	Cardioencephalomyopathy, Hepatic failure, early onset, and neurologic disorder
YKL148C	SDH1	SDHA	Sc-IV-A4	Leigh syndrome
YJL045W	SDH1b	SDHA	Sc-IV-A5	Leigh syndrome
YDR511W	SDH7	SDHAF3	Sc-III-C4	Mitochondrial disease
YDR393W	SHE9 (MDM33)	None	Sc-IV-A9	
YGR112W	SHY1	SURF1	Sc-III-I2	Leigh Syndrome, due to COX def.
YHR008C	SOD2	SOD2	Sc-IV-E7	Microvascular complications of diabetes 6
YLR369W	SSQ1	HSPA9 (?)	Sc-III-H4	
YML052W	SUR7	None	Sc-IV-B7	
YLR251W	SYM1	MPV17	Sc-III-B7	Hepatocerebral mtDNA depeltion syndromes (MDDS)
YPR140W	TAZ1	TAZ	Sc-IV-C3	Barth syndrome
YDR058C	TGL2	None	Sc-III-E5	
YGR181W	TIM13	TIMM13	Sc-IIIH9	
YJR135W-A	TIM8	TIMM8A	Sc-III-H8	Deafness-dystonia syndrome (DDON), Mohr-Tranebjaerg syndrome, Jensen syndrome.
YNL121C	TOM70	TOMM70A	Sc-IV-C4	
YJR066W	TOR1	MTOR	Sc-III-D6	

Extended Data Table 1. Y3K target strains (continued)

Deleted gene (systematic)	Deleted gene (standard)	Human homolog(s)	D.J.P. Archive #	Associated human disease(s)
YDR470C	UGO1	None	Sc-III-G5	
YLR193C	UPS1	PRELID1	Sc-III-C5	
YLR168C	UPS2	SLMO1, SLMO2	Sc-III-C6	
YDR185C	UPS3	SLMO2, SLMO1	Sc-III-C7	
YDL077C	VPS39 (VAM6)	VPS39	Sc-III-D8	
YAL044W-A	YAL044W-A	BOLA1, BOLA2	Sc-III-G1	
YBR230W-A	YBR230W-A	None	Sc-II-I3	
YBR242W	YBR242W	HDDC2	Sc-III-F4	
YDL157C	YDL157C	None	Sc-IV-F2	
YDR109C	YDR109C	FGGY	Sc-III-C1	ALS
YFR045W	YFR045W	SLC25A1 (?)	Sc-IV-F4	Combined D-2- and L-2-hydroxyglutaric aciduria
YGL117W	YGL117W	None	Sc-IV-E4	
YGR015C	YGR015C	ABHD11 (?)	Sc-III-A7	*ABHD11* is deleted in Williams syndrome
YMR241W	YHM2	SLC25A21 (?)	Sc-IV-B8	
YJR120W	YJR120W	None	Sc-IV-E1	
YKR018C	YKR018C	TTC39C	Sc-III-B1	
YKR070W	YKR070W	CECR5	Sc-III-A8	Cat eye syndrome
YHL014C	YLF2	OLA1 (?)	Sc-II-F8	
YPR125W	YLH47	LETM1	Sc-III-I3	Wolf-Hirschhorn syndrome
YLR253W	YLR253W	ADCK1, ADCK5	Sc-II-B8	
YPR058W	YMC1	SLC25A29	Sc-III-I6	
YPR024W	YME1	YME1L1	Sc-II-C8	
YMR302C	YME2	None	Sc-IV-A2	
YKL067W	YNK1	NME1, NME2	Sc-III-F6	
YNL200C	YNL200C	APOA1BP	Sc-III-F8	
YPL109C	YPL109C	ADCK2	Sc-II-B9	
YPR011C	YPR011C	SLC25A16	Sc-III-I7	Graves' Disease.
YPR098C	YPR098C	TMEM205	Sc-III-B8	
YMR089C	YTA12	SPG7 (Paraplegin)	Sc-II-D1	Hereditary spastic paraplegia 7

References

Aebersold, R., and Mann, M. (2003). Mass spectrometry-based proteomics. Nature *422*, 198-207.

Alexander, C., Votruba, M., Pesch, U.E., Thiselton, D.L., Mayer, S., Moore, A., Rodriguez, M., Kellner, U., Leo-Kottler, B., Auburger, G.*, et al.* (2000). OPA1, encoding a dynamin-related GTPase, is mutated in autosomal dominant optic atrophy linked to chromosome 3q28. Nat Genet *26*, 211-215.

Archer, S.L. (2013). Mitochondrial dynamics--mitochondrial fission and fusion in human diseases. N Engl J Med *369*, 2236-2251.

Branda, S.S., and Isaya, G. (1995). Prediction and identification of new natural substrates of the yeast mitochondrial intermediate peptidase. J Biol Chem *270*, 27366-27373.

Casanovas, A., Sprenger, R.R., Tarasov, K., Ruckerbauer, D.E., Hannibal-Bach, H.K., Zanghellini, J., Jensen, O.N., and Ejsing, C.S. (2015). Quantitative analysis of proteome and lipidome dynamics reveals functional regulation of global lipid metabolism. Chem Biol *22*, 412-425.

Delettre, C., Lenaers, G., Griffoin, J.M., Gigarel, N., Lorenzo, C., Belenguer, P., Pelloquin, L., Grosgeorge, J., Turc-Carel, C., Perret, E.*, et al.* (2000). Nuclear gene OPA1, encoding a mitochondrial dynamin-related protein, is mutated in dominant optic atrophy. Nat Genet *26*, 207-210.

DeRisi, J.L., Iyer, V.R., and Brown, P.O. (1997). Exploring the metabolic and genetic control of gene expression on a genomic scale. Science *278*, 680-686.

Elbaz-Alon, Y., Rosenfeld-Gur, E., Shinder, V., Futerman, A.H., Geiger, T., and Schuldiner, M. (2014). A dynamic interface between vacuoles and mitochondria in yeast. Dev Cell *30*, 95-102.

Giaever, G., Chu, A.M., Ni, L., Connelly, C., Riles, L., Veronneau, S., Dow, S., Lucau-Danila, A., Anderson, K., Andre, B.*, et al.* (2002). Functional profiling of the Saccharomyces cerevisiae genome. Nature *418*, 387-391.

Green, E.D., Guyer, M.S., and National Human Genome Research, I. (2011). Charting a course for genomic medicine from base pairs to bedside. Nature *470*, 204-213.

Guernsey, D.L., Jiang, H., Campagna, D.R., Evans, S.C., Ferguson, M., Kellogg, M.D., Lachance, M., Matsuoka, M., Nightingale, M., Rideout, A.*, et al.* (2009). Mutations in mitochondrial carrier family gene SLC25A38 cause nonsyndromic autosomal recessive congenital sideroblastic anemia. Nat Genet *41*, 651-653.

Hales, K.G., and Fuller, M.T. (1997). Developmentally regulated mitochondrial fusion mediated by a conserved, novel, predicted GTPase. Cell *90*, 121-129.

He, C.H., Xie, L.X., Allan, C.M., Tran, U.C., and Clarke, C.F. (2014). Coenzyme Q supplementation or over-expression of the yeast Coq8 putative kinase stabilizes multi-subunit Coq polypeptide complexes in yeast coq null mutants. Biochim Biophys Acta *1841*, 630-644.

Hebert, A.S., Richards, A.L., Bailey, D.J., Ulbrich, A., Coughlin, E.E., Westphall, M.S., and Coon, J.J. (2014). The one hour yeast proteome. Mol Cell Proteomics *13*, 339-347.

Hermann, G.J., Thatcher, J.W., Mills, J.P., Hales, K.G., Fuller, M.T., Nunnari, J., and Shaw, J.M. (1998). Mitochondrial fusion in yeast requires the transmembrane GTPase Fzo1p. J Cell Biol *143*, 359-373.

Hughes, T.R., Marton, M.J., Jones, A.R., Roberts, C.J., Stoughton, R., Armour, C.D., Bennett, H.A., Coffey, E., Dai, H., He, Y.D.*, et al.* (2000). Functional discovery via a compendium of expression profiles. Cell *102*, 109-126.

Isaya, G., Kalousek, F., and Rosenberg, L.E. (1992). Amino-terminal octapeptides function as recognition signals for the mitochondrial intermediate peptidase. J Biol Chem *267*, 7904-7910.

Jonikas, M.C., Collins, S.R., Denic, V., Oh, E., Quan, E.M., Schmid, V., Weibezahn, J., Schwappach, B., Walter, P., Weissman, J.S.*, et al.* (2009). Comprehensive characterization of genes required for protein folding in the endoplasmic reticulum. Science *323*, 1693-1697.

Kellis, M., Birren, B.W., and Lander, E.S. (2004). Proof and evolutionary analysis of ancient genome duplication in the yeast Saccharomyces cerevisiae. Nature *428*, 617-624.

Kemmeren, P., Sameith, K., van de Pasch, L.A., Benschop, J.J., Lenstra, T.L., Margaritis, T., O'Duibhir, E., Apweiler, E., van Wageningen, S., Ko, C.W.*, et al.* (2014). Large-scale genetic perturbations reveal regulatory networks and an abundance of gene-specific repressors. Cell *157*, 740-752.

Koopman, W.J., Willems, P.H., and Smeitink, J.A. (2012). Monogenic mitochondrial disorders. N Engl J Med *366*, 1132-1141.

Kornmann, B., Currie, E., Collins, S.R., Schuldiner, M., Nunnari, J., Weissman, J.S., and Walter, P. (2009). An ER-mitochondria tethering complex revealed by a synthetic biology screen. Science *325*, 477-481.

Mardis, E.R. (2011). A decade's perspective on DNA sequencing technology. Nature *470*, 198-203.

Mourier, A., Motori, E., Brandt, T., Lagouge, M., Atanassov, I., Galinier, A., Rappl, G., Brodesser, S., Hultenby, K., Dieterich, C.*, et al.* (2015). Mitofusin 2 is required to maintain mitochondrial coenzyme Q levels. J Cell Biol *208*, 429-442.

Nakahara, K., Ohkuni, A., Kitamura, T., Abe, K., Naganuma, T., Ohno, Y., Zoeller, R.A., and Kihara, A. (2012). The Sjogren-Larsson syndrome gene encodes a hexadecenal dehydrogenase of the sphingosine 1-phosphate degradation pathway. Mol Cell *46*, 461-471.

Nunnari, J., and Suomalainen, A. (2012). Mitochondria: in sickness and in health. Cell *148*, 1145-1159.

Pagliarini, D.J., Calvo, S.E., Chang, B., Sheth, S.A., Vafai, S.B., Ong, S.E., Walford, G.A., Sugiana, C., Boneh, A., Chen, W.K.*, et al.* (2008). A mitochondrial protein compendium elucidates complex I disease biology. Cell *134*, 112-123.

Pagliarini, D.J., and Rutter, J. (2013). Hallmarks of a new era in mitochondrial biochemistry. Genes Dev *27*, 2615-2627.

Picotti, P., Bodenmiller, B., Mueller, L.N., Domon, B., and Aebersold, R. (2009). Full dynamic range proteome analysis of S. cerevisiae by targeted proteomics. Cell *138*, 795-806.

Quiros, P.M., Langer, T., and Lopez-Otin, C. (2015). New roles for mitochondrial proteases in health, ageing and disease. Nat Rev Mol Cell Biol *16*, 345-359.

Richards, A.L., Hebert, A.S., Ulbrich, A., Bailey, D.J., Coughlin, E.E., Westphall, M.S., and Coon, J.J. (2015). One-hour proteome analysis in yeast. Nat Protoc *10*, 701-714.

Sesaki, H., Southard, S.M., Yaffe, M.P., and Jensen, R.E. (2003). Mgm1p, a dynamin-related GTPase, is essential for fusion of the mitochondrial outer membrane. Mol Biol Cell *14*, 2342-2356.

Steinmetz, L.M., Scharfe, C., Deutschbauer, A.M., Mokranjac, D., Herman, Z.S., Jones, T., Chu, A.M., Giaever, G., Prokisch, H., Oefner, P.J.*, et al.* (2002). Systematic screen for human disease genes in yeast. Nat Genet *31*, 400-404.

Vafai, S.B., and Mootha, V.K. (2012). Mitochondrial disorders as windows into an ancient organelle. Nature *491*, 374-383.

Vogtle, F.N., Prinz, C., Kellermann, J., Lottspeich, F., Pfanner, N., and Meisinger, C. (2011). Mitochondrial protein turnover: role of the precursor intermediate peptidase Oct1 in protein stabilization. Mol Biol Cell *22*, 2135-2143.

Winzeler, E.A., Shoemaker, D.D., Astromoff, A., Liang, H., Anderson, K., Andre, B., Bangham, R., Benito, R., Boeke, J.D., Bussey, H.*, et al.* (1999). Functional characterization of the S. cerevisiae genome by gene deletion and parallel analysis. Science *285*, 901-906.

Zuchner, S., Mersiyanova, I.V., Muglia, M., Bissar-Tadmouri, N., Rochelle, J., Dadali, E.L., Zappia, M., Nelis, E., Patitucci, A., Senderek, J.*, et al.* (2004). Mutations in the mitochondrial GTPase mitofusin 2 cause Charcot-Marie-Tooth neuropathy type 2A. Nat Genet *36*, 449-451.